



Description of ILW modelling results and recommendations for future experiments and numerical work: Deliverable 2.15

Work Package [2](#)

EURAD Deliverable 2.15 – ILW modelling results and recommendations

The project leading to this application has received funding from the European Union's Horizon 2020 research and innovation programme under grant agreement No 847593.



Document information

Project Acronym	EURAD
Project Title	European Joint Programme on Radioactive Waste Management
Project Type	European Joint Programme (EJP)
EC grant agreement No.	847593
Project starting / end date	1 st June 2019 – 30 May 2024
Work Package No.	2
Work Package Title	<u>A</u> ssessment of <u>C</u> hemical <u>E</u> volution of ILW and HLW <u>D</u> isposal Cells
Work Package Acronym	ACED
Deliverable No.	D2.15
Deliverable Title	Description of ILW modelling results and recommendations for future experiments and numerical work: Deliverable 2.15
Lead Beneficiary	BRGM
Contractual Delivery Date	M53
Actual Delivery Date	M60
Type	Report
Dissemination level	PU
Authors	Philippe Blanc (BRGM), Joan Govaerts (SCK CEN), Yushan Gu (VTT), Diederik Jacques (SCK CEN), Georg Kosakowski (PSI), Markku Leivo (VTT), Nicolas Marty (BRGM), Erika Neeft (COVRA), Haibing Shao (UFZ), Falko Vehling (UFZ)

To be cited as:

Blanc P, Govaerts J, Gu Y, Jacques D, Kosakowski G, Leivo M, Marty N, Neeft E, Shao H, Vehling F (2024): Description of ILW modelling results and recommendations for future experiments and numerical work: Deliverable 2.15 of the HORIZON 2020 project EURAD. EC Grant agreement no: 847593.

Disclaimer

All information in this document is provided "as is" and no guarantee or warranty is given that the information is fit for any particular purpose. The user, therefore, uses the information at its sole risk and liability. For the avoidance of all doubts, the European Commission has no liability in respect of this document, which is merely representing the authors' view.

Acknowledgement

This document is a deliverable of the European Joint Programme on Radioactive Waste Management (EURAD). EURAD has received funding from the European Union’s Horizon 2020 research and innovation programme under grant agreement No 847593.

Status of deliverable		
	By	Date
Delivered (Lead Beneficiary)	BRGM	2023-12-15
Verified (WP Leader)	Diederik Jacques (SCK CEN)	2024-01-05
Revised (Lead Beneficiary)	BRGM	2024-01-25
Reviewed (Reviewers)	Andres Idiart (Amphos25)	2024-02-14
Revised (Lead Beneficiary)	BRGM	2024-02-29
Verified (WP Leader)	Diederik Jacques (SCK CEN)	2024-03-08
Approved (PMO)	Tara Beattie	2024-05-07
Submitted to EC	Andra (Coordinator)	2024-05-15

Executive Summary

EURAD WP2 ACED aims at modelling the chemical evolution at the disposal cell scale of geological disposal facilities for intermediate level (ILW) and high level (HLW) waste packages. The disposal cell scale is defined as the system consisting of the host rock and the engineered barrier system (EBS), which includes the waste packages. The disposal cells differ between the various European countries. To ensure the evaluation of the modelling methodologies for a wide but representative range of properties and conditions relevant for different national programs, two representative disposal cells were proposed.

Task 3 of EURAD WP2 ACED concerns the waste package scale, which includes the experimental assessment of different aspects of waste package degradation (task 3.1), the mechanistic modelling of these experiments and the modelling of the long-term chemical evolution of ILW packages (Task 3.3). The subtask 3.3 concerns the modelling of the chemical evolution at the waste package scale, for Intermediate Level Wastes (ILW). A smaller part of the work was devoted to analysing experiments 1 and 2 conducted in Subtask 3.3 with process-based models. The focus of modelling was on running upscaled process models that explore the long-term chemical evolution of waste packages taking into account relevant processes.

This report provides the summary of modelling work on ILW waste packages that was conducted in subtask 3.3 and provides input for an updated state-of-the-art report on the geochemical evolution of ILW waste disposal cells, which is the final deliverable of the EURAD-ACED project.

After an introduction the **Integration of knowledge into models** is summarized in **Chapter 2**.

For ILW, a generic concept was defined in Samper et al. (2022) that was adapted to two host rocks, a clay and a granitic host rock. For both host rocks, the volume in which waste packages are stapled is surrounded by cementitious materials (backfill mortar, shotcrete liner). After closure of the repository, cement-based barrier materials should sustain a stable high pH environment as long as possible to slow corrosion of metals and suppress microbial activity.

Within the ACED project we have defined two typical ILW waste sorts one for activated steel and one for organic matter, because they are present in larger quantities; and because metal corrosion and organic matter degradation are expected to influence strongly the long-term chemical evolution of surrounding materials. We assume that the organic waste materials are cemented in 200 l steel drums. The drums will be placed into disposal containers and the void space between drums will be filled with a low viscosity mortar. The waste sort design for metallic waste uses a reinforced concrete container and contains (carbon) steel waste in a cement matrix.

The most important external process that influences the long-term evolution of waste packages is the evolution of the surrounding near field in terms of water saturation. The re-saturation of the repository is highly dependent on the type of host rock and the gas generation by degradation of wastes. A granitic host rock provides transport pathways for water and gas, which will cause a relatively fast re-saturation of the disposal cells. For a repository in a low permeable clay host rock, full water saturation might be achieved only after very long times, because gas pressure build up can prevent inflow of formation water. In such a case humidity transport in gas phase might be the dominating water transport process in a disposal cell and will be a limiting process if waste package walls are largely intact.

Evolution of waste packages is controlled by several tightly coupled processes that will act inside waste packages, and/or outside in the surrounding barrier materials of the disposal cell. Most influential are:

Anoxic corrosion of metals, specifically iron/steel, that generate large amounts of hydrogen gas and consumes large amounts of water. It is assumed that magnetite will be the final mineral formed, which

would also largely increase the volume occupied by the corrosion products. Corrosion rates are pH dependent and will be very low for porewater pH >12 and 50-100 times higher at pH < 10.5.

Degradation of organic matter (waste materials) by abiotic, biotic or radiolytic processes. Such reactions would produce significant amounts of gases, like CH₄ and CO₂, and would also consume water. Degradation rates for most organic substances are highly uncertain. Most data is available for cellulose, therefore the organic waste sort investigated in Subtask 3 of ACED is assumed to contain mainly cellulose. At high pH, most processes (e.g., biotic processes) are suppressed or very slow, but may become significant for (local) conditions with porewater pH < 11.

Degradation of cementitious materials might occur by carbonation or aggregate-cement reactions or by interactions with water from the host rock.

Carbonation might occur due to the reaction with atmospheric CO₂ during interim storage or during the operational phase of a repository. After carbonation hydrated cement phases are completely transformed into carbonates and some amount of water is released. The porewater in the carbonated materials is close to neutral pH. Experience from engineered structures and from experimental investigations in Subtask 3.1 of ACED shows that the carbonation fronts into cementitious materials progresses slowly and depends highly on the water saturation of the medium. It is not expected that large parts of cementitious materials in a waste package are degraded by this. Of potential higher impact is the CO₂ that originates from degradation of organic wastes, because the potentially produced amounts could degrade large parts of the cement-based materials in the repository.

Aggregate-cement reactions are commonly observed in engineered structures. The pH of affected cement-based materials can be lowered to values < pH 11 over hundreds to (ten-)thousands of years if they can contain reactive (alumino-)silicate minerals. The dissolution of reactive (aggregate) minerals is accelerated at high pH and depends on the reactive surface area, which is known to (inversely) scale with aggregate size.

Degradation of materials in waste packages (e.g., cement leaching) due to water flow across the repository is even in a fully water saturated repository assumed to be negligible, because water fluxes are assumed to be very small, and it can be assumed that reaction/degradation fronts will reach the waste packages only after very long times (c.f. Idiart and Laviña 2019).

Water availability in terms of water saturation and water (humidity) transport is a key process in waste packages during pre-disposal (interim storage) and could be important for storage in low permeable clay host rock. (Bio-)chemical processes might consume considerable amounts of water and will slow down if water cannot be replenished by water flow or humidity transport in gas phase.

The report continues with description of **model implementation and validation by experiments (Chapter 3)**.

Subtask 3.1 includes three experiments that deal with different aspects of the evolution of ILW packages. The experimental details and results are summarized in deliverable 2.13 (Mladenovic et al., 2024).

Experiment 1 is dedicated to the long-term investigation of gas generation and associated chemical changes in 200-liter carbon steel drums filled with organic waste materials under repository conditions. The experiment is in operation since 1997 and gives valuable insight into processes that control degradation of organic waste materials.

Modelling of the experiment is based on the work of Small et al. (2017). With this approach it is possible to reproduce gas generation and measured water composition in the waste packages. In the gas generation experiment, we confirm that gas generation rates increase over time due to metal corrosion and organic matter degradation. CH₄ and CO₂ are the main generated gases, and they show an increasing gas generation rate ranging from 0.0301 to 0.1098 mol/kg/y and from 0.0003 to 0.0114 mol/kg/y, respectively. The pH value of the tank water drops from 11.5 to around 6.8 during the experiment, which is the main reason influencing the gas generation rates. It indicates the importance

of placing cementitious materials in the waste package as a barrier material buffering the pH and thus reducing microbial activities.

Experiment 2 investigates the transport of water in cementitious materials and the oxidation of iron sulphide minerals in blended cement in contact with saline solutions (host rock waters) and the carbonation of cement (CO₂ produced by degradation of organic waste) at different water/gas saturation.

Based on model comparison it was found, that dry out and re-saturation of concrete samples can be described as a non-linear diffusion process. Based on experimental data, a diffusion coefficient for water was fitted for the different investigated concrete.

The non-linear-diffusion description of water transport was used for a reactive transport model that considers for water transport, the saturation dependent diffusion of reactive gases in the gas phase, and a chemical reaction approach that links mineral dissolution rates to size of spherical mineral grains and to pore sizes. This model was used to analyse the observed oxidation and carbonation fronts in concrete. It could be confirmed that progress of carbonation fronts is slowed down if relative humidity is below a certain threshold value. This indicates that some chemical reactions are suppressed if relative humidity is lowered, although there should be still enough water available to drive the reaction. It can be speculated that water bound in relatively small nanometre sized pores, in cements this are typical “gel pores”, is not available for reactions, or that those reactions do not happen in nano-meter sized pores.

Experiment 3 analyses samples from 70–100-year-old concrete from old hydroelectric power plant dams for indications of long-term aggregate reactivity. Due to their age the samples give valuable insight into long-term aggregate reactivity, which cannot be tested with standard short term reactivity tests. This experiment was not modelled in Subtask 3.3, because initial cement composition of concrete and the water saturation history was not known.

In addition, experimental data from EURAD CORI on degradation of polymers (hard polyvinyl chloride) due to hydrolysis/radiolysis are available to estimate organic matter degradation rates. These experimental values are supplemented with data from literature on cellulose and PVC degradations. It can be stated, that gas generation due to radiolysis need very high doses in order to become significant, and that compared to metal corrosion, and (a)biotic degradation of organic matter, gas generation is small.

The focus of work in Subtask 3.3 of EURAD ACED was on **model implementation, abstraction, and application on waste package scale (Chapter 4)**.

- PSI modelled both waste sorts, organic waste in 200l drums and metallic (decommissioning) waste in concrete containers with help of so-called mixing-tank models. These models allow to calculate evolution of a homogenized waste package considering time-dependent internal (or external) processes, namely the degradation of organic matter, the corrosion of steel, the dissolution of aggregates in cementitious materials and the consumption (or release) of water by reactions. The models ignore the effects of liquid saturation, transport of water in the drum, transport in aqueous and gas phase, and spatial material heterogeneities. Therefore, they will not provide a very realistic evolution in time but give information on overall mass balances and possible evolution pathways.

The simple mixing tank model for metal waste container by PSI suggests that more than ~ 3 m³ of water are needed to completely corrode the steel inventory. Because only about 0.5 m³ of water could be stored in the accessible porosity, most of this water must be provided from outside. Furthermore, about ~ 3720 m³ gaseous H₂ (at standard conditions) is released. The period for metal corrosion depends on the initial composition of the container infill mortar, and specifically on the reactivity of the aggregates. Any potential process that might cause degradation of cementitious materials and lowers pore water pH will accelerate metal corrosion. If aggregates are reactive and pH dependence of steel corrosion for pH 10.5 – 12 is assumed, corrosion of complete steel inventory takes about 1000 years, while for non-reactive aggregates and high pH (>12) this takes 100x longer.

In the model for the organic waste sort defined in the ACED project, not excessive amounts of external water are needed to drive steel corrosion and cellulose degradation. If there is initially enough water present in the waste package, water consumption by before mentioned processes is balanced with water production by cement carbonation caused by CO₂ released during organic matter degradation. For a waste drum there are about 1070 mol of H₂ released by steel corrosion, 100 mol CO₂ and 1100 mol CH₄. Both waste degradation processes, steel corrosion and degradation of cellulose, happen at about the same time scale and are completed within a few thousands of years. Similarly, cement degradation by aggregate-cement reaction and cement carbonation happen initially at similar time scales. In the end, carbonation will be the dominating process, because of pH decrease with cement degradation progress, dissolution of reactive aggregates will slow down, while CO₂ release by organic matter degradation will (only) slow down with decreasing organic matter inventory.

- UFZ used a specialized variant of the OpenGeosSys code that allows to calculate two-phase (gas, liquid) multi-component transport in connection with a lookup-table that describes degradation of cementitious materials by aggregate-cement reaction and by carbonation (Huang et al., 2018, 2021). They investigated a setup, where multiple organic waste drums were stapled in concrete containers. The simulation results show how the water supply and gas generation feedback loop works in a waste package, in which the gas generation rates depend on the initial water availability and water transport. The latter in turn depends on gas pressure and properties of the backfill material and the host rock. Through the modelling results, they have identified and characterized four stages in the hydrological evolution of the multiple-drum container setup. In the first stage, an initial (gas) pressure build-up due to metal corrosion and drying of the waste compartment of the drum is observed. In the second stage the metal corrosion and associated gas production is controlled by water fluxes inside the drum towards metal surfaces. In the third stage the water potentials in the waste drums are so low, that water from outside is sucked into the drum. The fourth stage is characterized by an equilibrium between gas generation and water supply from outside the drum. The counter-flow of gas (leaving the drum) and liquid leads to an increase in gas saturation within the entire outer mortar area.
- SCK CEN calculated the alterations in backfill mortar and concrete as a consequence of degradation of organic waste which produces CO₂. They explicitly considered drum geometry in their 2D coupled-reactive-diffusive transport model. They assumed fully water saturated conditions with diffusive transport of water dissolved CO₂. It seems that under diffusive saturated conditions and in the considered time frame of few hundred years, there is a somewhat small reactive shell where CO₂ diffusing from the waste zone and Ca diffusing from the backfill meet and precipitate as calcite. To calculate possible positions of carbonation fronts for partially water saturated conditions, information of saturation states at given moments obtained with the mixing-tank models and boundary conditions from two-phase flow models on vault scale could be combined with the more detailed geochemical calculations.
- BRGM extracted a degradation model for cellulose and PVC by hydrolysis and radiolysis from literature and from an experiment carried out in CORI. Kinetics were applied to a generic case using MARTHE-PHREEQC. A 1D radial geometry was chosen based on the intermediate-level radioactive waste described in Huang et al. (2021). Such a geometry aimed to study interactions between organic waste (PVC, cellulose and phthalate), steel and concrete. Unfortunately, code capabilities do not allow to perform multiphase flow and therefore, modelling cannot give a realistic evolution of the waste drum materials. Results provide insight on expected chemical processes. Despite the presence of cementitious material and the anoxic corrosion of iron releasing OH⁻ and Fe⁺² into solution, results showed an acidification of the organic waste mainly due to the HCl(g) generation following the PVC degradation. To a lesser extent, CO₂(g) and CH₄(g) were concomitantly produced from cellulose degradation. Magnetite and siderite were expected at the intrados of the steel tube whereas magnetite was the main corrosion product

expected at its extrados. Alteration of concrete was characterized by the dissolution of portlandite followed by conversion of CSH1.6 to CSH1.2.

The results of experimental analysis and package scale models are summarized in a **synthesis for upscaled modelling (Chapter 5)** and as **recommendations for future experimental and numerical work (Chapter 6)**.

Most important processes that need to be considered in cavern scale models are the water consumption due to chemical reactions inside the different waste packages, and the possible production of large amounts of (partly reactive) gases, which will affect the water saturation on cavern scale, specifically in clay host rocks. Water consumption and gas generation rates depend to a large degree on water availability and water transport in the vicinity of waste packages. Therefore, it is not always possible to completely de-couple waste package evolution from large-scale processes in the disposal cell.

The availability of water to drive reactions is a factor that will limit or control reactions. Of specific interest is the dependence between the water saturation in waste packages and the chemical reaction rates. It is well known that reactions proceed under saturated conditions and will stop at dry conditions, but at which saturation and for which reasons specific reactions stop is not well investigated. One should note that the initial water saturation and water availability in waste packages after possibly decades of interim storage is probably very low.

For modelling of gas generation in waste packages, there are large uncertainties related to the effective long-term gas generation rates for metal corrosion and organic matter degradation. Specifically rates for the latter are highly uncertain and dependence on pH is not known. The experiments of VTT give some indication on rates, but information on rates under partially water saturated conditions, at different chemical conditions (pH) and for slowly degrading materials are scarce. For metallic waste sorts, corrosion rates at partially saturated conditions should be investigated.

Table of content

Executive Summary	5
1 Introduction and context	22
2 Integration of knowledge into models (concepts and processes)	24
2.1 Storage scenarios and concepts	24
2.1.1 200 l drum with organic waste	25
2.1.2 Concrete container with metallic (steel) waste	26
2.1.3 Narrative for evolution of waste packages.....	27
2.2 Materials and processes.....	32
2.2.1 Cement degradation related processes.....	32
2.2.2 Organic wastes and related processes	37
2.2.3 Metallic wastes and related processes.....	39
2.2.4 Degradation of organic matter	41
2.2.5 Influence of water availability on chemical reactivity	43
3 Model implementation and validation by experiments.....	45
3.1 VTT experiment	45
3.1.1 Introduction	45
3.1.2 Biogeochemical modelling.....	46
3.1.3 GGE experimental results and modelling validation.....	47
3.1.4 Analyses and conclusions	52
3.2 COVRA experiment	55
3.2.1 Interpretation of experimental results with models for the transport of water.....	55
3.2.2 Modelling of reaction fronts with a reactive gas	64
3.2.3 Modelling of reaction fronts with a reactive gas and water production/consumption	72
3.2.4 Concluding perspective: transport of water and reactive transport modelling.....	80
3.3 CORI experiment and CEA experiment (on PVC).....	81
3.3.1 Introduction	81
3.3.2 ILW wastes, packages and storage scenarios	81
3.3.3 Models for polymer degradation: general concepts and mechanisms	82
3.3.4 Models for polymer degradation: implementation into geochemical codes and verification	86
4 Model implementation, abstraction, and application on waste package scale.....	90
4.1 Generic system for modelling at waste package scale	90
4.1.1 ILW/steel.....	90
4.1.2 ILW/steel/organics	91
4.2 Definition of cementitious materials at waste package scale	94

EURAD Deliverable 2.15 – ILW modelling results and recommendations

4.2.1	Reference cement	94
4.2.2	Infill mortar	97
4.2.3	Container concrete	98
4.3	Description of models used for modelling at waste package scale	101
4.3.1	Models used by PSI (ILW/organics/steel, ILW/steel)	102
4.3.2	Models used by UFZ.....	106
4.3.3	Models used by SCK CEN	113
4.3.4	Models used by COVRA.....	115
4.3.5	Models used by BRGM.....	121
4.4	Results of the modelling cases at waste package scale	123
4.4.1	Modelling cases and results by PSI.....	123
4.4.2	Modelling cases and results by UFZ	137
4.4.3	Modelling cases and results by SCK CEN	145
4.4.4	Modelling cases and results by COVRA.....	147
4.4.5	Modelling cases and results by BRGM.....	151
5	Synthesis for upscaled modelling	154
5.1	Input from the experiments and their modelling	154
5.1.1	Gas generation from metal corrosion and organic matter degradation.....	154
5.1.2	Water transport in concrete	154
5.2	Modelling the waste packages	155
5.2.1	Mixing tank models	155
5.2.2	Reactive transport in a drum	156
5.2.3	Water transport towards waste packages	156
5.2.4	Reactive multi-phase models	157
6	Recommendations for future experimental and numerical work	159
7	References	161

List of Figures

Figure 1-1: Organization of ACED (from Jacques et al., 2019).....	23
Figure 2-1. Left: Layout of the representative ILW disposal cell concept in a clay and granitic host rock. Disposal cell height is about 13 m and width 11 m. Right: Example placement of waste containers in the “waste zone” according to the disposal cell in clay. Figures extracted from Samper et al. (2022).	24
Figure 2-2. Examples for the two waste sorts investigated (from Nagra 2014). Left: Container for 200 l drums filled with cemented organic waste. The void space between drums will be filled with mortar. Right: Container filled with metal waste from decommissioning of power plants. The void space in the container will be filled with a highly flowable mortar.....	25
Figure 2-3: Schematic sketch of the generic waste package, which contains four pucks (compacted 30 l drums used for collecting cellulose waste).	26
Figure 2-4: Container for metallic waste (Nagra 2008a; Stein 2014). The steel bars shown here are loosely stacked, but after complete conditioning there will be a cement matrix (infill mortar) surrounding these bars.	27
Figure 2-5: Process couplings in a waste drum between cement degradation, metal corrosion, organic matter degradation, and water and gas transport (from Huang et al., 2021).	28
Figure 2-6: Overview of expected evolution of main processes in an L/ILW repository situated in a clay host rock (from Leupin et al., 2016).....	29
Figure 2-7: Plot of pH dependence of normalized dissolution rates for some common rock-forming minerals at 25 °C, at mineral saturation degree $\Omega \approx 0$ and normalized to a reactive surface of 1.0 m ² . Kinetic data from Thermoddem D B (Marty et al., 2015) are plotted as solid lines, while data from Palandri and Kharaka (2004) are plotted as dashed lines. Experimental data for dissolution of quartz, albite, microcline and amorphous silica at 40 °C and pH > 12 from Bagheri et al. (2022) are added for comparison (from Kosakowski et al., 2023).	37
Figure 2-8: Bulk amount of organic material in national inventories, data from A) ANDRA (France), ONDRAF/NIRAS (Belgium) and C) SKB (Suede)	38
Figure 2-9: Reaction scheme implied in the radiooxydation of a polymer.....	39
Figure 2-10: Pourbaix diagrams for the system Fe-H ₂ O with an activity of dissolved species of 10 ⁻⁷ M; 0.002 M Ca is a reasonable concentration for tap water and 0.02 M Ca is the maximum dissolved calcium concentration without alkalis (Berner, 1992) and (Vehmas and Itälä 2019) and 3M HCO ₃ ⁻ is the concentration found in Spanish and Czech granitic rocks and French indurated clay (see Appendix B) Magnetite (green) is Fe ₃ O ₄ (s) and Hematite (orange) is Fe ₂ O ₃ (s) and Siderite (yellow) FeCO ₃ (s).	40
Figure 2-11: Pourbaix diagrams for the system Cr-Fe-H ₂ O with an activity of dissolved species of 10 ⁻⁷ M; 0.002 M NaCl is a reasonable concentration for tap water, 0.6 M NaCl is suitable chlorine concentration for seawater. Chromite (green) is FeCr ₂ O ₄ (s).	41
Figure 2-12: Total absorbed doses and dose rates relevant to the geodisposal of radioactive waste and bioremediation of radionuclide contaminated land (after, Brown et al., 2014)	42
Figure 3-1: Schematic of the GGE showing different types of sampling lines (a, b, c) and online analyses (d) and location of Lines 104, 110, 116, 121, 122 and 123 that were used to take water samples. The dead volumes of the tubing are approximately 0.1–0.4 dm ³ . Also capsules containing a piece of drum steel and LLW were loaded to the experiment (b, drum solid). Drums are normal size 200 l steel drums with a height of 0.9 m and a diameter of 0.6 m. (Small, et al. 2008).....	45
Figure 3-2: Comparison of the measured gas volume with the modelled results (Small, et al. 2017). .	48

Figure 3-3: Comparison of the gas (in vol%) generated in GGE during the year 1997 to 2018 between the measurements (plotted in dots) and the modelling (plotted in line), concerning (a) CH₄; and (b) CO₂ (Small, et al. 2017). 49

Figure 3-4: Comparison of the average pH of the waste, water and concrete cells predicted by GRM model with the measurements from GGE. 50

Figure 3-5: Comparison of the concentration of reactive aqueous species in tank water between the measured data and simulations in the aspects of: (a) sulfate and sulfide; (b) inorganic and organic carbon; (c) iron; and (d) calcium and magnesium. 51

Figure 3-6: Modelled population size of microbial groups in the GGE (Small et al., 2019)..... 52

Figure 3-7: Updated data regarding the cumulative volume of generated gas until August, 2021. 53

Figure 3-8: Concrete phase alteration due to carbonation (GEMS-calculation) 54

Figure 3-9 Modelled time dependent pressure head and saturation of waste package concrete at 20°C when exposed to a relative humidity of 75.47%. Parameters used for the simulations: $\phi=0.13$, $\alpha(20^\circ\text{C})=2.0\times 10^{-4} \text{ m}^{-1}$, $n=2$, $K_{\text{sat}}=7.3\times 10^{-20} \text{ m}^2$ (Mladenovic et al., 2024); C_p assumed to be 10^{-6} Pa^{-1} ; 32442 mesh elements. 57

Figure 3-10: Measured (symbols) and NaCl simulated (lines) weight of water in cubical specimens with an edge of 5 cm of waste package concrete at 20°C; ▲ Mg(NO₃)₂ had become undersaturated in the solution by which the requested relative humidity might not be achieved. Parameters used for the simulations $\phi=0.13$, $\alpha(20^\circ\text{C})=2.0\times 10^{-4} \text{ m}^{-1}$, $n=2$, $K_{\text{sat}}(20^\circ\text{C})=7.3\times 10^{-20} \text{ m}^2$ (Mladenovic et al., 2024), assumptions for C_p are indicated..... 58

Figure 3-11: Measured (symbols) and Mg(NO₃)₂ simulated (lines) weight of water in cubical specimens with an edge of 5 cm of waste package concrete at 5 °C; ◆ KCl-salt was found on the surface of the specimen. ▲ Mg(NO₃)₂ had become undersaturated in the solution by which the requested relative humidity might not be achieved. Parameters used for the simulations $\phi=0.13$, $\alpha(5^\circ\text{C})=1.5\times 10^{-4} \text{ m}^{-1}$, $n=2$, $K_{\text{sat}}(5^\circ\text{C})=4.6\times 10^{-20} \text{ m}^2$ (Mladenovic et al., 2024), assumptions for C_p are indicated..... 59

Figure 3-12: Modelled time dependent saturation of waste package concrete and the diffusion values of water at 20°C when exposed to a relative humidity of 75.47%. Porosity of 13 vol% is assumed to be constant. 60

Figure 3-13: Measured (symbols) and simulated (lines) weight of water in cubical specimens with an edge of 5 cm of waste package concrete at 20°C; ▲ Mg(NO₃)₂ had become undersaturated in the solution by which the requested relative humidity might not be achieved. Parameters used for the simulations $\phi=13 \text{ vol } \%$ unless stated otherwise, $D_{0,w}(20^\circ\text{C})=2.032\times 10^{-9} \text{ m}^2\text{s}^{-1}$, pre-factors are indicated, 399701 mesh elements. 61

Figure 3-14: Measured (symbols) and simulated (lines) weight of water in cubical specimens with an edge of 5 cm of waste package concrete at 5 °C; ◆ KCl-salt was found on the surface of the specimen. ▲ Mg(NO₃)₂ had become undersaturated in the solution by which the requested relative humidity might not be achieved. Parameters used for the simulations $\phi=13 \text{ vol } \%$ unless stated otherwise, $D_{0,w}(5^\circ\text{C})=1.317\times 10^{-9} \text{ m}^2\text{s}^{-1}$, pre-factors are indicated, 399701 mesh elements. 62

Figure 3-15: Measured (symbols) and simulated (lines) weight of water in cubical specimens with an edge of 5 cm of foamed concrete at 20 °C; ▲ Mg(NO₃)₂ and +,x NaOH had become undersaturated in the solution by which the requested relative humidity might not be achieved. Parameters used for the simulations $\phi=21 \text{ vol } \%$ unless stated otherwise, $D_{0,w}(20^\circ\text{C})=2.032\times 10^{-9} \text{ m}^2\text{s}^{-1}$, pre-factors are indicated, 399701 mesh elements. 63

Figure 3-16: Measured (symbols) and simulated (lines) weight of water in cubical specimens with an edge of 5 cm of foamed concrete at 5°C; ▲ Mg(NO₃)₂ had become undersaturated in the solution by

which the requested relative humidity might not be achieved Parameters used for the simulations $\phi=21$ vol%, $D_{0,w}(5^{\circ}\text{C})=1.317\times 10^{-9} \text{ m}^2\text{s}^{-1}$, pre-factors are indicated, 399701 mesh elements..... 64

Figure 3-17: Modelled saturation and time-dependent diffusion values of water, concentration of FeS and dynamic trapping rate (consumption rate) as function of time and space and the progression of a reaction front at relative humidity of 54% at 20°C. Gaseous and dissolved oxygen are in Figure 3 10 and Figure 3 11. Initial FeS assumed to be 2 wt% in cement, 17.6 wt% cement (see recipe waste package concrete in Mladenovic et al. (2019)) and r_{FeS} 222 μm , porosity of 13 vol% and pre-factor of $1/16$ are assumed to be constant, 32439 mesh elements. $D_{0,w}(20^{\circ}\text{C})=2.032\times 10^{-9} \text{ m}^2\text{s}^{-1}$ 67

Figure 3-18: Modelled concentration of gaseous oxygen, time-dependent diffusion value and dynamic consumption rate during exposure to a relative of 54% at 20°C, 32439 mesh elements $D_{0,02,\text{gas}}(20^{\circ}\text{C})=10.000\times D_{0,02,\text{aq}}(20^{\circ}\text{C})$ 68

Figure 3-19: Modelled concentration of dissolved oxygen, time-dependent diffusion value and dynamic consumption rate during exposure to a relative of 54% at 20°C, porosity of 13 vol% is assumed to be constant, 32439 mesh elements. $D_{0,02,\text{aq}}(20^{\circ}\text{C})=2.01\times 10^{-9} \text{ m}^2\text{s}^{-1}$ 68

Figure 3-20: Calculated oxidation fronts after 1000 days at different trapping rate dependency, FeS assumed to be 2 wt%, recipe for fabrication of concrete 17.6 wt% of concrete, r_{FeS} 2.2 μm (7.7×10^{13} FeS sites per m^3), 22 μm (7.7×10^{10} FeS sites per m^3) and 222 μm (7.7×10^7 FeS sites per m^3) at a relative humidity of 75% at 20°C, 32439 mesh elements. $D_{0,w}(20^{\circ}\text{C})=2.032\times 10^{-9} \text{ m}^2\text{s}^{-1}$ and $D_{0,02,\text{aq}}(20^{\circ}\text{C})=2.01\times 10^{-9} \text{ m}^2\text{s}^{-1}$ 69

Figure 3-21: Modelled reaction fronts after 1000 days at 20°C when exposed to a relative humidity of 85%, 75%, 54% and 43%. Initial FeS assumed to be 2 wt% in cement, 17.6 wt% cement in waste package concrete (see recipe waste package concrete in Mladenovic et al. (2019)) and r_{FeS} 222 μm , porosity of 13 vol% is assumed to be constant, $D_{0,w}(20^{\circ}\text{C})=2.032\times 10^{-9} \text{ m}^2\text{s}^{-1}$ and $D_{0,02,\text{aq}}(20^{\circ}\text{C})=2.01\times 10^{-9} \text{ m}^2\text{s}^{-1}$ 69

Figure 3-22: Modelled reaction fronts after 1000 days at 5°C when exposed to a relative humidity of 76%, 59%, 43% and 34%. Initial FeS assumed to be 2 wt% in cement, 17.6 wt% cement in waste package concrete (see recipe waste package concrete in Mladenovic et al. (2019)) and r_{FeS} 222 μm , porosity of 13 vol% and pre-factor $1/16$ are assumed to be constant, $D_{0,w}(5^{\circ}\text{C})=1.317\times 10^{-9} \text{ m}^2\text{s}^{-1}$, $D_{0,02,\text{aq}}(5^{\circ}\text{C})=1.12\times 10^{-9} \text{ m}^2\text{s}^{-1}$ 70

Figure 3-23: Modelled reaction fronts after 1000 days at 20°C and 5°C when exposed to different relative humidity's. Initial FeS assumed to be 2 wt% in cement, 24.2 wt% cement (see recipe foamed concrete in (Mladenovic et al., 2019)) and r_{FeS} 222 μm , porosity of 21 vol% and pre-factor $1/16$ are assumed to be constant, $D_{0,w}(20^{\circ}\text{C})=2.032\times 10^{-9} \text{ m}^2\text{s}^{-1}$ and $D_{0,02,\text{aq}}(20^{\circ}\text{C})=2.01\times 10^{-9} \text{ m}^2\text{s}^{-1}$, $D_{0,w}(5^{\circ}\text{C})=1.317\times 10^{-9} \text{ m}^2\text{s}^{-1}$, $D_{0,02,\text{aq}}(5^{\circ}\text{C})=1.12\times 10^{-9} \text{ m}^2\text{s}^{-1}$ 70

Figure 3-24: Modelled reaction fronts after 1000 days at 20°C and 5°C when exposed to different relative humidity's. Initial FeS assumed to be 0.2 wt% in cement, 24.2 wt% cement (see recipe foamed concrete in (Mladenovic et al., 2019)) and r_{FeS} 22 μm , porosity of 21 vol% and pre-factor $1/16$ assumed to be constant, $D_{0,w}(20^{\circ}\text{C})=2.032\times 10^{-9} \text{ m}^2\text{s}^{-1}$ and $D_{0,02,\text{aq}}(20^{\circ}\text{C})=2.01\times 10^{-9} \text{ m}^2\text{s}^{-1}$, $D_{0,w}(5^{\circ}\text{C})=1.317\times 10^{-9} \text{ m}^2\text{s}^{-1}$, $D_{0,02,\text{aq}}(5^{\circ}\text{C})=1.12\times 10^{-9} \text{ m}^2\text{s}^{-1}$ 71

Figure 3-25: Modelled oxidation fronts in different dimensions for foamed concrete exposed to a relative humidity of 76% at 5°C; same parameter used as Figure 3-23. Same mesh size i.e. 32439 mesh elements (3D-right), 928 mesh elements (2D-middle) and 27 mesh elements (1D-left)..... 72

Figure 3-26: Water (left), gaseous CO_2 (middle) dissolved CO_2 (right). Modelled saturation, concentration of gaseous and dissolved CO_2 , time-dependent diffusion values of water, and dynamic trapping rate (consumption rate) as function of time and space at a relative humidity of 75% at 20°C; 24.2 wt% cement (see recipe foamed concrete in Mladenovic et al. (2019)) and radius of cement minerals 22 μm , size of pores 12.9 nm, porosity of 21 vol%, and pre-factor $1/16$ assumed to be constant, $D_{0,w}(20^{\circ}\text{C})=2.032\times 10^{-9} \text{ m}^2\text{s}^{-1}$ and $D_{0,\text{CO}_2,\text{aq}}(20^{\circ}\text{C})=1.67\times 10^{-9} \text{ m}^2\text{s}^{-1}$. Number of mesh elements: 27. 77

Figure 3-27: Modelled concentration of (simplified) cement minerals and consumption rate; same parameters as in Figure 3-26. Number of mesh elements: 27	78
Figure 3-28: Modelled SH concentration at 20°C at different relative humidity's; same parameters as in Figure 3-26. Number of mesh elements: 27	79
Figure 3-29: Modelled SH concentration; same parameters and exposure conditions as in Figure 3-26. Number of mesh elements: 27, 50 and 100.	79
Figure 3-30: ILW concrete overpack, including the 4 primary containers (Vernaz and Bonin, 2008) ...	82
Figure 3-31: Modelling of the HCl(g) release during the radiolysis of PVC using PHREEQC	84
Figure 3-32: Cellulose end groups, displaying reducing and non reducing chain end.....	86
Figure 3-33: Modelling of pure PVC radiolytic and hydrolytic degradation. Experiment from BenZeineb et al. (2021), modelling from this study.	87
Figure 3-34: Modelling of the radiolytic and hydrolytic degradation of 3 industrial PVC samples. Experiment from BenZeineb (2021), modelling from this study.	88
Figure 3-35: Cellulose degradation, modelling implementing Glaus and Van loon (2008) model into PhreeqC. Experimental data are gathered from Van Loon and Glaus (1997) and Glaus and Van Loon (2008)	89
Figure 3-36: Modelling of the degradation (radiolysis + hydrolysis) of cellulose, depending on irradiation dose rate.....	89
Figure 4-1: Container for metallic waste (Nagra, 2008a; Stein, 2014).	90
Figure 4-2: Schematic sketch of the generic waste package, which contains four pucks (super-compacted 30 l drums used for collecting cellulose waste)	91
Figure 4-3: Assumed sieve curve for aggregate sizes normalized to 1600 kg, the mass of aggregates in 1 m ³ concrete.....	99
Figure 4-4: Possible interpolation of pH dependencies of iron corrosion between pH 10.5 – 12.	104
Figure 4-5: Example of the packing of 200-litre drums into one standard disposal container (type LC-86H) (NAGRA NTB 16-05 (2016)).....	107
Figure 4-6: Waste drum (modified after Huang et al. (2021))	107
Figure 4-7: Chemical process coupling	111
Figure 4-8: Chemical reactivity R^{β} computed with equation (4-20) (4-20)and (4-23) (Huang et al., 2021)	111
Figure 4-9: Numerical model configuration, the green colour shows the waste compartment and blue colour shows concrete and backfill mortar materials. The red lines show the impermeable drum walls and inner tube.....	112
Figure 4-10: Disposal container with 6 waste drums. The model geometry is limited to area within the yellow box.	113
Figure 4-11: Details on conceptual model. The green area represents the waste zone (cellulose), the light blue area represents the waste drum backfill, and the dark blue area represents the container backfill. The steel of the drum (black zones) are excluded from the model.	114
Figure 4-12: Discretization of the simulation domain.	115
Figure 4-13: Carbonation after 7 days as a function of relative humidity from von Greve-Dierfeld, et al., (2020) when exposed to 50 vol% CO ₂ , paste with water / binder ratio of 0.4, additions in purple.....	116

Figure 4-14: Boundaries used for the 2D modelling without indurated clay, left a water concentration, right a water flux leaving concrete 117

Figure 4-15: Saturation degree, diffusion values for gas and hydrogen gas pressure ($J/m^3=Pa$) inside a wall of waste package concrete at 20°C when exposed to a relative humidity of at 75.47%. Parameters used in the simulations $r_{pore}=3$ nm; $N_{pore}=1.15 \times 10^{24}$ m⁻³. $D_{0,w}(20^\circ C)=2.032 \times 10^{-19}$ m²s⁻¹; $D_{0,H_2,diss}(20^\circ C)=4.89 \times 10^{-9}$ m²s⁻¹. 119

Figure 4-16: Boundaries used in the 2D modelling with indurated clay, Dirichlet (saturated), Neumann (symmetry, no flux and consumption). 119

Figure 4-17: Initial saturation degrees in the 2D modelling with indurated clay 120

Figure 4-18: Geometries considered by (a) Huang et al. (2021) and (b) in the present study 121

Figure 4-19: Time dependent evolution of pH (upper left), aggregate amount and C-S-H (upper right), iron (middle left), cellulose (middle right), liquid water (lower left), and gases (lower right) for the model variant with reactive aggregates. 126

Figure 4-20: Time dependent evolution of pH (upper left), aggregate amount and C-S-H (upper right), iron (middle left), cellulose (middle right), liquid water (lower left), and gases (lower right) for the model variant with inert aggregates. 126

Figure 4-21: Temporal evolution of Phase volumes for reactive aggregates (top) and inert aggregates (bottom). Phase names are as in PSI/Nagra / CEMDATA/zeolite TDB. MOR: mordenite, GIS-LS-P: gismondine low-silica P zeolite, CHA: chabazite, MSH: magnesium-silicate-hydrate, CSHQ: C-S-H solid solution model following Kulik (2011), C2ASH8: strätlingite. 127

Figure 4-22: Time dependent evolution of pH (upper left), aggregate amount and C-S-H (upper right), iron (middle left), cellulose (middle right), liquid water (lower left), and gases (lower right). 130

Figure 4-23: Temporal evolution of Phase volumes. Phase names are as in PSI/Nagra / CEMDATA/zeolite TDB. 131

Figure 4-24: Time dependent evolution of pH (upper left), aggregate amount and C-S-H (upper right), iron (middle left), cellulose (middle right), liquid water (lower left), and gases (lower right). 132

Figure 4-25: Temporal evolution of Phase volumes. Phase names are as in PSI/Nagra/CEMDATA/zeolite TDB. 133

Figure 4-26: Time dependent evolution of pH (upper left), aggregate amount and C-S-H (upper right), iron (middle left), cellulose (middle right), liquid water (lower left), and gases (lower right). 134

Figure 4-27: Temporal evolution of Phase volumes. Phase names are as in PSI/Nagra / CEMDATA/zeolite TDB. 135

Figure 4-28: pH evolution of the pore solution with time for different modelled scenarios (left) and cumulative hydrogen gas released by metal corrosion (right). Scenarios differ in terms of cementitious infill and the rate laws used for iron corrosion. sf: silica fume, clino: clinoptinolite (from Kosakowski and Wieland, 2022). 136

Figure 4-29. Total gas generation rate (positive values) and CO2 sink of cement carbonation reaction (negative values) for the base case: $k = 5e-19$ m², $p_d = 1e5$ Pa 138

Figure 4-30: Gas pressure (face colour) and gas flux (arrows, legend in log scale) for the base case. 139

Figure 4-31: Capillary pressure (face colour) and liquid flux (arrows, legend in log scale) for the base case. 139

Figure 4-32: Liquid saturation (face colour) and liquid flux (arrows) for the base case after 10, 40, 100, 200, 340, 500 years. 141

Figure 4-33: Time series plots. Continuous lines show the base case and dashed lines show the base case without cement carbonation and ASR. Panel (a) shows the location of mesh nodes corresponding to the time plots. The other panels show gas pressure (b), capillary pressure (c) total gas generation rate (d), liquid saturation (e), chemical reactivity (f), relative humidity (g)..... 142

Figure 4-34: Time series plot for different mortar permeability. The van Genuchten characteristic pressure is set to $p_d = 1e5$ MPa and the mortar chemical reactions are activated. Panels show gas pressure (a), capillary pressure (b), liquid saturation (c), total gas generation rate (d). Location of nodes are shown in Figure 4-33a..... 144

Figure 4-35: Time series plot for different van Genuchten characteristic pressure of the mortar. Mortar permeability is set to $k = 5e19$ m² and the mortar chemical reactions are activated. Panels show gas pressure (a), capillary pressure (b), liquid saturation (c), total gas generation rate (d). Location of nodes are shown in Figure 4-33a..... 144

Figure 4-36: Contours of pH, CSH1.6, CSH1.2, CSH0.8, calcite and $\text{Log}_{10}(P_{\text{CO}_2})$ after 300 y in a waste drum with organic waste and container backfill. Mineral amounts are in mol/dm³; distance is in meter. 146

Figure 4-37: Amounts of calcite (top) and CSH1.2 (bottom) along the transect showed in the left plot (extending from the waste zone through the waste drum backfill) at selected times..... 147

Figure 4-38: Saturation degree of concrete at two positions of the inside of concrete for a water consumption rate of 3.2 mol H₂O m⁻²year⁻¹ and 1.6 mol H₂O m⁻²year⁻¹ (half). The moisture storage function and parameters for diffusion as found for waste package concrete at 20°C in section 3.2.1 are used. 148

Figure 4-39: Saturation degree and water content for a water consumption rate of 3.2 mol H₂O m⁻²year⁻¹ at start (0 years; all upper figures) and after 33 years (all lower figures). The parameters for diffusion as found for waste package concrete and foamed concrete at 20°C in section 3.2.1 are used. Saturation degree for the backfill is overestimated since a porosity of 13% was used instead of 21%. 149

Figure 4-40: Saturation degree for a water consumption rate of 6×10^{-3} mol H₂O m⁻²year⁻¹ at $x=0$ in Figure 4-39 The parameters for diffusion as found for waste package concrete and foamed concrete at 20°C in section 3.2.1 are used. Saturation degree for the backfill is overestimated since a porosity of 13% was used instead of 21%..... 150

Figure 4-41: Simulated polymer profiles at 100 years..... 151

Figure 4-42: Simulated alteration products at 100 years. 152

Figure 4-43: Simulated gas saturation indices at 100 years. 152

Figure 4-44: Simulated iron corrosion and corrosion products at 100 years 153

Figure 4-45: Simulated concrete alteration at 100 years. 153

List of Tables

Table 2-1: Main organic materials present in ILW wastes (adapted from Altmaier et al., 2021)	37
Table 3-1: Measured cumulative gas generation rates (CGGR), gas composition in volume fraction (VF %), and calculated gas generation rates (GGR).	53
Table 3-2: Examples of diffusion values in air and water at 20° C (Handbook of Chemistry and Physics)	65
Table 3-3: Cement minerals used in the modelling, data from (Berner, 1992; Höglund, 2014).....	73
Table 3-4: Change in porosity during carbonation for the simulated samples	74
Table 3-5 - Yields measured by Colombani (2006) for PVC radiolysis, in moles.J ⁻¹	84
Table 3-6 - Analysis of the PVC samples, including 3 industrial samples.	86
Table 4-1: Amounts and volumes for different materials considered in the model. Waste and reinforcement steel volumes are back-calculated from weight of steel. Amounts of concrete and infill are calculated based on the volumes to be filled.....	90
Table 4-2: Materials, amounts and volumes for the organic waste package.	91
Table 4-3: Steel inventory and associated surface areas	92
Table 4-4: Definition of a predefined composition “OPC-Norm” in GEM-Selektor.	94
Table 4-5: Input for hydration of cement paste with w/c ratio of 0.58 in GEM-Selektor.....	95
Table 4-6: Elemental (independent component) composition and molal concentrations for total dissolved independent components after hydration calculation with GEM-Selektor.....	95
Table 4-7: Phase composition of the fully hydrated cement paste after equilibration with GEM-Selektor.	96
Table 4-8: Other properties of aqueous phase after equilibration with GEM-Selektor.....	96
Table 4-9: Composition for representative infill mortar as given in Nagra (2014).....	97
Table 4-10: Simplified infill mortar: Input for a system T=25°C, P=1 bar in GEM-Selektor for inert SiO ₂ aggregates (Inrt). OPC-Norm is a “compos” record as defined for the CEM I 42.5 N following Lothenbach et al. (2008) and Liu et al. (2014).	97
Table 4-11: Desired composition for 1 litre concrete T=25°C, P=1 bar, w/c = 0.45 in GEM-Selektor. .	98
Table 4-12: Input in GEM-Selektor for SiO ₂ aggregates (Inrt). OPC-Norm is a “compos” record as defined for the CEM I 42.5 N following Liu et al. (2014). Aggregate is represented by Inrt, an inert phase with the properties of quartz. For reactive aggregates, Inrt is replaced by the same amount of quartz.....	98
Table 4-13: Input in GEM-Selektor for CaCO ₃ aggregates. OPC-Norm is a “compos” record as defined for the CEM I 42.5 N following Liu et al. (2014).....	98
Table 4-14: Aggregate sizes, amounts and (reactive) surface areas, as well as grain numbers and grain properties for each size class.	99
Table 4-15: Decrease of surface area with dissolution of aggregates.	100
Table 4-16: Overview of models used by the Partners.	101
Table 4-17: Rates for iron consumption, hydrogen production and water consumption due to corrosion of steel.	104
Table 4-18: Organic degradation parameters, gas generation rates and rates for water consumption for two waste groups (Wieland et al., 2018).	105

Table 4-19: Properties of different materials used in the UFZ numerical model from Huang et al. (2021)	108
Table 4-20: Liquid and gas properties used in the UFZ numerical model	109
Table 4-21: Organic degradation parameters, gas generation rates and rates for water consumption for two waste groups from Huang et al. (2021)	110
Table 4-22: Input physical data from experimental results	120
Table 4-23: Amounts of initial organic polymers assuming a porosity of 0.33.	122
Table 4-24: Input for waste package modelling	123
Table 4-25: Initial pore water properties of the equilibrated system	124
Table 4-26: Initial equilibrated phase composition.	124
Table 4-27: Initial pore water properties of the equilibrated metal waste container system.	128
Table 4-28: Initial phase composition of the equilibrated metal waste container	129

Glossary

AAS	Atomic absorption spectroscopy
ABM1, ABM2	Alternative Buffer Material Tests performed at Äspö Hard Rock Laboratory (S)
ACED	<u>A</u> ssessment of <u>C</u> hemical <u>E</u> volution of ILW and HLW <u>D</u> isposal Cells
BaM	Commercial name of Czech bentonite (Bentonite and Montmorillonite)
BC	Base Case
BCF	Boda Claystone Formation
BO-ADUS	Name of borehole at Grimsel test site
BPW	Bentonite Porewater
CEC	Cation exchange capacity
CIEMAT	Centro de Investigaciones Energéticas, Medioambientales y Tecnológicas, Spain
CoPr	Corrosion Products (Abbreviation for experiments performed at ÚJV)
ČSN	Czech technical standard
DGR	Deep Geological Repository
EBS	Engineered Barrier System
EURAD	European Joint Programme on Radioactive Waste Management
FB experiment	Fe/Bentonite interface cells
FEBEX	Full-scale Engineered Barriers Experiment
GGW	Grimsel groundwater
GRM	Generalised Repository Model
GTS	Grimsel test site
HLW	High Level Waste
ICP	Inductive coupled plasma
IF	Interface
ILW	Intermediate Level Waste
LAB	Laboratory
MTA	Hungarian Academy of Sciences Centre for Energy Research
MaCoTe	Material Corrosion Test (Experiment at Grimsel test site)

EURAD Deliverable 2.15 – ILW modelling results and recommendations

MX-80	Bentonite of Wyoming
NRG	Nuclear Research and Consultancy Group, Netherlands
PEBS	Long-term performance of Engineered Barrier Systems EU project
SCK-CEN	Belgian nuclear research centre in Mol, Belgium
SEM/TEM	Scanning electron microscopy / Transmission electron microscopy
SGW	Synthetic ground water (based on Červinka and Gondolli 2015)
SNF	Spent nuclear fuel
SURAO	Radioactive Waste Repository Authority of Czech Republic
SWy-2 / SWy-3	Na-montmorillonites (Wyoming) from source clay repository
THCM model	Thermo-hydro-chemical-mechanical model
UAM	Autonomous University of Madrid, Spain
UDC	University of A Coruña, Spain
ÚJV	Nuclear Research Institute, Czech Republic
UOS	Disposal container project (Abbreviation for experiments performed at ÚJV)
VLJ repository	A Finnish acronym which translates to “reactor operating waste”
VTT	Technical research center of Finland
X, N-CT	X-ray, neutron-computed tomography
XRD	X-ray diffraction
XRF	X-ray fluorescence
WP	Work package

1 Introduction and context

The main objective of the EURAD project ACED (Assessment of Chemical Evolution of ILW and HLW Disposal Cells) is to improve methodologies to obtain multi-scale quantitative models for the description of the chemical evolution at the disposal cell scale and to derive robust mathematical models including the most relevant processes.

These ILW (intermediate level waste) and HLW (high level waste) disposal cells differ between the various European countries. Details about this are given in Neef et al. (2019). Generally, a HLW disposal cell can be characterized by a simplified geometry as many identical waste packages are emplaced always with the same kind of engineered barrier design. Whereas a typical ILW disposal cell contains many different waste sorts in a complex geometric arrangement of the engineered barrier system.

The ACED approach focuses on (i) process integration and (ii) model abstraction on three scales, i.e., interface scale, waste package scale and disposal cell scale (Figure 1-1).

- In process integration, we aim at the integration of existing scientific knowledge (and models) into models at the relevant space and time scales.
- With model abstraction, we aim at the development of methodologies to reduce model complexity in a systematic way such that an acceptable description of the chemical evolution is preserved.

This report (D 2.15) is related to modelling of the evolution of ILW waste packages (Task 3.3). The general goals in Task 3 are:

- to evaluate how adequate available phenomenological concepts and models describe the chemical evolution of typical materials at an intermediate scale – i.e., parts of a repository composed of several materials in a fixed geometry (representative for ILW or HLW waste packages) well below the disposal cell scale.
- to identify critical processes and features driving and controlling the chemical evolution at the waste package scale.
- to provide information on relevance and influence of processes for implementation at disposal cell scale and for model abstraction (Task 4).

This report describes the concepts, processes and models that were identified and used for modelling on ILW waste package scale.

In **Chapter 2** processes are summarized that might influence evolution of wastes and waste package (barrier) materials. Some of the process descriptions are based on experiments conducted in Task 3.1 experiments on HLW and ILW waste package scale. The results are published in Gin et al. (2023) for HLW waste package related experiments and Mladenovic et al. (2024) for ILW waste-package related experiments.

For the ILW waste, the focus is on cemented waste packages with metallic (iron/steel) waste and organic waste. From wide varieties of possible waste forms (c.f. Uras et al., 2021) we created two generic example waste forms.

In **Chapter 3** the model implementation for selected processes and their validation with help of the ILW related experiments from Task 3.1 are given. This relates specifically to the degradation of organic matter in presence of cementitious materials and related gas production (VTT experiment), the degradation of organic matter by radiolysis based on data from EURAD CORI WP and other experiments, and the carbonation of cementitious materials (COVRA Experiment).

Chapter 4 contains the implementation, abstraction and application for models that describe the long-term chemical evolution of the two generic waste sorts.

Finally, in **Chapter 5** the results from different modelling studies at waste package scale are synthesised and information is extracted that can be used for disposal cell scale models in Task 4 of ACED.

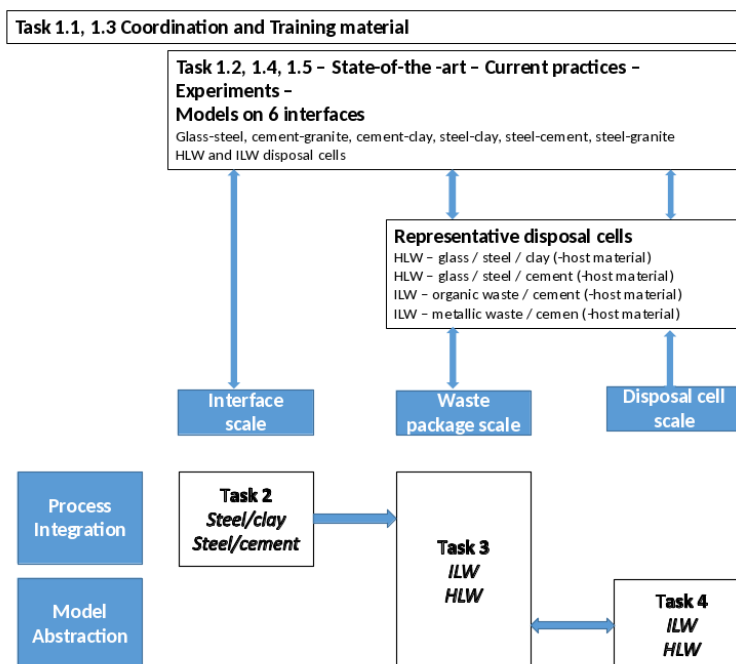


Figure 1-1: Organization of ACED (from Jacques et al., 2019).

2 Integration of knowledge into models (concepts and processes)

According to the IAEA safety standard on classification of radioactive waste (IAEA, 2009), "Intermediate level waste is defined as waste that contains long-lived radionuclides in quantities that need a greater degree of containment and isolation from the biosphere than is provided by near surface disposal.... As stated ... the boundary between the LLW class and the ILW class cannot be specified in a general manner with respect to activity concentration levels, because allowable levels will depend on the actual waste disposal facility and its associated safety case and supporting safety assessment." For HLW it is defined: "Waste with levels of activity concentration high enough to generate significant quantities of heat by the radioactive decay process or waste with large amounts of long-lived radionuclides that need to be considered in the design of a disposal facility for such waste."

2.1 Storage scenarios and concepts

Several ILW storage concepts do exist in several countries as is listed in Neef et al. (2019). In the framework of this project one generic concept was defined in Samper et al. (2022) that was adapted to host rocks, a clay and a granitic host rock (Figure 2-1). For both host rocks, the volume in which waste packages are stapled is surrounded by cementitious materials (backfill mortar, shotcrete liner).

After closure of the repository, cement-based barrier materials should sustain a stable high pH environment as long as possible to slow corrosion of metals and suppress microbial activity.

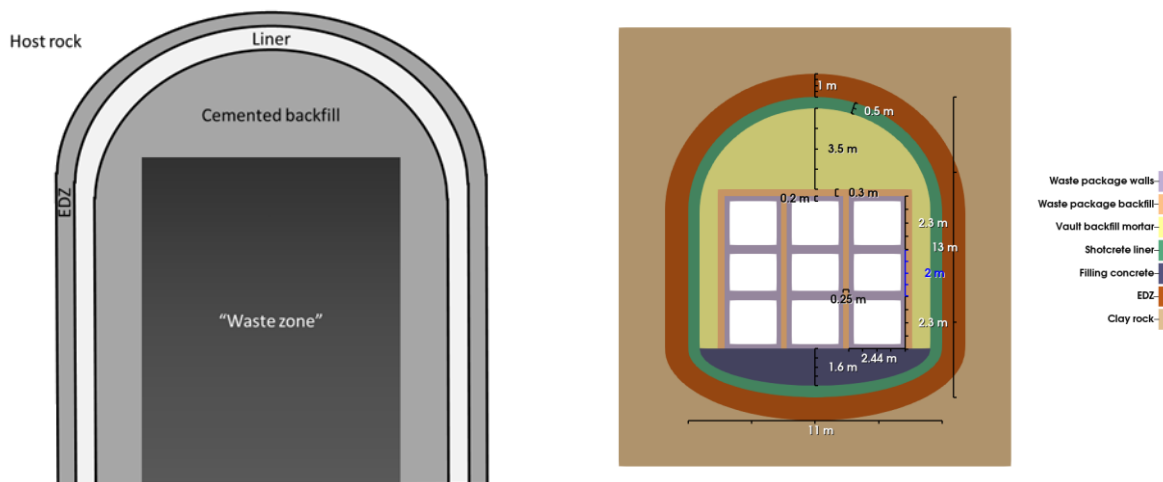


Figure 2-1. Left: Layout of the representative ILW disposal cell concept in a clay and granitic host rock. Disposal cell height is about 13 m and width 11 m. Right: Example placement of waste containers in the "waste zone" according to the disposal cell in clay. Figures extracted from Samper et al. (2022).

Note: The EDZ (excavated disturbed zone) and the liner considered in the ILW clay disposal cell are not part of the disposal ILW cell in crystalline rock.

For both host rocks it is assumed that, for fully water saturated conditions, the cementitious barrier materials that surround the waste package can isolate the waste from the influence of host rock pore water for very long times. If interaction with host rock pore waters might cause degradation of cementitious materials, e.g. by carbonation or by sulphate attack, first the outer barrier materials are affected and only after long times reaction fronts driven by diffusive transport or slow advection will reach the waste zone in Figure 2-1 (see e.g. Kosakowski and Berner, 2013; Idiart and Lavina, 2019). Therefore, it is assumed that the evolution of waste packages are largely independent from the host rock porewater composition.

This does not mean that hydraulic properties of the host rock do not have any influence on waste package evolution. While for a granitic host rock it is assumed that gas release from ILW waste packages does not significantly influence water saturation in the repository near field (see e.g. Silva et al., 2019), this is probably not the case in potential clay host rocks. Kosakowski et al. (2014, 2023) postulate a

strong feedback system between gas-generating waste degradation reactions and the saturation evolution of a cement based near-field in Opalinus Clay, the host rock foreseen in the Swiss concept. For the case of a partially de-saturated disposal cell, availability of water in waste packages might be a limiting factor for biochemical reactions. In addition, the existence of a continuous gas phase might provide possibility to accelerate CO₂ transport and drive carbonation of cementitious materials.

The existence of a gas phase, in combination with the heterogeneous structure of the ILW disposal cell might cause a compartmentalization of the disposal cell into small compartments which might evolve differently with time (c.f. Kosakowski et al., 2023). In such a scenario a heterogeneous near-field would evolve, where chemical conditions might be very difficult to predict.

LLW and ILW wastes have a wide variety of possible compositions (c.f. Uras et al., 2021), but the actual waste materials are often conditioned with cementitious materials. We have chosen to concentrate on two typical ILW waste sorts that contain waste materials, activated steel and organic matter, because they are present in larger quantities; and because metal corrosion and organic matter degradation are expected to influence strongly the long-term chemical evolution of surrounding materials.

For the waste form that contains major amounts of organic material, we choose one that might represent waste from research on fuel fabrication processes. We concentrate on organic waste materials that are cemented in 200 l steel drums contaminated with long lived (alpha emitting) radionuclides. It is a modified waste form previously investigated by Huang et al. (2021). As organic waste material we choose cellulose to represent common fast degrading organics, because degradation of cellulose is relatively well investigated (see section 2.2.2). Wieland et al. (2018) lists in the fast-degrading group: cellulose, LMW organics, gluconic/citric/tartaric/oxalic acids, EDTA, tensides/detergents, cement admixtures. For final disposal, the waste drums are assumed to be stapled in a concrete container and the void space will be filled with an infill mortar (left Figure 2-2).

For waste forms that contain mainly activated iron/steel, a typical waste form produced during decommissioning of nuclear power plants was considered (right Figure 2-2). We extracted information for the package design and materials in the waste package from a database for model waste forms (Nagra, 2008a). The design uses a reinforced concrete container with an outer volume of close to 6 m³. The container will contain (carbon) steel waste in a cement matrix.

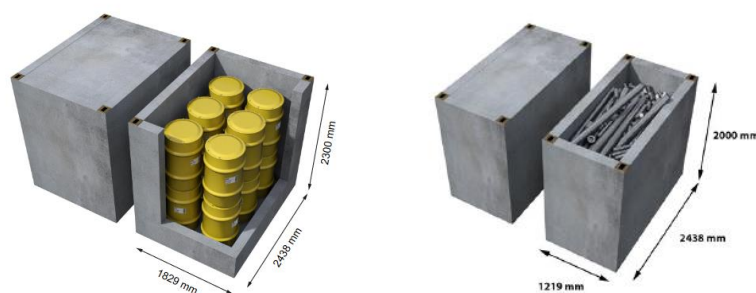


Figure 2-2. Examples for the two waste sorts investigated (from Nagra 2014). Left: Container for 200 l drums filled with cemented organic waste. The void space between drums will be filled with mortar. Right: Container filled with metal waste from decommissioning of power plants. The void space in the container will be filled with a highly flowable mortar.

2.1.1 200 l drum with organic waste

For the waste form that contains major amounts of organic material we choose one that might represent mixed operational waste contaminated with long lived (possibly alpha emitting) radionuclides that are cemented in 200 l drums.

Description of the waste form

It is assumed that the 200 l waste package is in dimensions identical to a previously investigated waste form that is representative for cemented mixed operational waste (Wieland et al., 2018; Kosakowski et al., 2020; Huang et al., 2021). This is a “200 l steel drum” made from 1.2 mm thick zinc coated “mild carbon steel” (type DC01 (old 12.03) steel, typically about 0.12% total C).

The (organic) waste is assumed to be collected in 30 l stainless-steel drums with a diameter of about 30.5 cm and a height of 51.0 cm. The steel wall thickness will be 1 mm and for simplicity, it is assumed they are also made from mild carbon steel. For the “reference case”, it is assumed that 30 l waste collection drum shall contain 15 kg of dry cellulose waste. The drums should not contain any free water. These smaller drums will be compacted into “pucks”, which will reduce the waste volume by about 50%. Four pucks will be placed in the centre of the 200 l waste package (Figure 2-3). Part of the void space in the drum will be pre-casted with an infill mortar. After emplacement of pucks, the remaining void space will be filled with the same mortar, such that there is only one infill material in the waste package.

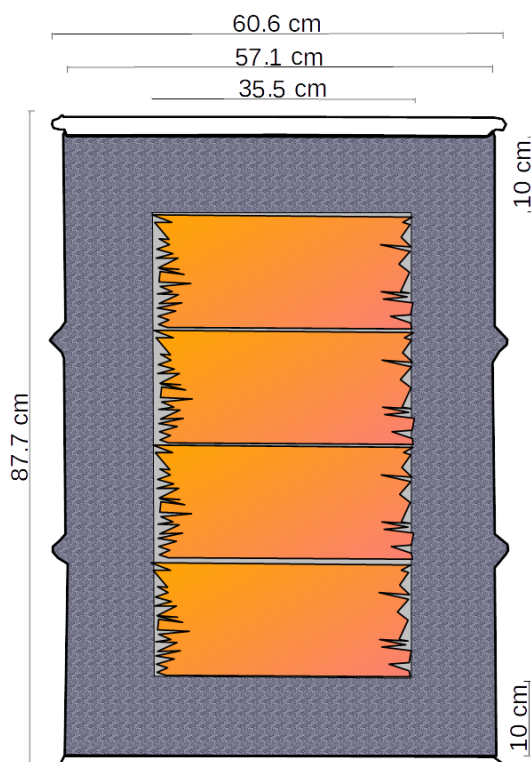


Figure 2-3: Schematic sketch of the generic waste package, which contains four pucks (compacted 30 l drums used for collecting cellulose waste).

2.1.2 Concrete container with metallic (steel) waste

As an example for a waste form containing mainly iron/steel, a typical potential waste produced during decommissioning of nuclear power plants was considered for this study from a database for model waste forms (Nagra, 2008a). The design uses a reinforced concrete container with an outer volume of close to 6 m³. The container will contain (carbon) steel waste in a cement matrix and steel reinforcement in the container walls.

The design uses a reinforced concrete container with 15 cm thick walls and an outer volume of close to 6 m³ (see Figure 2-4). The container will be filled with 6640 kg of waste (carbon steel). The remaining void space is backfilled with 2.5 m³ infill mortar. According to the initial waste inventory, the waste is mainly steel, but also various other metals are present. For simplicity, it is assumed that waste and steel reinforcement is composed solely of carbon steel. The mortar recipe is identical to the one used for 200 l drums. The volume to be backfilled is estimated close to 2.5 m³.

L3
LC-84 Nagra

Form:	Quader
Länge:	2.44 m (8 ft)
Breite:	1.22 m (4 ft)
Höhe:	2.00 m
Wandstärke:	0.15 m
Aussenvolumen:	5.946 m ³
Eigenmasse:	6670 kg
Nutzvolumen:	3.3 m ³

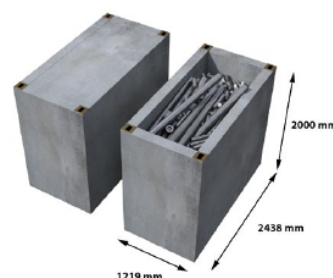


Figure 2-4: Container for metallic waste (Nagra 2008a; Stein 2014). The steel bars shown here are loosely stacked, but after complete conditioning there will be a cement matrix (infill mortar) surrounding these bars.

2.1.3 Narrative for evolution of waste packages

2.1.3.1 Evolution during interim storage

A detailed overview of packaging, pre-disposal storage and monitoring of cemented wastes is given in the state-of-the-art report of the Euratom PREDIS project by Uras et al. (2021). They state that “*medium to long-term storage of cemented wastes, is indicated in the National Programmes of many European countries as the strategy to deal with the delays of available disposal solutions, requires monitoring of waste packages for possible degradation phenomena and managing any arising issues prior to transport to the final repositories.*” They give a list of chemical reactions that might occur during interim storage and could potentially lead to degradation of the waste packages and eventually a loss of waste package integrity. They list the following reactions:

- abiotic and/or biotic degradation of the organic waste components,
- carbonation of the cementitious materials,
- alkali-aggregate reactions,
- corrosion of metallic waste components and steel surfaces of the drums.

The extent to which such reactions take place depends largely on the presence of water in the waste packages and on local chemical conditions e.g., water pH in waste materials. These processes normally consume water (Kosakowski et al., 2014, Huang et al., 2021) and therefore contribute to dry out of waste forms. In summary, all these chemical reactions are highly coupled to gas and water transport in the waste package and provide multiple intertwined feedback loops (Figure 2-5).

The beforementioned reactions in waste packages are the same that might still occur after deep geological disposal and are described in Section 2.2 of this report.

Uras et al. (2021) state, that based on their survey cemented waste packages are “mostly stored in ventilated and controlled areas.” They state that “*the majority (of End Users) employs visual monitoring (either in person or using TV cameras) on a periodic basis to identify metal corrosion, cracks and external contamination, swelling, leakage, lifting feature deformation, and external dose. Almost half of the respondents collects information about gas emission from packages checking in real-time the whole storage area.*” They conclude that “most of the respondents have observed degradation phenomena in the past such as internal and external corrosion, damages linked to the handling of the package, Alkali–Silica Reaction, leakages, swelling therefore putting in place options for preventive or remedial actions to be taken in connection with the extended storage of the waste packages.”

During the dry storage of the L/ILW waste packages, cementitious materials will hydrate, and residual water will slowly evaporate and diffuse out at the top of the containers, if they are open to the environment.

This drying process might take decades of storage (Huang et al. 2021). During the dry storage of L/ILW, the increasingly lower availability of water limits the possibility of chemical reactions within the waste. As a result, waste and cement/other materials in L/ILW waste packages will be highly de-saturated (“dry”) when emplaced in the cavern.

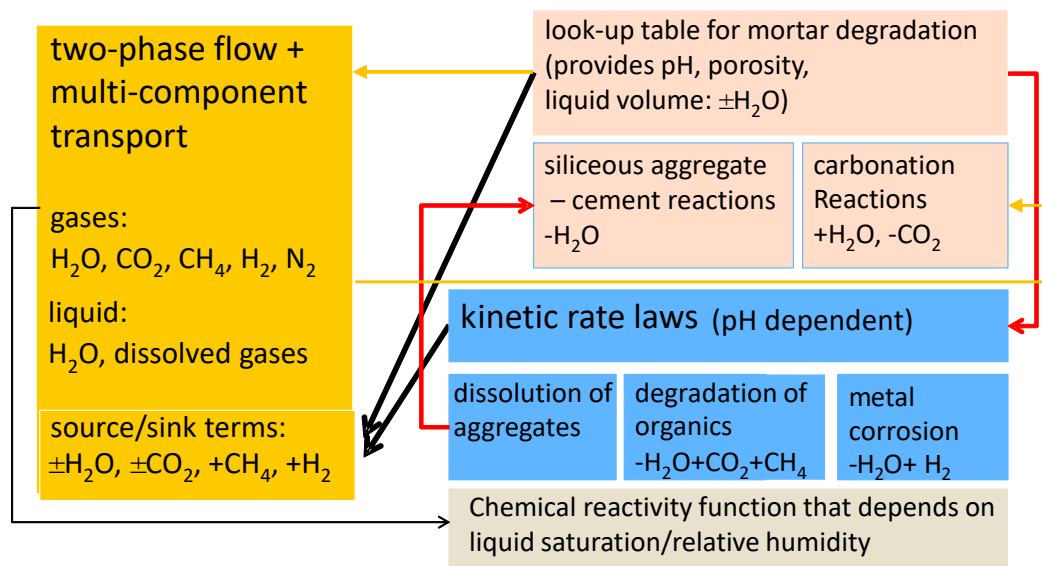


Figure 2-5: Process couplings in a waste drum between cement degradation, metal corrosion, organic matter degradation, and water and gas transport (from Huang et al., 2021).

2.1.3.2 Packaging and Emplacement

The waste containers with metal waste can be stapled in the emplacement cavern. The drums will be placed into disposal concrete containers and the void space between drums will be backfilled with a low viscosity backfill mortar. Once disposal containers are emplaced, the smaller voids between the containers are backfilled with a specifically designed near field mortar with low viscosity and high porosity.

A high viscosity local backfill mortar will be used to fill void space between containers in the upper part of the cavern and between the concrete lining wall of the cavern and the container stacks. The mortar is designed such that it has a high porosity and that grain-to-grain contact of the incompressible aggregate will prevent convergence of the near-field.

2.1.3.3 Evolution after waste emplacement and closure of repository

The general repository evolution is a boundary condition for the evolution of the waste packages (Figure 2-6 for repository in clay). In the disposal cell, outer conditions will change and several chemical and physical processes in the drum will progress simultaneously (c.f. Kosakowski et al., 2014, 2023, Uras et al., 2021).

The mortar and waste within the L/ILW containers may be partially de-saturated due to drying prior to emplacement, while the backfill grout within the L/ILW caverns will be fully saturated after its emplacement. Some drying of the emplaced grout may occur during the continued operation of a cavern. More specifically, water will be re-distributed between materials according to the capillary pressure – saturation relations for the materials. Higher capillary tension (suctions) in small pores draws water out of larger pores into smaller pores. In the disposal container with drums, the outer environment will be a backfill mortar, which will be after hydration nearly (but not completely) liquid saturated. This effectively stops drying out of the drum and might initially enhance humidity transport into the drum if the outer hull

is not completely intact. Also, ingress of oxygen from outside into the drum is expected to be effectively stopped. The residual oxygen inside and outside the waste packages will be consumed rather quickly by the corrosion and anoxic conditions will stabilize in the disposal cell (oxic corrosion rates around $0.1 \mu\text{m a}^{-1}$ for “non-carbonated concrete” see e.g. Pabalan et al., 2013).

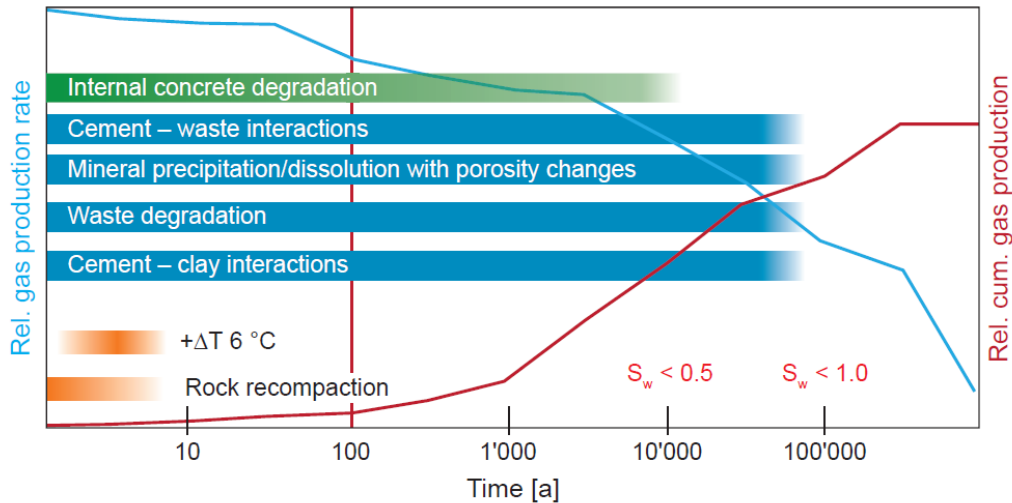


Figure 2-6: Overview of expected evolution of main processes in an L/ILW repository situated in a clay host rock (from Leupin et al., 2016)

The hydration of mortars/grout might cause a short-term increase in temperature. Some waste forms might produce some heat, but it can be assumed that the temperature increase is very limited and does not exceed a few degrees. According to Leupin et al. (2016) the short-term release of hydration heat after backfilling with mortar in a repository for L/ILW in a clay host rock results in a very short term temperature increase by $50 \text{ }^\circ\text{C}$ in the caverns and $10 \text{ }^\circ\text{C}$ in the adjacent clay host rock. Temperatures then fall within a few years to decades to become similar to the ambient temperature in the surrounding rock.

The key process that governs the long-term evolution of waste packages is the evolution of the surrounding near field in terms of water saturation. The re-saturation of the repository is highly dependent on the type of host rock. In the following narrative we strongly rely on the Swiss case for a repository in clay rock following Kosakowski et al. (2014). For the evolution of repository situated in granite, the Swedish case could be a good example.

As described before, the disposal cell after an initial 100-year period is not completely dry, nor fully water saturated. The longer-term saturation evolution is an interplay between the gas pressure increase (anoxic corrosion of metals and degradation of organic matter) and the inflow of water from the host rock. Clay host rocks are generally less permeable and restrict the flow of water and gases, while fractured granite host rocks allow much higher liquid and gas flow rates. On the one hand, complete re-saturation of the near field might need more than 100 000 years for a clay host rock (Leupin et al. 2016), while the vaults in granite host rock are liquid saturated much faster within a few years to few decades (Moreno et al. 2001; Holmén and Stigsson, 2001)

For a waste package, we can assume two states of contact with the outer environment:

Partially saturated state: The outside of the waste package is de-saturated and water transport between waste package and outside is controlled by humidity transport in the gas phase. Availability of water to drive chemical reactions inside the waste package might be a limiting factor. Gases can freely escape the waste package, but transport in a liquid phase connected to the outside is not possible.

Fully saturated state: As soon as the waste package is in contact with a fully liquid saturated outer environment, the package itself gets liquid saturated and chemical reactions are not limited by the availability of water.

The partially saturated state remains for very long times for a large fraction of waste packages for a repository in clay. Only some waste packages reach the fully saturated stage when the water level in repository does reach the waste package. For a repository in granite all waste packages reach the fully saturated state soon after closure of the repository.

Chemical processes that were already active during interim storage will proceed after emplacement. This includes abiotic and/or biotic degradation of the organic waste components eventually resulting in the formation of CO₂ and CH₄, carbonation of the cementitious materials, aggregate-cement reactions, (oxic) corrosion of metallic waste components and steel surfaces of the drums

For 200 l drum (or other waste sorts with impermeable “steel” walls) the outer drum walls will very slowly corrode under anoxic conditions due to contact with high pH infill materials. It can be assumed that steel walls are still intact for decades or longer¹. The time needed to completely corrode the walls of a waste container (at least 1mm thick steel walls) in an alkaline environment at pH 12.5 is expected to be between 5'000 years (“homogeneous” two sided corrosion) and 10'000 years (“homogeneous” corrosion only from one side) after emplacement on the basis of corrosion rates reported by (Smart et al. 2004; Kursten et al. 2011; Diomidis 2014).

As intact waste packages are still assumed to be water de-saturated, it can be assumed that abiotic and biotic degradation, as well as corrosion of metals might be limited in many waste forms, as long as waste packages are de-saturated.

If not limited by lack of water inside tight waste forms, easily corroding metal wastes (e.g. magnesium, aluminium) will give an initial peak in H₂ production and might cause an increase of gas pressure in the disposal cell (Moreno et al. 2001; cf. Diomidis et al. 2016). The exact amount of gas produced will of course depend on waste inventory, type of waste containers and availability of water/humidity. A peak of gas production is expected at early times (cf. Section 3.3.3 in Diomidis et al. 2016, which also applies on waste package scale and Poller et al. 2016).

Once waste packages are fully or partly immersed in water, several competing physical and chemical processes might interact inside waste packages: degradation of cementitious materials, degradation of organic matter, corrosion of metals, hydrolysis.

Concrete/cement degradation might be promoted by the composition of the water that re-saturates the disposal cell. As long as there is a limited steady water flow across the cavern, it can be expected that first the cementitious materials surrounding the waste packages are degraded. Strong degradation of waste package materials due to ingressing formation waters seems unlikely (Silva et al., 2019). Some limited increase in salinity is possible and might influence e.g. corrosion of metals.

For waste sorts that contain reactive aggregates in concrete: Kinetic controlled cement-aggregate reactions cause transformation of portlandite into C-S-H and furthermore change in C-S-H composition towards lower C/S ratio (until quartz aggregate is in thermodynamic equilibrium with cement phases and the equilibrium pH is lowered towards 10-11). This process might be fast at fully saturated conditions and if reactive aggregates with small diameter are present. In case of de-saturated conditions and if grain sizes are big this process might take very long times. Porosity will decrease, if the denser rock minerals are transformed into hydrated cement phases (mainly C-S-H). Once the pH drops enough also

¹ For 200 l drum (or other waste sorts with impermeable “steel” walls): value for pH > 10.5 and anoxic conditions: carbon steel: 2.0×10⁻⁸ m a⁻¹ ; stainless steel: 1.0×10⁻⁹ m a⁻¹ (Diomidis, 2014 Tab. 3.6, Diomidis et al. 2016 Tab 2.2))

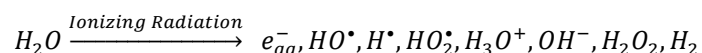
zeolites might be formed. The whole process also consumes some amount of water (Kosakowski et al., 2020, 2023).

Carbonation of cementitious materials: Degradation of organic matter will produce i.a. CO₂ that will carbonate surrounding cementitious materials. In case there are preferred gas pathways for escaping the waste package (small holes in otherwise intact waste package hulls), carbonation will proceed along those pathways. In that case, a “homogeneous” or “complete” carbonation of cementitious materials inside the waste package might be not happening. The timescale and the extent of carbonation is directly dependent on the amount of CO₂ produced by the degradation of organic matter.

Degradation of organic matter: For the investigated waste sort is assumed to be possible i.e. microbial mediated degradation of cellulose will happen. CO₂ and CH₄

Degradation rates will be limited by availability of water for closed/intact waste packages. Exponential decrease of degradation rates and gas production can be assumed in an ideal case. For fast degradation rates are decreasing strongly within a few thousand years. Wieland et al. (2018) used for example a rate law that correspond to a simple decay with a half-life of 367 years for cellulose and 10 631 years for polystyrene. The corresponding time to reduce a mass of 1 kg organics to 0.01 kg is 2 437 years for cellulose and 70 165 years for polystyrene.

Radiolysis of water: The radiolysis of water due to ionizing radiation is bound to occur in ILW packages, because of the activity of the unstable isotopes present within the waste. The reaction will result in the production of electrons, H[•] atoms, •OH radicals, H₃O⁺ ions and molecules (dihydrogen H₂ and hydrogen peroxide H₂O₂). The framework in which water radiolysis occurs is now well understood experimentally (Le Caër, 2011). The reaction proceeds with three stages which can be summarized by the following schematic reaction:



Such reaction is producing H_{2,g} but it can be disregarded for the disposal of low- and intermediate-level nuclear waste because the activity developed within the waste packages is not able to produce a significant gas release, compared to other processes (Kónya and Nagy, 2018). As reported by Johnson et al. (2004) and Román-Ross et al. (2015), assessments of the disposal of ILW waste indicate that gases produced by the radiolytic degradation of the aqueous media would represent only a small fraction of the total gas produced by corrosion because of the substantial wall thickness of the canister and the relatively rapid decay of the gamma intensity.

However Donohoe (2010) enhances a possible indirect effect on corrosion rates themselves, consecutive to hydrogen peroxide production as the stable molecule species with the longest lifetime. Donohoe (2010) reports that, since such species is oxidizing in neutral waters, it would be able to raise the corrosion potential of passive stainless steel by a few hundred of millivolts.

Corrosion of steel: The corrosion rate will be constant in time, if “reactive surface area” of steel and the pH of water in contact with the surface is not changing. This is for example the case for waste package hulls. As soon as the steel is consumed, rate will decrease to zero of course. For at least 1 mm steel walls under reducing conditions at high pH this takes about 5 000 to 10 000 years. Metal waste corrosion rates might change in time more strongly, as the corrosion rate is assumed to change with shape of metal object upon dissolution. Metal waste might be nearly consumed within 100 000 years (see estimated gas generation rates as proxy for metal corrosion in Diomidis et al., 2016).

If we follow Poller et al. (2016) also on waste package level, steel corrosion will be constant for about 10 0000 years although H₂ gas production will decrease in subsequent steps as metal pieces of different size are fully corroded.

2.2 Materials and processes

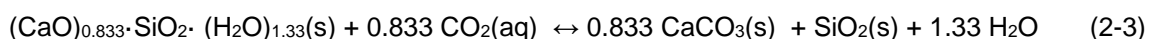
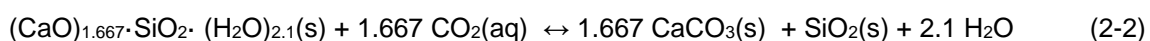
2.2.1 Cement degradation related processes

In engineering, degradation of cement-based materials is investigated extensively for the timescale related to lifetime of engineered structures, typically about 50 – 100 years, and typically with focus on mechanical properties and corrosion of concrete rebars (e.g. Dyer 2014). For deep geological disposal of radioactive waste, the very long-term (100k years or more) evolution of cementitious materials is investigated with respect to the safety functions of the engineered barriers. These are related to the fixation and retardation of radionuclides in cementitious materials with low-permeability, low-diffusivity and favourable sorption properties. Generally, a cement-based near-field provides a high-pH environment that slows down or even suppresses degenerating chemical processes (e.g. waste degradation, microbial activity, metal corrosion). In this section we summarize some processes that might be active in a cementitious near-field following Wieland et al. (2018), Kosakowski et al. (2020) and Kosakowski et al. (2023).

2.2.1.1 Carbonation

Carbonation of hydrated cements involves the transformation of C-S-H phases ($x\text{CaO}\cdot\text{SiO}_2\cdot n\text{H}_2\text{O}$), portlandite ($\text{Ca}(\text{OH})_2$), ettringite ($\text{Ca}_6\text{Al}_2(\text{SO}_4)_3(\text{OH})_{12}\cdot 26\text{H}_2\text{O}$) and AFm to calcium carbonate, gypsum and aluminium and silica oxyhydroxides (Venhuis and Reardon, 2001). Portlandite and C-S-H phases are the most abundant Ca-bearing cement phases in cement paste while ettringite and calcium monocarboaluminate (AFm- CO_3 : $3\text{CaO}\cdot\text{Al}_2\text{O}_3\cdot\text{CaCO}_3\cdot 11\text{H}_2\text{O}$) are only minor Ca-bearing phases (Kosakowski et al., 2014; Lothenbach and Wieland, 2006). Thus, about 90% of Ca bound in cement paste is associated with portlandite and C-S-H phases and therefore, carbonation is mainly attributed to the conversion of these phases into CaCO_3 . Note that ettringite is the main SO_4^{2-} bearing cement phase in cement paste and therefore carries the SO_4^{2-} inventory relevant to the sulphate-reducing pathway of the degradation of organics provided that no other SO_4^{2-} sources are available.

As examples, the reaction of CO_2 with the main Ca-bearing phases, portlandite, jennite-like endmembers of C-S-H ($(\text{CaO})_{1.67}\cdot\text{SiO}_2\cdot(\text{H}_2\text{O})_{2.1}$) and tobermorite-like endmembers ($(\text{CaO})_{0.833}\cdot\text{SiO}_2\cdot(\text{H}_2\text{O})_{1.33}$) can be expressed as follows:



Equations (2-2) to (2-4) reveal that water will be liberated during carbonation of portlandite and C-S-H phases. In addition, the interlayer/gel porosity (C-S-H interlayers) are reduced upon dissolution of C-S-H. The conversion of one mol portlandite to CaCO_3 generates approximately one mol H_2O . Note that water release in the course of carbonation of C-S-H phase is higher due to the higher stoichiometric content of water in these cement phases. Note further that the liberation of SiO_2 from C-S-H occurs during carbonation which influences also the composition of the phase assemblage.

The most notable consequence of carbonation is a drop of pH to values below 10.

In a repository atmospheric carbonation is only possible during operational phase when tunnels are ventilated. However, after closure of the repository the availability of CO_2 is controlled by the degradation of organic matter (Section 2.2.2) and might be influenced by the interaction with (carbonate enriched) host rock pore waters.

2.2.1.2 Aggregate-cement reactions

It is known that many common aggregates are not chemically stable in an alkaline (high-pH) environment. The so-called alkali-aggregate reaction (AAR) can cause the expansion of altered aggregate, leading to spalling and loss of strength of the concrete (Thomas et al., 2013). The AAR reaction can be subdivided into two main reactions (Leemann et al., 2016; Sims and Brown, 1998; Winter, 2009):

- Alkali-silica reaction (ASR), which is an expansive reaction originating from the interaction of alkalis (and hydroxyl) in alkaline pore fluid with reactive forms of silica in the aggregate.
- Alkali-carbonate reaction (ACR), which is an expansive reaction originating from the interaction of the alkaline pore fluid and some aggregates in which dolomite is present.

In addition, the pozzolanic reaction that occurs in the setting of the mixture of lime and pozzolanic materials has also features similar to ASR, but is not considered a deteriorating reaction in the sense of AAR.

Commonly the potential of aggregates regarding AAR are investigated with the help of tests which investigate the mechanical deformation/expansion of prisms or cylinders stored at elevated temperatures for times typically not more than one month (Grattan-Bellew and Katayama, 2019). Such tests are able to provide information on the potential degree of AAR within the lifetime of engineered structures of typically 50 years. The focus in these tests (Lindgård et al., 2012; Thomas et al., 2013) and associated model development (Esposito and Hendriks, 2019) is on the deterioration of mechanical properties, not so much on the induced changes in the chemical environment (mineralogy and pore water). Other test methods are based on petrographic examination of aggregates. Such information will give insight if rock forming minerals can be identified which are not in thermodynamic equilibrium with highly alkaline pore solution in concretes.

2.2.1.3 (Alumino-)Siliceous aggregates and pozzolans

In their overview on AAR, Leemann et al. (2016) lists silica (SiO₂ independent of speciation) as a major source for reacting minerals. Specifically opal, chalcedony, certain forms of quartz, cristobalite, tridymite, rhyolitic, dacitic, latitic, or andesite glass, or cryptocrystalline devitrification products and synthetic siliceous glass are listed as reactive substances by Thomas et al. (2013).

The reactivity of quartz is related to the degree of crystallinity. Lemann et al. (2016) write that “overall, quartz is responsible for slowly developing ASR and leads to damage in concrete structures after one to a few decades”. Furthermore, they write that “common rock-forming minerals such as feldspars, micas, nepheline, clays and zeolites may release alkalis especially when weathered, thus contributing to deleterious ASR.”

As most important deleteriously alkali-reactive rocks (containing excessive amounts of one or more reactive minerals) Thomas (2013) list:

“opaline cherts, chalcedonic chert, quartose cherts, siliceous limestones, siliceous dolomites, rhyolites and rhyolitic tuffs, dacites and dacitic tuffs, andesites and andesitic tuffs, siliceous shales, phyllites, opaline concretions, fractured, strained, and limestone-filled quartz and quartzites.”

The pozzolanic reaction is the chemical reaction that occurs in portland cement upon the addition of pozzolans (“Pozzolanic activity - Wikipedia,” n.d.). A pozzolan is defined according to ACI Committee 116 (2000) as “a siliceous or siliceous and aluminous material that in itself possesses little or no cementitious value but that will, in finely divided form and in the presence of moisture, chemically react with calcium hydroxide (a hydration product of portland cement) at ordinary temperatures to form compounds having cementitious properties”. A very broad overview on “pozzolana and pozzolanic cements” is given by Massazza (1998) in Chapter 10 of “Lea’s Chemistry of Cement and Concrete” (Hewlett, 1998).

In chemical terms, the pozzolanic reaction occurs between portlandite (Ca(OH)₂), and silicic acid (H₄SiO₄) and produces calcium-silicate-hydrate C-S-H:



According to Thomas (2013) “typically, the C/S ratio ... of the C-S-H that forms from this reaction will be lower than the C/S ratio measured for C-S-H in hydrated portland cement without pozzolan, and the difference will vary depending on the age, type, and amount of pozzolan”.

Thomas (2013) writes that “The alumina present in pozzolans will also react with the portlandite from portland cement and may produce a variety of phases, the principal ones including strätlingite or gehlenite hydrate (C_2ASH_8) and hydrogarnet (C_3AH_6), and others being calcium aluminate hydrate (C_4AH_{13}), ettringite ($C_3A \cdot 3CS \cdot H_{32}$), calcium monosulfoaluminate ($C_3A \cdot CS \cdot H_{12}$), and calcium carboaluminate ($C_3A \cdot CC \cdot H_{12}$)”.

Pozzolans that are commonly used in concrete include fly ash, silica fume, and a variety of natural pozzolans, such as calcined clay and shale, and volcanic ash (La Plante et al., 2019; Masateru et al., 2007; Moropoulou et al., 2004; Shi et al., 2005; Sims and Brown, 1998; Thomas, 2013).

Pozzolanic materials are typically mixed with portland cement clinker such that the pozzolanic reaction(s) occur during curing. Control of reactivity of pozzolans can be obtained by different measures, for example increase of temperature, use of chemical activators such as Na_2SO_4 and $CaCl_2$, or prolonged grinding of pozzolans which reduces the grain size (Shi et al., 2005; Shi and Day, 2001).

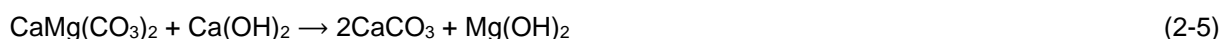
2.2.1.4 Calcareous aggregates

Calcareous aggregates are mostly made from calcium carbonate rocks, e.g. limestone, dolomite or even marble. The main constituent of limestone is the mineral calcite ($CaCO_3$). Calcite is the most stable calcium carbonate form under standard conditions. During carbonation of cementitious materials CO_2 together with calcium leached from cement hydrates forms calcium carbonate as main reaction product. Calcite is formed during carbonation only at very high relative humidity, whereas at lower relative humidity other crystalline polymorphs (vaterite and aragonite) are formed (Steiner et al., 2020).

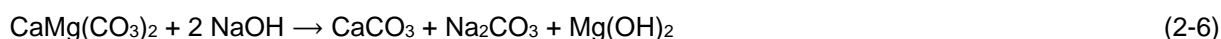
Calcium carbonate itself is an important addition to Portland cement (Matschei et al., 2007). Its addition causes alterations in the hydrated cement paste. If calcite addition is high enough, calcite – or more generally calcium carbonate - is in thermodynamic equilibrium with the cement phases and is not subject to long-term reactions with cement phases anymore.

The term “alkali-carbonate reaction” (ACR) is mainly used for the reaction between alkaline pore fluids and calcium-magnesium carbonates, i.e. dolomite (Grattan-Bellew and Katayama, 2019; Winter, 2009).

The alkalis in the cement pore water might react with the dolomite crystals present in the aggregate inducing the production of brucite, $(MgOH)_2$, and calcite ($CaCO_3$)



This mechanism was tentatively proposed by Swenson and Gillott (1964) and may be written as follows for sodium:



According to Leemann et al. (2016) the precipitation of brucite ($Mg(OH)_2$) itself happens in pockets within the dolomite and is not connected to expansion. Alkalis (Na, K) and CO_3 will react with portlandite to form calcite in the cement paste adjacent to aggregates. This reaction is a kind of de-dolomitisation and can be regarded as ACR in a narrower sense (Leemann et al., 2016).

2.2.1.5 Mineral dissolution kinetics (for aggregate – cement reactions)

Out-of-equilibrium geochemical processes are often described with the help of reaction rates. This makes it possible to include a timeline in the process description. Many kinetic models exist, often specialized for certain applications. For reactive transport the so-called “Lasaga”-type kinetic models are popular. They are based on transition state theory (TST) as detailed in Lasaga (1981a, 1981b). Data from two databases for rate laws are used in this study: the collection of Palandri and Kharaka (2004) and the data from Marty et al. (2015) which are part of the Thermoddem thermodynamic database.

2.2.1.5.1 Rate law for mineral dissolution

Both databases use a typical “Lasaga” type rate law for the dissolution of minerals in the following formulation from Palandri and Kharaka (2004):

$$\frac{dm}{dt} = -SA \left[\begin{array}{l} k_{acid}^{298.15K} e^{-\frac{E_{acid}}{R}(\frac{1}{T} - \frac{1}{298.15K})} a_{H^+}^{n_1} (1 - \Omega^{p_1})^{q_1} \\ + k_{neutral}^{298.15K} e^{-\frac{E_{neutral}}{R}(\frac{1}{T} - \frac{1}{298.15K})} (1 - \Omega^{p_2})^{q_2} \\ + k_{base}^{298.15K} e^{-\frac{E_{base}}{R}(\frac{1}{T} - \frac{1}{298.15K})} a_{OH^-}^{n_3} (1 - \Omega^{p_3})^{q_3} \end{array} \right] \quad (2-7)$$

The reaction rate dm/dt [mol/s] depends on a (reactive) surface area SA [m²] and on three terms that describe three different reaction mechanisms: a standard “neutral”, an H⁺-catalysed “acid” and an OH⁻-catalysed “base” mechanism. Each mechanism is parameterized with the help of a kinetic reaction constant k [mol m⁻² s⁻¹] at a temperature of 298.15 K and an exponential term (Arrhenius law) for the temperature T [K] dependence with a mechanism specific activation energy E [J mol⁻¹] and the gas constant R .

The last term for each mechanism includes the mineral saturation degree $\Omega=Q/K$ where Q is the activity product of the dissolved mineral constituents and K the equilibrium constant (solubility product). This term describes the distance to the equilibrium state. The parameters p and q are empirical and dimensionless and describe the influence of the reaction rate on mineral saturation index. They have to be obtained by fitting experimental data (Marty et al., 2015; Palandri and Kharaka, 2004).

Additionally the “acid” and “base” mechanism includes a dependence on the activity of H⁺ and OH⁻. The power exponents n_i are typically obtained by fitting experimental values measured at different pH. Note that in Palandri and Kharaka (2004) the “base” mechanism (third term) in equation (2-7) uses the activity of H⁺ raised to a reaction order with negative sign instead of the activity of OH⁻.

2.2.1.5.2 Uncertainties related to reaction rates

The publication of Marty et al. (2015) includes an extended discussion on the sources of uncertainties for rate laws and parameters. Also, in chapter 3.2 of Jenni et al. (2019) uncertainties related to thermodynamic and kinetic modelling of bentonite (also under high pH conditions) are discussed extensively.

Marty et al. (2015) clearly stated the following:

“Moreover, laboratory experimental rates and those measured in situ vary by up to several orders of magnitudes (Lüttge et al., 2013; Marty et al., 2009; Velbel, 1990; White and Brantley, 2003; Zhu, 2005). Significant differences are also observed in similar experiments dealing with the same material. For Lüttge et al. (2013), these discrepancies cannot be attributed to experimental artifacts (analytical uncertainties, data acquisition methods, etc.). Authors identify extrinsic and intrinsic sources of rate variations (depending on the observation scale). Extrinsic sources come from heterogeneities (porosity, mineralogical and chemical compositions, etc.) inside the media that should be represented. From this point of view, their consideration is the responsibility of the modeler. Intrinsic sources of rate variations are also attributed to heterogeneities at the crystal scale (crystal-defect distributions, impurities, etc.). Only kinetic Monte-Carlo models are able to show a large variation in total rate over time (Luttge et al., 2013). However, this method is limited at the crystal scale. Therefore, the use of TST kinetic models appears to be currently unavoidable for large-scale simulation, even if the use of a mean or rate-limiting value describing the reaction rate appears to be questionable.”

2.2.1.5.3 Reactive surface area

One important, if not the most important, source of uncertainty is the value of the surface area SA in equation (2-8). Kinetic rates are frequently measured with dissolution experiments of small mineral particles suspended in a relatively high amount of solution (which is constantly stirred/mixed). Firstly, it is straightforward to measure the BET surface area for mineral powder and secondly during the

experiment the whole grain surface is in equal contact with the solution, although possibly not all surfaces dissolve at the same rate (Fischer et al., 2014).

In petrology, commonly reaction rates estimated from field observations are often significantly lower than those measured in lab experiments (Brantley, 2008; see discussion in White and Brantley, 2003). In rocks and artificial media like concrete, the liquid to solid ratio is much lower and the surface of mineral grains is not evenly in contact with the pore fluid. Recent experimental studies demonstrate that the pore-scale reactivity of minerals in combination with microscopic and macroscopic transport controls the evolution of the corresponding material at macroscopic scale (Kurganskaya and Rohlfs, 2020; Noiriél and Daval, 2017; Poonoosamy et al., 2020; Prasianakis et al., 2017).

In addition, e.g. disconnected pores or partial water saturation might compartment the pore space and slow down or interrupt microscopic transport of solutes. For such a compartmented pore the pore water composition might vary considerably. All these conditions make it very difficult to assign a single effective surface area. In addition, the pore space geometry, the mineral grain size and surface roughness of mineral grains might change significantly during dissolution (and precipitation of other reaction products). Frequently, this effect is lumped into a “chemical reactivity” function which links liquid water saturation with a reduction of kinetic rates (Huang et al., 2021; Thouvenot et al., 2013).

It should be noted that the reactive surface area is normally used as a lumping factor in reactive transport calculations (Beckingham et al., 2017). As all other variables in equation (2-8) are fixed by either database entries or thermodynamic constraints, the only “free” variable is the surface area that is used to scale the rates to desired values, if necessary.

2.2.1.5.4 Kinetic rates constants and pH dependence

As noted by Marty et al. (2015) similar experiments for the “same” material might results in significantly different experimental results. The choice of datasets for fitting kinetic rates in general and specifically the pH dependence might be very different between kinetic databases. In addition, Palandri and Kharaka (2004) and Marty et al. (2015) show that the use of different regression methods might give significant order-of-magnitude differences in rate constants (c.f. Figure 2-7). Reported models deal with far-from-equilibrium dissolution rates. Note that the “distance” from equilibrium can have an impact of several orders of magnitude on reaction rates.

In addition, experiments do not necessarily cover all chemical conditions of interest. Specifically, data on very high or very low pH might be missing. For such a case, it is unknown if rates can be extrapolated to other chemical conditions. This is a problem for some minerals in Palandri and Kharaka (2004), as they specifically limit the applicability of their fits due to lack of data for alkaline chemical conditions.

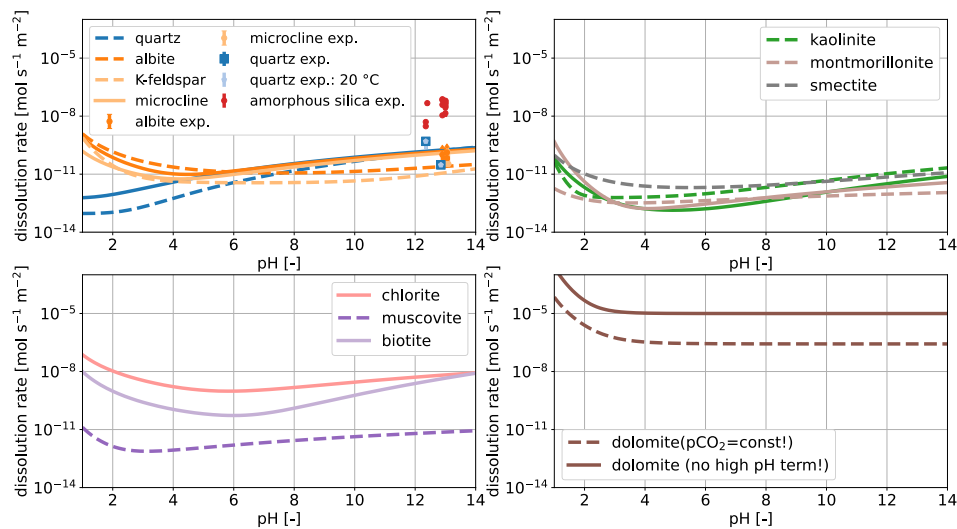


Figure 2-7: Plot of pH dependence of normalized dissolution rates for some common rock-forming minerals at 25 °C, at mineral saturation degree $\Omega \approx 0$ and normalized to a reactive surface of 1.0 m². Kinetic data from Thermoddem D B (Marty et al., 2015) are plotted as solid lines, while data from Palandri and Kharaka (2004) are plotted as dashed lines. Experimental data for dissolution of quartz, albite, microcline and amorphous silica at 40 °C and pH > 12 from Bagheri et al. (2022) are added for comparison (from Kosakowski et al., 2023).

2.2.2 Organic wastes and related processes

Organic waste is present in technological waste and process waste produced during operating, maintenance and decommissioning operations performed in fuel cycle facilities and during the recovery and conditioning of legacy waste (Altmaier et al., 2021). Such materials do present a radioactivity because of the presence of contamination by fission products, activation products and/or actinides.

Organic materials are present in technological wastes in various forms: paper, gloves, boots, over-clothing, flasks, filters, seals, cables, etc. Process waste includes powder waste recovered from pits, tanks and silos. Most of these organics corresponds to polymers of which list is presented in Table 2-1.

Table 2-1: Main organic materials present in ILW wastes (adapted from Altmaier et al., 2021)

<p>Chloropolymers</p> <p>Polyvinyl chloride (PVC)</p> <p>Polychloroprene (Neoprene®)</p> <p>Chlorosulfonated polyethylene (Hypalon®)</p> <p>Fluoropolymers</p> <p>Polytetrafluoroethylene (PTFE, Teflon®)</p> <p>Polyvinylidene fluoride (PVDF)</p> <p>Vinylidene fluoride-hexafluoropropylene copolymer (Viton®)</p> <p>Polyacrylate</p> <p>Polymethyl methacrylate (PMMA)</p> <p>Polyacrylonitrile (PAN)</p>	<p>Polyolefins and associated copolymers</p> <p>Polyethylene (PE)</p> <p>Polypropylene (PP)</p> <p>Ethylene Propylene Rubber (EPR) copolymer</p> <p>Ethylene propylene diene monomer (EPDM)</p> <p>Terpolymer</p> <p>Miscellaneous</p> <p>Polycarbonate (PC)</p> <p>Polyurethane (PUR)</p> <p>Polyamides (Nylon®)</p> <p>Polyimide (PI)</p> <p>Cellulose</p> <p>Epoxy resin</p>
---	---

Ion exchange resins (IER)	Silicone
Styrene-divinylbenzene copolymer	Polybutadiene
Polyacrylonitrile based resins	Superplasticizers

The percentages in mass are highly variables, due to the nature of the waste and of the national inventory, which itself reflect the diversity of the national ILW waste processing. This diversity is reflected in the example reported in Figure 2-8, numbers issued from the French, Belgium and Swedish nuclear waste management agencies (Altmaier et al. 2021). However, the main part of the organics is still associated with plastics, cellulose, bitumen and IER resins.

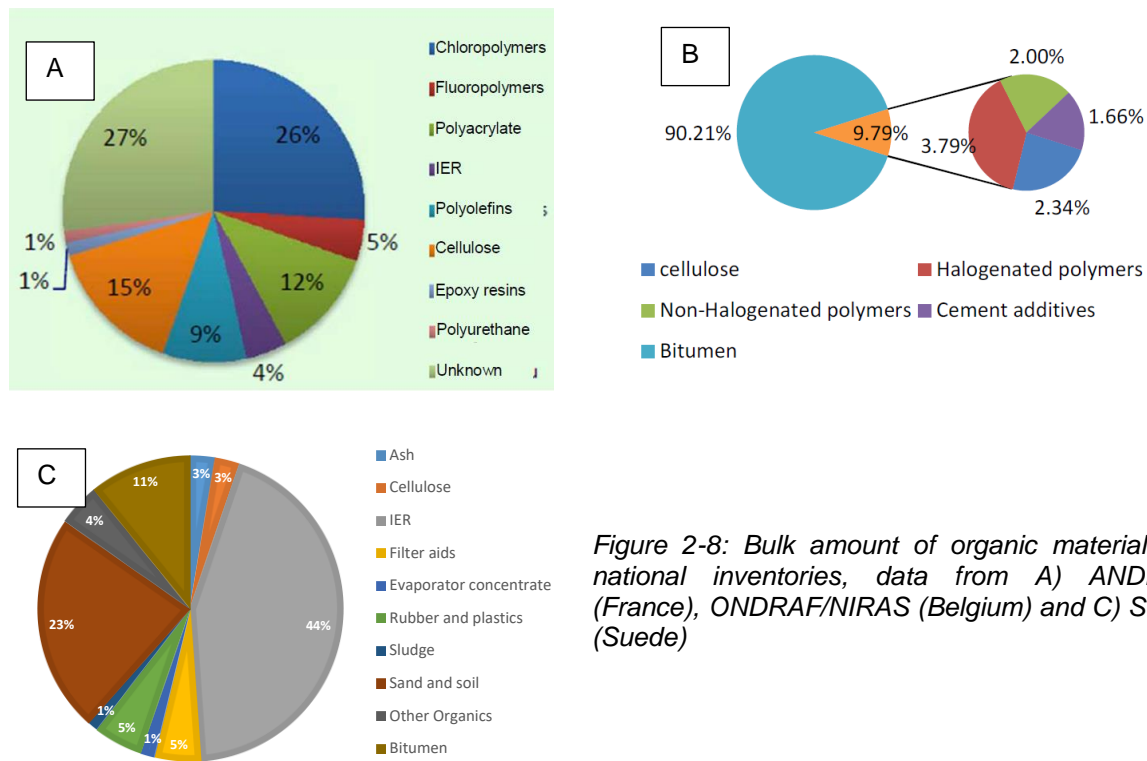


Figure 2-8: Bulk amount of organic material in national inventories, data from A) ANDRA (France), ONDRAF/NIRAS (Belgium) and C) SKB (Suede)

The decomposition of organic materials in the waste may take place both through abiotic (both radiolysis and hydrolysis) and biotic processes (Uras et al., 2021). For hydrolysis and biotic processes, the presence of water is mandatory for the reactions to proceed, while for radiolysis, the degradation will depend on the activity of the isotopes present in the package. In addition, biotic processes will be hindered by the alkaline environment (high pH) induced by the presence of cementitious materials in the vicinity of microorganisms and could also undergo irradiation effect in their growth rate (Brown et al., 2014).

Wieland et al. (2020) divide the organic material in cemented ILW waste packages into:

- slowly decomposable and rapidly decomposable organic materials (high molecular weight (HMW) organic materials (bitumen, polystyrene (ion exchange resins), plastics, and rubber),
- rapidly decomposable organic materials (cellulose, low molecular weight organics and cement additives).

The literature is somehow heterogeneous regarding for the description and the data available for the degradation of the different organic compounds.

The degradation of cellulose under highly alkaline conditions (pH > 11), is controlled by abiotic hydrolysis processes producing mainly isosaccharinic acid and minor quantities of other organic acids. Further abiotic decomposition to CO₂ and/or CH₄ is strongly kinetically hindered (Uras et al., 2021). For the time being it is not possible to assess the radiolytic degradation of cellulose due to lack of experimental data.

Altmairer et al. (2021) recently provided a literature review for the radiolytic degradation of plastic polymers. They underline a possible significant contribution from the degradation of such compounds to the global gaseous release, considering two main pathways. In anoxic conditions, polymer degradation mechanisms do not imply chain reactions, as there are with radiooxidation in the presence of oxygen. The latter correspond to the reaction scheme reported on Figure 2-9:

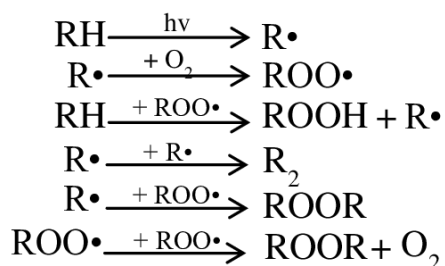


Figure 2-9: Reaction scheme implied in the radiooxydation of a polymer

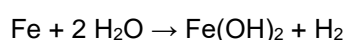
Such reaction scheme terminates in producing ketones, alcohols, carboxylic acids, vinyls, etc., from the last two termination reactions. The main gases produced by radiolysis are H₂, CO₂, CO, and CH₄. For halogenated polymers HCl or HF may also form. Among those gaseous species, H₂ would be produced in all scenarios while CO and CO₂ require oxidizing conditions. The release of halogenated gaseous species is not to be minored since chlorinated organic materials, for example, represent the most abundant polymers in ILW packages.

2.2.3 Metallic wastes and related processes

During use of nuclear facilities, some of the metallic structures activate due to neutron absorption. During decommissioning, the produced active waste (pipes, valves etc) is stored according to the measured radiation level of each the component. The waste is mainly carbon steel and some stainless steel. Intermediate level waste will be packed inside reinforced concrete containers, which are backfilled with concrete to fill gaps (see Figure 2-4). The container will then be stored in a concrete silo in crystalline (granite) host rock or clay host rock depending on the country. Gaps in the silo will be filled with concrete or mortar.

During the dry storage of the ILW waste packages, cementitious materials will hydrate and residual water will slowly evaporate and diffuse out at the top of the containers. Oxidic conditions then mainly prevail during the operational phase and when the disposal cell is not completely saturated. Anoxic conditions will be established soon after repository backfilling and closure. Many different processes in a ILW or HLW disposal compete for oxygen (corrosion, oxidation of minerals, microbial respiration). In addition, also the cement used to produce the mortar or concrete can contribute to an anoxic environment. In a concrete-based geological disposal concept, the followed strategy is usually to demonstrate that localised corrosion phenomena cannot occur in highly alkaline disposal conditions.

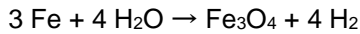
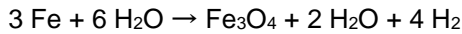
The process of anoxic corrosion of carbon steel can occur in various condition through the Schikorr reaction. Anaerobic corrosion of metallic iron to give iron(II) hydroxide and hydrogen:



followed by the Schikorr reaction:



give the following global reaction:



Degradation of the cementitious materials (carbonation, aggregate-cement reactions, leaching) will eventually lower the pH of the pore water towards neutral conditions. The corrosion rate will increase and possibly, localised corrosion mechanisms (e.g., pitting corrosion, crevice corrosion, and stress corrosion cracking) may initiate. If bicarbonate ions are present in solution, they can also evolve towards more stable carbonate phases such as iron carbonate (FeCO_3), or iron(II) hydroxycarbonate ($\text{Fe}_2(\text{OH})_2(\text{CO}_3)$). Stability diagrams can be used to predict stable phases through shifts in pH range although local conditions in crevices, pits and under biomass can be different compared to the general environment, resulting in a layered structure of deposits.

Figure 2-11 shows the Pourbaix diagrams with the available phases of calcium, iron-oxides with and without calcium and bicarbonate in the pore solution.

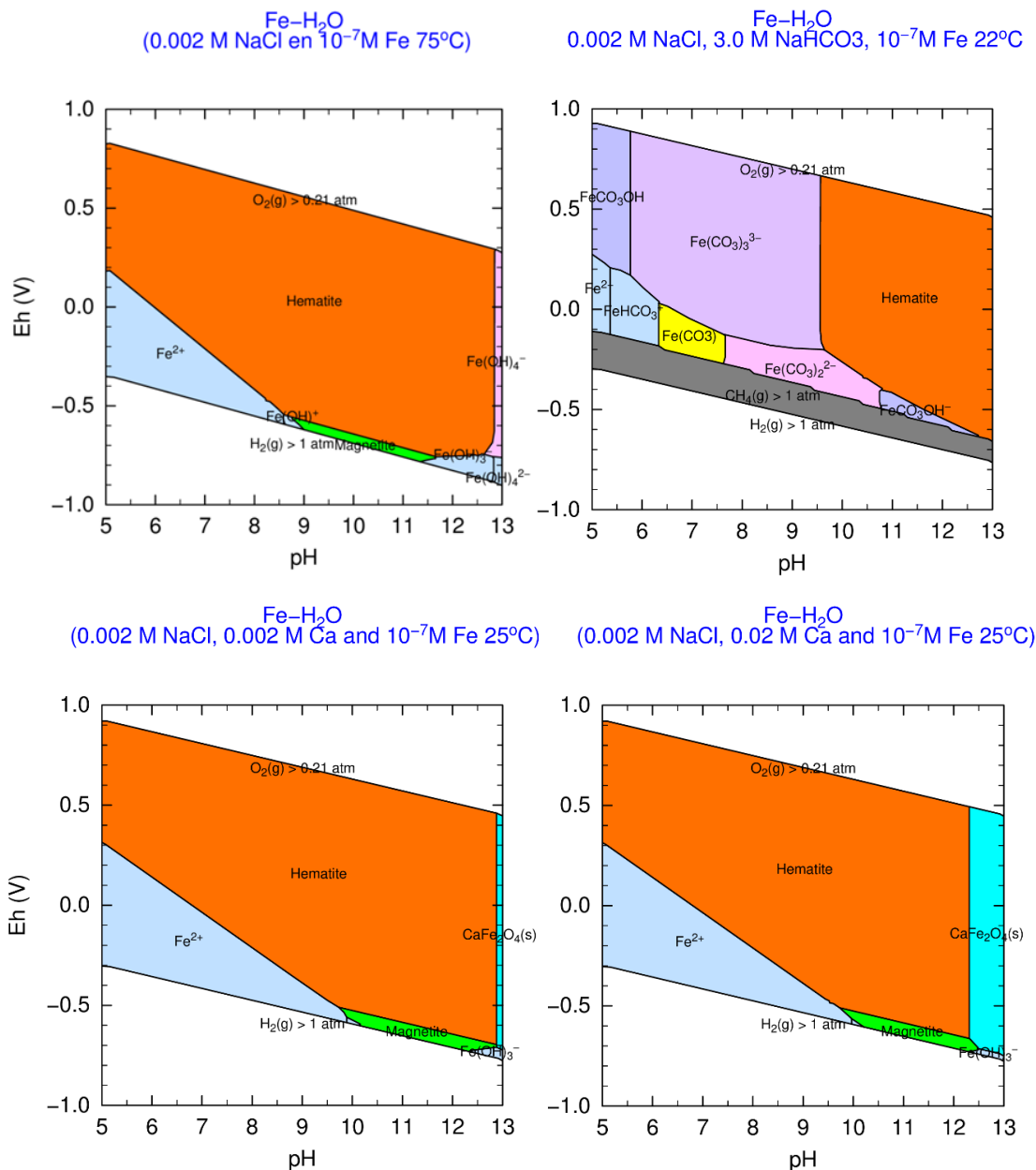


Figure 2-10: Pourbaix diagrams for the system Fe-H₂O with an activity of dissolved species of 10⁻⁷ M; 0.002 M Ca is a reasonable concentration for tap water and 0.02 M Ca is the maximum dissolved calcium concentration without alkalis (Berner, 1992) and (Vehmas and Itälä 2019) and 3M HCO₃⁻ is the

concentration found in Spanish and Czech granitic rocks and French indurated clay (see Appendix B) Magnetite (green) is $Fe_3O_4(s)$ and Hematite (orange) is $Fe_2O_3(s)$ and Siderite (yellow) $FeCO_3(s)^2$.

According to a recent article by Furcas et al. (2022), commonly forming iron oxide phases that constitute corrosion product films and oxide rusts are iron hydroxide ($Fe(OH)_2(s)$), hematite ($\alpha-Fe_2O_3(s)$), maghemite ($\gamma-Fe_2O_3(s)$), goethite ($\alpha-FeOOH(s)$), akaganéite ($\beta-FeOOH(s)$), lepidocrocite ($\gamma-FeOOH(s)$), feroxyhite ($\delta-FeOOH(s)$), iron trihydroxide or ferrihydrite ($Fe(OH)_3(s)$) and magnetite ($\alpha-Fe_3O_4(s)$). Their stability in the $Fe_2O_3-H_2O$ system determines which phase is most favoured.

Similar Pourbaix diagrams for basic stainless steel (Fe-Cr) in tap- and sea water saturated environment are shown in Figure 2-12.

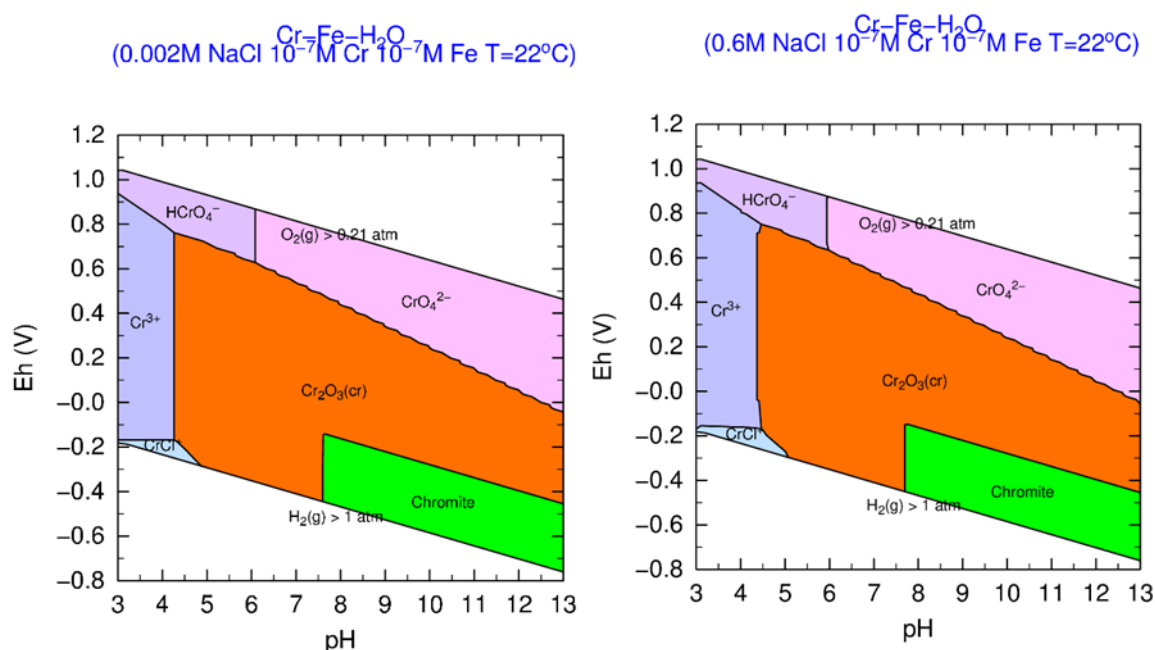


Figure 2-11: Pourbaix diagrams for the system Cr-Fe-H₂O with an activity of dissolved species of 10^{-7} M; 0.002 M NaCl is a reasonable concentration for tap water, 0.6 M NaCl is suitable chlorine concentration for seawater. Chromite (green) is $FeCr_2O_4(s)^3$.

2.2.4 Degradation of organic matter

Biotic degradation processes involving microbial activity is bound to occur in the vicinity of waste storage sites. In most of the studies related to organic waste degradation, biodegradation is presented as a major degradation mechanism, producing significant amounts of gases (mainly CO_2 and CH_4 (Uras et al., 2021)). It should be noted that several studies did not consider constraints imposed by amount of available water and the high pH due to the contact with cementitious materials. The dependence of microbial life on the availability of water is detailed in the section 2.2.5. Bacterial growth could also be hindered by ionizing radiations (Brown et al., 2014). For ILW waste packages, Abrahamsen et al. (2015)

² These figures have been made with Phreeplot (Kinniburgh and Cooper 2018), a free available software programme that makes geochemical plots using Phreeqc (Parkhurst and Appelo 2013). The SIT database has been used as input for these calculations. This database corresponds to the PHREEQC version of the ThermoChimie V.7.b, developed by Amphos 21, BRGM and HydAsa for ANDRA, the French National Radioactive Waste Management Agency.

³ These figures have been made with Phreeplot (Kinniburgh and Cooper 2018), a free available software programme that makes geochemical plots using Phreeqc (Parkhurst and Appelo 2013). The SIT database has been used as input for these calculations. This database corresponds to the PHREEQC version of the ThermoChimie V.7.b, developed by Amphos 21, BRGM and HydAsa for ANDRA, the French National Radioactive Waste Management Agency.

have assessed the total adsorbed dose to more than 1 MGy after thousand years, for a dose rate ranging from 0.05 to 0.6 G.h⁻¹. Brown et al. (2014) has summarised the range of total adsorbed dose and dose rate of nuclear storage and disposal environments and compared them to conditions of experimental studies that examine microbial radiation tolerance (Figure 2-12). This figure reports essentially the total doses and dose rates related to HLW waste packages. Abrahamsen et al. (2015) have determined these parameters for ILW waste packages, based on the calculations in Stankovskiy (2011). Their assessment corresponds to the blue circle reported in Figure 2-12. From its location, it appears that bacterial activity could be severely hindered by ionizing irradiations, inside ILW packages. It is important to note that an important source of data for such topic, the WIPP disposal project (Cohen, 2006) is based on observation and experiment related to the growth of bacteria in the vicinity of the packages and not inside the packages, which makes a difference.

However, since some microorganisms have developed mechanisms to survive in extreme environments even under alkaline conditions, it is necessary to provide an overview for such mechanism. In addition, as enhanced by Uras et al. (2021), the heterogeneity of the contents of the waste packages will result in strong spatial variation in the chemical conditions and local pH values may be much lower.

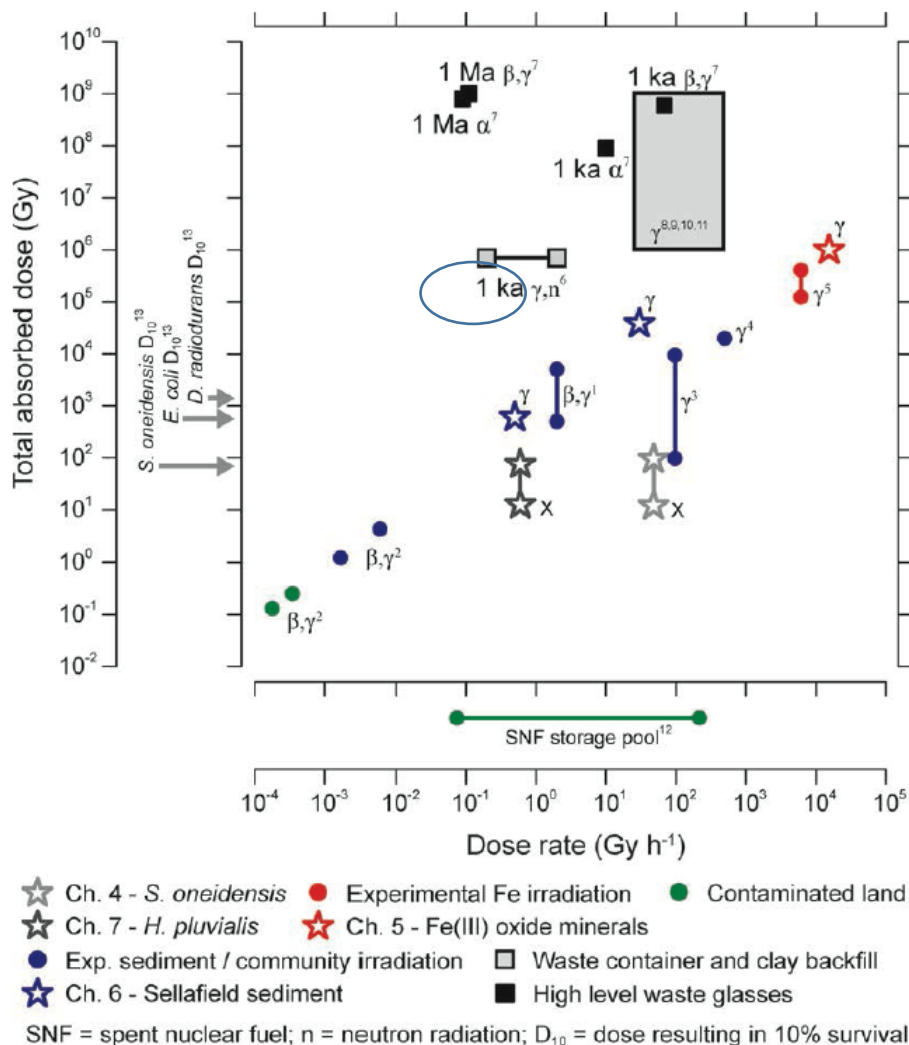
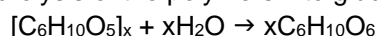


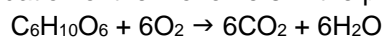
Figure 2-12: Total absorbed doses and dose rates relevant to the geodisposal of radioactive waste and bioremediation of radionuclide contaminated land (after, Brown et al., 2014)

In the case of cellulose, Cohen (2006) approximated the polymer to the chemical formula C₆H₁₀O₅. Then, as proposed by Uras et al. (2021), cellulose degradation can be described by a suite of succeeding reactions:

Hydrolysis of the polymers into glucose monomers



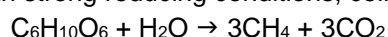
Oxidation of the monomers in the presence of O₂



Without O₂, cellulose degradation uses the reduction of electron acceptors, like sulfate



With strong reducing conditions, cellulose undergo a fermentation called methanogenesis



It is interesting to note that the net water balance thus depends on the nature of the redox conditions.

2.2.5 Influence of water availability on chemical reactivity

It is well known that iron corrosion rates (Stefanoni et al., 2018) and more generally (bio)chemical reactions are strongly inhibited in a dry environment where water availability is limited. As soon as the relative humidity is lower than a threshold value, the reaction almost stops (Roberge, 2019). In fact, threshold values might be different for different reactions (Roberge, 2019). For example, corrosion of an iron surface exposed to atmosphere was found to slow down strongly below a first threshold relative humidity of 55% and was reduced even more below a second threshold value of 20% (Watkinson and Lewis, 2004).

For reactions in porous media, the threshold value depends specifically on the pore size distribution, which connects the (partial) water saturation of the medium with the relative humidity of the gas phase (Ahlström, 2015). In contrast, carbonation fronts move faster at about 50-70% relative humidity in most cementitious materials (Russell et al., 2001; Šavija and Luković, 2016; Winter, 2009). At higher humidity, the CO₂ fluxes slow down as increasingly more pores are water-filled and fast diffusion in gas-filled pores is replaced by slow diffusion in water-filled pores. At lower humidity, however, there is insufficient water in larger pores to drive carbonation reactions.

According to Warthmann et al. (2013) the availability of water in the cementitious near field and specifically in waste packages is a limiting factor for microbial activity. In their review paper on biophysical processes that support diversity of microbial life in soil, Tecon and Or (2017) give more details on impact of pore size and water-saturation-related parameters (water potential, relative humidity and water film thickness) on microbial activity. They state that for slightly desaturated soil media, “*the thickness of aqueous films on most smooth mineral surfaces is in the range of 10 to 20 nm, too thin to support immersion of typical microbial cells (~ 0.5 to 2 μm) or flagellated motion.*” Furthermore, they state that for rough surfaces, film thickness is about an order of magnitude thicker. Such film thicknesses will still not allow cell motion but will allow microbial activity as nutrient transport in such films is possible.

To account for the slowing down of chemical reactions at dry conditions Trotignon et al. (2011) multiplied the various mineral dissolution/precipitation rates with a function $R(t,x)$ to scale chemical reactivity with relative humidity RH of the gas phase. This chemical reactivity R was calculated for each time step and each discretized volume. R varies between zero, if no reactions take place due to lack of water, and one, if the reactions are not limited by the availability of water. R was calculated with a phenomenological approach proposed by Bazant and Najjar (1972) for the hydration of cement paste under partially liquid saturated conditions:

$$R = (1 + (7.5 - 7.5RH)^4)^{-1}$$

in which the reactivity decreases progressively from 1 to zero as the water saturation approaches the residual saturation.

Another function was implemented by Suckling et al. (2011) in the T2GGM code, where the reactivity varies linearly between 0.6 and 1.0.

$$R = \begin{cases} 1 & 1 < X \\ X & 0 < X < 1 \\ 0 & x < 0 \end{cases} \quad \text{where } X = \frac{RH - RH_{min}}{RH_{max} - RH_{min}}$$

These reactivity functions are defined in terms of RH, but they are connected to the saturation of the medium via Kelvins equation, which relates the relative humidity with the radius of the largest water filled pore in a porous medium (Evans et al., 1986).

3 Model implementation and validation by experiments

In this section, we describe the modelling of three experiments used to validate models which will be implemented thereafter in reference cases calculations. The experimental results are presented in Mladenovic et al. (2024). Ideally, the modelling of the experiments would be used to validate the models and model parameters, but often the experiments are used to construct the models and to determine the parameters.

3.1 VTT experiment

3.1.1 Introduction

In Finland low level radioactive waste (LLW) contains considerable amounts of cellulose, hemicellulose-based material and metal material. Steel containers are used to store and dispose of the waste. The microbial degradation of cellulose and hemicellulose, together with the utilisation of hydrogen (H₂) generated by metal corrosion, will result in gas generation under final repository conditions. The chemical environment inside the container and steel drums will also be strongly affected. Microbially mediated LLW degradation and gas generation processes can influence the performance of multi-barrier systems, such as by accelerating corrosion and can affect the mobility of radionuclides from the repository.

A large-scale in situ Gas Generation Experiment (GGE) was established in 1997 and operated continually until 2023 in Olkiluoto, Finland, to simulate the gas generation and chemical changes in the environment of LLW under geological repository conditions. A brief description of the experiment has been given in Mladenovic et al. (2019, 2024), and some important information is recalled here. The schematic layout of the experiment is shown in Figure 3-1. The GGE comprises sixteen 200 l carbon steel drums containing LLW from nuclear power plants at the Olkiluoto site. The drums are placed within a concrete box (mass 4000 kg), as used in the Finish referred as VLJ repository, that is enclosed in a 20 m³ acid proof stainless steel gas tight reaction vessel. The LLW contained in the drums represents routine reactor operating waste and included cellulose (paper, cardboard, cotton), polyethylene, polyvinylchloride, polycarbonate, natural rubber, metal wastes, glass fibre and electrical components. The total masses of metal (including mild steel drums), cellulose and other organic polymers in the GGE at the start of the experiment were 379 kg, 620 kg and 596 kg, respectively. The GGE tank was filled with 16 m³ of locally sourced river water to reflect the fact that was intentionally planned to fill the disposal silos with water at the closure of the repository. The GGE has operated continuously and largely uninterrupted from 1997. A more detailed explanation is available in Small, et al. (2008, 2017).

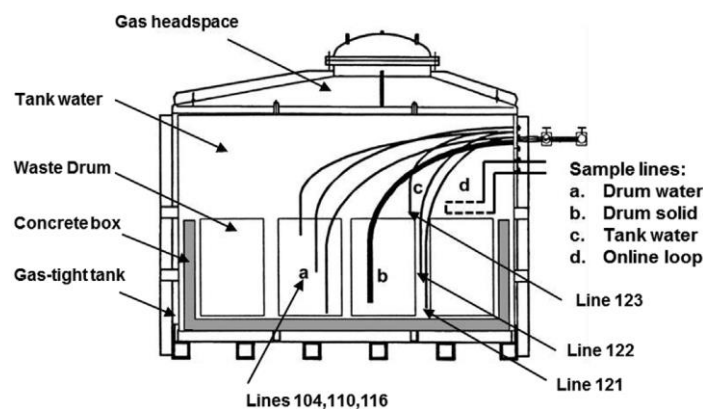


Figure 3-1: Schematic of the GGE showing different types of sampling lines (a, b, c) and online analyses (d) and location of Lines 104, 110, 116, 121, 122 and 123 that were used to take water

samples. The dead volumes of the tubing are approximately 0.1–0.4 dm³. Also capsules containing a piece of drum steel and LLW were loaded to the experiment (b, drum solid). Drums are normal size 200 l steel drums with a height of 0.9 m and a diameter of 0.6 m. (Small, et al. 2008)

Microbial degradation of organic materials and metal corrosion are considered the two main processes contributing to the gas generation in nuclear waste repositories. CO₂ and CH₄ are the main gasses produced by microbial degradation of organic materials, and H₂ is considered as the main gas produced from the corrosion of steel and other metals under anaerobic repository conditions. The composition of the three mixed gasses depends on the environmental factors: i) the amount of methanogenic bacteria that compete with electron acceptors for electron donors (e.g., metabolizable organic species, metals and H₂ produced from corrosion processes) (Fenchel et al., 2012); ii) CO₂ generated from the degradation of organic materials participates in the reaction with cementitious materials to form CaCO₃, lowering the pH of concrete; iii) the activity of microbes that generate gas is influenced by the alkaline repository environment.

The experiment has been monitored since 1997, in the aspects of the rate and composition of gas generated, and the aqueous geochemistry and microbe populations present at various locations within the experiment. To be more specific, the monitored and analysed aspects include:

- (1) a continuous monitoring of pH, Eh, electrical conductivity, and dissolved O₂ in the tank water by monitoring the composition of water sample with an on-line system of electrodes;
- (2) analyses of major cations (Ca²⁺, K⁺, Na⁺, Mg²⁺, Fe²⁺) and anions (Cl⁻, SO₄²⁻, HS⁻; alkalinity) in water samples;
- (3) characterisations of the microbial populations present in solid samples comprising a small plate of waste drum steel, waste materials, and cellulose control materials.

The experiment has been modelled by a biogeochemical reaction-transport code (Small, et al. (2008, Small, et al. 2017)) considering the microbial degradation of organic materials and metal corrosion, to predict the rate and composition of gas generation, water composition, and microbial activity. A summary of the biogeochemical model will be presented in section 3.1.2, and a comparison between modelling results and experimental data will be described in section 3.1.3.

3.1.2 Biogeochemical modelling

A biogeochemical reaction-transport code, the Generalised Repository Model (GRM), has been used to simulate the gas generation. A blind-test model was firstly developed in Small et al. (2008), where a minimum amount of information was provided to the model, e.g., dimensions of the initial set-up of the experiment, the materials inventory, composition of initial water, etc. The model was further updated in Small et al. (2017) by fitting to the pH evolution and gas generation data set, and the corresponding modelled results are summarised and presented in this report. Individual waste containers are considered in the model to simulate the heterogeneous chemical system, e.g., various pH values are observed ranging from 5.5 to 10.0 between organic-rich waste and water associated with concrete. The model simulates the transport of chemical species in saturated groundwater, coupling to an equilibrium chemical calculation using the PHREEQC source code (Parkhurst and Appelo, 2013) that calculates the reaction of aqueous, mineral, and gaseous species under a given redox potential (pe). The redox potential is determined by the main processes involved in the gas generation: corrosion, cellulose hydrolysis, and microbial processes. Therefore, the kinetics corresponding to the main processes are considered in the model.

(i) Corrosion model

An empirical model concerning the corrosion process is considered in the GRM. The steel corrosion in the GGE is simulated as under saturated groundwater conditions in anaerobic environments, though the GRM is also able to simulate an unsaturated condition and an aerobic environment. The anaerobic

corrosion process is represented by a linear corrosion rate (C_{plt} $\mu m/year$), and the volumetric corrosion rate of the plate steel that represents the waste drums present in the GGE can be expressed as:

$$\frac{V_{plt}}{\Delta t} = SA_{plt} C_{plt} \quad (3-1)$$

where SA_{plt} is the surface area depending on the initial plate thickness, mass, and density of steel.

Ferrous hydroxide and carbonate corrosion products in CO_2 environment are assumed to form under anaerobic conditions, with producing H_2 . The H_2 produced during the corrosion process participate in the microbial processes depending on the availability of other substrates, and the remaining is transferred to a gas headspace associated with each finite difference cell.

(ii) Hydrolysis of polymeric substrates

The hydrolysis of polymeric organic substrates within GRM considers cellulose hydrolysis to form glucose ($C_6H_{12}O_6$), and the rate can be expressed as:

$$\frac{dS_p}{dt} = -V_p S_p F_{pH} \quad (3-2)$$

where V_p is the hydrolysis rate of the polymer, S_p is the concentration of the polymer, and F_{pH} is a pH control factor in an expression:

$$F_{pH} = \exp [-(pH - pH_{opt})^2 f] \quad (3-3)$$

where pH_{opt} is an optimum pH for microbial growth and f is a pH dependence factor.

(iii) Microbial and redox potential model

The microbial kinetic model considered within the GRM is based on Monod kinetics (Koch 1998; Graham, J. and Smalley 2003), and the utilisation rate of microbial substrate is in a formulation of:

$$\frac{dS}{dt} = -\frac{VSX}{K_m + S} F_{pH} \quad (3-4)$$

where S is the concentration of microbial substrate, V is the maximum substrate removal rate, K_m is the half saturation constant that defines the nutrient uptake characteristics of different microbes, and X is the biomass concentration in an expression of:

$$\frac{dX}{dt} = Y \frac{dS}{dt} - DX \quad (3-5)$$

which describes the growth of the microbial population in relation to substrate utilisation. Y is the yield factor expressing the proportion of organic substrates utilised in growth, and D is the death rate of microbe biomass.

A dominant redox couple is selected by the model to define a redox potential based on the extent of the microbial processes, and six redox couples are considered with a sequence starting with the most oxidising couple: oxygen, nitrate, iron, sulphate, methane, and fermentation. Once the controlling couple is identified, the redox potential is then calculated using mass action expressions for the selected redox reaction.

3.1.3 GGE experimental results and modelling validation

The 2D finite difference grid of the GRM is used to represent the waste drums, water, and concrete regions of the GGE, and each cell of the grid includes two parts: a lower saturated zone and an upper unsaturated zone. The unsaturated zone has a gas-filled pore-space, and the GRM gas model considers the pressure developed in the headspace and releases excess pressure above 1 bar to the atmosphere. Moreover, no chemical or gas reactions are considered in the unsaturated zone and no mixing of gases is present in adjacent headspace cells. A linear corrosion rate of $5 \mu m/year$ (BNFL 2002) for the anaerobic corrosion of mild steel was used in the model. A ca silicate hydrate phase and an amorphous

silica phase were considered representing the initial cement mineral present in the system, and secondary mineral phases considered were: calcite (CaCO_3), siderite (FeCO_3), brucite ($\text{Mg}(\text{OH})_2$), troilite (FeS), and FeOOH . In this subsection, the major experimental data and a comparison with modelling results are described.

3.1.3.1 Gas generation and composition

Within the first year of experiment, little gas was generated. It is believed to be caused by the saturation of the waste materials through the movement of water into the bagged waste, the displacement of trapped air, and the establishment of gas generation processes. A gas generation rate of $0.53 \text{ m}^3/\text{year}$ between 1998-2004 was found. The rate increased to $1.24 \text{ m}^3/\text{year}$ between 2004 and 2006, then decreased to $0.96 \text{ m}^3/\text{year}$ until 2016, as shown in Figure 3-2. Two models (A and B) investigating the effect of CO_2 solubility were developed in Small et al. (2017) predicting the gas generation. Model A compensates for the underestimation in CO_2 solubility, while model B considers the equilibrium case. As shown in Figure 3-2, the cumulative volume of the generated gas is well predicted by Model A.

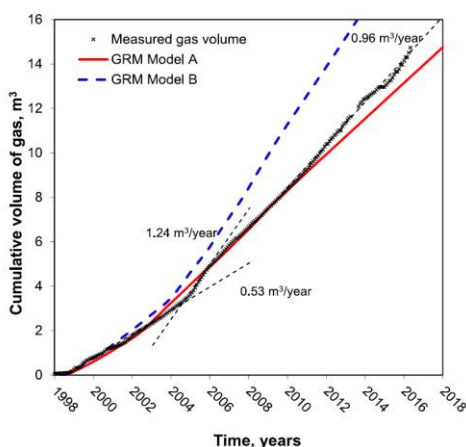


Figure 3-2: Comparison of the measured gas volume with the modelled results (Small, et al. 2017).

The major gasses present in the gas generated by the GGE include H_2 , CH_4 , CO_2 , O_2 , and N_2 . CH_4 was detected as the first generated gas after 6 months, and it occupies a vol% between 50% and 90% in the following years. H_2 was only detected during the first 18 months of operation, and the content of O_2 was at a level in a range of 0.1-12.7 vol%. A significant amount (10-47 vol%) of N_2 was found, even though it was not analysed during the initial period. A CO_2 concentration of 3 vol% was present in the gas phase during the first two years of the operation, which is higher than the content in tank water that is in equilibrium with a pH value of 10-11. It was because the CO_2 generated in the neutral pH waste drums was not able to reach equilibrium with the alkaline tank water during the initial 4 years of the experiment, and it was released. The pH in tank water was decreased with time and the CO_2 vol% in the gas phase is close to the amount that is in equilibrium with the tank water.

According to the modelling results developed in (Small, et al. 2008), H_2 was simulated as the predominant gas for the beginning period and dropped to a vol% of around 1% when CH_4 became the dominant gas for the following years. The majority of the initial N_2 and O_2 present in the headspace was replaced by CH_4 during the first 2 years according to the simulation. The model underestimated the content of N_2 and O_2 since the trapped air present within the waste cannot be represented by the GRM. As shown in Figure 3-3(b), a good consistency is obtained by model A, while model B overestimates the volume of CO_2 . Model B also underestimates the proportion of CH_4 in the gas phase (Figure 3-3(a)) because of a relatively higher proportion of CO_2 . In general, the predominant presence of H_2 and replacement by the generated CH_4 was well captured by the model. The behaviour of other main

gaseous phases is reasonably represented by the model, even though its volume variation is overestimated.

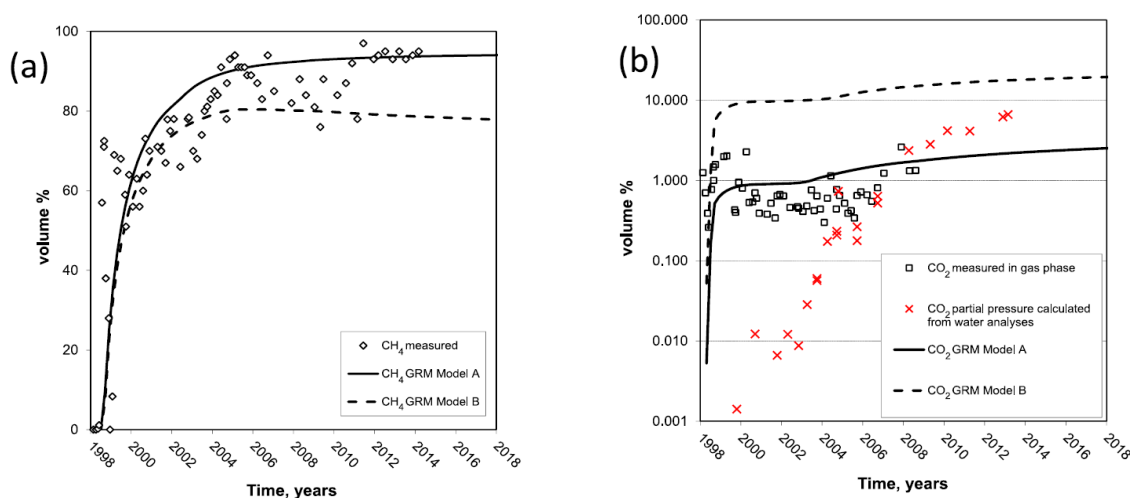


Figure 3-3: Comparison of the gas (in vol%) generated in GGE during the year 1997 to 2018 between the measurements (plotted in dots) and the modelling (plotted in line), concerning (a) CH₄; and (b) CO₂ (Small, et al. 2017).

3.1.3.2 Water composition

The pH values measured within the GGE is presented in Figure 3-4 where a noticeable variation at locations is observed. For instance, the pH measured at the drum lid level dropped from a value in a range of 9.5-11.2 to 7.0, while the pH was stable at neutral values within the drums and water at the bottom of the tank. Figure 3-4 also presents the modelled pH in the tank water and waste drum. The modelled pH in the waste drum initially has a spike where pH rises from an initial value of 5.0 to 9.2. This is due to the initial processes of anaerobic corrosion and H₂ generation which produces alkalinity. However, it is subsequently neutralised by CO₂ and acetic acid generated from organic degradation processes. The resulting stable pH in the waste at a value of around 6.1 is close to the experimental data measured in the waste and the tank water at the bottom. The modelled pH in water shows an initial value of around 11.2 after 1 year of operation resulting from the interaction through the transport model, and it decreases to around 7.0 due to the acidity generated by waste cells and to the buffering effects of secondary mineral phases.

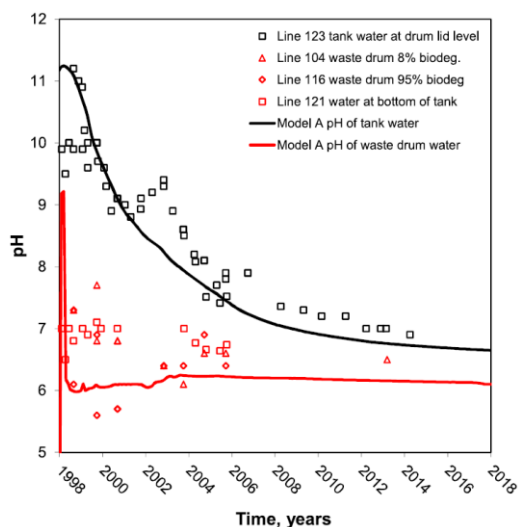


Figure 3-4: Comparison of the average pH of the waste, water and concrete cells predicted by GRM model with the measurements from GGE.

An increasing concentration of Na^+ and Cl^- was detected in the water sample at the drum lid level, which indicates the leaching of the ions from waste material to the tank water. Ca^{2+} was maintained at a constant level during the first years of operation, reflecting the buffering by mineral phases. Ammonia ($\text{N}(-3)$) showed a progressive increase in concentration in the tank water, which may be sourced from the waste drums. In general, most species have a higher concentration in the waste drums than in the tank water, which means that the waste may provide the source of these species for the increasing Na^+ , Cl^- , and NH_3 detected in the tank water. Among them, Ca^{2+} has a significantly higher concentration in the waste drums than in the tank water, particularly in the drum with 95% biodegradable waste.

Sulphate was only detected during the first 3 years of operation and became out of detection afterwards when sulfide was found, see Figure 3-5(a). The presence of sulfide corresponds to the decline of SO_4^{2-} , consistent with a reduction process. Figure 3-5(b) indicates that the total dissolved carbonate concentration measured in the tank water has increased during the 18 years of operation, which results from the biodegradation of cellulose materials present in the waste drums that generate CO_2 in addition to CH_4 . Aqueous concentrations of Fe, Ca and Mg measured in the tank water increased during the experiment, and their concentrations in tank water were lower than measured in the waste drums during the first 8 years of the operation (not shown in the figure). The increase of concentration observed is a consequence of transport of species through diffusion and mixing of water from the waste drums to the tank water. Moreover, the decrease of pH and increasing carbonate levels in the tank water affects the equilibria of mineral phases and thus the concentration of the elements.

The reduction from SO_4^{2-} to $\text{S}(-2)$ in tank water is well represented by the model (see Figure 3-5 (a)), as well as the subsequent decline in $\text{S}(-2)$ concentration due to the formation of FeS corrosion products. Figure 3-5(b) presents a comparison of the measured concentration of acetate in tank water with the modelled values, which shows a good consistency in the later stage. However, the peak value is underestimated. Figure 3-5(b) also presents a comparison of the measured and modelled concentration of carbonate in tank water. A lower concentration was modelled, while it is in consistent with the increasing trend found in the GGE. The variation of the modelled data is a result of the variation in pH and CO_2 partial pressure, which affects the formation/dissolution of CaCO_3 . The GRM model reproduces the trends of increasing Fe and Ca concentrations observed in the tank water (see Figure 3-5(d)), but the average modelled concentrations are underestimated. The increasing concentration of Mg observed in the experiment is not represented by the model, which mostly shows a constant value.

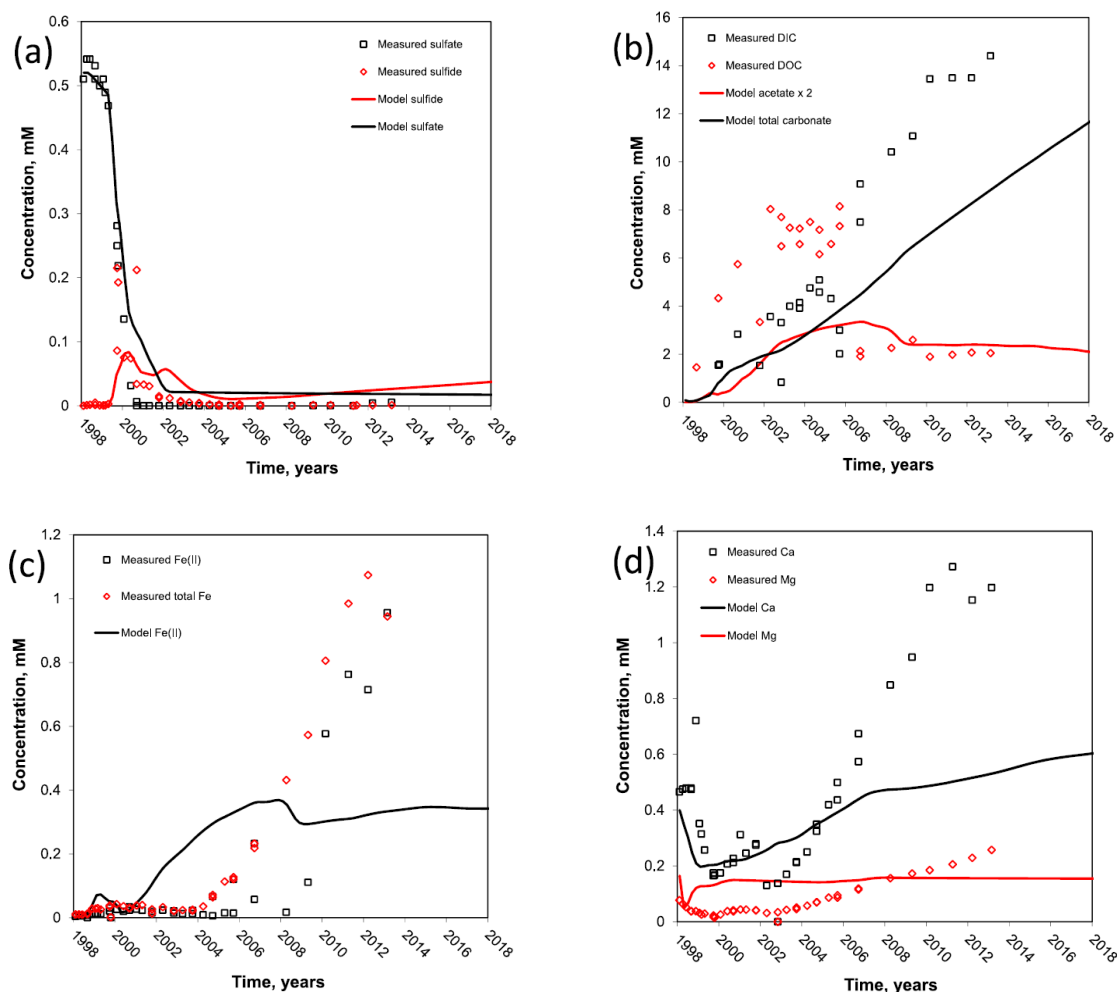


Figure 3-5: Comparison of the concentration of reactive aqueous species in tank water between the measured data and simulations in the aspects of: (a) sulfate and sulfide; (b) inorganic and organic carbon; (c) iron; and (d) calcium and magnesium.

3.1.3.3 Microbiology

Anaerobic bacteria were present in tank water and in representative waste materials, and the groups studied include alkaliphilic, SO_4^{2-} reducing, and methanogenic bacteria. Bacteria were notably more abundant in the water samples taken from the bottom of the tank ($10^2 - 10^5$ colony forming units (cfu)/mL) compared to the water samples taken from the top of the tank (1-100 (cfu)/mL), and this may be induced by the accumulation of the organic matter at the bottom of the tank and the fact that the alkaline pH in the upper level of the tank water may inhibit the bacteria growth. According to the microbial community analysis using direct DNA extraction and PCR-DGGE analysis, it was found that the predominant microbial groups in tank water have changed during the years 1999-2005, and the change is more obvious in the water sample taken from the top of the tank compared to that at the bottom. Figure 3-6 presents the modelled average concentration of the most abundant microbial groups that are simulated by the GRM model. The model results indicate an initial process of sulphate reduction fuelled by hydrogen generated by anaerobic corrosion. Cellulose degrading bacteria develop rapidly during the initial years of the operation. Organo-methanogens become significant from approximately 2004 and are developed in the water filled regions of the experiment.

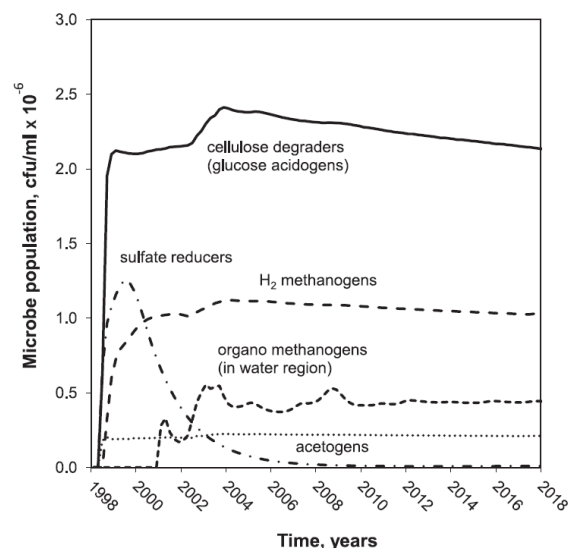


Figure 3-6: Modelled population size of microbial groups in the GGE (Small et al., 2019).

3.1.4 Analyses and conclusions

3.1.4.1 Gas generation rates

Figure 3-7 updates the cumulative volume of the generated gas during GGE until August 2021. It is worth mentioning that sulfate and KOH were added in June 2020 and August 2021 to investigate their impacts on gas generation, and no impacts of sulfate on gas generation were observed. However, this is out of the scope of the study in ACED. Interested readers are referred to Vikman and Sohlberg (2022). It is observed from the figure that the gas generation rate increases over time, and it can be generally expressed in three stages: (i) 0.530 m³/y between 1997 and 2004; (ii) 0.913 m³/y between 2004 and 2015; and (iii) 1.695 m³/y between 2015 and 2021. During 1997 – 2004, the gas composition varied significantly within the first year of GGE, then it stabilised with a composition in average as: CH₄ (78.75%), CO₂ (0.73%), H₂ (<0.1%), O₂ (1.01%), and N₂ (11.73%). During the second stage, the major gas is CH₄ with an average volume fraction of 89.21%. N₂ and O₂ tend to be less than 1 vol% and 0.1 vol % since 2012. The stabilised gas composition measured in May 2020 includes: CH₄ (90.00%), CO₂ (9.42%), H₂ (<0.1%), O₂ (<0.1%), and N₂ (0.38%). The volume fraction of CO₂ is considered the remaining value in addition to the measured volume fraction of CH₄, H₂, O₂, and N₂. A summary of the gas composition during each stage and corresponding calculations of the gas generation rate is listed in Table 3-1. The gas generation rate of CH₄ and CO₂, which are the main generated gases, increases with decreasing pH value in the tank water. The measured gas generation rate of CH₄ increases from 0.0301 to 0.1098 mol/kg/y, which is quite close to the value considered in Huang et al. (2021), especially during the first two stages where pH is relatively higher. In Huang et al. (2021), the pH value of the solution in waste package is considered 12.5 assuming sufficient cementitious material as barrier. This indicates the importance of placing cementitious material in waste package buffering the pH and thus reducing microbial activities.

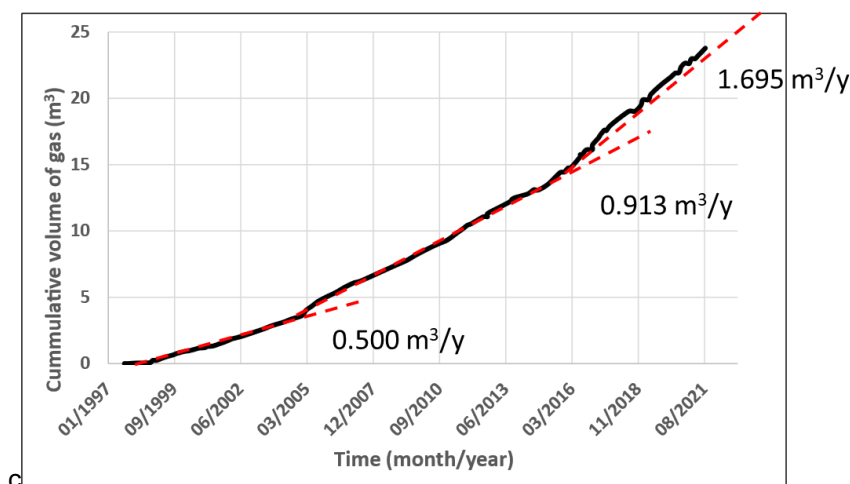


Figure 3-7: Updated data regarding the cumulative volume of generated gas until August, 2021.

Table 3-1: Measured cumulative gas generation rates (CGGR), gas composition in volume fraction (VF %), and calculated gas generation rates (GGR).

Gas	CH ₄	CO ₂	H ₂	O ₂	N ₂
CGGR 1 (1997 - 2004)	0.530 m ³ /y; pH decreases from 11.5 to 9.0				
VF (%)	78.75	0.73	<0.1	1.01	11.73
GGR (mol/kg/y)	0.0301	0.0003	-	-	0.0045
CGGR 2 (2004 - 2015)	0.913 m ³ /y; pH decreases from 9.0 to 7.0				
VF (%)	89.21	9.59*	<0.1	<0.1**	<1.0**
GGR (mol/kg/y)*	0.0586	0.0063	-	-	0.0007
CGGR 3 (2015 - 2021)	1.695 m ³ /y; pH is stabilised at around 6.8				
VF (%)	90.00	9.42*	0.1	0.1	0.43
GGR (mol/kg/y)	0.1098	0.0114	-	-	-

Note: * The volume fraction of CO₂ was calculated as the remaining value in addition to the measured volume fraction of CH₄, H₂, O₂, and N₂.

** Values since 2012.

3.1.4.2 Carbonation

As quite an amount of CO₂ was generated in the waste package, it may induce carbonation in concrete. The first carbonation reaction with ordinary Portland cement is with portlandite. Later other calcium-containing hydrates will react. Portlandite carbonation does not have major detrimental effect of the mechanical properties of concrete. When C-S-H and other hydrates are carbonating, the mechanical and permeability properties are suffering somewhat. Figure 3-8 presents how cement hydration products

are altered due to carbonation. It is noticeable that carbonation itself does not destroy concrete, but the porosity will increase and then also permeability will increase. Ordinary Portland cement clinker contains about 63.5% CaO (Neeft, 2022). During hydration of the clinkers, C-S-H, portlandite and other hydroxides are formed. The CaO is bound to CO₂ to form calcium carbonate CaCO₃ when carbonation occurs. This simplified calculation will give us indication of alteration of concrete during carbonation.

1 mole of carbon dioxide consumes 1 mole of calcium oxide. CO₂ release was 12 moles/y, CaO mole weight is 56, so 672kg of calcium oxide is carbonated annually. This corresponds in concrete volume 3 dm³ with 350 kg/m³ cement content. Waste container box has a surface area about 42 m². Carbonation front is then calculated to proceed about 0.07 mm/y. When all the organic cellulose and hemicellulose has disintegrated, the totally carbonated layer is between 17 mm and 27 mm. So there is still lot of noncarbonated concrete left.

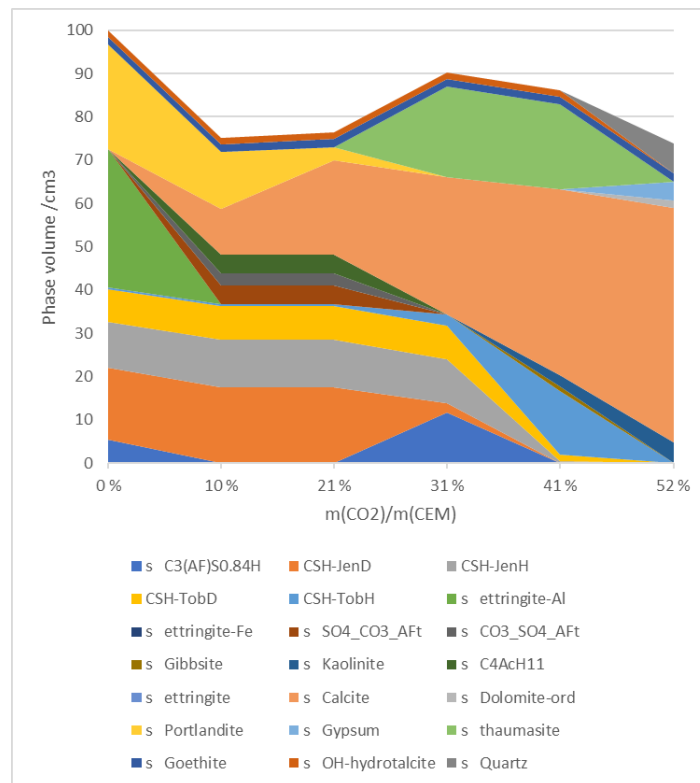


Figure 3-8: Concrete phase alteration due to carbonation (GEMS-calculation)

3.1.4.3 Leaching

Leaching will also be a reason for concrete deterioration. Calcium is leaching out of concrete when it is in contact with water. Calcium is first leached from Ca(OH)₂. The solubility of calcium hydroxide is about 1.5 g/litre. When the Ca²⁺ is in the water phase it will react with the CO₂ dissolved in the water and precipitates as CaCO₃, which has much lower solubility (about 15 mg/litre). This reactivity has already taken in account in previous section. Part of the calcite presented in Figure 3-8 will be precipitated from the liquid phase outside concrete. In the GGE Ca²⁺ content is increasing about 0.13 mM/y (after some years from the beginning of experiment start). As the total water volume is 20 000 litre, leached calcium amount is 2.5 M/y. This is about 140 g in the form of CaO. Then about 21% of calcite presented in Figure 3-8 will precipitate outside of concrete and this increases the porosity. Molar volume of calcite at the end is 54% of original solid volume of cement. This is then decreased to 44%. Total solid volume is then reduced for 10% from original volume. Potassium and sodium content in water are increasing in the GGE, e.g., the potassium content in water has increased to 6 mM/litre and sodium content to 5 mM/litre.

When compared the total amount of alkalis in concrete it can be noted that all of the alkalis have leached out of concrete during the first 20 years of GGE. This leaching has very little effect on concrete mechanical properties. Chemical composition of pore water will be affected, and pH slightly lowered in pore water.

3.2 COVRA experiment

The transport of water in cementitious materials may limit the access of water that is necessary for the degradation of organic and metallic waste. In ACED, representative disposal cells are studied but saturated dependent transport (diffusion, permeability) values of water of mortars and concrete - representative for waste packaging - are scarce or absent, especially for concrete made with blended cement. A design requirement for the waste package concrete may be that the manufactured concrete is impermeable. What is usually meant, is that water at a pressure (5 bar) is applied to manufactured concrete after 28 days hardening for a specific period (72 hours) and that the water penetration front may not exceed a couple of mm after this period (European standard EN 12390-8). This is a so-called engineered impermeability. This European standard was also used in Cebama to assure the concrete quality for the plug (Vehmas et al., 2017). For disposal of waste, more precise understanding of the transport of water in 'engineered impermeable' concrete is needed. Hereto, about 40 initially saturated waste package concrete specimens were dried at 11 different relative humidity's at 20°C and 9 different relative humidity's at 5°C to obtain sufficient experimental results that can be used for modelling. A similar amount of initially saturated foamed concrete specimens with the same type of cement and content but different porosity than waste package concrete was also dried in order to investigate the effect of a different distribution in size of pores.

The weight of samples of waste package concrete and foamed (cellular) concrete had been monitored during the exposure to the different relative humidity's and ordinary air and the two different temperatures. The porosity of the waste package concrete was gravimetrically determined to be 13 % and 21 % for foamed concrete. The carbonation rims had been measured to be very small after 1000 days of exposure due to ingress of carbon dioxide present in ordinary air. Both concretes were manufactured with a blended cement with Portland cement and blast furnace slag cement (CEM III/B). The traces of iron-sulphide were oxidized into iron-sulphates due to oxygen present in ordinary air. The oxygen reaction fronts were clearly dependent on the porosity of concrete, exposure to relative humidity and temperature (Mladenovic et al., 2024).

3.2.1 Interpretation of experimental results with models for the transport of water

3.2.1.1 Data handling

It was proposed that the loss in weight of initially saturated concrete samples was attributed to the loss in water due to the small carbonation rims (Mladenovic et al., 2024). The maximum in measured weight of water in the concrete specimen is here assumed to be achieved within the samples after 6 months of submersion in tap water. The assumed measured weight of water w within a sample as a function of time is determined by:

$$w(t) = M(t) - M(0) + \varphi \times \rho_w(T) = M(t) - M(0) + w_{\max} \quad (3-6)$$

where $M(t)$ is the measured weight at time t , φ is the porosity and ρ_w is the density of liquid water. The maximum in water content (w_{\max}) is determined with the last two parameters. The changes in measured weight increase with reducing relative humidity and decrease with the exposure period. The best measured data to investigate the transport of water are the data with the largest monitored changes in weight and the data without experimental errors. Unfortunately, there are no data of the weight of the samples after exposure for days, weeks or months but only after more than one year. The data obtained for the relative humidity's lower than 58.86 % have not always been exposed to the requested relative

humidity, except for 6 % (Mladenovic et al., 2024). These data are therefore not included in Figure 3-10 to Figure 3-16, except for 54.38 % at 20 °C.

3.2.1.2 Model unsaturated permeability– the Richards equation

The migration of water during the exposure of samples to the different relative humidities can be simulated through modified Darcy’s law for unsaturated systems. This modification is the definition of the relative permeability, the use of a moisture function and - as implemented in COMSOL - also the compressibility of the porous solid medium. The Richards equation is implemented as (COMSOL, 2021):

$$\rho_w \left(S_e S_p + \frac{C_m}{\rho_w g} \right) \frac{\partial p}{\partial t} = \nabla \cdot \left(\rho_w \frac{K_w}{\mu_w} \nabla p \right) \quad (3-7)$$

where S_e the effective saturation which has the value 1 with the head pressure (h) equal to 0 m or larger than 0 m. The van Genuchten parameters (van Genuchten, 1980) have been included in this modelling interface to determine the effective saturation at pressure heads smaller than 0 m:

$$S_e = \left[\frac{1}{1 + (\alpha h)^n} \right]^m \quad (3-8)$$

where α in the Genuchten equation was defined to be temperature-dependent for waste package concrete and foamed concrete (Mladenovic et al., 2024). The Genuchten parameter n has been taken to be independent of the temperature for the fitting and $m=1-1/n$. S_p is the storage coefficient that is defined by (COMSOL, 2021):

$$S_p = \varphi C_w + (1 - \varphi) C_p \quad (3-9)$$

where C_w is the compressibility of water and C_p is the compressibility of the porous medium. The compressibility of water is $4.6 \times 10^{-10} \text{ Pa}^{-1}$ i.e. incompressible. The compressibility is usually the inverse of the bulk modulus. The bulk modulus of concrete varies between 10 to 20 GPa by which the compressibility’s become $1 \times 10^{-10} \text{ Pa}^{-1}$ and $5 \times 10^{-11} \text{ Pa}^{-1}$. These compressibility’s are smaller than the pore compressibility for Opalinus clay of $2.0 \times 10^{-8} \text{ Pa}^{-1}$ and $1 \times 10^{-9} \text{ Pa}^{-1}$ that have been used an input for modelling (Levasseur et al., 2021). The specific moisture capacity (C_m) is 0 m^{-1} when the head pressure (h) equal to 0 m or larger than 0 m. At a head pressure smaller than 0 m, this capacity defined by (COMSOL, 2021):

$$C_m = \frac{\alpha m}{1-m} \varphi S_e^{\frac{1}{m}} \left(1 - S_e^{\frac{1}{m}} \right)^m \quad (3-10)$$

The gravitational constant in equation 3-7 is g and the permeability of water, K_w , is defined by (COMSOL, 2021):

$$K_w = K_{sat} \times K_{rel}(S_e, m) = K_{sat} \times S_e^l \left[1 - \left(1 - S_e^{\frac{1}{m}} \right)^m \right]^2 \quad (3-11)$$

The relative permeability, K_{rel} becomes 1 at saturation ($S_e=1$) and μ_w is the dynamic viscosity of water assumed to be $1 \times 10^{-3} \text{ Pa s}$.

Equation 3-7 is solved by assuming:

- an initial pressure head of 0 m; a relative humidity of 99.9% was actually used in order to be able to make calculations with this Richard’s modelling interface, i.e. a pressure head of -14 m at 20 °C and -13 m at 5 °C;
- a pressure head at the boundaries determined by the relative humidity and temperature.

3.2.1.3 Comparison measurements waste package concrete and calculated results

Figure 3-9 shows that the calculated pressure head within concrete decreases and the calculated Darcy velocity logarithmically changes as a function of time and space. The impact of gravity on this velocity is very small and cannot be observed in the calculation at time steps 0, 25 and 250 days.

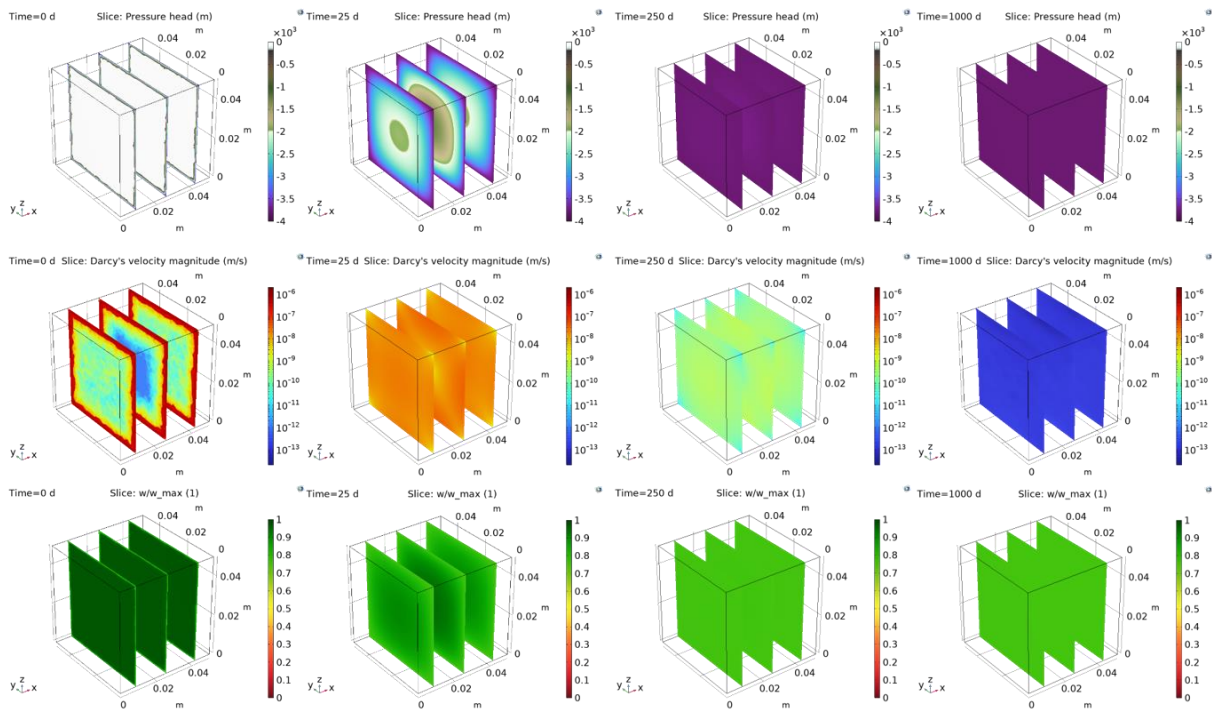


Figure 3-9 Modelled time dependent pressure head and saturation of waste package concrete at 20°C when exposed to a relative humidity of 75.47%. Parameters used for the simulations: $\phi=0.13$, $\alpha(20^\circ\text{C})=2.0\times 10^{-4} \text{ m}^{-1}$, $n=2$, $K_{\text{sat}}=7.3\times 10^{-20} \text{ m}^2$ (Mladenovic et al., 2024); C_p assumed to be 10^{-6} Pa^{-1} ; 32442 mesh elements.

The calculated pressure head in Figure 3-9 can also be transferred into the water content by the moisture storage function determined by Genuchten parameters (Mladenovic et al., 2024). The concentration of water integrated over the volume of the specimen provides the weight of water of the specimen. Figure 3-10 and Figure 3-11 show the calculated results for concrete specimens exposed to a relative humidity of 75.47 % (20 °C) and 58.86 % (5 °C). The pore compressibility of concrete is smaller than clay, but higher compressibility's needed to be used to obtain some fit with the measured data. Figure 3-9 shows that Darcy's velocity highly varies, and these high ranges makes the calculation highly non-linear by which it is difficult to achieve convergence. The reason why this velocity diminishes with decreasing saturation degree can be understood by interpreting the calculated negative pressure head as a suction force in the capillary pores. This force renders further transport of water. It has not been possible to calculate the integrated water content for concrete specimens exposed to a relative humidity of 6 % at 20 °C in Figure 3-10 with Richard's equation, i.e. convergence was not achieved. It can be questioned whether Richard's equation describes the transport of water within concrete correctly since Figure 3-11 also shows that a more realistic pore compressibility but 16 times smaller permeability values have a small influence on the calculated integrated water content. A calculated result for a 100 times smaller permeability value has not been achieved due to lack in convergence in the modelling.

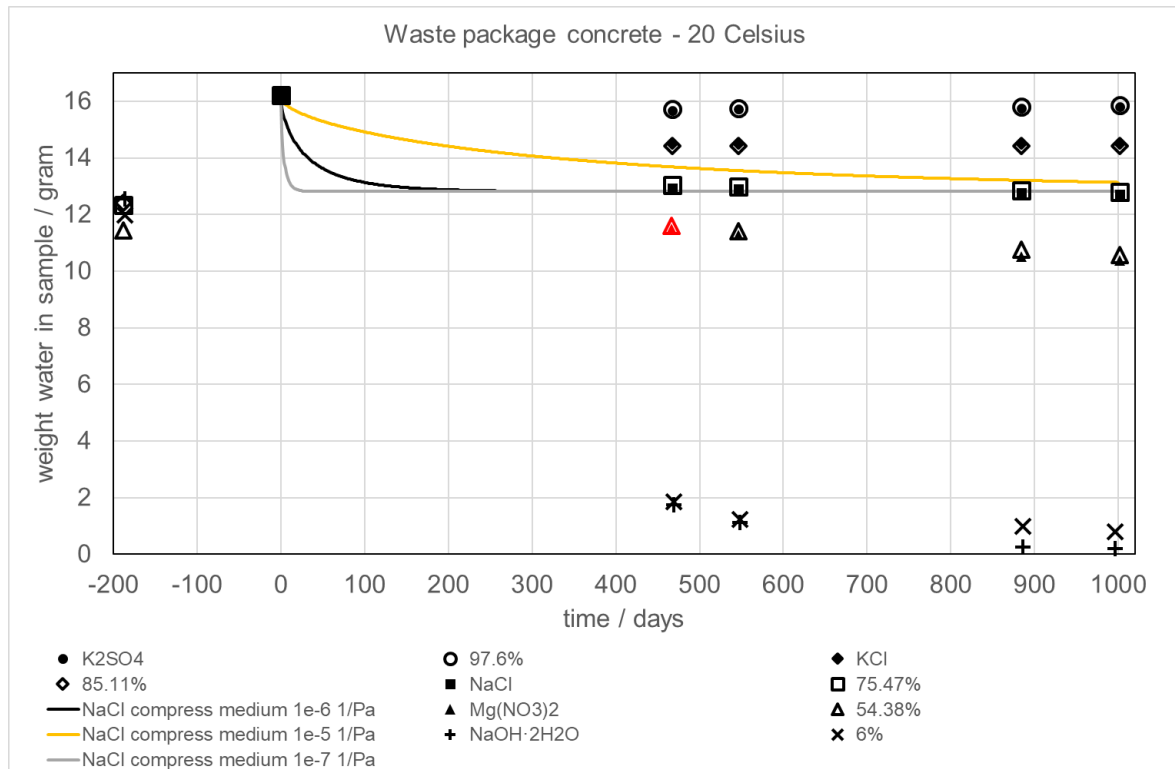


Figure 3-10: Measured (symbols) and NaCl simulated (lines) weight of water in cubical specimens with an edge of 5 cm of waste package concrete at 20°C; ▲ Mg(NO₃)₂ had become undersaturated in the solution by which the requested relative humidity might not be achieved. Parameters used for the simulations $\phi=0.13$, $\alpha(20\text{ °C})=2.0\times 10^{-4}\text{ m}^{-1}$, $n=2$, $K_{\text{sat}}(20\text{ °C})7.3\times 10^{-20}\text{ m}^2$ (Mladenovic et al., 2024), assumptions for C_p are indicated.

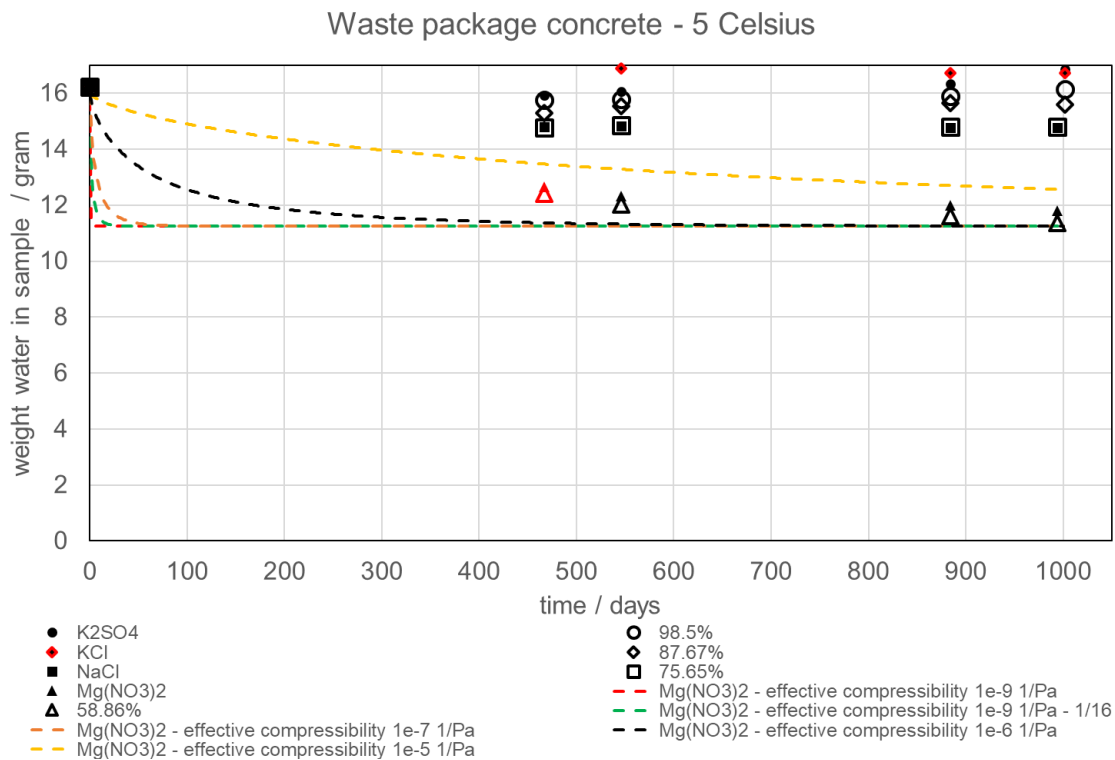


Figure 3-11: Measured (symbols) and $Mg(NO_3)_2$ simulated (lines) weight of water in cubical specimens with an edge of 5 cm of waste package concrete at 5 °C; ♦ KCl-salt was found on the surface of the specimen. ▲ $Mg(NO_3)_2$ had become undersaturated in the solution by which the requested relative humidity might not be achieved. Parameters used for the simulations $\varphi=0.13$, $\alpha(5\text{ °C})=1.5\times 10^{-4}\text{ m}^{-1}$, $n=2$, $K_{sat}(5\text{ °C})=4.6\times 10^{-20}\text{ m}^2$ (Mladenovic et al., 2024), assumptions for C_p are indicated.

3.2.1.4 Model unsaturated diffusion coefficient– Millington-Quirk non-linear diffusion of water

Millington-Quirk have defined a simpler expression for the relative permeability and also an expression for the saturated permeability (Millington and Quirk, 1961). In this model, a porous material is envisaged of solid spheres which interpenetrate each other, separated by spherical pores which also interpenetrate. The solid and pore systems are therefore symmetrical. The porous medium must be inert in terms of swelling and shrinkage response to the liquid used in obtaining pore-size distribution data and permeability measurements. The permeability as a function of the saturation degree is defined by:

$$K_w = K_{sat} \times K_{rel} = \frac{1}{8} \times \varphi^{4/3} \times r_c^2 \times S_w^{10/3} \quad (3-12)$$

where r_c is the characterizing pore radius, S_w is the saturation degree that is defined as w/w_{max} where w is the water content and w_{max} is the maximum in water content (see equation 3-6 if density is expressed in kg/m^3 times the volume of the sample). $K_{rel} = S_w^{10/3}$. Their model is valid for a fractional volume in porosity between 0.1 and 0.6. Their model has been successfully used in modelling transport of ions in unsaturated cement-based materials e.g. Samson and Marchand (2007). Like ions, the variation in water content can also be determined by diffusion in low permeable materials (i.e. small permeability):

$$\frac{\partial w}{\partial t} = \nabla (D_w \nabla w) \quad (3-13)$$

where w is the water concentration and D_w is the diffusion value of water. The diffusion value can like the permeability also be determined to be saturation dependent which is similar to an extension of Archie's law:

$$D_w = D_{0,w} \times \varphi^{4/3} \times S_w^{10/3} \quad (3-14)$$

$D_{0,w}$ is the self-diffusion value of water in water. This value has been measured to be $2.023\times 10^{-9}\text{ m}^2\text{s}^{-1}$ at 20 °C using MRI (Tofts et al., 2000) which is also the recommended value at 20 °C (Holz et al., 2000). This self-diffusion value at 5 °C becomes $1.317\times 10^{-9}\text{ m}^2\text{s}^{-1}$ assuming an Arrhenius relationship⁴ with the other measured values at 15 °C, 25 °C and 30 °C.

Equation 3-13 is solved by the following conditions:

- The initial (i.e. maximum) water content is equal to fractional volume in porosity of waste package concrete times the density of liquid water i.e. assuming the density of water vapour to be negligible compared to the liquid density of water;
- The water content at all surfaces of the cubical specimens is the equilibrium content of water as a function of the relative humidity. This content is described through a so-called moisture storage function. The van Genuchten parameters for this function for the investigated waste package concrete can be found in Mladenovic et al. (2024).

3.2.1.5 Comparison measurements waste package concrete and calculated results – Non-linear diffusion

Figure 3-12 shows an example of the modelled saturation and the variation in diffusion values as a function of time and space. The variation in diffusion value in Figure 3-12 is not multiple orders in

⁴ The self-diffusion value of water slightly deviates from an Arrhenius relationship but the obtained value of $1.317\times 10^{-9}\text{ m}^2\text{s}^{-1}$ at 5°C is within the experimental error. Other measured values are $1.313 \times 10^{-9}\text{ m}^2\text{s}^{-1}$ and $1.303\text{ m}^2\text{s}^{-1}$ (Holz et al., 2000).

magnitude like the calculated Darcy velocities in Figure 3-9. This smaller variation in water transport parameter enhances the achievement in convergence i.e. to obtain a calculated result.

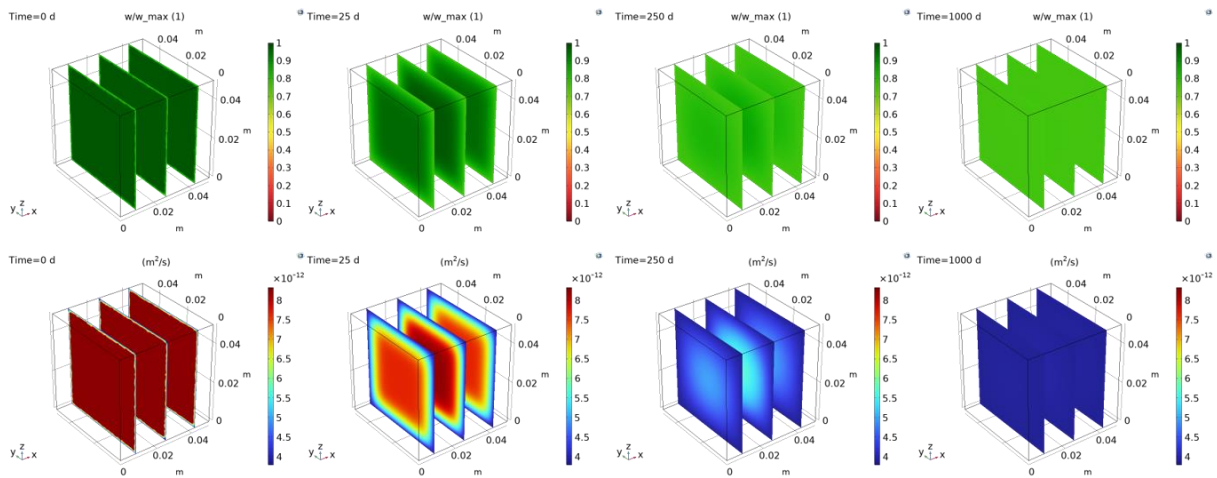


Figure 3-12: Modelled time dependent saturation of waste package concrete and the diffusion values of water at 20°C when exposed to a relative humidity of 75.47%. Porosity of 13 vol% is assumed to be constant.

The water concentration integrated over the volume of the specimen provides the weight of water of the specimen. Figure 3-13 and Figure 3-14 show the calculated results. The data obtained at a relative humidity of 58.86% are the best data and the simulations show that the obtained calculated result in red in Figure 3-14 with the diffusion coefficient in equation 3-14 predicts a too fast decrease in weight at 5 °C. Therefore, simulations have been performed with pre-factors. The pre-factor $1/16$ fits the measurements obtained at 5 °C best. The same diffusion coefficient has been used to simulate the data obtained at 20 °C i.e. equation 3-14 times $1/16$. The only variation between 5 °C and 20 °C is the self-diffusion of water which changes with temperature.

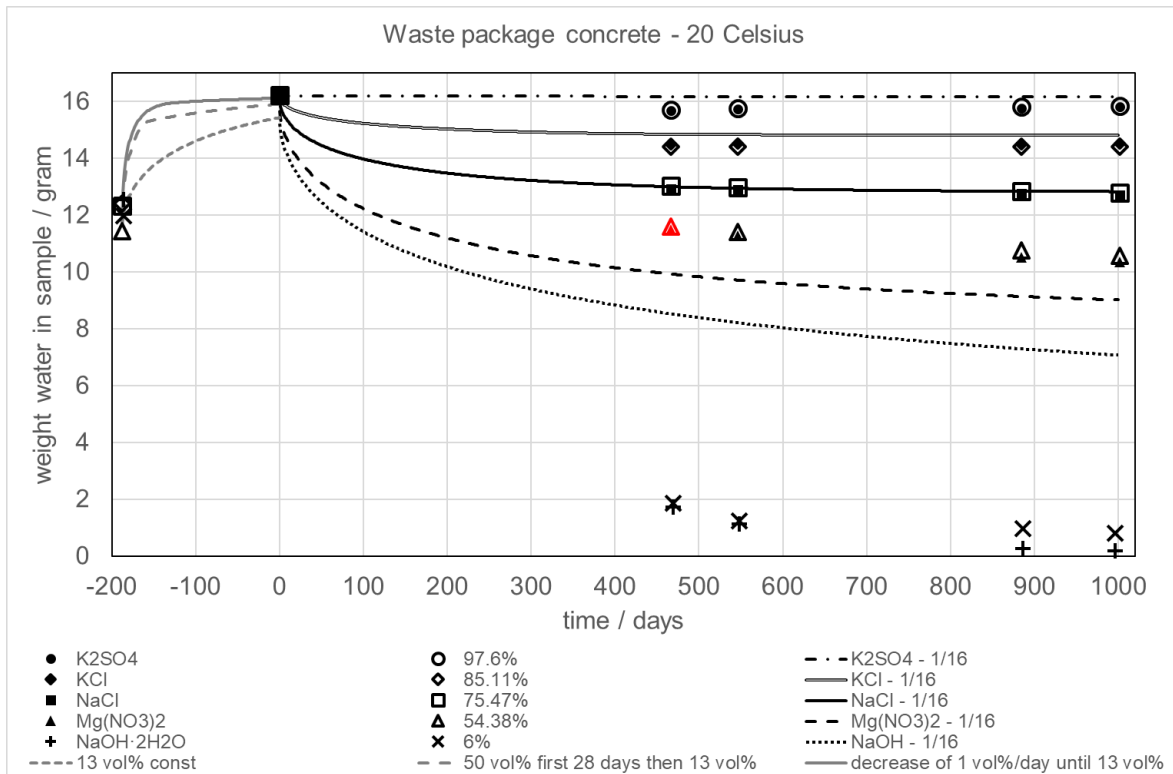


Figure 3-13: Measured (symbols) and simulated (lines) weight of water in cubical specimens with an edge of 5 cm of waste package concrete at 20°C; ▲ Mg(NO₃)₂ had become undersaturated in the solution by which the requested relative humidity might not be achieved. Parameters used for the simulations $\phi=13$ vol % unless stated otherwise, $D_{0,w}(20\text{ °C})=2.032\times 10^{-9}\text{ m}^2\text{ s}^{-1}$, pre-factors are indicated, 399701 mesh elements.

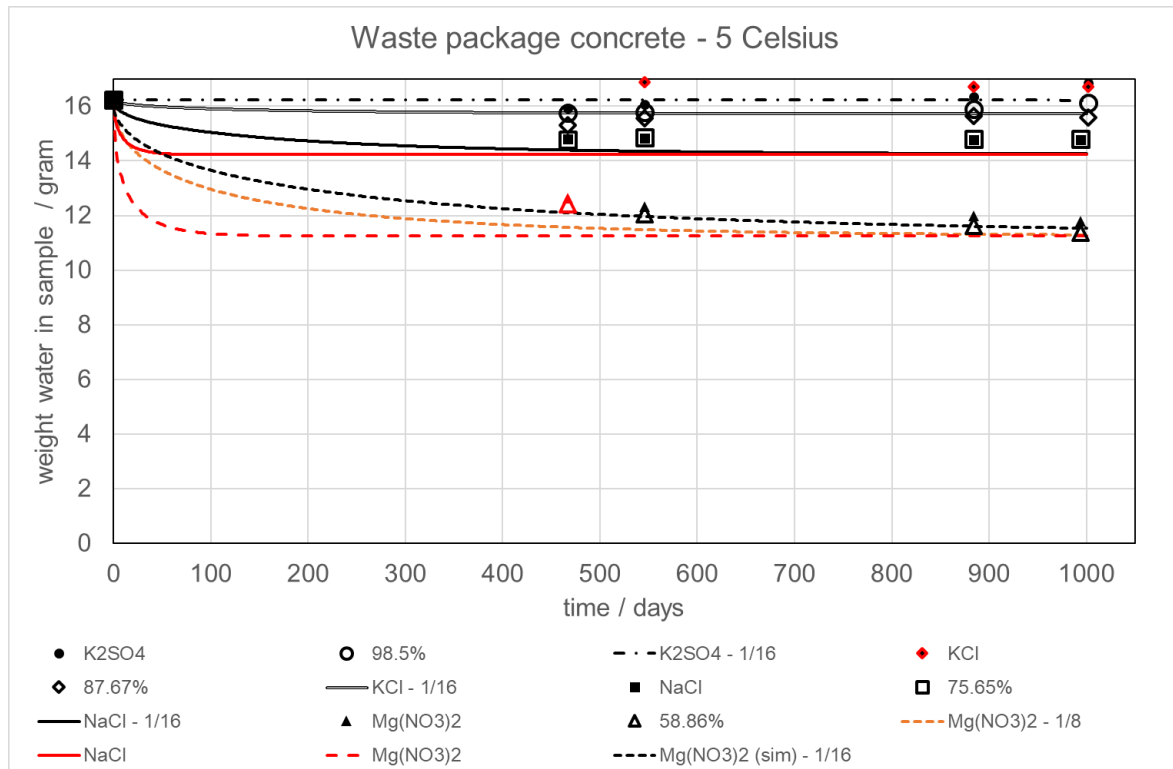


Figure 3-14: Measured (symbols) and simulated (lines) weight of water in cubical specimens with an edge of 5 cm of waste package concrete at 5 °C; ◆ KCl-salt was found on the surface of the specimen. ▲ Mg(NO₃)₂ had become undersaturated in the solution by which the requested relative humidity might not be achieved. Parameters used for the simulations $\varphi=13$ vol% unless stated otherwise, $D_{0,w}(5\text{ °C})=1.317\times 10^{-9}\text{ m}^2\text{s}^{-1}$, pre-factors are indicated, 399701 mesh elements.

The simulations fit the data - that were obtained from experiments in which intended relative humidity exposure was verified and no salt was present on the surfaces of the specimens - well, except for the data measured for samples exposed to a relative humidity of 6 %. Unlike Richard's equation interface in the previous paragraph, a calculated result for concrete specimens exposed to a relative humidity of 6 % could be achieved but it predicts a too slow release of water. Other mechanisms may become more dominant at this low relative humidity. Simulations at other relative humidity's below 40 % learn that steady state would not be achieved within 1000 days with this used model although a constant weight has been monitored. Validation of the range between 40 % and 100 % is however sufficient for modelling geological disposal of waste and further efforts for another (more complicated) model have therefore not been performed.

The weight of the samples after demoulding was smaller than after submersion of the concrete samples in tap water after 6 months at room temperature. This increase in weight in Figure 3-13 and Figure 3-15 is attributed to the ingress of tap water within these samples. This attribution implies that the saturation of waste package concrete after manufacturing is about 70 %. The use of the same diffusion value as used to simulate decrease in weight of water in the sample would not obtain the required weight of water. The porosity in this period is therefore varied due to hardening e.g. van Eijk and Brouwers (2000). The solid grey line shows the calculated result in which the porosity started at 75 vol % and was assumed to decrease 1 vol % every day until a porosity of 13 vol % was achieved. The required weight in water can be achieved with this assumption.

3.2.1.6 Comparison measurements foamed concrete and calculated results – Non-linear diffusion

Foamed concrete has a porosity of 21 % which is 1.6 times larger than for the waste package concrete. The same simulations have been made as for waste package concrete. The diffusion value is larger due to the larger porosity but the weight of water that is released is also larger. The same pre-factor has been used as found to obtain the best fit for waste package concrete.

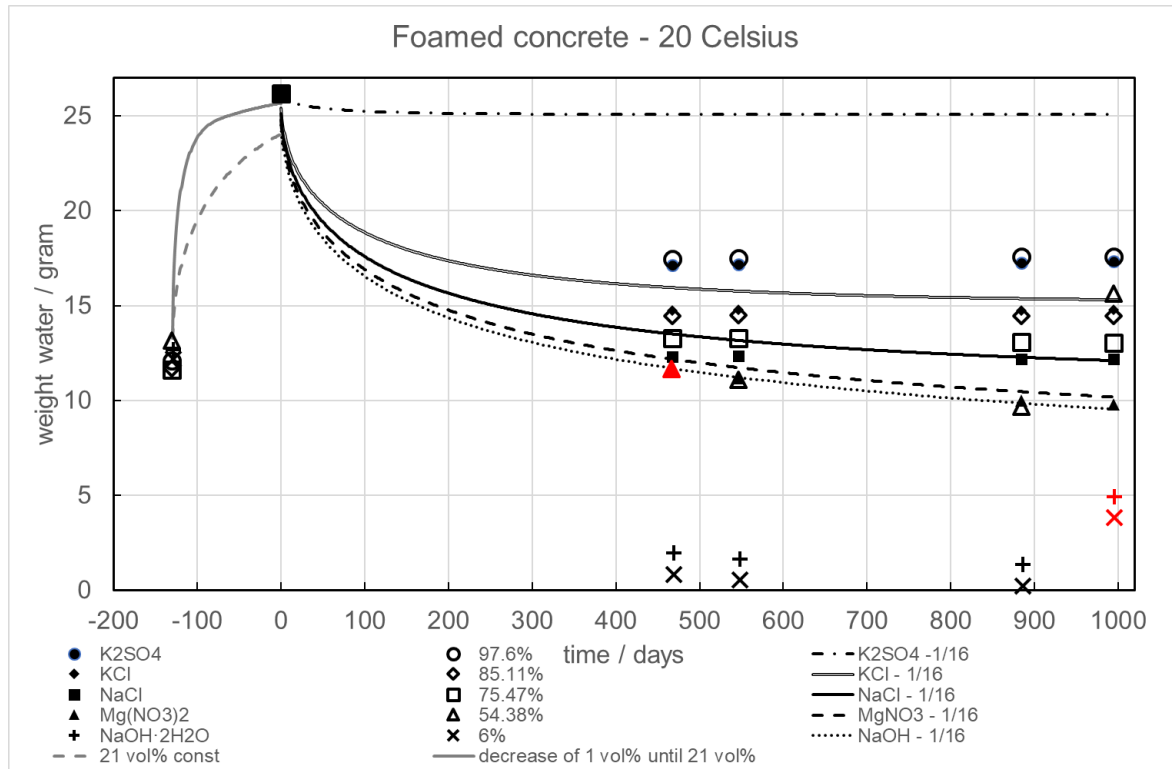


Figure 3-15: Measured (symbols) and simulated (lines) weight of water in cubical specimens with an edge of 5 cm of foamed concrete at 20 °C; ▲ Mg(NO₃)₂ and +, x NaOH had become undersaturated in the solution by which the requested relative humidity might not be achieved. Parameters used for the simulations $\phi=21$ vol % unless stated otherwise, $D_{0,w}(20\text{ °C})=2.032\times 10^{-9}\text{ m}^2\text{ s}^{-1}$, pre-factors are indicated, 399701 mesh elements.

As for waste package concrete, the simulations fit the data – obtained from experiments in which the intended relative humidity was verified – well, except the data measured for samples exposed to a relative humidity of 6%.

The weight of the samples after demoulding was smaller than after submersion of the concrete samples in tap water after 6 months at room temperature. This increase in weight in Figure 3-15 is attributed to the ingress of tap water within these samples. This attribution implies that the saturation degree of foamed concrete after manufacturing is about 47 %. The use of the same diffusion value as used to simulate decrease in weight of water in the sample would not obtain the required weight of water. Like for waste package concrete, the porosity in this period is therefore varied due to hardening. The solid grey line shows the calculated result in which the porosity started at 75 vol % and was assumed to decrease 1 vol % every day until a porosity of 21 vol % was achieved. The required weight in water can be achieved with this assumption.

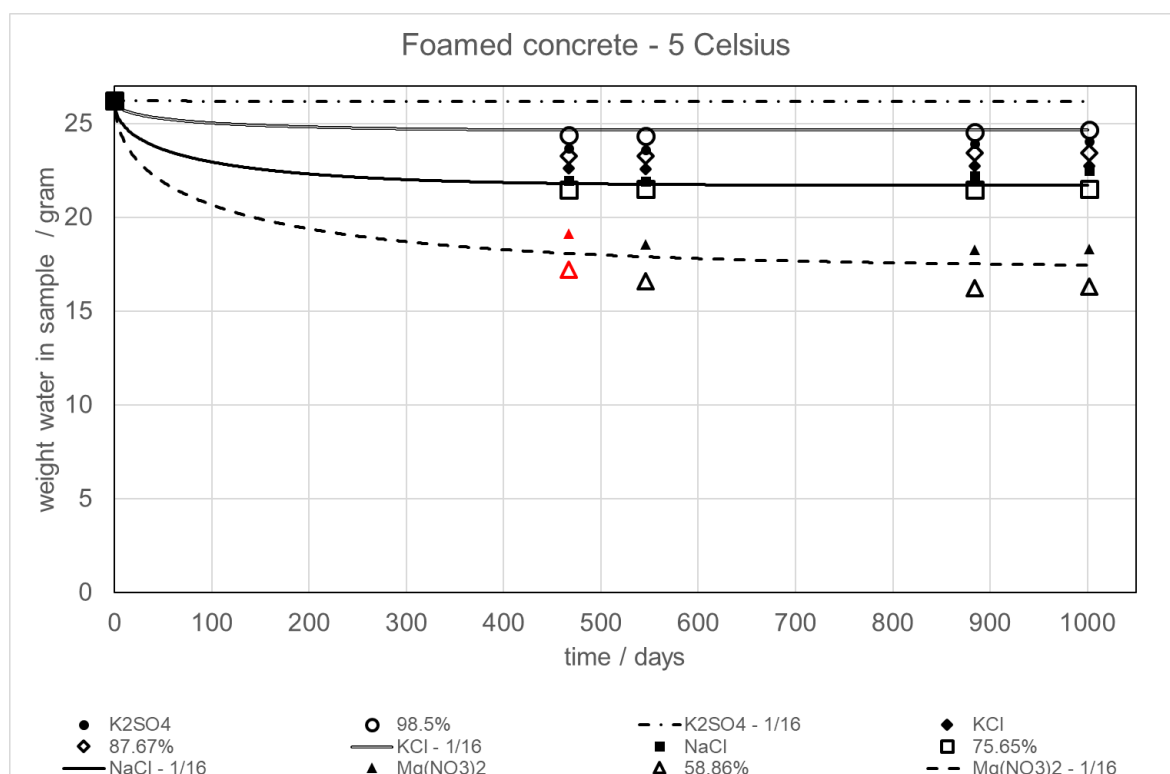


Figure 3-16: Measured (symbols) and simulated (lines) weight of water in cubical specimens with an edge of 5 cm of foamed concrete at 5°C; ▲ Mg(NO₃)₂ had become undersaturated in the solution by which the requested relative humidity might not be achieved Parameters used for the simulations $\varphi=21$ vol%, $D_{0,w}(5^{\circ}\text{C})=1.317\times 10^{-9}$ m²s⁻¹, pre-factors are indicated, 399701 mesh elements.

3.2.2 Modelling of reaction fronts with a reactive gas

3.2.2.1 Model: non-linear diffusion of water and gas – dynamic reaction rate

Concrete made with a cement that is blended with blast furnace slag contains traces of iron sulphide. The cement paste appears to be dark blue. Oxidation of iron sulphide changes this colouring to light grey. Waste package concrete showed clear reaction fronts after exposure to relative humidity's smaller 59% and ordinary air for about 1000 days. The investigated foamed concrete has a 1.6 times large porosity than COVRA's waste package concrete and the trace amounts of iron sulphide have uniformly reacted at almost any relative humidity i.e. clear reaction fronts as observed for waste package concrete are not visible (Mladenovic et al., 2024). These observations indicate that the oxidation of iron sulphide pyrite can take place at a faster rate if the water content in the pores is very small. Consequently, the oxidation of iron sulphide in the concrete samples have assumed to be primarily dependent on the availability of oxygen gas in the sample. The submerged foamed concrete specimens in saline water showed some oxidation at the corners of the cubical specimens after 4¹/₃ years that continued after 5¹/₂ years. These oxidation fronts could not yet be observed for waste package concrete. The iron sulphide is assumed to be mackinawite and the following reaction is used in the modelling:



The disappearance rate in concentration of FeS is determined by:

$$\frac{d[\text{FeS}]}{dt} = \{-R_{\text{gas}}[\text{O}_2(\text{gas})](t) - R_{\text{aq}}[\text{O}_2(\text{aq})](t)\} \times N_{\text{FeS}}(t) \quad (3-16)$$

where R_{gas} and R_{aq} are reaction rates and $N_{\text{FeS}}(t)$ is the time dependent number of FeS-sites that can react with oxygen. Millington and Quirk defined a model in which a porous material is envisaged of solid spheres which interpenetrate each other, separated by spherical pores which also interpenetrate. The

same approach is used here except that the spherical pores are into spherical particles that react with gaseous and dissolved species. The spherical particle traps species and is present in an imaginary spherical cell. The reaction rates with oxygen with such a spherical particle are determined by:

$$R_{gas} = 4\pi r_{FeS} D_{O_2,gas}(S_w, T, \varphi) \quad \& \quad R_{aq} = 4\pi r_{FeS} D_{O_2,aq}(S_w, T, \varphi) \quad (3-17)$$

where r_{FeS} is the radius of particles that reacts with oxygen, $D_{O_2,gas}$ is the diffusion coefficient of oxygen gas in concrete and $D_{O_2,aq}$ is the diffusion coefficient of dissolved oxygen. This determination of the fully definition of the reaction rates is derived from the trapping rates of gas by vacancies and pores in single crystals and polycrystalline materials by Neeft (2004) that built upon the trapping rate of interstitials in vacancies in metals defined by Dienes and Vineyard (1957). The minimum in radius is as a first approximation assumed to be defined by:

$$r_{FeS} = \frac{3}{\sigma_{cement} \times \rho_{cement}} \quad (3-18)$$

where σ_{cement} is the fineness of the used cement i.e. Blaine number e.g. 450 m² kg⁻¹ and ρ_{cement} is the density of cement e.g. 3000 kg m⁻³. The number of initial sites with FeS in equation 3-16 is determined by:

$$N_{FeS} = \frac{\rho_{cement}}{W_{sphere}} \times \frac{cement}{\Sigma cement+water+aggregates} = \frac{1}{4/3\pi r_{FeS}^3} \times \frac{FeS \text{ in cement}}{\Sigma cement+water+aggregates+..} \quad (3-19)$$

The fraction of cement in concrete is determined by the concrete recipe⁵ e.g. 0.176 for waste package concrete (Mladenovic et al., 2019) and the amount of FeS in cement is a trace amount based on the oxide composition of cement and predominance of cement minerals in literature e.g. 0.0025. The diffusion coefficient of oxygen dissolved in waste is similarly defined as water diffusion in equation 3-14:

$$D_{O_2,aq} = f_w D_{O_2,aq,0} \varphi^{4/3} S_e^{10/3} \quad (3-20)$$

where f_w is the pre-factor⁶ to obtain a fit between the measured changes in weights of the samples and modelling i.e. 1/16 for waste package concrete and foamed concrete (see from Figure 3-10 until Figure 3-16), and $D_{O_2,aq,0}$ is the temperature dependent diffusion value of dissolved oxygen in water. The diffusion coefficient of oxygen gas is similarly defined except that the diffusion value increases with a reduction in saturation:

$$D_{O_2,gas} = f_w D_{O_2,gas,0} \varphi^{4/3} (1 - S_e)^{10/3} \quad \text{if} \quad S_e < 1 - \left(\frac{1}{10.000}\right)^{3/10} \quad (3-21)$$

where $D_{O_2,gas,0}$ is the diffusion value for oxygen free air. This diffusion value is unknown but these diffusion values for hydrogen gas and carbon dioxide gas shows that this diffusion value is about 10.000 times larger than oxygen dissolved in water as shown in Table 3-2.

Table 3-2: Examples of diffusion values in air and water at 20° C (Handbook of Chemistry and Physics)

Chemical compounds	Diffusion value in air	Diffusion value in water
CO ₂	1.60×10 ⁻⁵ m ² /s	1.67×10 ⁻⁹ m ² /s
O ₂	Not indicated	2.01×10 ⁻⁹ m ² /s

⁵ The investigated concrete samples have been submerged in water for several months by which the actual water content could be higher than the water content in the concrete recipe.

⁶ This pre-factor can also be called tortuosity and a value of 1/16 is similar to the value of 0.06 as used by Shah, V., and Bishnoi, S., (2021). Understanding the process of carbonation in concrete using numerical modelling, Journal of advanced concrete technology, v. 19, p. 1148-1161.

H ₂	7.56×10 ⁻⁵ m ² /s	4.58×10 ⁻⁹ m ² /s
----------------	---	---

The transport of gaseous oxygen is determined by:

$$\frac{\partial [O_2(\text{gas})]}{\partial t} = \nabla \left(D_{O_2, \text{gas}} \nabla O_2(\text{gas}) \right) - R_{\text{gas}} [O_2(\text{gas})(t)] N_{\text{FeS}} \quad (3-22)$$

The transport of dissolved oxygen is determined by:

$$\frac{\partial [O_2(\text{aq})]}{\partial t} = \nabla \left(D_{O_2, \text{aq}} \nabla O_2(\text{aq}) \right) - R_{\text{aq}} [O_2(\text{aq})(t)] N_{\text{FeS}} \quad (3-23)$$

The transport of FeS is assumed to be 0 i.e. diffusion values of FeS are 0. Equation 3-13, 3-16, 3-22, 3-23 are solved by the following initial conditions:

- The initial water content is equal to fractional volume in porosity of waste package concrete times the density of liquid water;
- The initial dissolved oxygen content as determined by Henry's law (719.4 L×atm/mol at 20 °C; 519.8 L×atm/mol at 5 °C) for ordinary air (0.21 atm O₂) where p:

$$[O_2(\text{aq})] = \frac{p_{O_2}}{K_{\text{Henry}}(O_2, T)} \times \varphi \quad (3-24)$$

- The initial gaseous oxygen content to be 0;
- Assuming fully oxidation of a FeS particle, the initial reactive concentration of FeS is determined by:

$$[\text{FeS}]_{\text{reactive}} = \frac{W_{\text{sphere}}}{m_{\text{FeS}}} \times N_{\text{FeS}} \quad (3-25)$$

where m_{FeS} is the molar mass of FeS, W_{sphere} and N_{FeS} have been determined in equation 3-19, and the following boundary conditions:

- The water content at all surfaces of the cubical specimens is the equilibrium content of water as a function of the relative humidity as described in Mladenovic et al. (2024).
- The dissolved oxygen content is the saturation degree times dissolved oxygen content in equilibrium with ordinary air:

$$[O_2(\text{aq})] = \frac{p_{O_2}}{K_{\text{Henry}}(O_2, T)} \times \varphi \times S_w \quad (3-26)$$

- The gaseous oxygen content is 1 minus the saturation degree times the gaseous content in ordinary air:

$$[O_2(\text{g})] = \frac{p_{O_2}}{RT} \times \varphi \times (1 - S_w) \quad (3-27)$$

- No flux of FeS.

3.2.2.2 Calculation oxidation results for waste package concrete

Equation 3-15 assumed that no water is involved in the oxidation reaction. The time-dependent saturation and change in diffusion values is therefore equal to the calculations in section 3.2.1.4 for a specific relative humidity and temperature. Figure 3-17 shows these values at another relative humidity for completeness since at a relative humidity of 54% the waste package concrete turned grey for waste package concrete (Mladenovic et al., 2024).

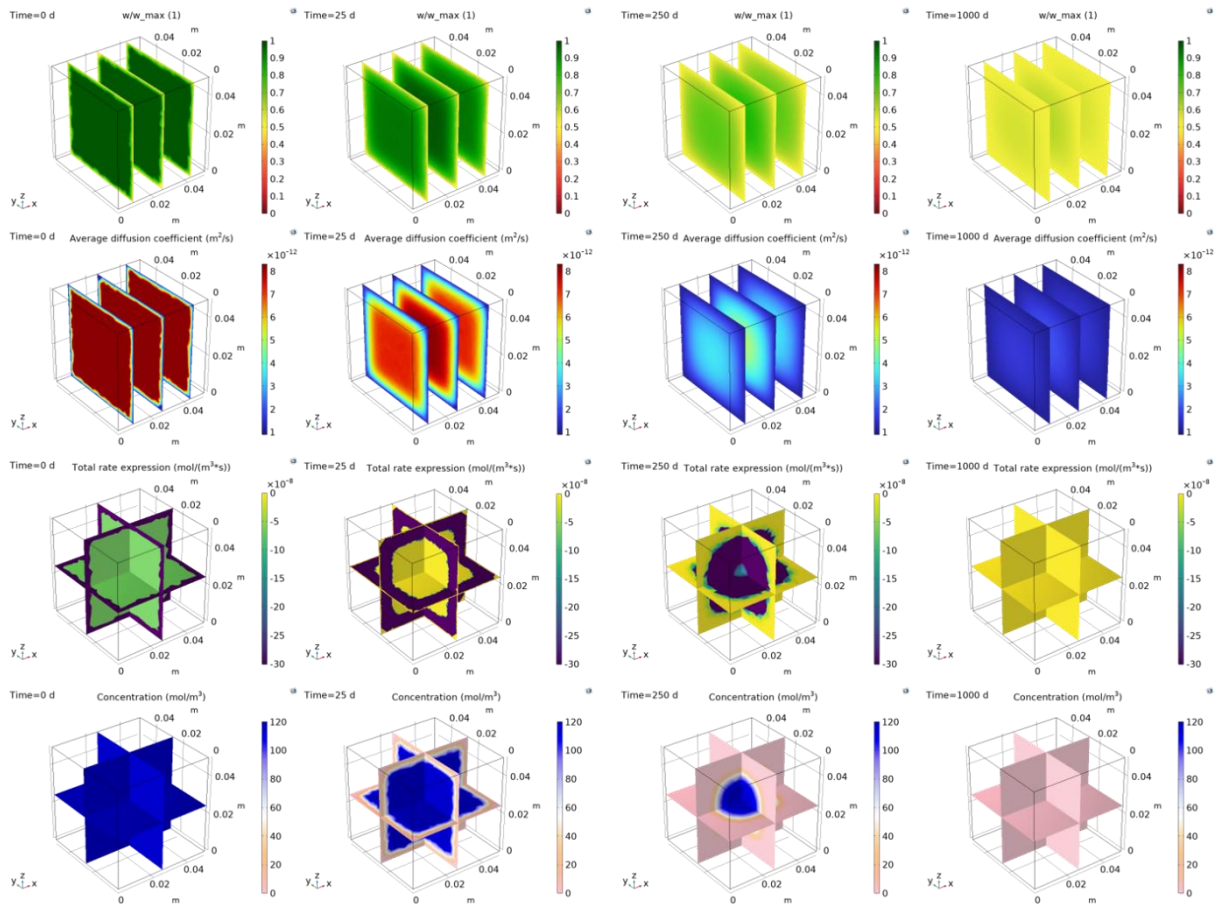


Figure 3-17: Modelled saturation and time-dependent diffusion values of water, concentration of FeS and dynamic trapping rate (consumption rate) as function of time and space and the progression of a reaction front at relative humidity of 54% at 20°C. Gaseous and dissolved oxygen are in Figure 3 10 and Figure 3 11. Initial FeS assumed to be 2 wt% in cement, 17.6 wt% cement (see recipe waste package concrete in Mladenovic et al. (2019)) and r_{FeS} 222 μ m, porosity of 13 vol% and pre-factor of $1/16$ are assumed to be constant, 32439 mesh elements. $D_{0,w}(20^{\circ}C)=2.032 \times 10^{-9} \text{ m}^2 \text{ s}^{-1}$.

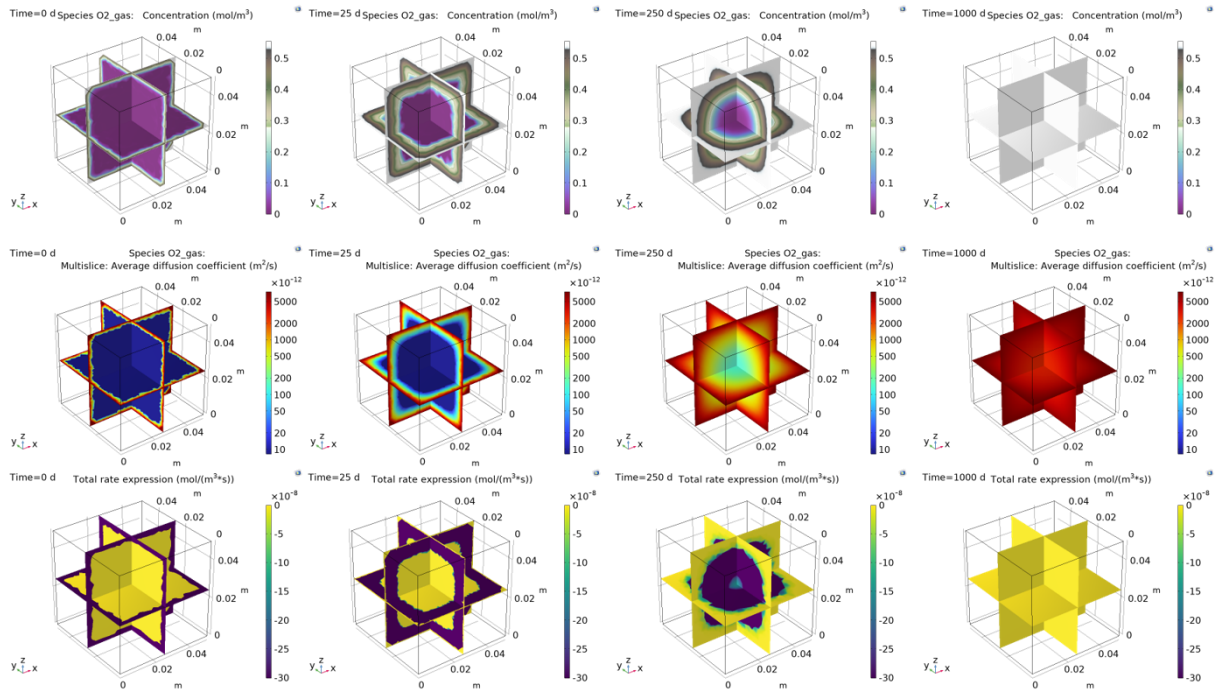


Figure 3-18: Modelled concentration of gaseous oxygen, time-dependent diffusion value and dynamic consumption rate during exposure to a relative of 54% at 20°C, 32439 mesh elements $D_{0,02,gas}(20^{\circ}C)=10.000 \times D_{0,02,aq}(20^{\circ}C)$.

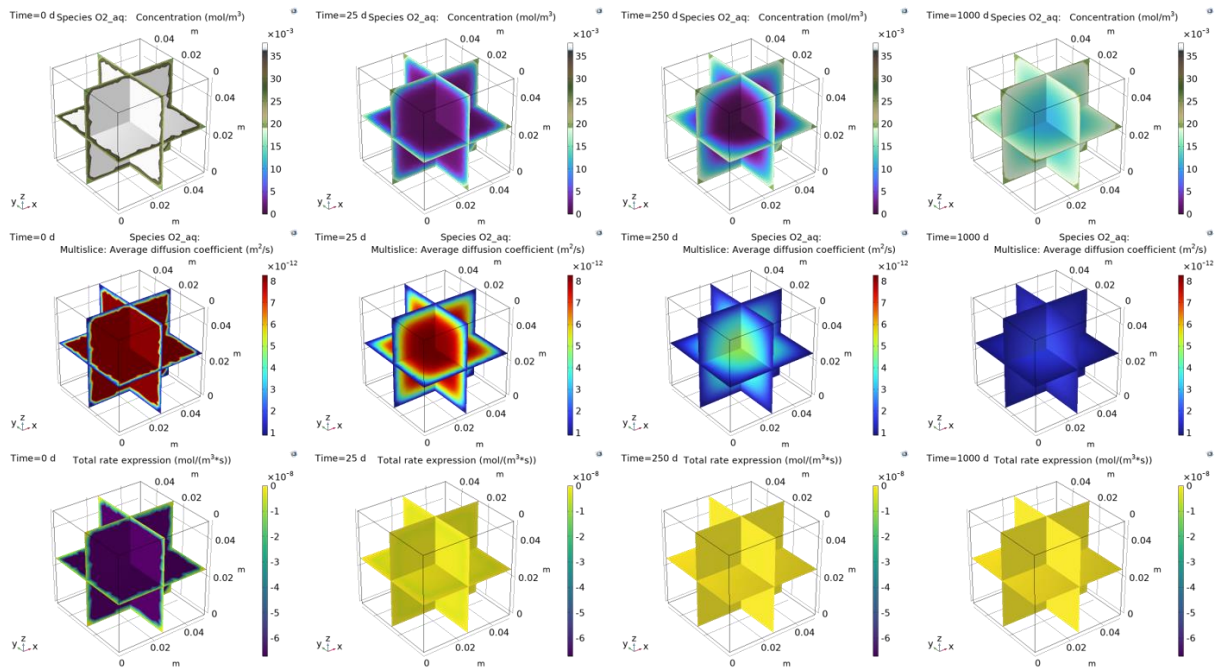


Figure 3-19: Modelled concentration of dissolved oxygen, time-dependent diffusion value and dynamic consumption rate during exposure to a relative of 54% at 20°C, porosity of 13 vol% is assumed to be constant, 32439 mesh elements. $D_{0,02,aq}(20^{\circ}C)=2.01 \times 10^{-9} \text{ m}^2\text{s}^{-1}$.

The disappearance rate highly depends on the mineral size and sites for trapping oxygen. The radius of the FeS mineral would be 2.2 μm with a Blaine number of 450 m²/kg and a density of 3000 kg/m³. The calculation result with a minimum value of 2.2 μm is almost disappearance of FeS during exposure to a relative humidity of 75 % at 20 °C. This disappearance has not been observed i.e. the reaction rate

needs to be reduced or the content of FeS should be higher. The variation in parameters is however restricted e.g. the FeS content needs to remain a trace concentration. The trapping rate can also be reduced by increasing the radius of the FeS mineral that automatically results in a reduction in the number of sites with FeS. Figure 3-20 shows the calculation results for three different radii of FeS. A radius of 222 μm may still be sufficiently small enough to be overlooked in cement however SEM/EDX mapping of iron of the Cebama reference paste (Vehmas et al., 2017) does show rather sizes of 22 μm than 222 μm .

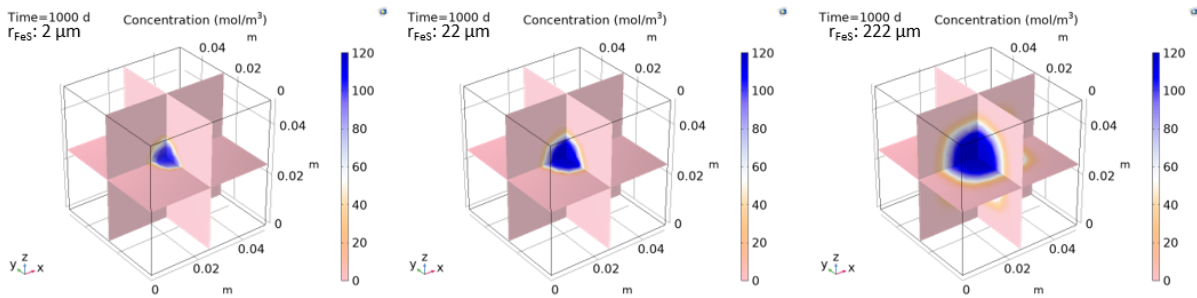


Figure 3-20: Calculated oxidation fronts after 1000 days at different trapping rate dependency, FeS assumed to be 2 wt%, recipe for fabrication of concrete 17.6 wt% of concrete, r_{FeS} 2.2 μm (7.7×10^{13} FeS sites per m^3), 22 μm (7.7×10^{10} FeS sites per m^3) and 222 μm (7.7×10^7 FeS sites per m^3) at a relative humidity of 75% at 20°C, 32439 mesh elements. $D_{\text{O},\text{w}}(20^\circ\text{C}) = 2.032 \times 10^{-9} \text{ m}^2\text{s}^{-1}$ and $D_{\text{O},\text{O}_2,\text{aq}}(20^\circ\text{C}) = 2.01 \times 10^{-9} \text{ m}^2\text{s}^{-1}$.

Figure 3-21 and Figure 3-22 show the calculated impact of temperature. The oxidation fronts are at 5°C less progressed than at 20°C despite the solubility of dissolved oxygen at 5°C being larger than at 20°C. This difference in temperature has also experimentally been observed (Mladenovic et al., 2024) except that the progression of oxidation fronts is slightly less than calculated. A better fit would be obtained with a higher FeS content and/or larger radius of the FeS minerals. The used parameters of 2 wt% for FeS and a radius of 222 μm are, however, already at their maximum for physical realistic values.

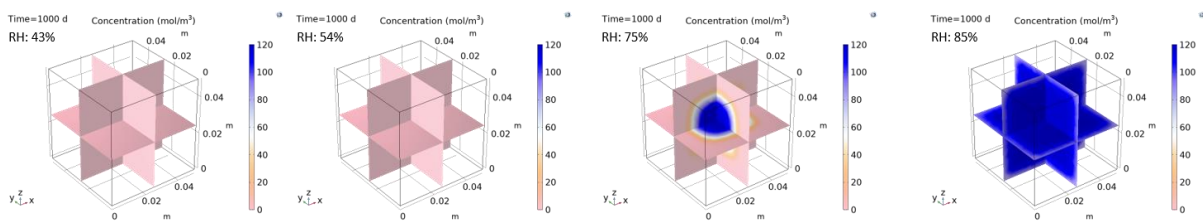


Figure 3-21: Modelled reaction fronts after 1000 days at 20°C when exposed to a relative humidity of 85%, 75%, 54% and 43%. Initial FeS assumed to be 2 wt% in cement, 17.6 wt% cement in waste package concrete (see recipe waste package concrete in Mladenovic et al. (2019)) and r_{FeS} 222 μm , porosity of 13 vol% is assumed to be constant, $D_{\text{O},\text{w}}(20^\circ\text{C}) = 2.032 \times 10^{-9} \text{ m}^2\text{s}^{-1}$ and $D_{\text{O},\text{O}_2,\text{aq}}(20^\circ\text{C}) = 2.01 \times 10^{-9} \text{ m}^2\text{s}^{-1}$.

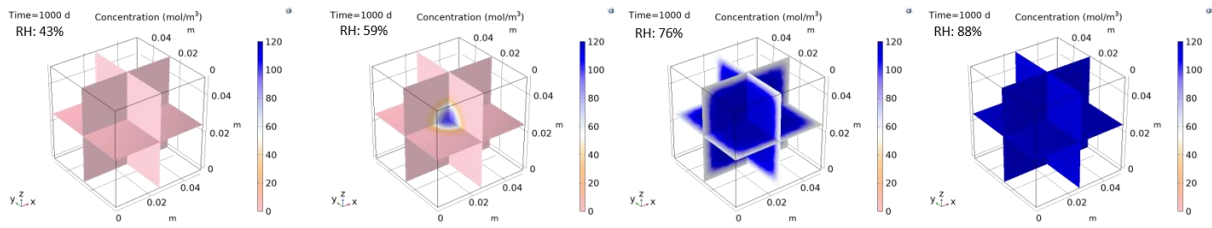


Figure 3-22: Modelled reaction fronts after 1000 days at 5°C when exposed to a relative humidity of 76%, 59%, 43% and 34%. Initial FeS assumed to be 2 wt% in cement, 17.6 wt% cement in waste package concrete (see recipe waste package concrete in Mladenovic et al. (2019)) and r_{FeS} 222 μm , porosity of 13 vol% and pre-factor $1/16$ are assumed to be constant, $D_{0,w}(5^\circ\text{C})=1.317 \times 10^{-9} \text{ m}^2\text{s}^{-1}$, $D_{0,02,aq}(5^\circ\text{C})=1.12 \times 10^{-9} \text{ m}^2\text{s}^{-1}$

The above listed calculations in this section are all predictions for waste package concrete CEM III/B. Oxidation fronts for an almost 30-year old sample made with CEM III/A is also presented in (Mladenovic et al., 2024) but there are no validated values for the transport of water available which makes it speculative for performing modelling calculations.

3.2.2.3 Calculated oxidation results for foamed concrete

Clear reaction/oxidation fronts have been observed for waste package concrete but not for foamed concrete. Despite the slightly higher fraction in cement for foamed concrete compared to waste package concrete, the concrete specimen seems to be completely oxidised already at a relative humidity of 85% (Mladenovic et al., 2024). Figure 3-23 shows that this difference in extent of oxidation can also be predicted by modelling. The calculated results at 20°C with no observation of oxidation fronts is also observed i.e. either no oxidation or complete oxidation. At 5°C, also no oxidation fronts are observed but a front is calculated at a relative humidity of 76%.

Figure 3-24 shows that physically more realistic iron contents and size of the FeS mineral fits the observations in Mladenovic et al. (2024) better. Concluding, while the modelling of waste package concrete predicts a slightly faster oxidation than observed, the modelling of foamed concrete predicts a slightly slower oxidation than observed if only the porosity is allowed to be different in the modelling. Above all, the distinct different oxidation fronts between waste package concrete and foamed concrete can be well modelled with just a 1.6 times difference in the porosity. Fine-tuning with trace amounts of iron sulphide and size of minerals results in the calculated results as observed.

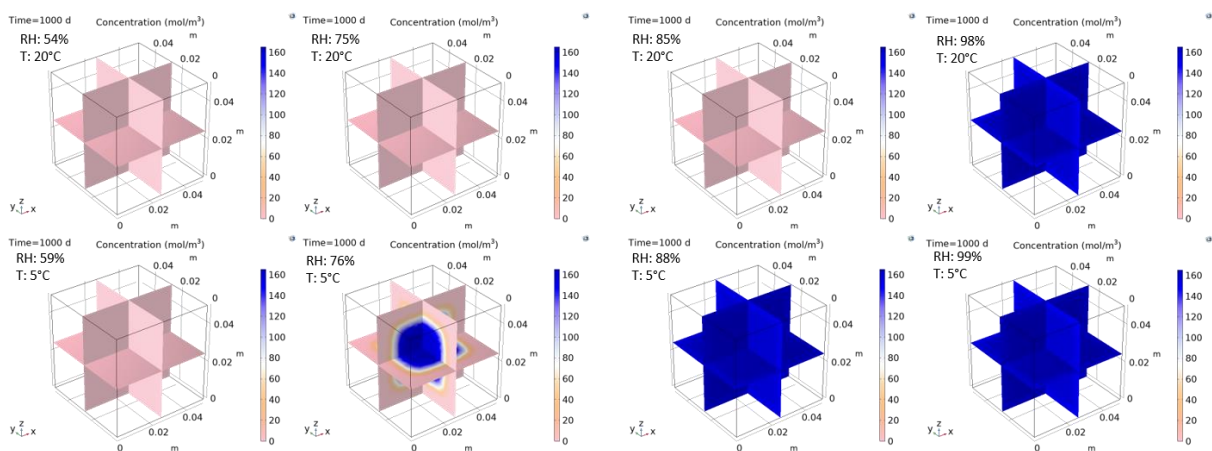


Figure 3-23: Modelled reaction fronts after 1000 days at 20°C and 5°C when exposed to different relative humidity's. Initial FeS assumed to be 2 wt% in cement, 24.2 wt% cement (see recipe foamed concrete in (Mladenovic et al., 2019)) and r_{FeS} 222 μm , porosity of 21 vol% and pre-factor $1/16$ are assumed to be

constant, $D_{0,w}(20^{\circ}\text{C})=2.032\times 10^{-9} \text{ m}^2\text{s}^{-1}$ and $D_{0,02,aq}(20^{\circ}\text{C})=2.01\times 10^{-9} \text{ m}^2\text{s}^{-1}$, $D_{0,w}(5^{\circ}\text{C})=1.317\times 10^{-9} \text{ m}^2\text{s}^{-1}$, $D_{0,02,aq}(5^{\circ}\text{C})=1.12\times 10^{-9} \text{ m}^2\text{s}^{-1}$.

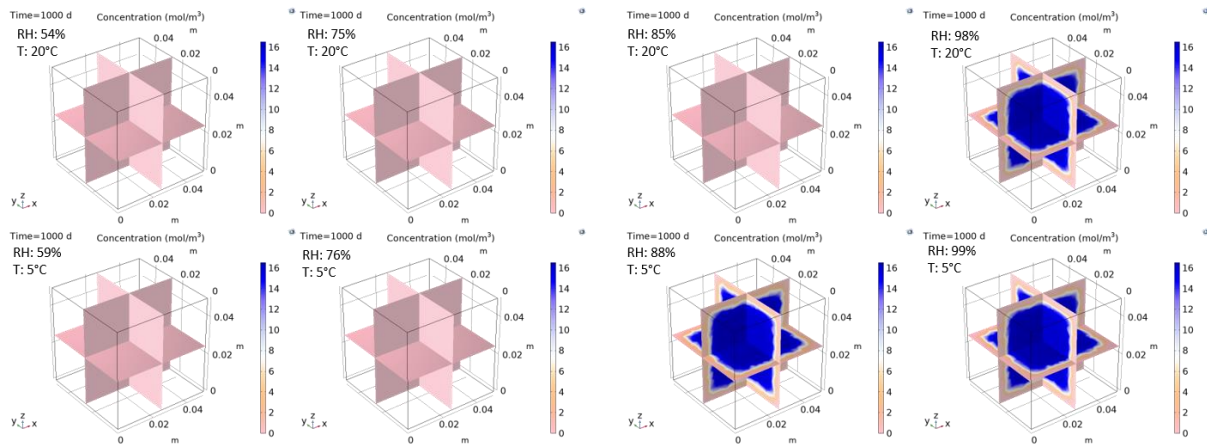


Figure 3-24: Modelled reaction fronts after 1000 days at 20°C and 5°C when exposed to different relative humidity's. Initial FeS assumed to be 0.2 wt% in cement, 24.2 wt% cement (see recipe foamed concrete in (Mladenovic et al., 2019) and $r_{\text{FeS}} 22 \mu\text{m}$, porosity of 21 vol% and pre-factor $1/16$ assumed to be constant, $D_{0,w}(20^{\circ}\text{C})=2.032\times 10^{-9} \text{ m}^2\text{s}^{-1}$ and $D_{0,02,aq}(20^{\circ}\text{C})=2.01\times 10^{-9} \text{ m}^2\text{s}^{-1}$, $D_{0,w}(5^{\circ}\text{C})=1.317\times 10^{-9} \text{ m}^2\text{s}^{-1}$, $D_{0,02,aq}(5^{\circ}\text{C})=1.12\times 10^{-9} \text{ m}^2\text{s}^{-1}$.

Apart from the number of mesh elements as explained in Govaerts et al. (2022), the dimensions for the calculations are also important for the validation of the reacted fronts: the access to oxygen is smallest in one dimension. Figure 3-25 clearly shows the extent in underestimation of the calculated oxidation front for example at the x-coordinate 0.04 m (i.e. 0.01 m from the surface of the specimen):

- 1D: the concentration is about 140 mol/m³;
- 2D: the concentration is less than about 100 mol/m³;
- 3D: the concentration is less than about 90 mol/m³.

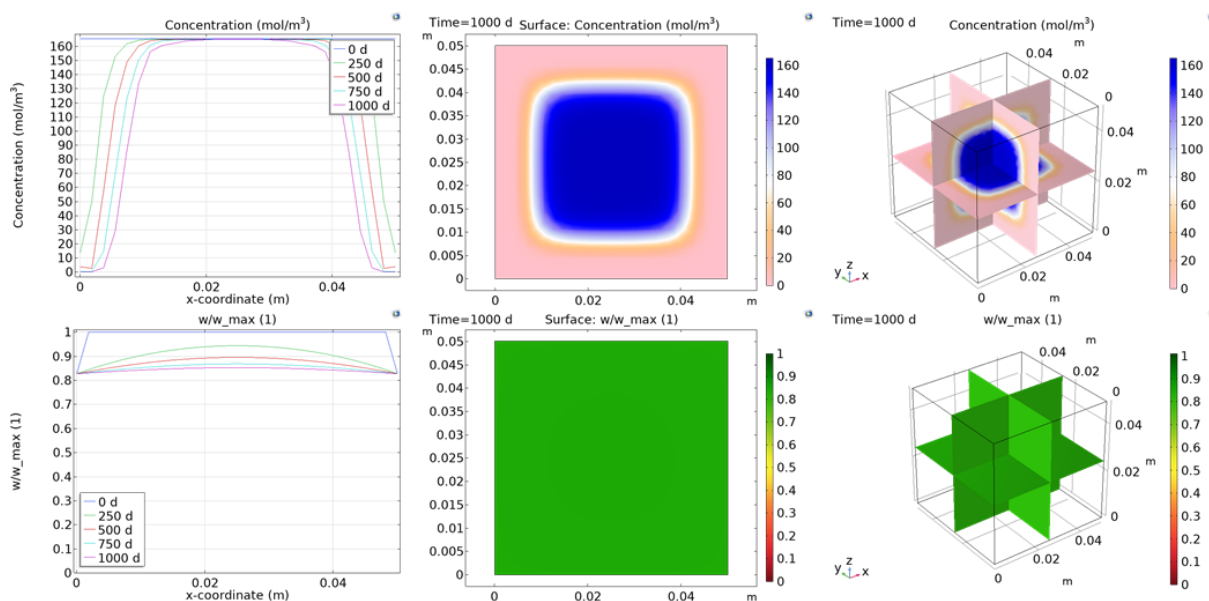


Figure 3-25: Modelled oxidation fronts in different dimensions for foamed concrete exposed to a relative humidity of 76% at 5°C; same parameter used as Figure 3-23. Same mesh size i.e. 32439 mesh elements (3D-right), 928 mesh elements (2D-middle) and 27 mesh elements (1D-left).

3.2.3 Modelling of reaction fronts with a reactive gas and water production/consumption

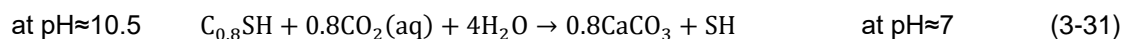
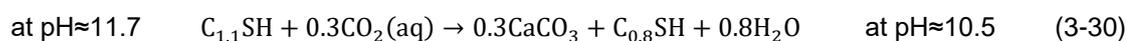
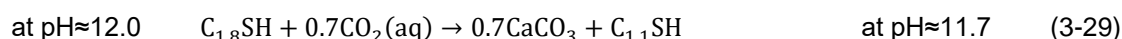
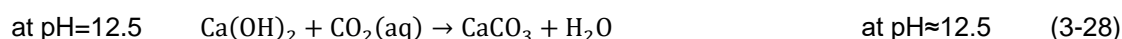
3.2.3.1 Model – non-linear diffusion of water and gas – dynamic reaction rate with water production

The investigated foamed concrete has a 1.6 times large porosity than COVRA’s waste package concrete and carbonation rims could clearly be observed after 1000 days for foamed concrete but hardly for waste package concrete. Carbonation rims with a thickness of about 2 mm could be observed for foamed concrete at a relative humidity below or equal to 75% (perhaps 85%) at 20 °C. At 5 °C, it was clear that relative humidity’s equal to or lower than 59 % are necessary to achieve a carbonation rim (Mladenovic et al., 2024). The reactive transport calculations for the oxidation of traces of iron sulphide clearly show the impact of the relative humidity and temperature. A similar approach is used for the carbonation of concrete except that some cementitious minerals produce water upon reaction with CO₂. In the modelling study by Shah and Bishnoi (2021), the release of water upon carbonation was assumed to be either 0, 1, 2 or 3 moles of water due to lack of information on the exact amount of water released upon carbonation. In this study, a mass balance is used for each reacted cementitious mineral. Table 3-3 shows the cement minerals used in this modelling study (Höglund, 2014) and the equilibrium calcium concentrations (Berner, 1992). At an atmospheric concentration of 417 ppm, the maximum in dissolved (bi)carbonate is 0.016 mmol/l using a solubility product of 3.36×10⁻⁹ for calcium carbonate. The minimum in dissolved calcium concentration becomes 0.2 mmol.

Table 3-3: Cement minerals used in the modelling, data from (Berner, 1992; Höglund, 2014).

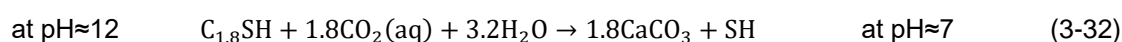
Cement mineral		Molar weight (g/mol)	Molar volume (cm ³ /mol)	Ca ²⁺ (mmol/l)	CO ₂ /HCO ₃ ⁻ /CO ₃ ²⁻	CO ₂ ppm
Name	Formula				(mmol/l)	
Portlandite	Ca(OH) ₂	74.1	33.26	≈ 20	1.68×10 ⁻⁴	
CSH _{high} Ca	C _{1.8} SH	193	78.96	≈ 17	1.98×10 ⁻⁴	
CSH _{mid} Ca	C _{1.1} SH	154	62.94	≈ 7	4.80×10 ⁻⁴	
CSH _{low} Ca	C _{0.8} SH	122	49.78	≈ 2	1.68×10 ⁻³	
SiO ₂ (gel)	SH	150	87.81			
Calcite	CaCO ₃	100.1	37.07	0.2	1.64×10 ⁻²	417

Unlike the reaction with iron sulphide, only dissolved gas is assumed to react since the difference in solubility between calcite and cement minerals is the driver of the reaction to proceed. Provided the dissolved CO₂ is larger than shown in Table 3-3, the following reactions are used in the modelling, in order to satisfy the mass balance:

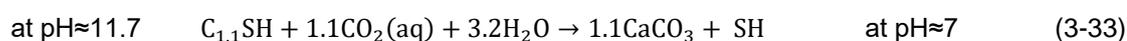


The pH in equilibrium with these cementitious minerals have been derived from Atkinson et al. (1985) and verified with Berner (1992) and Vehmas and Itälä (2019). The first three reactions satisfy the general assumption that water is generated or there can be no water generation during carbonation of C-S-H minerals e.g. references in Shah and Bishnoi (2021). In section 2, SiO₂ is assumed to be formed if CSH minerals react with CO₂ but silica gel (siliceous hydrates) may also be assumed e.g. Dauzères et al., (2022). The water content in these siliceous hydrates (SiO₂-gel) determine whether water is consumed or produced. In Höglund (2014), the molar weight of SiO₂-gel supersedes the molar weight of C_{0.8}SH. Therefore, it is assumed that water is consumed in the carbonation reaction in order to satisfy a mass balance. The majority of cementitious minerals in concrete are CSH minerals but the Portlandite content for CEM I can be three times larger than the Portlandite content for blended cements e.g. CEM III/B (Kempl and Copuroglu, 2015). It may therefore be questioned whether only water is produced during carbonation of concrete made with blended cement or that water may be consumed in the carbonation process.

The number of minerals increases the computational time in such an extent that a simplification needs to be done. All CSH minerals can be aggregated into:



And if no C_{1.8}SH is used in the educated guess of the cement mineralogy:



The change in porosity has been indicated as an important actor for carbonation e.g. the molar volume of portlandite is smaller than calcite in Table 3-3. Table 3-4 shows the initial concentrations of cement

minerals using the concrete recipes in Mladenovic et al. (2024) and the educated guess of the mineralogical composition from the SOTA (Neeft et al., 2022). Table 3-4 shows that the change in porosity by reaction of portlandite into calcite is negligible for the blended concrete used due to its small content. The decrease in porosity is mainly expected from decalcification of a CSH mineral that was not listed in educated guess of the initial cement mineralogy. As a first approximation, a change in porosity by the reaction of CO₂ is not included in the modelling.

Table 3-4: Change in porosity during carbonation for the simulated samples

Cement mineral	Foamed concrete	Max change in porosity	Waste package concrete	Max change in porosity
Name	CEM/III/B (mol/m ³)	(m ³ /m ³)	CEM III/B (mol/m ³)	(m ³ /m ³)
Portlandite	510	-0.00194	400	-0.00152
CSHhighCa (Ca/Si=1.8)	-			
CSHmidCa (Ca/Si=1.1)	2750	+0.00561	2155	+0.00440
CSHlowCa (Ca/Si=0.8)	-	-0.186		-0.146

Carbonation of concrete was identified by the observation of a colourless rim after spraying a phenolphthalein solution (Mladenovic et al., 2019, 2024). This methodology measures the pH of the concrete pore solution and a colourless rim means that the pore solution is in direct contact with SiO₂(gel) (SH in equation 3-31) or calcite. The precipitation of calcite from CSH-gels has been known to shield the cementitious mineral for further decalcification from natural analogues e.g. Knight (2003) and references in Shah and Bishnoi (2021). Reaction with all initial and generated cementitious minerals may not be necessary to observe a colourless rim. Without other experimental evidence, the fraction of cement minerals that have reacted is to be guessed. The disappearance rate of portlandite is modelled by:

$$\frac{d[Ca(OH)_2]}{dt} = -R_{aq}[CO_2(aq)](t) \times N_{Ca(OH)_2}(t) \quad (3-34)$$

where R_{aq} is the reaction rate and $N_{Ca(OH)_2}(t)$ is the time dependent number of Ca(OH)₂-sites that can react with carbon dioxide. Reaction rates are usually not defined in the fundamental modelling of concrete carbonation e.g. Papadakis et al. (1991) or understanding of the process of carbonation in concrete with modelling e.g. Shah and Bishnoi (2021), usually a value is chosen. Here the reaction rates with dissolved carbon dioxide is similarly defined as for the oxygen reaction with FeS in equation 3-17:

$$R_{aq} = 4\pi r_{Ca(OH)_2} D_{O_2,aq}(S_e, T, \varphi) \quad (3-35)$$

where $r_{Ca(OH)_2}$ is the radius of particles that reacts with carbon dioxide and $D_{CO_2,aq}$ is the diffusion coefficient of dissolved carbon dioxide. The minimum in radius of size of mineral is determined by:

$$r_{Ca(OH)_2} = \frac{3}{\sigma_{cement} \times \rho_{cement}} \quad (3-36)$$

where σ_{cement} is the fineness of the used cement i.e. Blaine number e.g. 450 m² kg⁻¹ and ρ_{cement} is the density of cement e.g. 3000 kg m⁻³. The number of initial sites with Ca(OH)₂ in equation 3-34 is determined by⁷:

⁷ This equation slightly overestimates the sites with Ca(OH)₂ since a part of the water remains within the pores and is not consumed during concrete hardening

$$N_{Ca(OH)_2} = \frac{\rho_{cement}}{W_{sphere}} \times \frac{cement+water}{\sum cement+water+aggregates} \times \frac{Ca(OH)_2}{\sum cementitious\ minerals} = \frac{1}{4/3\pi r_{Ca(OH)_2}^3} \times \frac{cement+water}{\sum recipe} \times \frac{Ca(OH)_2}{\sum cem.minerals} \quad (3-37)$$

The diffusion coefficients for dissolved and gaseous carbon dioxide are similarly defined as for oxygen in 3-20 and 3-21 and therefore not repeated here. The disappearance rate of the CSH-gels can be similarly defined as for portlandite. The reaction can be assumed to be stopped on a several century scale after a certain thickness of calcite or SiO₂-gel has been formed at the outside of the mineral⁸.

The reaction of gaseous carbon dioxide to be dissolved in water is an interplay between different sizes of pores. The smaller pores are dehydrated at smaller relative humidity than the larger pores. The larger pores ensure the transport of gaseous carbon dioxide into concrete and the smaller pores ensure the dissolution of carbon dioxide in order to react with cement minerals in this interplay. Although the distribution in size of pores has been determined (Mladenovic et al., 2024), it would be a too hard exercise computationally to calculate the dissolution of gaseous carbon dioxide as a function of the saturation degree of concrete. As a first approximation, a single size in pores is assumed:

$$R_{CO_2,gas} = 4\pi r_{pore} D_{CO_2,gas} (S_e, T, \varphi) \quad (3-38)$$

The single radius used in the modelling is the critical radius. The number of pores with this radius is determined by:

$$N_{pore} = \frac{\varphi}{4/3\pi r_{pore}^3} \quad (3-39)$$

The transport of water is differently defined than in the oxidation model in order to include the consumption and production of water during carbonation i.e. for the reactions described above:

$$\frac{\partial w}{\partial t} = \nabla (D_w \nabla w) + \frac{d[Ca(OH)_2]}{dt} + \frac{0.8 \times d[Ca_{1.1}SiH]}{dt} - \frac{4 \times d[Ca_{0.8}SH]}{dt} \quad (3-40)$$

The transport of dissolved carbon dioxide is determined by

$$\frac{\partial [CO_2(aq)]}{\partial t} = \nabla (D_{CO_2,aq} \nabla CO_2(aq)) - \frac{d[Ca(OH)_2]}{dt} - \frac{0.7 \times d[Ca_{1.8}SH]}{dt} - \frac{0.3 \times d[Ca_{1.1}SH]}{dt} - \frac{0.8 \times d[Ca_{0.8}SH]}{dt} + \frac{d[CO_2(gas)]}{dt} \quad (3-41)$$

The transport of gaseous carbon dioxide is determined by:

$$\frac{\partial [CO_2(gas)]}{\partial t} = \nabla (D_{CO_2,gas} \nabla CO_2(gas)) - R_{gas,CO_2} [CO_2(gas)] N_{pore} \quad (3-42)$$

All fundamental model descriptions so far for example Shah and Bishnoi (2021) and Papadakis et al. (1991) predict an increase in the carbonation rate with a decrease in the relative humidity. Experimental results show however a peak in the carbonation rate with relative humidity e.g. Papadakis et al. (1991), von Greve-Dierfeld (2015) and von Greve-Dierfeld et al. (2020). This peak can be understood with the current model description since:

- the reaction rate for gaseous carbon dioxide to become dissolved carbon dioxide increases with decreasing saturation degree of concrete
- the reaction rate for dissolved carbon dioxide to become calcium carbonate with cementitious minerals decreases with decreasing saturation degree of concrete;

⁸ The same process i.e. stopping of a reaction on a century scale, takes place between the cement paste and aggregates during hardening of concrete. Reaction rims are generated during hardening until thickening of reaction rim of hydrates covers the external surface of the aggregate. The reaction is then slowed down considerable and proceeds through a diffusion controlled process (Jackson et al., 2017). The diffusional through such a hydrate covering the aggregate is considerably smaller than diffusion through the pores within concrete.

- the consumption of water by CSH minerals to complete carbonation becomes further limited with decreasing saturation degree of concrete.

The saturation degree in equilibrium with a relative humidity depends on the distribution in size of pores of concrete and temperature.

The last part with the reaction requires the dissolved carbon concentration to be smaller than the dissolved concentration in equilibrium with gaseous carbon dioxide. All diffusion values for the cementitious minerals are assumed to be 0. Equation 3-34 and equations similarly for consumption of other cementitious minerals, 3-40, 3-41 and also for dissolved carbon dioxide are solved by the following initial conditions:

- 1) The initial water content is equal to fractional volume in porosity of waste package concrete times the density of liquid water;
- 2) The initial dissolved carbon dioxide is assumed to be 0
- 3) The initial gaseous carbon dioxide content to be 0;

Assuming fully carbonation of a Ca(OH)_2 particle, the initial reactive concentration of Ca(OH)_2 is determined by:

$$[\text{Ca(OH)}_2]_{\text{reactive}} = \frac{W_{\text{sphere}}}{m_{\text{Ca(OH)}_2}} \times N_{\text{Ca(OH)}_2} \quad (3-43)$$

where $m_{\text{Ca(OH)}_2}$ is the molar mass of Ca(OH)_2 in Table 3-3, W_{sphere} and $N_{\text{Ca(OH)}_2}$ have been determined in equation 3-37, the other initial reactive concentration of CSH-gels can be similarly defined.

and the following boundary conditions:

- 1) The water content at all surfaces of the cubical specimens is the equilibrium content of water as a function of the relative humidity as described in Mladenovic et al. (2024).
- 2) The dissolved carbon dioxide content is the saturation degree times dissolved carbon dioxide content in equilibrium with ordinary air:

$$[\text{CO}_2(\text{aq})] = \frac{p_{\text{CO}_2}}{K_{\text{Henry}}(\text{CO}_2, T)} \times \varphi \times S_w \quad (3-44)$$

- 3) The gaseous carbon dioxide content is 1 minus the saturation degree times the gaseous content in ordinary air:

$$[\text{CO}_2(\text{g})] = \frac{p_{\text{CO}_2}}{RT} \times \varphi \times (1 - S_w) \quad (3-45)$$

- 4) No flux of any cementitious mineral.

3.2.3.2 Comparison measurements foamed concrete and calculated results – carbonation

Clear carbonation rims have been observed for foamed concrete but not for waste package concrete, Therefore, foamed concrete has been modelled first. The calculation in three dimensions is computationally (too) expensive and therefore only 1D calculations have been made. Figure 3-26 and Figure 3-27 show the calculated results. The steps in time may have been too large with the used consumption rate of dissolved carbon dioxide by which the concentration of dissolved carbon dioxide appears negative in Figure 3-26. As the gaseous carbon dioxide replenishes dissolved carbon dioxide sufficiently, the consumption of the cement minerals proceeds as shown in Figure 3-27. The equilibrium concentration of water would not have been achieved according to the current calculations which is mainly due to the high consumption rates of water by carbonation of CSH that superseded the consumption of portlandite causing an inflow of water into the sample. The current model predicts however a higher concentration of fully carbonated minerals than portlandite after 1000 days exposure

at 75% relative humidity. Whether this prediction satisfies the observation of a carbonated rim of about 2 mm at 75% by spraying the phenolphthalein solution (Mladenovic et al., 2024) requires additional experimental investigations for example XRD (Rietveld analysis).

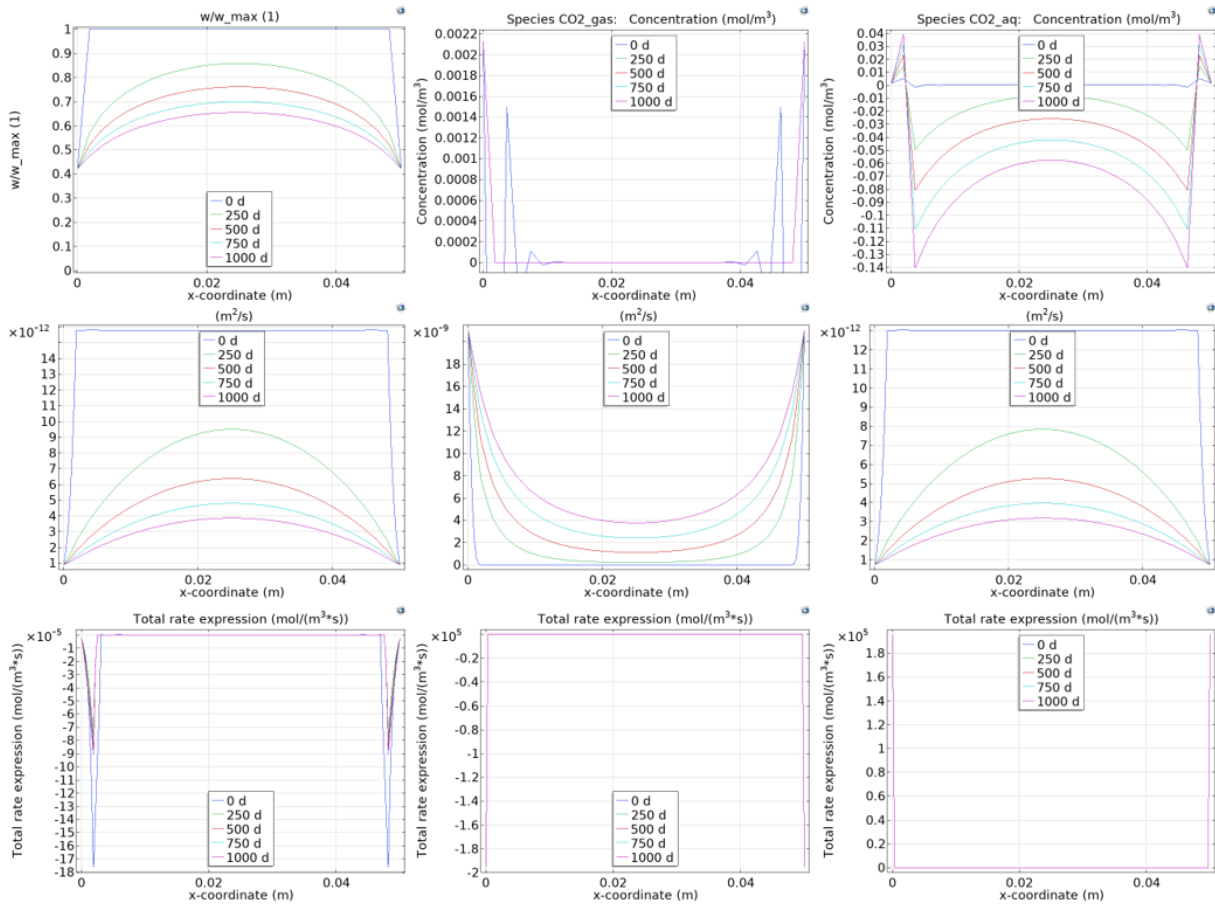


Figure 3-26: Water (left), gaseous CO₂ (middle) dissolved CO₂ (right). Modelled saturation, concentration of gaseous and dissolved CO₂, time-dependent diffusion values of water, and dynamic trapping rate (consumption rate) as function of time and space at a relative humidity of 75% at 20°C; 24.2 wt% cement (see recipe foamed concrete in Mladenovic et al. (2019) and radius of cement minerals 22 μm, size of pores 12.9 nm, porosity of 21 vol%, and pre-factor ¹/₁₆ assumed to be constant, $D_{0,w}(20^{\circ}C)=2.032 \times 10^{-9} \text{ m}^2 \text{ s}^{-1}$ and $D_{0,CO_2,aq}(20^{\circ}C)=1.67 \times 10^{-9} \text{ m}^2 \text{ s}^{-1}$. Number of mesh elements: 27.

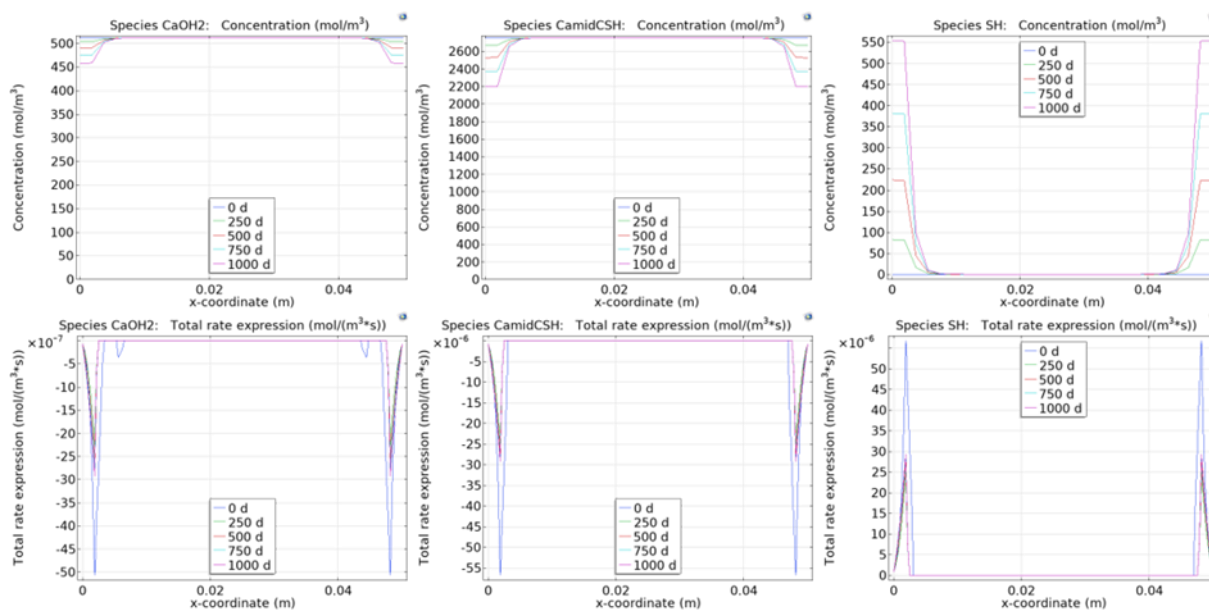


Figure 3-27: Modelled concentration of (simplified) cement minerals and consumption rate; same parameters as in Figure 3-26. Number of mesh elements: 27

Figure 3-28 shows that the carbonation rate does not linearly increase with decreasing relative humidity with the current model. The calculated SH concentration after exposure at 85% and 98% may be too low for the observation of a carbonation rim as experimentally observed (Mladenovic et al., 2024). But as earlier explained, additional experimental investigations are necessary. More importantly, the model description currently available do predict a linear increase with decreasing relative humidity e.g. Papadakis et al. (1991). Experimentally, however, a peak in the carbonation rate around 50-60% relative humidity is experimentally observed e.g. Papadakis et al. (1991) and von Greve-Dierfeld et al. (2020). The current calculations do not predict a peak in the carbonation rate but the calculated extent in carbonation is similar below a relative humidity below 43%. This prediction can also be entirely ascribed to the too slow predicted release of water at relative humidity's below 40% with the current equation used to calculate transport of water (see paragraph 3.2.1).

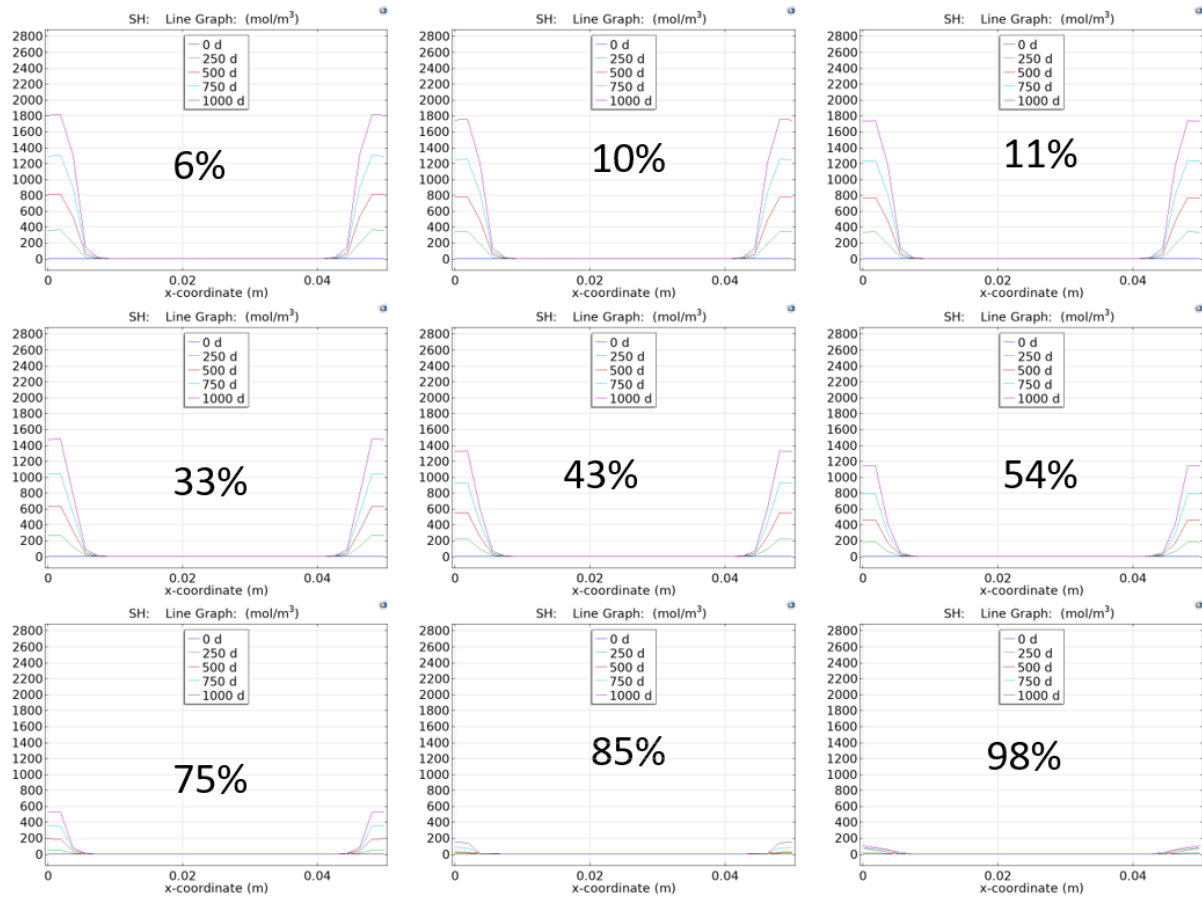


Figure 3-28: Modelled SH concentration at 20°C at different relative humidity's; same parameters as in Figure 3-26. Number of mesh elements: 27

The number of mesh elements has an impact on the thickness of the reaction front as explained in Govaerts et al. (2022). But the impact can be understood with the high concentration of cement minerals that react with ingress of species. Figure 3-29 clearly shows that the thickness of the calculated rim is smaller with increasing mesh elements but that locally more minerals have been consumed. This effect is similar to reducing the size of the - to be reacted - minerals as shown in Figure 3-20. For a calculation with an extremely fine mesh (100 elements), the consumption rate of CSH minerals with its associated consumption rate of water became too large by which the local concentration of water became 0 or negative during the calculation. This feature causes a singularity during the calculation by which the calculation terminates. A smaller step size could be a solution for 1 D calculation with such a fine mesh, but that calculation would require more time.

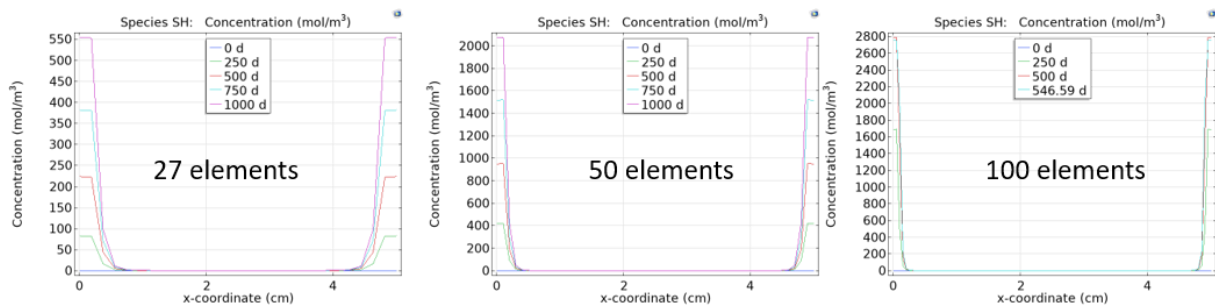


Figure 3-29: Modelled SH concentration; same parameters and exposure conditions as in Figure 3-26. Number of mesh elements: 27, 50 and 100.

3.2.4 Concluding perspective: transport of water and reactive transport modelling

Transport mechanisms of water and their associated parameter values within concrete are scarce, especially for concrete made with blended cements. In this study, a diffusion coefficient for water have been extracted from drying waste package concrete and foamed concrete specimens, the diffusion value is assumed to depend on the (local) saturation degree. Drying diffusion coefficients for concrete made with blended cements are scarce due to their large experimental period and in some cases also high costs of sensors. Consequently, the transport of water within concrete is modelled without experimental support for the verification of parameter values used to represent concrete (Shah and Bishnoi, 2021). In this report, experimental results of concrete samples exposed to a range in relative humidity from 6% till 100% for about 1000 days have been used. Due to lack of resources to control the relative humidity and monitor the weight of the samples, sufficient high-quality data have only been achieved for about half of the concrete specimens exposed to a relative humidity. More experimental data would be sensible.

Despite the limited availability of sufficient high quality of experimental data, a match between modelled and experimental results of transport of water in concrete made with blended cement has been achieved through Richards' equation as well as Millington-Quirk formulas. A preference for Millington-Quirk i.e. non-linear diffusion, has arisen for two reasons. The fitting with measured data requires the use of the physically unrealistic pore compressibility's for concrete. Another reason is that the high non-linearity in Richards' equation induces convergence problems. A well comparison between the measurements and calculated results was obtained for waste package concrete and foamed concrete with a minimum relative humidity of 40% using non-linear diffusion (Millington-Quirk) with the same parameters for the modelling except that the porosity was different as experimentally measured.

A reactive transport model has been developed with only physically realistic parameters. A reaction (or consumption) rate has been defined, that changes with the size of the mineral that is consumed in the reaction, the concentration of these minerals, the saturation dependent diffusion value for water, gas and gas dissolved in water, concentration of dissolved and non-dissolved gas. The model has been used for oxidation and carbonation except that for carbonation the solubility of the more thermodynamically preferable precipitate was introduced. A sphere has been used as the morphology of a mineral and a pore in order to make the calculation most easy. A decrease in the size of the minerals increases the reactive surface area by which the trapping rate is increased. A similar effect is achieved when increasing the number of mesh elements.

Concrete made with a cement blended with blast furnace slag contains some iron sulphide minerals with which a non-oxidised fractured surface appears dark blue. The observed oxidation fronts as a function of temperature and relative humidity has been predicted with this model. For waste package concrete, a relatively high concentration of these iron sulphide minerals has been used in order to make a prediction that matches the observations but the assumed concentration are still trace amounts. More realistic size of minerals and concentration of trace amounts has been used to predict the observed oxidation fronts for foamed concrete.

From the mass balance, it has been deduced that CSH minerals consume water to achieve a completed carbonated state. The transport of gaseous carbon dioxide increases with decreasing relative humidity since more pore space becomes available for gas. Consequently, the carbonation rate becomes larger. This is also experimentally measured and reported in literature but until a certain relative humidity, around 60%. The transport of water, however, decreases with decreasing relative humidity since the suction pressure of the smaller pores is higher. It is therefore cautiously assumed that the lack in water that is necessary to achieve the completed carbonated state might be responsible for the experimental observation in literature that the carbonation rate reduces at relative humidity's below 50-60%. Another physical reason for a peak in the carbonation rate at a certain relative humidity is also included in the model description. The rate to become dissolved carbon dioxide increases with decreasing relative humidity while the consumption rate for dissolved carbon dioxide decreases with decreasing relative humidity. The model can be easily extended to predict further decalcification of CSH-gels as

experimentally observed in natural analogues by assuming that precipitated calcite or the formation of SiO₂ gels is only possible for the part of the cementitious mineral that is in contact with pores. Experimentally, a carbonation rim would be observed after spraying with a phenolphthalein solution in this case.

Calculations in three dimensions were necessary to obtain the weight of water in the sample and oxidation fronts. Carbonation fronts have only been modelled in one dimension. Additional experimental results of the samples described in this report are required in order to make the computational effort in three dimensions worthwhile.

3.3 CORI experiment and CEA experiment (on PVC)

3.3.1 Introduction

Nuclear industry generates a variety of wastes, which are categorized depending on their activity. In that regard, intermediate level (ILW) wastes mostly contain radionuclides with half-life of less than 31 years (except for ⁶³Ni with a half-life = 100 years), with an overall activity which is considered as almost negligible after 500 years (Abadie, 2018).

This section describes the development of a model predicting the fate of polymers (cellulose and PVC) under irradiation, including the release of gases and of soluble molecules, able to form stable complexes with various cations. The development is based on experiments which have been previously published in the literature. In a second part, the models are applied to the case of waste containers, including metallic wastes and polymers, following storage scenarios consistent with current nuclear waste agencies concepts.

3.3.2 ILW wastes, packages and storage scenarios

ILW wastes are issued from spent fuel reprocessing and activities involved in the maintenance and operation of reprocessing plants, including structural waste from fuel assemblies (end caps and hulls), technological waste (used tools, equipment, plastics, etc.) and waste resulting from the treatment of effluents (conditioned fuels, resins, ...) (Abadie, 2018). Part of those wastes may also come from decommissioning operations. Because of those various origins, ILW are intrinsically heterogeneous, which makes it difficult to define a reference composition for such materials.

In ACED-Eurad project, ILW wastes are mainly of two types: metallic wastes, coming from fuel assemblies, used technological part and possibly of decommissioning origin. The second part corresponds to organic wastes, composed mainly by polymers of different origin (plastics, cellulose, resins, ...). In disposal concepts both type of waste are packed into drums (typically cylindrical or box-shaped). Metallic wastes are enclosed into a box-shaped concrete container (reinforced) concrete, ferro-concrete, steel). Organic wastes are packed into steel drums, the bulk waste is put in a waste drum. Four waste drums are placed in a reinforced concrete container and backfilled. The container has the same dimensions as for the metallic waste.

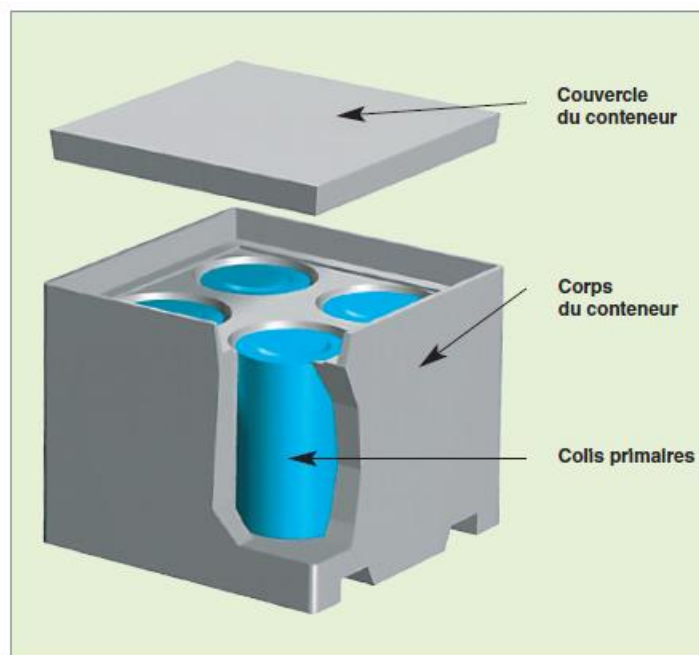


Figure 3-30: ILW concrete overpack, including the 4 primary containers (Vernaz and Bonin, 2008)

At the repository scale, a scheme is displayed in Figure 2-6, showing ILW qualitative evolution as a function of time. It includes the possible sequence of the repository-induced effects according to Leupin et al. (2016). Similar evolution has also been described in Andra (2016a, 2016b). This evolution is affected by various steps as a function of disposal duration:

- A pre-closure period (~100 years) which includes both building operations and the operating period, during which the container are undergoing desaturation due to the venting of the repository complex
- From 100 to 500-1000 years, following the closure of the disposal. The concrete and cementitious grouts resaturate with porewater migrating inwards from the host rock (Nagra, 2008b). Wastes undergo irradiation from the radioactive elements included in packages, which enhances organics degradation and gases release, which progressively replaces air (anoxic conditions). Temperature may rise up to 36-50°C (Leupin et al., 2016). In the Swiss concept, temperature changes in the range of 5-10°C and is considered to have minimal effects on chemical or physical processes
- After the radioactive period (~1000 years) the degradation follows up because of the contact with porewaters from the host rock formation. A significant quantity of gases (mainly hydrogen, carbon dioxide and methane) are generated for long periods of time by i) anaerobic corrosion of metals and ii) degradation of organic compounds by microbial and chemical processes (Poller et al., 2014).

Organic materials such as cellulose, halogenated (e.g. PVC) and non-halogenated plastics (e.g. polypropylene, polyethylen, thermoplastics), cellulose, ion-exchange resins and rubber will be present in the case of the organic wastes. The organic waste may consist of a single type of organic or a mixture of e.g. slow and fast degradable materials.

3.3.3 Models for polymer degradation: general concepts and mechanisms

This section describes the degradation models which have been implemented into a geochemical code. ILW wastes undergo degradation due to i) the active elements included into the packages (radiolysis) and ii) the highly alkaline characteristics of porewaters packages generated by the cementitious materials in the vicinity of organics in waste packages. The degradation model implemented should

consider both aspects, its formal implementation will also depend on the data available in the literature and necessary to parameterized the models.

3.3.3.1 Radiolysis of polymers

As for radiolysis the degradation is described by the yield (G) at which degradation are released from the initial products. The yield depends on the dose D received by the initial product, per kg of initial product, and it may also depend on the dose rate:

$$G(X) = \frac{n(X)}{D} \quad (3-46)$$

where X corresponds to the degradation product released, $n(X)$ corresponds to the number of moles of X per kg of initial product and D stands for the integrated dose absorbed per kg of initial product. D maybe expressed in Grays (Gy) where 1 gray corresponds to 1 joule absorbed per kilo of initial product ($J.kg^{-1}$). G is expressed in moles. J^{-1} also often expressed in moles.kg per 100 eV absorbed by the initial product, with $G(\text{moles}.J^{-1}) = G(100 \text{ eV})/(9.63 \cdot 10^6)$. Generally, G is not constant on the whole dose domain and the initial value G_0 depends on the intrinsic properties of the initial product (Lamouroux and Cochin, 2012). In the current ILW storage scenarios, the integrated dose absorbed by the waste would be in the range of 1 MGy, with a dose rate between 0.1 to 1 Gy.h⁻¹ (Brown et al., 2014).

In experiments, the dose rate \dot{D} is usually constant. Colombani (2006) irradiated an industrial PVC using an averaged dose rate 600 Gy.h⁻¹, monitoring HCl(g) and H₂(g) release:

$$\dot{D} = \frac{\partial D}{\partial t} = 600 \text{ Gy} \cdot \text{h}^{-1} = 0.167 \text{ Gy} \cdot \text{s}^{-1} \quad (3-47)$$

If the dose rate \dot{D} is constant over time, the integration is simple and it is possible to express the number of moles of released product directly as a function of time:

$$n(X) = G(X) \cdot \int_{t_0}^{t_1} \frac{\partial D}{\partial t} = \dot{D} \cdot (t_1 - t_0) \cdot G(X) \quad (3-48)$$

Additionally, a kinetic rate for the release of irradiation products can be defined as:

$$k = \frac{\partial n(X)}{\partial t} = G(X) \cdot \frac{\partial D}{\partial t} \quad (3-49)$$

For a constant 0.167 Gy.s⁻¹ dose rate and a yield obtained by Colombani (2006) of 0.44 H₂(g) moles/(100 eV) or 4.5 10⁻⁸ H₂(g) moles.J⁻¹, it comes that $k = 0.167 \cdot 4.5 \cdot 10^{-8} = 7.57 \cdot 10^{-9}$ moles.kg⁻¹.s⁻¹. Finally, knowing the yield and the dose rate (or a relation between the absorbed dose and reaction time), it is possible to extract a kinetic constant for the release of irradiation products, which can be directly introduced into a geochemical numerical model.

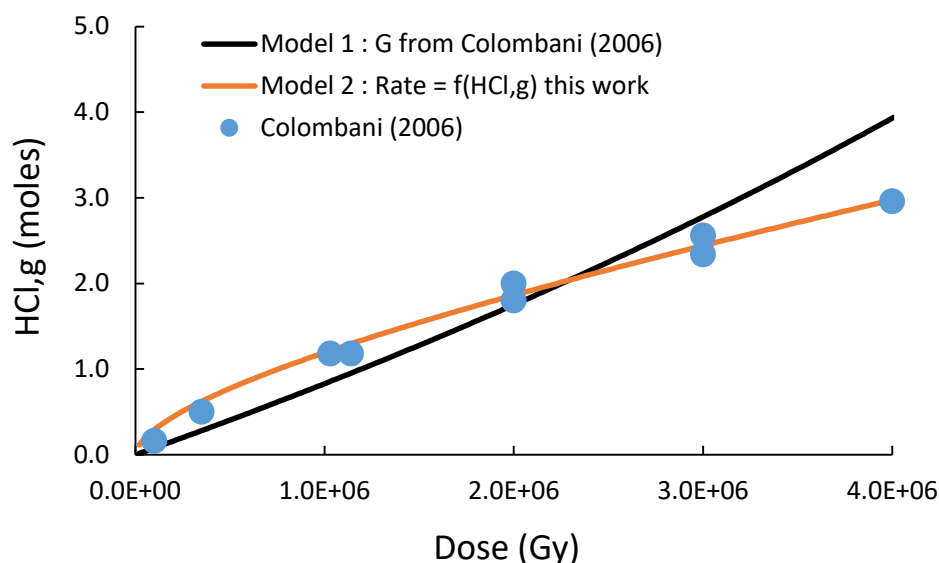


Figure 3-31: Modelling of the HCl(g) release during the radiolysis of PVC using PHREEQC

Figure 3-31 reports the modelling of the HCl(g) release during radiolysis of the PVC undergone by Colombani (2006). Model 1 corresponds to the plain introduction of the yield extracted by the author for industrial PVC under aerobic conditions ($G(\text{HCl}(\text{g})) = 7.6 \text{ moles/ } 100 \text{ eV}$). Model 2 involves in the expression of the rate the HCl(g) concentration according to:

$$k = B \cdot G(X) \cdot \frac{\partial D}{\partial t} \cdot [\text{HCl}_{,g}]^A \tag{3-50}$$

where A and B are fitting constants. Model 2 provides a better fit to the data but Model 1 is still acceptable in the range 0 to 3 MGy, which is enough to model radiolysis up to 1MGy, the scenario selected here for ILW. Concerning the radiolysis reaction, Model 1 is based on a very simple assumption, where 1 mass unit of the initial product is degraded into 1 mole of the reaction product. Such hypothesis does not involve stoichiometric constraints and it can be applied even when the reaction mechanism is poorly known. Model 2 supposes an additional knowledge of the reaction mechanism, to the point where a stoichiometric reaction can be proposed in order to bring constraints to coefficient A . Such knowledge is lacking for most of the polymers radiolytic degradation reactions and for this reason, we are selecting Model 1 for the rest of the study. Table 3-5 reports the radiolytic yields measured by Colombani (2006) for pure PVC and industrial PVC, for doses ranging from 0 to 2 MGy and under aerobic and anaerobic conditions. The values do not vary significantly with the dose rate. For HCl(g), the atmosphere is of importance for pure PVC only, where the presence of oxygen favors strong G values because the reaction essentially corresponds to an oxidation of the polymer. $G(\text{H}_2(\text{g}))$ values were not measured for pure PVC by Colombani (2006). Doe (2013) reports values 25 times lower than $G(\text{HCl}(\text{g}))$ in vacuum.

Table 3-5 - Yields measured by Colombani (2006) for PVC radiolysis, in moles.J⁻¹

	Aerobic conditions	$G(\text{HCl}(\text{g}))$ 0-2MGy	$G(\text{H}_2(\text{g}))$ 0-2MGy
Pure PVC	Yes	$1.8 \cdot 10^{-6}$	
	No	$3.7 \cdot 10^{-7}$	
Industrial PVC ⁽¹⁾	Yes	$7.9 \cdot 10^{-7}$	$5.2 \cdot 10^{-8}$
	No	$7.9 \cdot 10^{-7}$	$5.2 \cdot 10^{-8}$

(1) Normalised to pure PVC amounts

For industrial PVC, Colombani (2006) reports values from the literature from $1 \cdot 10^{-8}$ to $8 \cdot 10^{-7}$ J.mol⁻¹, depending on the nature of the initial product and the conditions of irradiation. Their own values are closer to the upper limit of this interval. Colombani (2006) explains that in several experiments, HCl(g) is in fact trapped within the solid matrix and additional treatment are required to obtain the proper values. The release of H₂(g) is found to be 15 times lower than that of HCl(g). Globally the G are lower than for pure PVC and independent on the presence of oxygen or the dose rate.

For cellulose, the main gases released from radiolysis would be CO(g), CO₂(g) and H₂(g). Published G are highly variable between the 3 gases, depending on the nature of the initial product and on the presence of oxygen. Doe (2013) proposes the values $3.3 \cdot 10^{-7}$, $1.5 \cdot 10^{-7}$ and $0.7 \cdot 10^{-7}$ moles.J⁻¹ for CO(g), CO₂(g) and H₂(g), which would correspond to the reaction:



For industrial PVC, Lamouroux and Cochin (2012) and Advocat et al. (2014) provided some results issued from an experiment where industrial PVC (Plastunion) was irradiated from 0 to 10 MGy and the irradiated product were thereafter hydrolysed using cementitious solutions and during 6 months. Yields can be extracted from these experiments for 4 organic acids:

- Acetic acid $G(\text{C}_2\text{H}_4\text{O}_2) = 2.6 \cdot 10^{-8}$ moles.J⁻¹
- Oxalic acid $G(\text{C}_2\text{H}_2\text{O}_4) = 3.6 \cdot 10^{-8}$ moles.J⁻¹
- Formic acid $G(\text{CH}_2\text{O}_2) = 4.8 \cdot 10^{-8}$ moles.J⁻¹
- Phthalic acid $G(\text{C}_8\text{H}_6\text{O}_4) = 9.0 \cdot 10^{-8}$ moles.J⁻¹

Similar experiments have not been realised for cellulose.

3.3.3.2 Hydrolysis of polymers

For PVC, no data have been published, so far, concerning the degradation of the polymer at moderated temperatures (typically ranging from 25 to 40°C).

For cellulose, a set of studies had been carried out with a 12 years research program focused on the alkaline degradation at room temperatures (Glaus and Van Loon, 2008, 2009; Van Loon and Glaus, 1997). These studies resulted in determining the extent of degradation, the resulting degradation products and allowed deriving kinetic parameters.

These studies clearly demonstrated that the degree of degradation is related to the mole fraction of end groups available which is related to the degradation products of the cellulose: the smaller the degradation products, the faster the degradation. The main degradation product is the isosaccharinic acid (ISA). Globally, degradation proceeds quickly at first, with soluble components and exposed reducing ends being consumed by the peeling reaction. The degradation rate then slows greatly as the number of ends is reduced by stopping reactions. Van Loon and Glaus (1997) developed a kinetic expression to model the alkaline decomposition of cellulose at room temperature according to this two-phase model:

$$(\text{celdeg}) = \frac{k_1}{k_t} (G_r)_0 (1 - e^{-k_t t}) + \frac{k_1 k_0}{k_t} \quad (3-52)$$

where:

- | | |
|-----------|--|
| (cel deg) | is the mole fraction of cellulose degraded |
| k_1 | is the first order rate constant for the peeling reaction |
| k_0 | is the rate constant for the formation of ISA |
| k_t | is the overall first order rate constant for the stopping reaction |
| $(G_r)_0$ | is the mole fraction of reducing end groups |

The major products generated from the alkaline degradation of cellulose are the α -isosaccharinic acid and the β -isosaccharinic acid. The identity of α and β -ISA has been confirmed using a combination of analytical techniques including HPLC, NMR, GC-MS and LC-MS/MS. In addition to the ISA isomers, a large number of small chain aliphatic acids have been detected including: formic, acetic, glycolic, pyruvic, glyceric, lactic, propionic, succinic, butyric, threonic and adipic (Glaus and Van Loon, 2008, 2009; Van Loon and Glaus, 1997).

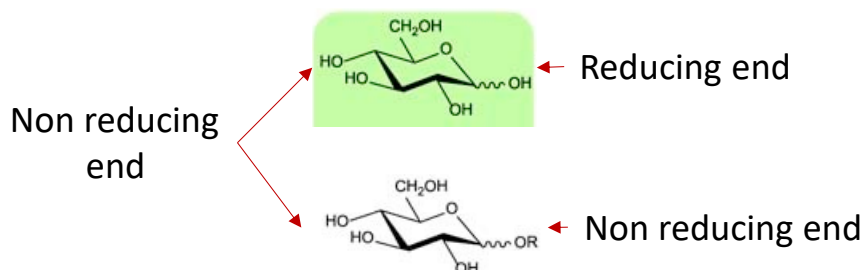


Figure 3-32: Cellulose end groups, displaying reducing and non reducing chain end

3.3.4 Models for polymer degradation: implementation into geochemical codes and verification

The implementation of models for the degradation of polymers includes both radiolysis and hydrolysis reactions and it is reported and illustrated in the current section.

3.3.4.1 Implementation and verification of PVC degradation

For PVC, the modelling is implemented into the Phreeqc code (Parkhurst and Appelo, 2013) according to the following steps:

- the production of gaseous species HCl(g) , $\text{H}_2(\text{g})$ is described through non-stoichiometric kinetic reactions (e.g. $\text{PVC} \Rightarrow \text{HCl(g)}$) with yields provided by Colombani (2006) reported in Table 3-5
- the yields for gaseous species are adjusted to match chloride concentration and redox potential
- the production of aqueous species, acetate, formate, oxalate and phthalates is also described through non-stoichiometric kinetic reactions (1 for each product) with yields extracted from experimental data (Lamouroux and Cochin, 2012).
- a verification is realized using data from Ben Zeineb et al. (2021a, b) on pure and industrial PVC degradation experiments.
- monitored parameters: total pressure p_{total} and global chemical parameters pH, Eh, Cl^- , Ca^{2+}
- the thermodynamic database used is Thermochemie 9. b (Giffaut et al., 2014).

In the framework of the EURAD-CORI WP2 task, Ben Zeineb et al. (2021a) carried out the radiolytic degradation of polymers (hard polyvinyl chloride HPVC) in solutions (L/S = 10, pure water and NaOH pH 13 solutions, with air and N_2 atmosphere). The suspensions have been irradiated using a ^{60}Co γ source, with a $0.55 \text{ kGy}\cdot\text{h}^{-1}$ dose rate during 7 months, to reach a final dose close to 2.5 MGy. The compositions of the initial products obtained by combining chemical elementary analyses, XRD, TGA, IR-TF and GC-MS are reported in Table 3-6.

Table 3-6 - Analysis of the PVC samples, including 3 industrial samples.

	Pure PVC	Nuc. PVC	San. PVC	HP PVC
PVC polymer	100	84.9	54.0	90.2
Minerals additives (%)	-	6.7	32.3	3.7
Carbonates (Calcite/Dolomite)	-	3.2	32.0	3.7
Rutile	-	2.3	0.3	-

Hydrotalcite	-	1.2	-	-
Organics additives (%)	-	8.4	14.3	6.4
Phthalates	-	0.6	1.1	0.7
Alkanes	-	7.0	10.2	5.7
Adipates	-	0.8	3.0	-
G(HCl(g)) in mol.J⁻¹	1.9 10 ⁻⁶	9.9 10 ⁻⁷	1.1 10 ⁻⁶	1.3 10 ⁻⁶
G(H₂)_{app}(^{*)} in mol.J⁻¹	1.9 10 ⁻⁷	2.1 10 ⁻⁷	2.3 10 ⁻⁷	2.1 10 ⁻⁷

(*) G(H₂)_{app} obtained are apparent values, including H₂O radiolysis effect

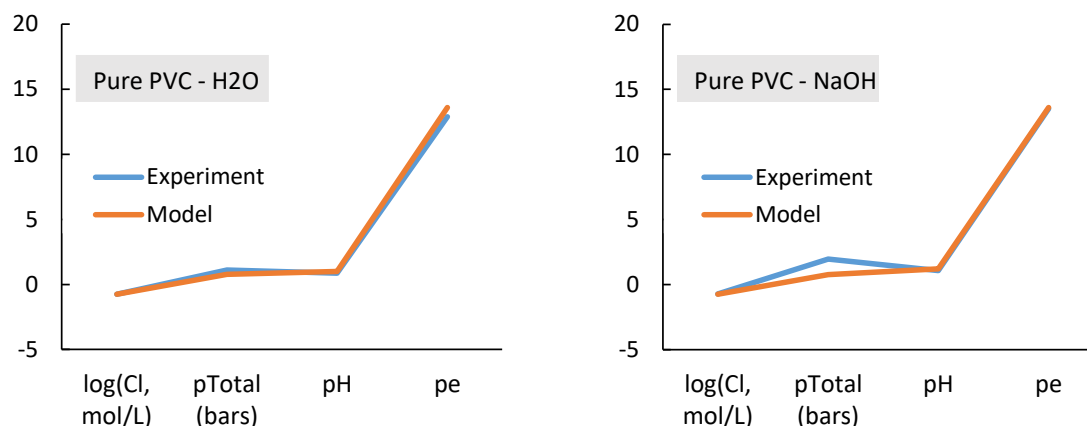


Figure 3-33: Modelling of pure PVC radiolytic and hydrolytic degradation. Experiment from BenZeineb et al. (2021), modelling from this study.

Results are shown in Figure 3-33 for pure PVC and Figure 3-34 for the industrial samples. Since chloride concentration and Eh (pe) are using to adjust yield values, total pressure, pH and calcium concentrations are considered to check the discrepancies between calculations and experiment results. Globally, results from calculations are consistent with experiments. It is interesting to note that for pure PVC, with respect to Colombani (2006) HCl(g) yields reported in Table 1 (1.8 10⁻⁶ mol.J⁻¹), the value extracted from BenZeineb et al. (2021) experiment and used in the modelling is almost identical 1.9 10⁻⁶ mol.J⁻¹ (see Table 3-6). This means that HCl(g) release is not modified by the aqueous solutions and that the radiolysis of water is of limited impact on pH values with respect to the HCl(g) release. G(HCl(g)) reported in Table 3-6 for industrial samples are normalized to the amount of PVC molecule and the values are clearly lowered than the value obtained for pure PVC by a factor 1.9 to 1.5. This result is in agreement with Colombani (2006) results where the industrial sample display a value 2.3 times lower than what is observed for the pure PVC sample in aerobic conditions and for a total dose between 0 and 2 MGy. For Colombani (2006), the difference would be explained by the presence of additives in the industrial sample which would hinder the HCl(g) release. The G(H₂)_{app} obtained are 4 times higher than those obtained by Colombani (2006). The difference could result from the contribution of H₂O radiolysis to the global H₂(g) release. For such reason, the values displayed in Table 3-6 must be considered with care for future use.

The modelling of PVC degradation (radiolysis + hydrolysis) and the agreement with experiment results confirms the buffering of the pH drop by the carbonate dissolution (primary phase in industrial samples) and the role of stabilizers in decreasing the HCl release rate. In details:

- for pure PVC, HCl(g) release strongly decreases the pH of the solution. The modelling indicates that HCl(g) release is not modified by hydrolysis because the yield found is almost identical to the yield obtained by Colombani (2006) for radiolysis in dry conditions.
- for industrial PVC, the pH drop is buffered first by the dissolution of calcium carbonate. This induces a release of calcium in solution which is correctly reproduced by the model

- when the amount of carbonates is lower, the pH drop can be buffered only for experiments performed in alkaline solutions. In that case, H⁺ cations are partially balanced by the OH⁻ anions, which limits the need for carbonate anions to achieve the buffering of the solution.

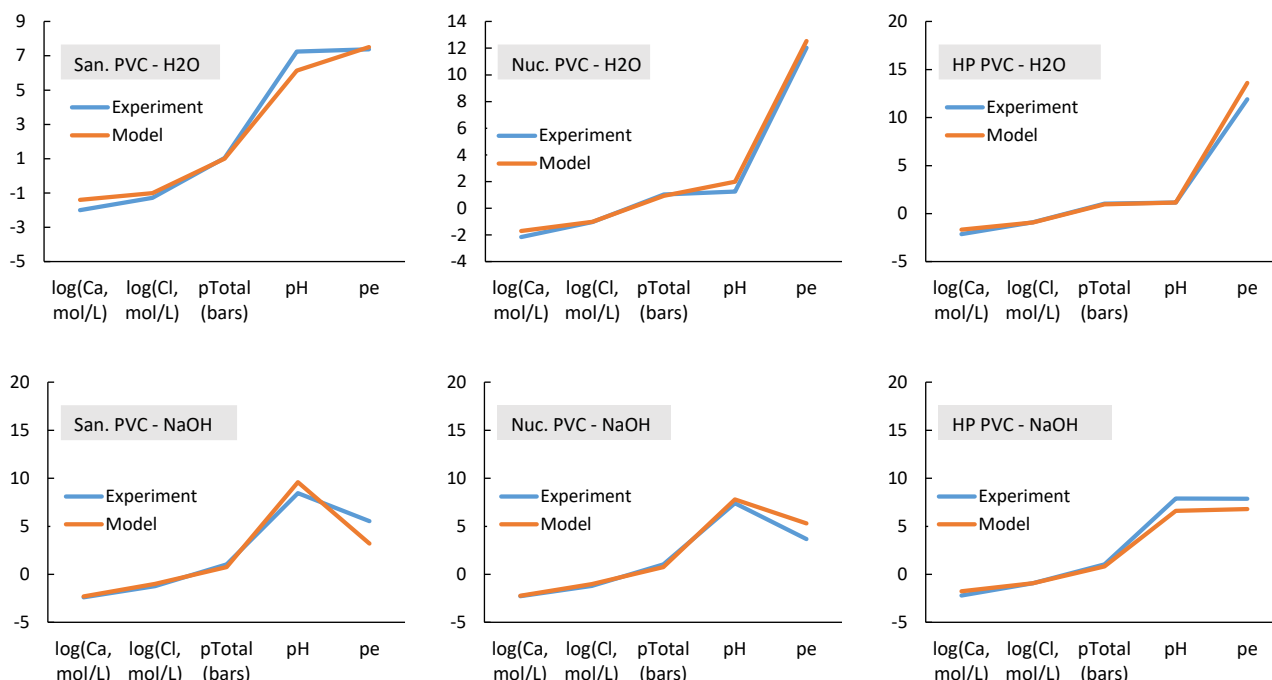


Figure 3-34: Modelling of the radiolytic and hydrolytic degradation of 3 industrial PVC samples. Experiment from BenZeineb (2021), modelling from this study.

The calculated amount of degraded PVC comes to 31% for pure PVC and 37% for sanitary PVC, in both neutral or alkaline solutions. For storage conditions (total dose = 1 MGy), these amounts are reduced to 13 and 15%, respectively.

3.3.4.2 Implementation of cellulose hydrolysis / radiolysis

Considering ISA as the only degradation product, the model has been implemented into PhreeqC, using the parameterization provided by Glaus and Van Loon (2008) for purified Aldrich cellulose. Results are reported in Figure 3-35, where the model is able to reproduce correctly both the cellulose degradation rate and the modification in the solution (pH, Ca⁺⁺).

The coupling of both hydrolysis and radiolytic degradation reaction can also be implemented provided that:

- Cellulose radiolytic degradation proceeds according to reaction (3-51) and yields previously reported

the yield for ISA radiolytic degradation is considered similar to that of acetate, which is reported in Doe (2013). It proceeds according to the reaction $C_2O_2H_4 = CO_2(g) + CH_4(g)$ with a global yield of $1.1 \cdot 10^{-6}$ moles.J⁻¹.

The results are reported in Figure 3-36, where the degradation (radiolysis + hydrolysis) of cellulose is calculated, depending on the irradiation dose rate: no radiolysis ($D = 0 \text{ Gy}\cdot\text{s}^{-1}$) or a high rate corresponding to experimental conditions (Colombani 2006, $D = 0.17 \text{ Gy}\cdot\text{s}^{-1}$ or a low rate, corresponding to storage conditions for ILW wastes ($3.2 \cdot 10^{-5} \text{ Gy}\cdot\text{s}^{-1}$).

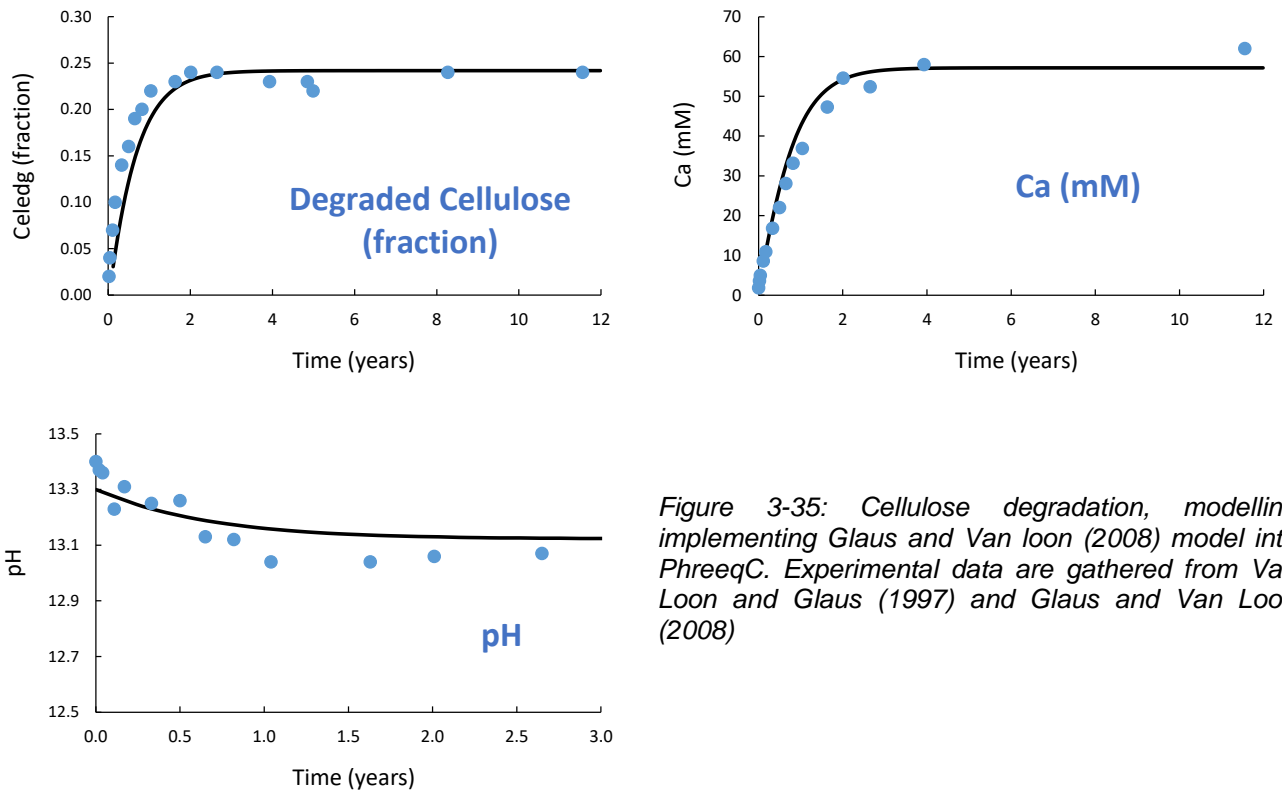


Figure 3-35: Cellulose degradation, modelling implementing Glaus and Van loon (2008) model into PhreeqC. Experimental data are gathered from Van Loon and Glaus (1997) and Glaus and Van Loon (2008)

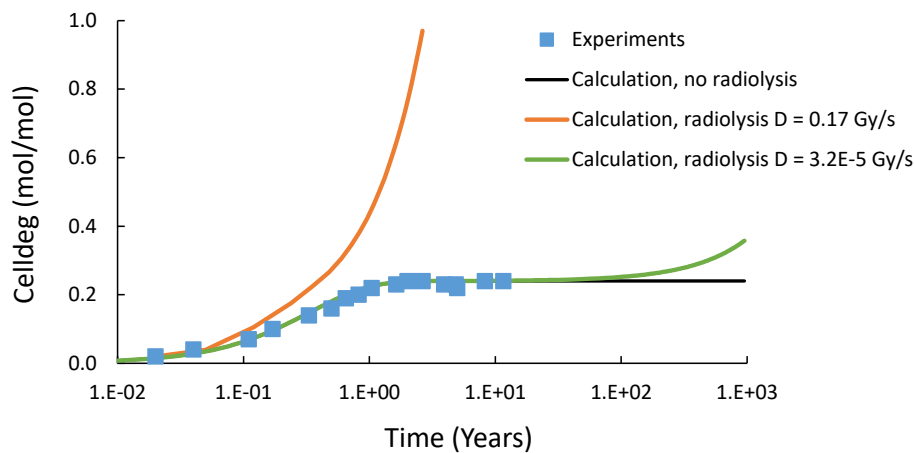


Figure 3-36: Modelling of the degradation (radiolysis + hydrolysis) of cellulose, depending on irradiation dose rate

Figure 3-36 indicates that the degradation of cellulose is actually modified by radiolysis, with an increase by 46% after 1000 years for a dose rate corresponding to disposal conditions.

4 Model implementation, abstraction, and application on waste package scale

4.1 Generic system for modelling at waste package scale

The basis of waste package definitions and processes that influence waste package evolution is given in Chapter 0. Descriptions for two waste sorts are given in this chapter. They are loosely based on Swiss waste sorts, which are generic enough to act as reference systems.

A reference composition of the young CEM I cement following the description in D2.16 (Samper et al., 2022) is given in Section 4.2.1 and is be used for the waste package modelling.

4.1.1 ILW/steel

The waste package for metallic (steel) waste is based on a design defined in Nagra (2008a). The design uses a reinforced concrete container with 15 cm thick walls and an outer volume of close to 6 m³ (see Figure 4-1). The container is filled with 6640 kg of carbon steel waste. The remaining void space is backfilled with 2.5 m³ infill mortar.

L3 LC-84 Nagra

Form:	Quader
Länge:	2.44 m (8 ft)
Breite:	1.22 m (4 ft)
Höhe:	2.00 m
Wandstärke:	0.15 m
Aussenvolumen:	5.946 m ³
Eigenmasse:	6670 kg
Nutzvolumen:	3.3 m ³

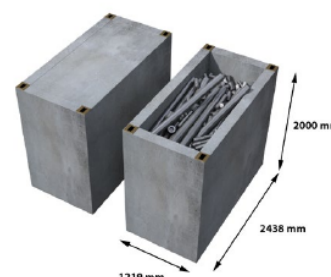


Figure 4-1: Container for metallic waste (Nagra, 2008a; Stein, 2014).

Table 4-1: Amounts and volumes for different materials considered in the model. Waste and reinforcement steel volumes are back-calculated from weight of steel. Amounts of concrete and infill are calculated based on the volumes to be filled.

	Material	Amount (mol)	Volume (m ³)	Weight (kg)	Surface to mass relation for corrosion (m ² kg ⁻¹) (Nagra, 2008a)
Container wall	Container concrete		2.5650	6279.1	
	Steel reinforcement	5855.5	0.4163	327.0	5.1e-2
Useable volume	Steel waste	118900.5	0.84532	6640.0	5.56e-2
	Waste package (infill) mortar		2.5016	5601.2	

According to the initial waste inventory (Nagra, 2008a), the waste is mainly steel, but also various other metals are present. For simplicity, it is assumed that waste is composed solely of carbon steel.

Volumes of container walls were estimated to be 2.60664 m³. The walls shall contain 327 kg of reinforcement steel according to Stein (2014). This gives a volume of about 2.565 m³ that is filled by container wall concrete.

The infill mortar recipe is given in Section 4.2.2. The volume to be backfilled is close to 2.5 m³.

4.1.2 ILW/steel/organics

It is assumed that the 200 l waste package is in dimensions identical to the one defined in Wieland et al. (2018) for waste sort BA-P-HL. This is a “200 l steel drum” with an effective volume of 216 l made from 1.2 mm thick zinc coated “mild carbon steel” (type DC01 (old 12.03) steel, typically about 0.12% total C). The total weight of an empty drum is about 25 kg, of which are 23.4 kg steel. For simplicity the 1.53 kg zinc coating and 0.036 kg of epoxy phenol are not considered in the model.

The organic waste was collected in 30 l steel drums with a diameter of about 30.5 cm and a height of 51.0 cm. The wall thickness will be 1 mm, total empty weight is about 5.5 kg and for simplicity, it is assumed they are also made from mild carbon steel. These smaller drums will be compacted into “pucks”, which will reduce the waste volume by about 50%. Four pucks will be placed in the centre of the 200 l waste package (Figure 2-3). Part of the void space in the drum will be precasted with an infill mortar defined in Section 4.2. After emplacement of pucks, the remaining void space is filled with the same infill mortar, such that there is only one backfill material in the waste package.

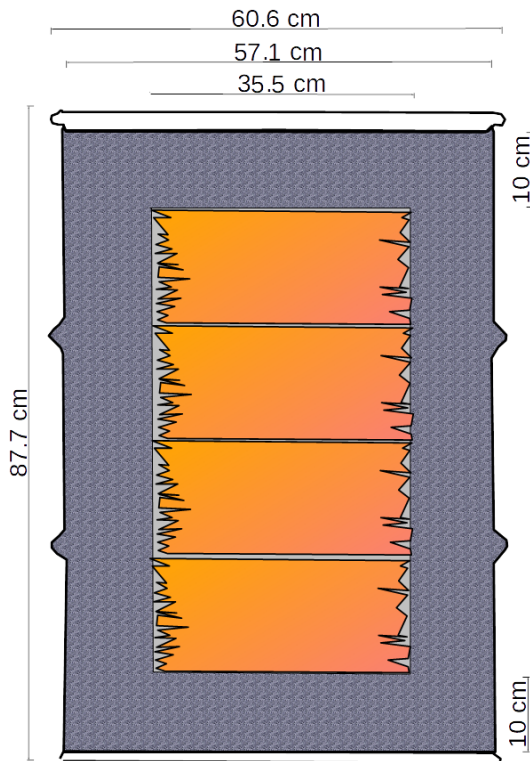


Figure 4-2: Schematic sketch of the generic waste package, which contains four pucks (super-compacted 30 l drums used for collecting cellulose waste)

The generic waste package is simplified such, that only three materials were considered: steel, organic waste and infill mortar.

Table 4-2: Materials, amounts and volumes for the organic waste package.

Material	Amount (kg)	Volume (m ³)	Density (kg m ⁻³)	Molar mass (kg mol ⁻¹)	Porosity (with interlayer/gel porosity)	Mol amount
Steel	45.4		7855	0.05585 (Fe)	0.0	812.965

Organic waste / Cellulose (C ₁₂ H ₂₀ O ₁₀)	60 (4x15kg)	0.06 includes void space!	1500	0.16214		370.048
Infill mortar		0.150			0.14 (0.27)	
total		0.216				

For the waste drums containing organic waste, the corrosion of steel is considered for the outer drum hull and the hulls of compacted 30 l drums in which the waste was collected.

This gives two kind of surfaces that can corrode:

- Corrosion of the outer drum from inside and outside where the hull is in contact with cementitious backfill material. Corrosion rates inside and outside the drum might differ, as long as the hull is largely intact.
- Corrosion of steel surfaces in compacted waste. At the outside in contact with cementitious backfill material, in the inside in contact with waste material. If it is assumed that the drum hulls are still intact after compaction, the inside of the drums will not corrode (due to lack of water).

The corresponding steel amount, approximate surface areas and specific surface areas are summarized in Table 4-3. In this work, the corrosion of steel is implemented based on corroding surface areas estimated for ideal cylinders. Please note, that specific surface areas are slightly lower than those calculated for two-sided corrosion of 1.2 mm and 1 mm thick steel plates. This is caused by the higher thickness of some elements in real drums and deviation from an assumed ideal cylinder geometry that hampers the estimation of real surface areas.

Table 4-3: Steel inventory and associated surface areas

compartment	Steel weight (kg)	Associated specific surface area (m ² /kg)	Total surface area (m ²)
(Outer) drum	23.4	0.175	~ 4.1 (inside and outside!)
Smaller waste drums	22 (4 x 5.5)	0.23	~5.1 (4x1.27) (inside and outside)
total	45.4		9.2

It is assumed that the organic waste is composed solely of water free cellulose. Each small 30 l drum for waste collection shall contain 15 kg of cellulose. The drums should not contain any free water.

The compacted cellulose should occupy a total volume of 60 l. The void space in the waste compartment after compaction is

$$1 - (60 \text{ kg} / 1500 \text{ kg m}^{-3}) / 0.06 \text{ m}^3 = 0.3333$$

The initial gas filling of the void space is ignored in the setup.

EURAD Deliverable 2.15 – ILW modelling results and recommendations

The total volume of backfill material in the drum shall be 150 l. The backfill material does not contain any steel reinforcements.

4.2 Definition of cementitious materials at waste package scale

4.2.1 Reference cement

All cement-based materials utilize the same CEM I 42.5 that is defined as “reference cement” in EURAD ACED project (cf. Samper et al., 2022).

Table 4-4: Definition of a predefined composition “OPC-Norm” in GEM-Selektor⁹.

Input			Output scaled to a mass of 1 kg	
Composition (Lothenbach et al., 2008)	unit	amount	Elemental composition	Amount [mol]
Ca3O5Si (alite)	kg	0.058	Al e	0.8712278
Ca2O4Si (belite)	kg	0.010	C e	0.47958276
Ca3O6A l2 (aluminate)	kg	7.6e-03	Ca e	11.094358
Ca4O10Al2Fe2 (ferrite)	kg	7.5e-03	Fe e	0.30866796
CaO	kg	0.6e-03	Inrt a	0.74728339
CaCO3	kg	4.8e-03	K e	0.20486471
Inrt	kg	4.49e-03	Mg e	0.34735661
K2SO4	kg	1.6e-03	Na e	0.030214622
CaSO4	kg	3.6e-03	O o	21.679913
Na2SO4	kg	0.1e-03	S e	0.38326859
K2O	kg	0.1e-03	Si e	3.1209215
Na2O	kg	0.05e-03		
MgO	kg	1.4e-03		
SO3	kg	0.16e-03		
Total mass	kg	0.100		

4.2.1.1 Hydrated cement paste

For hydration modelling and an extended discussion of phase composition for the hydration of the cement paste, see Lothenbach et al. (2008). The calculations were based on Cemdata2007 thermodynamic database.

We provide an example of a fully hydrated cement paste calculated based on CEMDATA 18.1 thermodynamic database (Lothenbach et al., 2019) in Table 4-6 to Table 4-8.

⁹ See <https://gems.web.psi.ch/> for more information on GEM-Selektor.

Table 4-5: Input for hydration of cement paste with w/c ratio of 0.58 in GEM-Selektor.

Name	Quantity	Units	Remark
Aqua	1	kg	H2O
OPC-Norm	1.724138	kg	Composition according to Table 4-4: Definition of a predefined composition “OPC-Norm” in GEM-Selektor
NaCl	1e-9	kg	Minimal amount of Cl needed as system setup contains Cl

Table 4-6: Elemental (independent component) composition and molal concentrations for total dissolved independent components after hydration calculation with GEM-Selektor.

Independent component	Bulk composition of system [mol]	Molal concentrations total dissolved independent components [mol/kg]
Al	1.502117	6.4867786e-05
C	0.82686687	0.00012709809
Ca	19.128205	0.0012214461
Cl	1.7110748e-08	4.7630382e-08
Fe	0.53218616	9.7545803e-08
H	111.01675	0.32452229
Inrt	1.2884197	0
K	0.35321502	0.31982892
Mg	0.59889073	1.6117537e-09
Na	0.052094194	0.008391125
O	92.887535	0.33663887
S	0.66080793	0.0028590361
Si	5.3808994	5.8763008e-05

Table 4-7: Phase composition of the fully hydrated cement paste after equilibration with GEM-Selektor.

Phase name	Number of components in phase	Total amount in phase [mol]	Value of phase stability criteria [-]	Phase volume [$\times 10^{-6}$ m ³]	Phase mass [kg]
a aq_gen	75	20.169761	2.2713066e-08	360.86483	0.36590639
s CSHQ	6	7.2143944	-4.5384368e-08	465.82146	1.0505821
s ettringite	1	0.21992695	-3.3186936e-09	155.49496	0.27603271
s C4AcH11	1	0.38139719	1.8637534e-09	99.910049	0.21680477
s Calcite	1	0.44542401	-8.825525e-11	16.45129	0.04458115
s C3FS0.84H4.32	1	0.26609306	0	39.520939	0.12139626
s Portlandite	1	6.8163795	8.2214147e-08	225.3495	0.50504395
s OH-hydratalcite	1	0.14972268	-1.9749427e-13	32.968936	0.06637684
s Inert_Quartz	1	1.2884197	0	29.231666	0.0.7741380

Table 4-8: Other properties of aqueous phase after equilibration with GEM-Selektor.

Ionic strength of solution (IS) [mol kg ⁻¹]	0.31339203
pH	13.357742
pe	3.317321
Eh [V]	0.19585581

Total volume of the system: 1.4256136e-03 m³

Total mass of the system: 2.724138 kg

Volume fraction of liquid phase: 372.78157/1429.1292 ~ 0.253

Volume fraction of interlayer and gel water: ~ 0.11

Total water content ("porosity") ~ 0.36

4.2.2 Infill mortar

The same recipe was used for drum infill and container infill mortar. It is based on the backfill material defined in NTB 14-04, Appendix B (SA-B-MX-L3-SMA) (Nagra, 2014) and shown in Table 4-9. For aggregate it is assumed that they are composed of spherical grains with 1 mm diameter.

The definition of the simplified recipe in GEM-Selektor software is shown in Table 4-10.

Table 4-9: Composition for representative infill mortar as given in Nagra (2014).

Materials from Nagra (2014)	mass	Units	Implementation/simplification
Water	748	kg	Water
micropoz	370	kg	Micro-silica
Zement HTS	1230	kg	CEM I 42.5 N
Clinoptinolith	185	kg	Not included in current setup: Add 200 kg inert SiO ₂ (to account for lower density of clinoptinolite vs. SiO ₂)
Sand (Quartz) (e.g. 0.5 mm or 1 mm diameter)	1930	kg	Aggregate (sand) can be either SiO ₂ or (inert) CaCO ₃
Other additives		kg	Not considered for modelling
Diethanolamin	6.66		
Formaldehyd	2.05		
Gluconsaeure	3.08		
Harnstoff	4.44		
LaurylaminPglcyoelether	0.912		
Tributylposphat C12H27O4P	0.074		

Table 4-10: Simplified infill mortar: Input for a system T=25°C, P=1 bar in GEM-Selektor for inert SiO₂ aggregates (Inrt). OPC-Norm is a “compos” record as defined for the CEM I 42.5 N following Lothenbach et al. (2008) and Liu et al. (2014).

Name	Quantity	Units	
Aqua	0.374	kg	
NaCl	1e-09	kg	Only for defining Cl as non zero
OPC-Norm	0.615	kg	
Inrt	1.065	kg	Aggregate (quartz)
SiO2	0.185	kg	Micro silica

4.2.3 Container concrete

The recipe for a container concrete is based on OPC based concrete with $w/c = 0.45$.

- The concrete is based on the standard CEM I 42.5 N cement, which is used for all cement-based materials in the ACED project.
- The recipe includes CaCO_3 as additive (filler).
- The simplified setup does not include any (required) super-plasticizer or other additives that would amount for example to 1.4 % of the cement.
- Aggregate can be either SiO_2 or CaCO_3 . As mineral density for both minerals are different, the amount of calcite aggregate needs to be increased to get the same aggregate volume: 1600 kg for SiO_2 corresponds to about 1637.2 kg CaCO_3 . Alternatively, the dissolution of quartz aggregate can be inhibited to model an “inert” aggregate.

Table 4-11: Desired composition for 1 litre concrete $T=25^\circ\text{C}$, $P=1$ bar, $w/c = 0.45$ in GEM-Selektor.

Name	mass	Units	Desired volume fraction	
Aqua	0.180	kg	0.175	
aggregate	1.600	kg	0.6	Aggregate amount needs maybe adjustment to reach desired volume fraction
NaCl	1e-6	kg		Needed to define non-zero value for Cl
OPC-Norm	0.400	kg	0.127	
CaCO_3	0.180	kg	0.067	filler

Table 4-12: Input in GEM-Selektor for SiO_2 aggregates (Inrt). OPC-Norm is a “compos” record as defined for the CEM I 42.5 N following Liu et al. (2014). Aggregate is represented by Inrt, an inert phase with the properties of quartz. For reactive aggregates, Inrt is replaced by the same amount of quartz.

Name	Quantity	Units
Aqua	0.180	kg
CaCO_3	0.180	kg
NaCl	1e-09	kg
OPC-Norm	0.400	kg
Inrt	1.600	kg

Table 4-13: Input in GEM-Selektor for CaCO_3 aggregates. OPC-Norm is a “compos” record as defined for the CEM I 42.5 N following Liu et al. (2014).

Name	Quantity	Units
Aqua	0.180	kg
CaCO_3	1.8172	kg
NaCl	1e-09	kg
OPC-Norm	0.400	kg

4.2.3.1 Aggregates

Aggregate size distribution in terms of a sieve curve is given in Table 4-14 and is visualized in Figure 4-3. The aggregate size distribution is discretized into size classes. For each size class it is assumed that aggregates have a spherical shape with a diameter defined from the mesh size for the corresponding class. I.e. particles that pass the 0.063 mm mesh are assumed to have a diameter of

0.063 mm, while particles that pass the 0.125 mm mesh, but not the 0.063 mm mesh, will have a diameter of 0.125 mm. Such a diameter mapping would slightly overestimate the average diameter for each size class from a real sieve curve.

Based on the sieve curve, the equivalent number of aggregate grains with their masses, volumes and surfaces can be calculated for each size class. Summation of particle surfaces over all size classes gives the total reactive surface area for the aggregates.

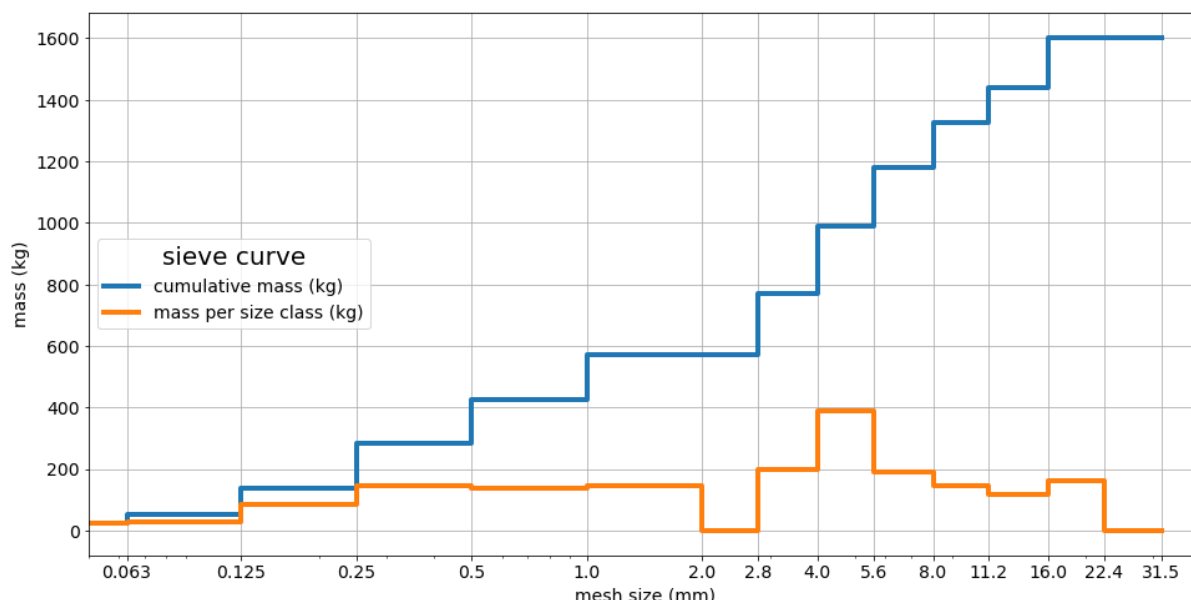


Figure 4-3: Assumed sieve curve for aggregate sizes normalized to 1600 kg, the mass of aggregates in 1 m³ concrete.

Table 4-14: Aggregate sizes, amounts and (reactive) surface areas, as well as grain numbers and grain properties for each size class.

Mesh size (m)	Cumulative amount (kg)	Amount per size class (kg)	Amount per size class (mol)	Volume per size class (m³)	Surface per size class (m²)	Cumulative surface (m²)	Volume one grain (m³)	Surface one grain (m²)	Number of grains per size class
0.00e+00	0.00	0.00	0.00	0.00e+00	0.00	0.00	0.00e+00	0.00e+00	0.00e+00
6.30e-05	23.76	23.76	395.36	8.97e-03	853.73	853.73	1.31e-13	1.25e-08	6.85e+10
1.25e-04	53.81	30.05	500.20	1.13e-02	544.37	1398.10	1.02e-12	4.91e-08	1.11e+10
2.50e-04	139.86	86.05	1432.19	3.25e-02	779.34	2177.44	8.18e-12	1.96e-07	3.97e+09
5.00e-04	284.70	144.84	2410.61	5.47e-02	655.88	2833.32	6.54e-11	7.85e-07	8.35e+08
1.00e-03	424.43	139.73	2325.53	5.28e-02	316.37	3149.69	5.24e-10	3.14e-06	1.01e+08
2.00e-03	569.84	145.41	2420.08	5.49e-02	164.61	3314.30	4.19e-09	1.26e-05	1.31e+07
2.80e-03	570.84	1.00	16.73	3.79e-04	0.81	3315.11	1.15e-08	2.46e-05	3.30e+04
4.00e-03	769.27	198.43	3302.51	7.49e-02	112.32	3427.43	3.35e-08	5.03e-05	2.23e+06
5.60e-03	989.88	391.01	6507.64	1.48e-01	158.09	3585.52	9.20e-08	9.85e-05	1.60e+06
8.00e-03	1178.85	188.97	3145.10	7.14e-02	53.48	3639.00	2.68e-07	2.01e-04	2.66e+05
1.12e-02	1324.70	145.85	2427.36	5.51e-02	29.48	3668.49	7.36e-07	3.94e-04	7.48e+04
1.60e-02	1440.76	116.06	1931.69	4.38e-02	16.42	3684.91	2.14e-06	8.04e-04	2.04e+04
2.24e-02	1603.00	162.24	2700.21	6.13e-02	16.40	3701.31	5.88e-06	1.58e-03	1.04e+04
3.15e-02	1603.00	0.00	0.00	0.00e+00	0.00	3701.31	1.64e-05	3.12e-03	0.00e+00

Smaller particles will dissolve faster and they will be eventually completely dissolved, which of course changes the total reactive surface area. To account for this a lookup table was created that gives the change of surface area upon dissolution of defined moles of aggregate.

** Procedure for change of surface area upon dissolution **

1) Starting point (zero SiO₂ dissolved) is the initial data set.

- 2) For each grain size the fraction of its surface area with respect to the total surface area is calculated
- 3) For each grain size: “mole aggregate” divided by “fraction of total surface area for the grain size class” is calculated, which gives the total amount of SiO₂ that needs to be dissolved, until all aggregates of the specific size are dissolved. For simplicity, a linear scaling of surface area with mass/amount is assumed.
- 4) The smallest (non-zero) amount to be added from the calculated values is selected (mole_dissolved).
- 5) Mass/moles from each size class is removed according to “current moles aggregate” – “mole_dissolved” * “surface fraction of size class”.
- 6) New particle diameters are estimated after dissolution for each size class. The particle number is assumed constant in time for each class. Then all other particle properties for each size class are updated based on new particle diameter and update surface area for the size class.
- 7) The new total surface area (sum over all size classes) is calculated.
- 8) goto 1) and repeat the procedure until all particle classes are dissolved.

Table 4-15: Decrease of surface area with dissolution of aggregates.

Amount aggregate dissolved (mol)	Reactive surface area (m ²)
0.0	15526.2
7190.2	1201.7
15926.9	992.3
29597.9	750.8
49910.2	489.9
76245.9	105.3
87538.3	66.6
95474.6	50.4
103716.7	29.3
110127.7	13.2
114271.3	6.6
117114.5	3.1
119075.0	1.1
120048.6	0.0

4.3 Description of models used for modelling at waste package scale

In this section 4.2, the models used by each modelling partner are described (processes, equations, parameters, other characteristics). An overview of the different models is given in Table 4-16 while the details on the implementations are given in the corresponding sub-sections for each partner.

Table 4-16: Overview of models used by the Partners.

Partner / model	Modelling approach / simulation time	Scope	Chemical processes	Transport processes / characteristic parameter	Numerical tools
PSI Drum: organics/steel waste Container: steel waste	geochemical batch calculations using a "mixing-tank" approach / 10 ⁵ years	For single waste packages: Long-term geochemical evolution of aqueous, gas and solid phases Creation of lookup tables for UFZ code (concrete degradation by carbonation and aggregate-cement reactions)	Chemical equilibrium calculations for 3 phase system (aqueous phase, gas phase, solid phases) Kinetic control of degradation for organic matter, corrosion of steel, and dissolution of aggregates in cement materials	no transport processes	GEM-Selektor, Jupyter notebooks with python interface to xGEMS
UFZ ILW drum container	2D reactive two-phase transport, Lookup-table approach for mortar degradation / 500 years	feedback system between water consuming reactions and water supply from host rock/outside	degradation of organics, corrosion of steel, dissolution of aggregates in cement materials, consumption (or release) of water by reactions, cement carbonation	componential advection and diffusion, / (CH ₄ , CO ₂ , H ₂ , N ₂ , H ₂ O, saturation)	OpenGeoSys (finite element discretisation)
SCK CEN Organic waste drum in a container	2D reactive transport / 500 years	calcite precipitation front, evolution of C-S-H phases	degradation of organic material (cellulose), cement carbonation	Diffusive transport in fully saturated conditions	HYDRUS 5 PHREEQC
COVRA waste package / disposal cell with	2D diffusive transport of water and hydrogen (in gas phase and dissolved in water)	Waste package evolution in context of different water consumption rates (reaction rates)	steel corrosion (water consumption / H ₂ production)	Diffusive transport / H ₂ O, H ₂ , water saturation	COMSOL

container of steel waste	/ 150 years				
BRGM Waste drum with steel tube	1D radial geometry Geochemical modelling with diffusion of aqueous species / 100 years	Geochemical evolution of concrete and steel tube corrosion with alteration products	Degradation of organics (cellulose, PVC), steel corrosion	Diffusive transport for unsaturated conditions / Portlandite, Calcite, C-S-H phases, corrosion alteration products	MARTHE-PHREEQC

4.3.1 Models used by PSI (ILW/organics/steel, ILW/steel)

The mixing-tank modelling approach used by PSI corresponds to that reported earlier by Wieland et al. (2018) and it is based on the following step-by-step procedure:

- The inventories of the waste materials were arranged for the geochemical modelling. Materials were decomposed into the individual components, i.e. unhydrated cement and water in the case of cement paste, and unhydrated cement, water and aggregate in the case of concrete;
- Modelling the initial composition of the new solidifying concretes used to condition the waste materials;
- Modelling the effect of the degradation of organic waste materials and metal corrosion, as well as reactive aggregate on the temporal evolution of the chemical conditions in the waste packages;
- Modelling scenarios: Use of solidifying materials with siliceous aggregates or calcareous aggregates (for sake of comparison), respectively, as well as limited and unlimited water availability. In addition, for the decommissioning (metal) waste sort, an alternative form for pH dependence of Fe corrosion was calculated.

In brief, the same modelling approach was applied as outlined by Wieland et al. (2018) and Kosakowski et al. (2020). This so called “mixing-tank” approach successively equilibrates all “reactive” materials of the waste package. Time dependent reactivity of (organic, iron/steel and aggregate) materials is controlled via kinetic laws described in Section 2.2.1.2. The “mixing-tank” approach ignores the spatial heterogeneity of waste package materials and ignores transport processes in the waste package. Therefore, it cannot realistically describe the evolution of waste packages (Huang et al., 2021). Instead, it is a fast and simple method to assess mass balances and give some indication on impact of material (e.g. carbonate vs. siliceous aggregates) and modelling choices (e.g. kinetic parameters).

The thermodynamic setup is based on PSI/Nagra TDB 12/07 (Thoenen et al., 2014) and Cemdata V18.1 (Lothenbach et al., 2019). The CSHQ solid solution model for C-S-H including the uptake of Na and K was used. In addition, the M-S-H solid solution model implemented in Cemdata was enabled. All other cement and mineral phases were select in their single component phase implementations. The following gases are included in the setup (CO₂, CH₄, H₂, O₂, H₂S).

The activities are calculated according to the extended Debye-Hückel equation taking into account short range interactions (Truesdell-Jones equation) as given as equation 4.1.10 of the document available as <http://gems.web.psi.ch/GEMS3/doc/pdf/Activity-Coeffs.pdf> or in (Wagner et al., 2012).

$$\log_{10}\gamma_j = \frac{-A_\gamma z_j^2 \sqrt{I}}{1 + aB_\gamma \sqrt{I}} + b_\gamma I + \log_{10} \frac{x_{jw}}{X_w}$$

This type of activity model is valid for an ionic strength of up to 1 molal.

4.3.1.1 Kinetic control of organic matter degradation, iron corrosion and aggregate dissolution

In GEM-Selektor, GEMS3K and xGEMS kinetic control of amounts of phase components is implemented via so-called upper and lower meta-stability constraints. In the GEM algorithm, the system is equilibrated by allowing component amounts between upper and lower meta-stability constraints. If those constraints are set to the same value, the component amount will be fixed to this value. If components are highly unstable (under calculated conditions), the equilibrated amounts will be equal to the lower limit.

The constraints are set via kinetic laws for the iron, cellulose and aggregate phase. The reaction products are not constraint and will be result of the equilibration of the system. Although it was found that only a minor fraction of hydrogen produced by iron corrosion and methane from organic matter degradation reacted with other phases upon equilibration, the produced amount of methane and hydrogen gas were constraint by setting the upper and lower allowed gas amounts to be the same.

During equilibration, CO₂ from organic matter degradation is consumed by carbonation reactions of the infill mortar. After completing carbonation of cement phases, CO₂ is released to the gas phase.

4.3.1.2 Corrosion of steel

The corrosion process of the steel is addressed in terms of the H₂ generation and subsequent water consumption. An overview on processes, known rates and the kinetic control of carbon steel corrosion in modelling are given in Deissmann et al. (2021) and de Windt et al. (2020). The overall reaction for the corrosion of the steel can be expressed in terms of the following overall reaction (Smart et al., 2004; Xu et al., 2008).



Anoxic corrosion of iron and steel is kinetically controlled and mainly pH dependent. The corrosion rate of the iron and steel is significantly accelerated under near neutral conditions compared to that of alkaline conditions.

As described in chapter 3.4 of de Windt et al. (2020) for a particular condition, when pH value is below 10.5 (see Figure 11 of de Windt et al., 2020), the corrosion rate R is chosen to be 5.0e-6 m/a, while under alkaline conditions at pH 12-13 the corrosion rate drops to 1.0e-7 m/a. The corrosion rates at moderately alkaline pH (10.5-11.5) are not well known.

For first calculations the following pH dependence for corrosion rates will be used:

- Reference (step function in Figure 4-4): < pH 10.5: 5.0e-6 m/a, > pH 10.5: 1.0e-7 m/a
- Alternative implementation (log-linear interpolation in Figure 4-4: pH 10.5 – pH 12: linear decrease of log₁₀(corrosion rates) from 5.0e-6 m/a at pH 10.5 to 1.0e-7 m/a at pH 12.

The corrosion rates are converted in rates R_{Fe} of mole Fe consumed per m² and year with the following relation:

$$R_{\text{Fe}} = R \rho / M \quad (4-2)$$

For the molar mass M of steel, the value for iron 0.05585 kg mol⁻¹ is used and for the density ρ of steel a value of 7855 kg m⁻³. This results in rates for iron consumption of 0.70322 mol Fe / (m² a) when pH value is below 10.5, while under an alkaline condition, the iron consumption rate drops to 0.01406 mol Fe / (m² a).

Using the stoichiometric relations in equation (4-1) and the iron consumption rates (equation (4-2)) hydrogen gas generation rates and water consumption rates given in Table 4-17 were calculated.

Table 4-17: Rates for iron consumption, hydrogen production and water consumption due to corrosion of steel.

condition	Iron consumption rate R_{Fe} (mol m ⁻² a ⁻¹)	Hydrogen production rate (mol m ⁻² a ⁻¹)	Water consumption rate (mol m ⁻² a ⁻¹)	Corrosion rate (m/a)
pH < 10.5	0.70322	4/3 R_{Fe}	4/3 R_{Fe}	5.0e-6
pH > 12	0.01406	4/3 R_{Fe}	4/3 R_{Fe}	1.0e-7

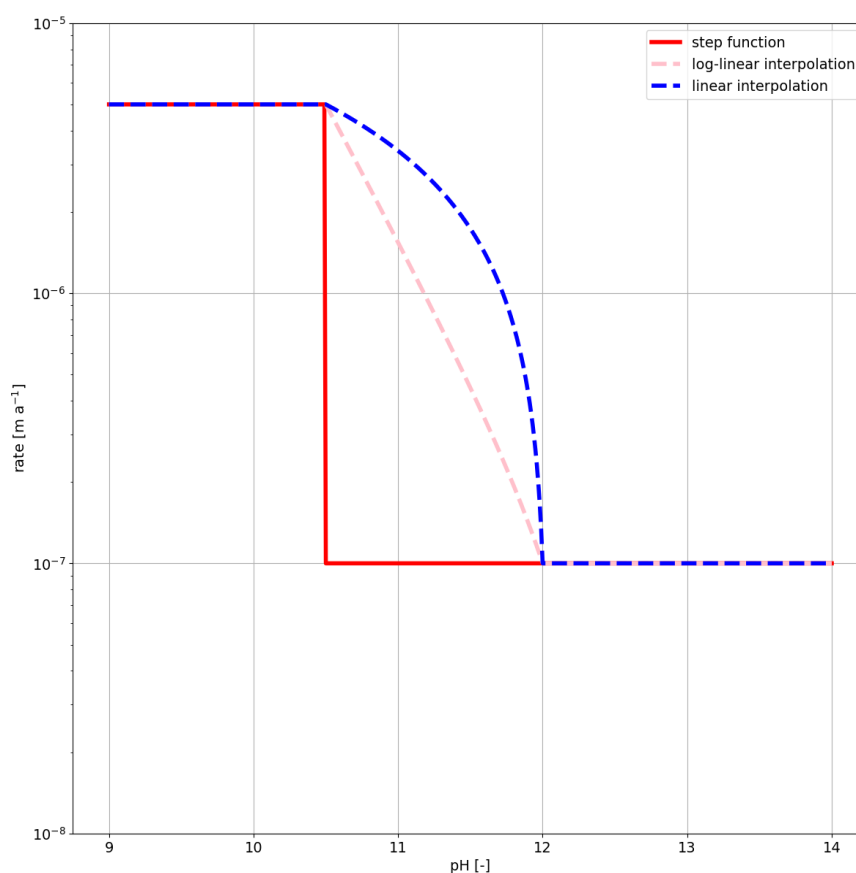


Figure 4-4: Possible interpolation of pH dependencies of iron corrosion between pH 10.5 – 12.

4.3.1.3 Degradation of organic waste

The approach for degradation of organic materials is described in detail in Wieland et al. (2018). In summary, the organic waste materials are classified into different groups: Group 1 contains the fast degrading organics, which mainly consists of cellulose. Group 2 resembles the slowly degrading organics and includes e.g. polystyrene, plastic materials and rubbers.

Group 1 organics are modelled as cellulose, which degrades in the presence of water according to the overall chemical reaction as:



with water consumed at the same molar amount as CO₂ and CH₄ generated.

The degradation of the slow organics (polystyrene, plastic) in Group 2 can be generalized as the following chemical reaction:



The gas generation rate as well as the water consumption rate correspond to the degradation rate of the organics. The temporal behaviour of degradation of organics can be expressed in terms of first order kinetics:

$$m(t) = m(0) \cdot \exp(-\lambda t) \quad (4-5)$$

$m(0)$: Initial mass of organic material [mol]

λ : Degradation rate [a^{-1}]

Using the gas generation rate k_D [$mol\ kg^{-1}\ a^{-1}$], which represents the amount of gas generated from one kg of waste in one year, the total amount of gas generated for each waste group is calculated (Wieland et al., 2018). The degradation rate λ and the total gas generation rate k_D are related to each other and their values cannot be varied independently (Wieland et al., 2018).

Table 4-18 lists the implemented parameters for the gas generation of the two waste groups for the organic waste. By using equation 4-5 in combination with the corresponding gas generation rate, the rates for production of CH_4 and CO_2 , and the water consumption rate for each waste group are calculated.

Table 4-18: Organic degradation parameters, gas generation rates and rates for water consumption for two waste groups (Wieland et al., 2018).

	Group 1 (cellulose): fast degradation	Group 2 (polystyrene): slow degradation
$m(0)$ (kg per waste package)	60.0	-
λ (a^{-1})	1.89e-3	6.51e-5
k_D ($mol\ kg^{-1}\ a^{-1}$)	0.07	0.005
Rate for CO_2 ($mol\ kg^{-1}\ a^{-1}$)	$k_d * 3/6$	$k_d * 3/8$
Rate for CH_4 ($mol\ kg^{-1}\ a^{-1}$)	$k_d * 3/6$	$k_d * 5/8$
Rate for water consumption ($mol\ kg^{-1}\ a^{-1}$)	$k_d /6$	$k_d * 6/8$

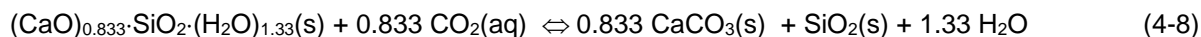
A similar approach was used in Moreno et al. (2001); they used gas generation rates of $0.2\ mol\ k^{-1}g\ a^{-1}$ for cellulose and $0.002\ mol\ k^{-1}g\ a^{-1}$ for slow degrading materials (bitumen, ion-exchange resins, plastics).

4.3.1.4 Carbonation

Carbonation of hydrated cements involves the transformation of C-S-H phases ($xCaO \cdot SiO_2 \cdot nH_2O$), portlandite ($Ca(OH)_2$), ettringite ($Ca_6Al_2(SO_4)_3(OH)_{12} \cdot 26H_2O$) and AFm to calcium carbonate, gypsum and aluminium and silica oxyhydroxides (Venhuis and Reardon, 2001). Portlandite and C-S-H phases are the most abundant Ca-bearing cement phases in cement paste while ettringite and calcium monocarboaluminate (AFm- CO_3 : $3CaO \cdot Al_2O_3 \cdot CaCO_3 \cdot 11H_2O$) are only minor Ca-bearing phases (Kosakowski et al., 2014; Lothenbach and Wieland, 2006). Thus, about 90% of Ca bound in cement paste is associated with portlandite and C-S-H phases and therefore, carbonation is mainly attributed to the conversion of these phases into $CaCO_3$. Note that ettringite is the main SO_4^{2-} bearing cement phase

in cement paste and therefore carries the SO_4^{2-} inventory relevant to the sulphate-reducing pathway of the degradation of organics, if no other SO_4^{2-} sources are available.

As examples, the reaction of CO_2 with the main Ca-bearing phases, portlandite, jennite-like endmembers of C-S-H $(\text{CaO})_{1.67} \cdot \text{SiO}_2 \cdot (\text{H}_2\text{O})_{2.1}$ and tobermorite-like endmembers $(\text{CaO})_{0.833} \cdot \text{SiO}_2 \cdot (\text{H}_2\text{O})_{1.33}$ can be expressed as follows:



Equations (4-6) to – (8) reveal that water will be liberated during carbonation of portlandite and C-S-H phases, if it is assumed that amorphous silica is the final most stable silica phase. In addition, the interlayer/gel porosity (C-S-H interlayers) are reduced upon dissolution of C-S-H, which will make this water available for chemical reactions. The conversion of one mole portlandite to CaCO_3 generates approximately one mole H_2O . Note that water release during carbonation of C-S-H phase is higher due to the higher stoichiometric content of water in these cement phases. Note further that the liberation of SiO_2 from C-S-H occurs during carbonation that also influences the composition of the phase assemblage.

The most notable consequence of carbonation is a drop of pH to values below 10.

The mixing-tank calculations assume that reactions of CO_2 with cement phases are fast and do not need kinetic control for long-term calculations. However, the availability of CO_2 is controlled by the degradation of organic matter.

4.3.1.5 Mineral dissolution kinetics (for aggregate – cement reactions)

Out-of-equilibrium geochemical processes as, for example cement-aggregate reactions are included following the description in Section 2.2.1.5 and using Equation (2-7).

4.3.2 Models used by UFZ

The model used by UFZ covers a single waste container surrounded by mortar and the nearby host rock in a ILW repository. The model presented here is configured according to a general waste storage strategy as published in Nagra (2016), where a vertical cross-section of a concrete waste container, with 12 waste drums, each with 200-liter volume of storage and following a 2x3x2 arrangement (see Figure 4-5). Inside of a drum, a certain amount of waste is placed in it surrounded by cementitious mortar filling the gap between the drum wall and the waste package (see Figure 4-6). The drum wall is considered to be steel with a 1.5 mm thickness and the gaps between the drums are filled again with cementitious backfill mortar. The concrete wall of the container has a thickness of 15 cm. To simplify the model in this study, the concrete of the container and the infill mortar are given the same hydraulic and chemical properties.

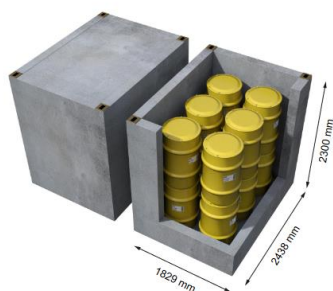


Figure 4-5: Example of the packing of 200-litre drums into one standard disposal container (type LC-86H) (NAGRA NTB 16-05 (2016)).

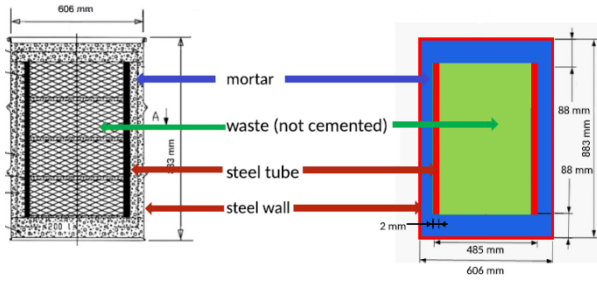


Figure 4-6: Waste drum (modified after Huang et al. (2021))

4.3.2.1 Transport model

In order to investigate the controlling factors of the gas production process, the coupled reactive transport model of component based two-phase flow in the OpenGeoSys (OGS) framework (Kolditz et al., 2016) is adopted here. A detailed description of the reactive transport model can be found in Huang et al. (2017; 2021). In this section, a brief summary of the model is provided.

For the two-phase module in OGS, the standard Galerkin finite element (FE) method is employed for spatial discretization with a fully implicit backward Euler scheme for the time integration. The infill mortar and waste are treated as porous and permeable medium with two mobile phases, i.e. gas and liquid. The gas phase is composed of the component water vapour, nitrogen, methane, hydrogen and CO₂. These components can dissolve into water dominated liquid phase. As for the mass transport model the generalized Darcy law is implemented in combination with diffusive transport given by Fick's law:

$$\frac{\partial}{\partial t} \sum_{\alpha \in \{G,L\}} (N_{\alpha} S_{\alpha} x_{\alpha}^i) + \nabla [\sum_{\alpha \in \{G,L\}} N_{\alpha} (x_{\alpha}^i \mathbf{q}_{\alpha} + \mathbf{J}_{\alpha}^i)] = F^i \quad (4-9)$$

Where α denotes the gas phase G or the liquid phase L, x is the molar fraction of component i in phase α , S_{α} is the saturation of phase α , and N_{α} represents the phase molar density. F^i is a source or a sink term for each component. The Darcy law is given as:

$$\mathbf{q}_{\alpha} = - \frac{k k_{\alpha}^{rel}}{\mu_{\alpha}} (\nabla p_{\alpha} - \rho_{\alpha} \mathbf{g}) \quad (4-10)$$

Here ρ_{α} is the phase density and p_{α} is the phase pressure. The diffusive flux \mathbf{J}_{α}^i is obtained by Fick's law:

$$\mathbf{J}_{\alpha}^i = - D_e \nabla x_{\alpha}^i \quad (4-11)$$

where $D_e = \Phi \cdot S_{\alpha} \cdot D_{\alpha}$ is the effective diffusion coefficient and Φ is the material porosity. Model parameters applied to the two-phase flow process can be found in Table 4-18. For unsaturated conditions the capillary pressure p_c has to be taken into account and is obtained by the van Genuchten model:

$$p_L = p_G - p_c \quad (4-12)$$

$$p_c(S_L^{\text{eff}}) = p_d \left((S_L^{\text{eff}})^{\frac{-1}{m}} - 1 \right)^{\frac{1}{n}} \quad (4-13)$$

Here $m = 1 - 1/n$ and n are the van Genuchten parameters and p_d is the characteristic van Genuchten pressure. Model parameters related to the van Genuchten curve is listed in Table 4-19. The effective saturation S_L^{eff} is given by

$$S_L^{\text{eff}} = \frac{S_L - S_L^{\text{res}}}{1 - S_L^{\text{res}} - S_G^{\text{res}}} \quad (4-14)$$

The relative humidity, which is relevant for the chemical reactivity model is related to the capillary pressure p_c via the Kelvin equation:

$$p_c = \frac{\rho_w R T}{M_w} \ln(\varphi) \quad (4-15)$$

where ρ_w is the density of water (with dissolved gases). T is the temperature and M_w is the molecular weight of water. As the small temperature changes have a small impact on the transport and chemical processes (Leupin et al., 2016), heat transport is neglected and the temperature is constant. The relative permeabilities are derived by following expressions:

$$k_L^{\text{rel}} = \sqrt{S_L^{\text{eff}}} \left[1 - \left(1 - (S_L^{\text{eff}})^{\frac{1}{m}} \right)^m \right]^2 \quad (4-16)$$

$$k_G^{\text{rel}} = \sqrt{1 - S_L^{\text{eff}}} \left[1 - (S_L^{\text{eff}})^{\frac{1}{m}} \right]^{2m} \quad (4-17)$$

The dissolution of the gases into the pore water is described by Henry's law and evaporation of water into water vapor is described by the Raoult's law.

Table 4-19: Properties of different materials used in the UFZ numerical model from Huang et al. (2021)

Parameter	Symbol	Mortar	Waste matrix	Host rock (Granite)	Unit
Intrinsic permeability	k	5e-19 variable	1e-16	8.7e-19	m ²
Porosity	ϕ	0.0995*	0.2	0.005	-
Residual liquid saturation	S_L^{rel}	0.2	0.2	0.2	-
Residual gas saturation	S_G^{rel}	0.0	0.0	0.0	-

Van Genuchten characteristic (entry) pressure	ρ_d	1e5 variable	1e4	1e6	Pa
Van Genuchten parameter	m	0.36	0.5	0.4	-
References	-	Huang et al. (2021)	Huang et al. (2021)	k and Φ from Samper et al. (2008); others this study	-

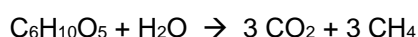
* Mortar porosity changes with cement carbonation and aggregate cement reaction

Table 4-20: Liquid and gas properties used in the UFZ numerical model

Parameter	Symbol	value	Unit
Liquid viscosity	μ_L	1e-3	Pa s
Liquid density	ρ_L	1000	kg m ³
Gas viscosity	μ_G	9e-6	Pa s
Pore diffusion coefficient for gas	D_G	3.3e-7	m ² s ⁻¹
Pore diffusion coefficient for liquid	D_L	3e-9	m ² s ⁻¹

4.3.2.2 Chemical reaction model

(Microbial) Degradation of organic waste resulting in the production of CO₂ and CH₄. The degradation process is further divided into two groups. Group 1 organics were modelled in terms of cellulose degradation which can be described in the presence of water according to the following overall chemical reaction:



The degradation of the slowly degrading organics (polystyrene, plastic) in Group 2 was tentatively represented in terms of the following chemical reaction:



The total gas generation rate Q_o^w [mol a⁻¹] for each organic waste group is computed with a first-order kinetic approach:

$$\frac{\partial m(t)}{\partial t} = -m(t) \cdot \lambda \cdot R \quad (4-18)$$

$$Q_o^w = m(t) \cdot k_d \cdot R_\varphi^w \quad (4-19)$$

where $m(t=0)$ refers to the initial mass of organic material [kg], λ denotes the degradation rate [a^{-1}] and R_{φ}^w is the chemical reactivity in respect of relative humidity φ of the gas phase. The approach in this study accounts for the slowing down of chemical reactions at dry conditions. For calculating R_{φ}^w we use a linear function for the range [$\varphi_{min}=0.6$, $\varphi_{max}=1$], which is adapted from Suckling et al. (2011):

$$\left(R_{\varphi}^w = (\varphi - \varphi_{min}) / (\varphi_{max} - \varphi_{min}) \forall \varphi \in \forall [\varphi_{min}, \varphi_{max}] \right) \quad (4-20)$$

$$R_{\varphi}^w = 0 \forall \varphi < \varphi_{min}$$

Table 4-21: Organic degradation parameters, gas generation rates and rates for water consumption for two waste groups from Huang et al. (2021)

Symbol	Unit	Group 1 (Cellulose)	Group 2 (Polysterene)	Reference
$m(t=0)$	kg	24.7	51.8	Huang et al. 2021
λ	a^{-1}	$1.89 \cdot 10^{-3}$	$6.51 \cdot 10^{-5}$	Wieland et al. 2018, Wieland et al. 2020
k_D	$mol\ kg^{-1}\ a^{-1}$	0.07	0.005	Leupin et al. 2016
Rate for CO ₂	$mol\ kg^{-1}\ a^{-1}$	$k_D \cdot 3/6$	$k_D \cdot 3/8$	Huang et al. 2021
Rate for CH ₄	$mol\ kg^{-1}\ a^{-1}$	$k_D \cdot 3/6$	$k_D \cdot 5/8$	Huang et al. 2021
Rate for water consumption	$mol\ kg^{-1}\ a^{-1}$	$k_D \cdot 1/6$	$k_D \cdot 6/8$	Huang et al. 2021

The degradation parameter for the organic waste is listed in Table 4-21. The anoxic corrosion affects the steel surfaces of the drum hull, the inner tube and the waste:



For the metal waste the hydrogen production Q_h^w is a function of the steel surface area per volume, which is $A_v = 71.73\ m^2\ m^{-3}$ corresponding to a total steel surface area of $9.37\ m^2$ per drum. The hydrogen production rate is set to $q = 0.373\ mol\ m^{-2}\ a^{-1}$ corresponding to a corrosion rate of $2.0e-6\ m\ a^{-1}$ (Wieland et al., 2020).

$$Q_h^w = A_v \cdot q \cdot R_{\varphi}^w \quad (4-21)$$

The hydrogen flux f_h generated at the steel surfaces of the drum hull and the inner tube we obtain:

$$f_h^{\beta} = q \cdot R_{\varphi}^{\beta} \cdot R_{pH}^{\beta} \quad (4-22)$$

The exponent β refers to either waste (w) or mortar (m) material that is attached to the steel surface. R_{pH}^w is set to 1. For the mortar, the chemical reactivity R_{φ}^m is adapted from Bazant and Najjar (1972) and R_{pH}^m is adapted from Wieland et al. (2020):

$$R_{\varphi}^m = (1 + (7.5 - 7.5\varphi)^4)^{-1} \quad (4-23)$$

$$\left(\begin{matrix} R_{\phi}^m = 1 & \forall \text{ pH} < 10.5 \\ R_{\phi}^m = 0.01 & \forall \text{ pH} \geq 10.5 \end{matrix} \right) \quad (4-24)$$

The water availability also effects the mortar degradation. Therefore, the chemical reactivity R_{ϕ}^m is also multiplied with the quartz dissolution rate (for aggregate-cement reaction) and with the amount of CO_2 used for the cement carbonation reaction for each time step (see Huang et al. (2021) for further descriptions of the mortar degradation model). In Figure 4-7 an overview of the chemical processes and their couplings is given. In this model we use the mortar composition as given in section 4.1

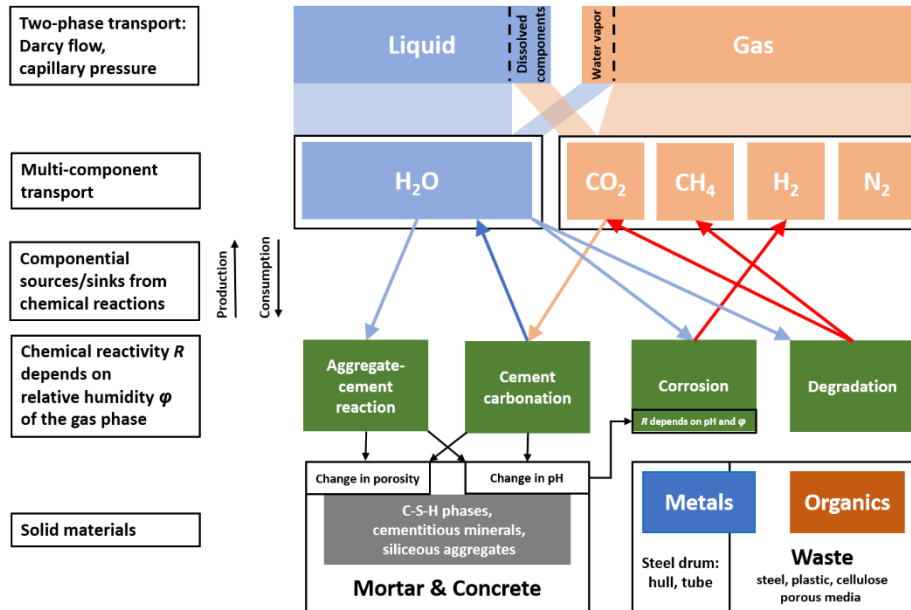


Figure 4-7: Chemical process coupling

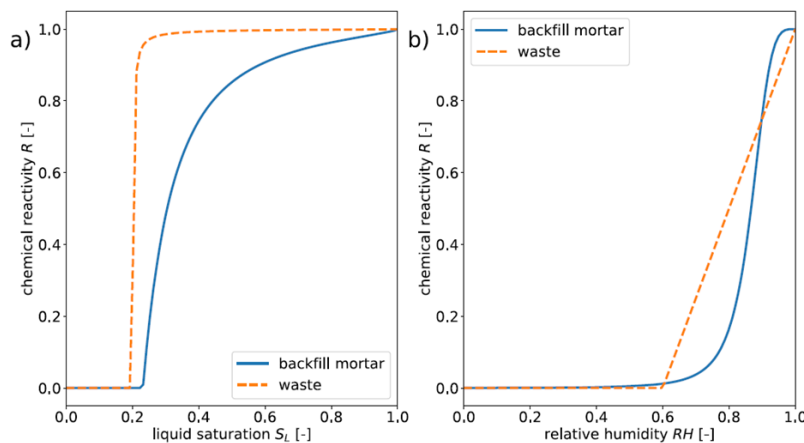


Figure 4-8: Chemical reactivity R^{β} computed with equation (4-20) (4-20)and (4-23) (Huang et al., 2021)

4.3.2.3 Numerical model configuration

The two-dimensional modelling domain covers one half of the container because of the symmetry with respect to the middle axis (Figure 4-9). Therefore, at the middle axis we apply no boundary condition leading to no mass flux here. At the other/remaining sides Dirichlet boundary conditions with a

hydrostatic pressure gradient are set to enable free flow conditions. The initial gas is a mixture of N₂ and H₂O vapor.

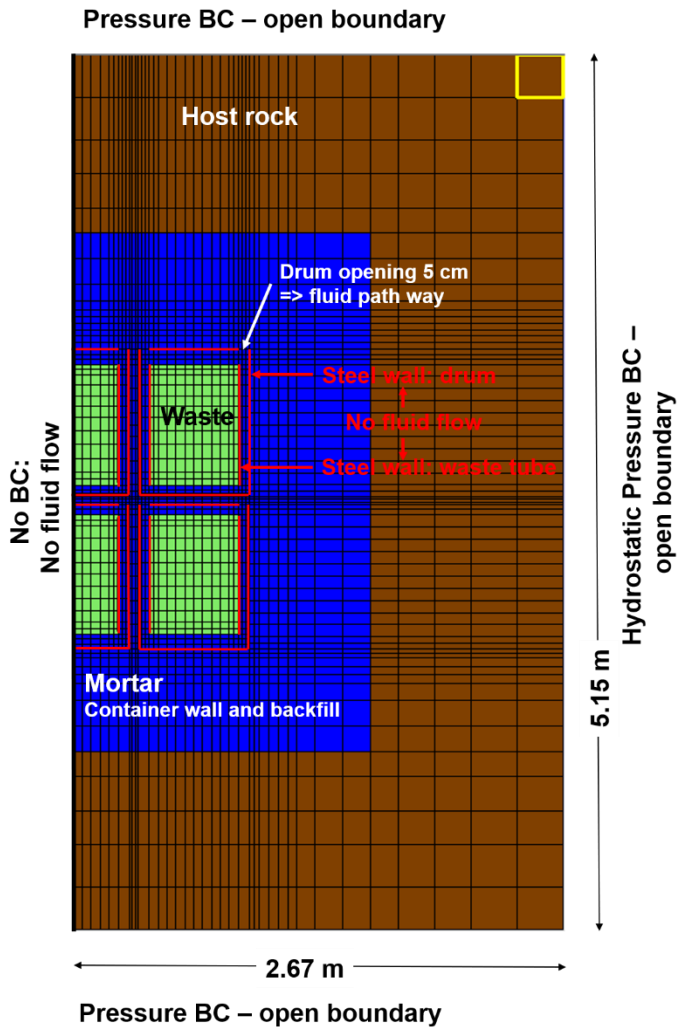


Figure 4-9: Numerical model configuration, the green colour shows the waste compartment and blue colour shows concrete and backfill mortar materials. The red lines show the impermeable drum walls and inner tube.

The initial liquid saturation is set to 0.9 for the back fill mortar, 0.33 for the waste and 0.996 for the host rock. At the domain boundary, the capillary pressure is set to a value that the corresponding liquid saturation there is set to 1. The physical background here is to assume a nearly fully-saturated host-rock formation, allowing abundant amount of water to be available throughout the entire life-span of the repository.

4.3.3 Models used by SCK CEN

The objective of the waste package model is to simulate the alterations in backfill mortar and concrete as a consequence of degradation of the organic waste which produces CO₂ that leaks from the waste drum via small gaps (similar as in section 4.3.2). The main difference with the approach described in section is that (i) water is always available and fully saturated conditions are preserved during the complete calculation time, (ii) no pressure gradients, thus no water flow and only pure diffusive transport phenomena, (iii) smaller domain, namely a single waste drum only with the surrounding container backfill material.

4.3.3.1 Conceptual model

Model geometry

The geometry consists of a single drum with its detailed geometry (Figure 4-6) with the container backfill in the upper right corner of the disposal container (Figure 4-10).

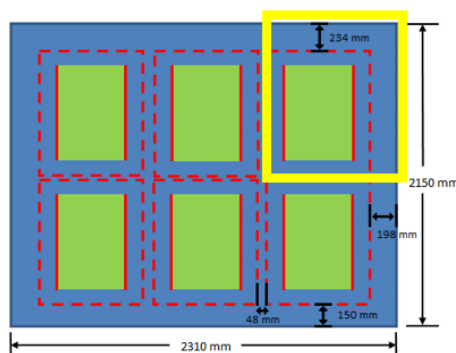


Figure 4-10: Disposal container with 6 waste drums. The model geometry is limited to area within the yellow box.

Model processes

Three reactive materials are discriminated in the model (Figure 4-11): (i) the waste zone consisting of organic material with kinetic degradation of the organic material (cellulose) water consumption is neglected (assuming water ingress is fast enough to counter water consumption), production of inert gases (CH₄) is neglected, (ii) the waste package backfill and (iii) the container backfill cementitious material. In these two latter materials, geochemical alterations (mainly due to interaction with CO₂ originating from the degradation of organics) are calculated with a thermodynamic model for cement chemistry. The steel of the drum wall and the tube (thickness of 2mm, Figure 4-6) is considered non reactive and is therefore excluded from the simulation domain. A opening of 5 cm at both sides of the drum is present to allow exchange of matter between the inside and outside of the drum (similar to the model described in section 4.3.2, see Figure 4-9).

As no water consumption is considered, fully saturated conditions were assumed during the whole simulation period without any water flow. Only diffusive transport in the aqueous phase is relevant. Feedback of geochemical reactions on transport properties is neglected.

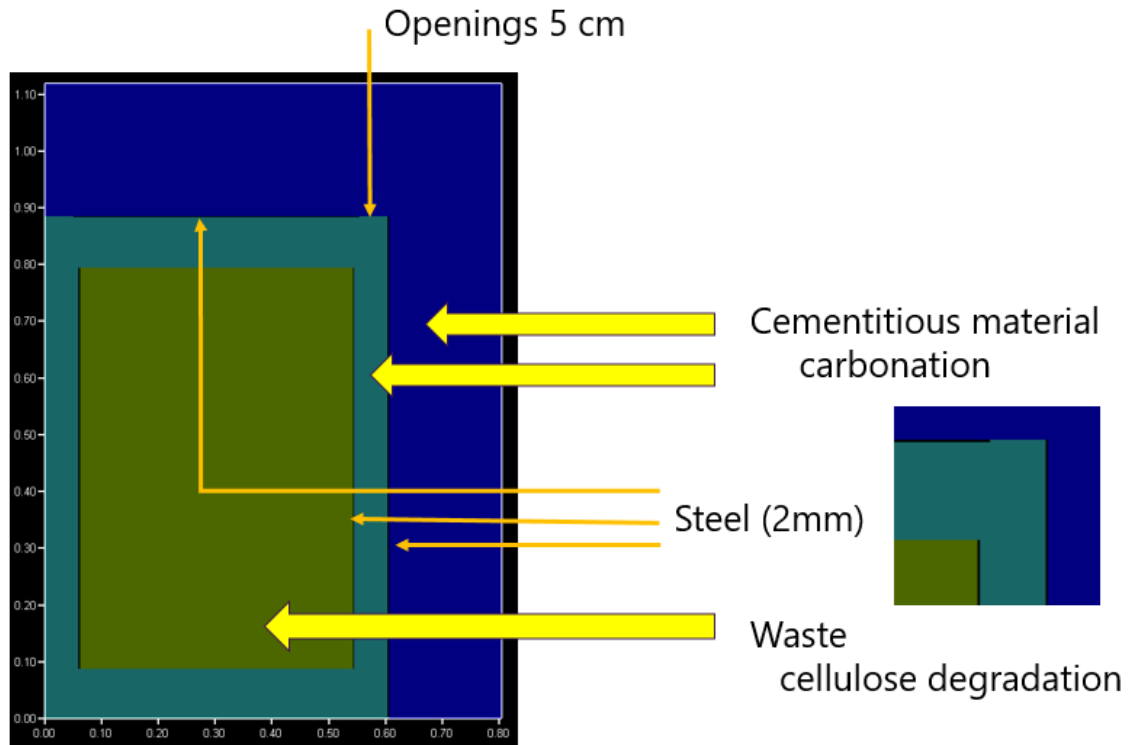


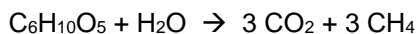
Figure 4-11: Details on conceptual model. The green area represents the waste zone (cellulose), the light blue area represents the waste drum backfill, and the dark blue area represents the container backfill. The steel of the drum (black zones) are excluded from the model.

4.3.3.2 Mathematical model

A 2D coupled-reactive diffusive transport model is considered. The transport properties are:

- Porosity of 0.2 and 0.0995 for the waste zone and the cementitious materials, similar as the value Table 4-19, which is used by the UFZ model.
- The aqueous diffusion coefficient for all components and species is 1×10^{-9} m²/s. The pore diffusion coefficient is calculated with the Millington and Quirk (1961) model.

Cellulose degradation is described by following reaction equation,



neglecting the consumption of H₂O and the production of CH₄. The rate equation is identical to that in Eq. (4-18) with parameters as given in Table 4-21.

The chemical reactions in the cementitious backfill are mainly due by the ingress of dissolved CO₂ and the reaction of it with first portlandite and later on with C-S-H phases leading to calcite precipitation. A fairly simple cement model is used here but capturing the key processes of reaction with these two phases. The hardened cement paste consists initially only of a C-S-H phase with high Ca/Si ratio (represented by a phase CSH1.6 with a Ca/Si ratio of 1.6) and calcite. The initial amounts are equal to those used in section 4.3.2. Upon reaction with CO₂, also calcite will further precipitate; to represent the decalcification of the C-S-H phase due to carbonation, a discrete phase model for C-S-H is used with, in addition of a C-S-H with a Ca/Si of 1.6, also phases with a Ca/Si of 1.2 and 0.8 (initial amount is zero) are included.

The components considered for transport are C(4), Ca, Si, H and O(0). Thermochemie (v10) is used as the thermodynamic database.

4.3.3.3 Numerical model

The generic coupled reactive transport model HPx (Jacques et al., 2018) as embedded in HYDRUS 5 (Simunek et al., 2024) is used for the numerical simulations. HPx couples the HYDRUS software for flow, solute transport and heat transport in saturated-variable porous media (Simunek et al., 2020a,b) with the geochemical solvers PHREEQC (Parkhurst and Appelo, 2013) and ORCHESTRA (Meeussen, 2003) via a non-iterative sequential approach (Jacques et al., 2006).

The simulation domain is discretized in an unstructured mesh with finer meshing at the interface between the waste zone and the waste package backfill material, and at the openings in the drums. In total, there are 9938 nodes and 19313 2D elements (Figure 4-12). Time steps were calculated according to the von Neumann condition. The total simulation time is 300 y.

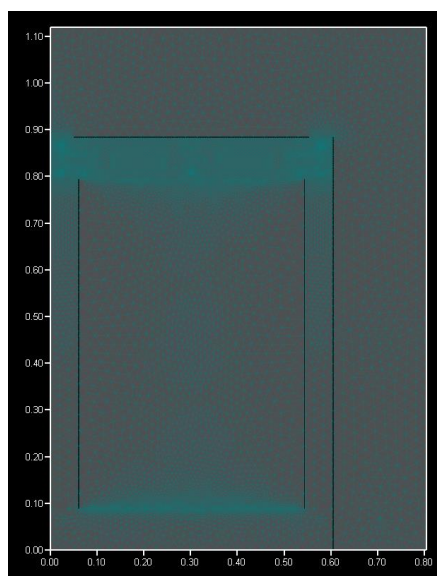


Figure 4-12: Discretization of the simulation domain.

4.3.4 Models used by COVRA

4.3.4.1 Conceptual model

For ILW/steel: Stefanoni et al., (2018) provided the evidence that the corrosion rate of carbon steel in (carbonated) cement-based materials decreases with decreasing water/binder ratio used to fabricate the mortar and decreasing relative humidity to which the reinforced mortar was exposed. Smaller water/binder ratios result in hardened mortar with a smaller porosity and lower relative humidity's result in a smaller fraction in pores being saturated. With decreasing relative humidity, first the larger pores become no longer filled with water since the capillary suction force of these large pores is smaller than the smaller pores. A smaller porosity as well as a smaller saturation degree results in a smaller possible flux of water available for anaerobic corrosion of steel in carbonated concrete.

In concrete that is not carbonated, cement minerals react with ingress CO_2 . The reaction products can be CaCO_3 and H_2O in case of portlandite $\text{Ca}(\text{OH})_2$. Reaction with CO_2 and CSH minerals results in a decalcified CSH mineral i.e. a CSH mineral with a smaller ratio in Ca/Si and also CaCO_3 . In section 3.2.3.1, it was assumed that completion of this decalcification consumes water based on mass balance. The requirement to consume water to complete decalcification may also provide the understanding why there is a maximum in the carbonation rate at a certain relative humidity. Initially, the carbonation rate increases as a function with decreasing relative humidity (see Figure 4-13) as the larger pores do not

have water and allow CO₂ to enter a cementitious specimen at a faster rate than at a saturated state. This access to CO₂ further increases with further decreasing relative humidity but the water required to complete decalcification of CSH minerals becomes more and more rare with decreasing relative humidity. Consequently, at a certain relative humidity, the carbonation rate decreases with decreasing relative humidity.

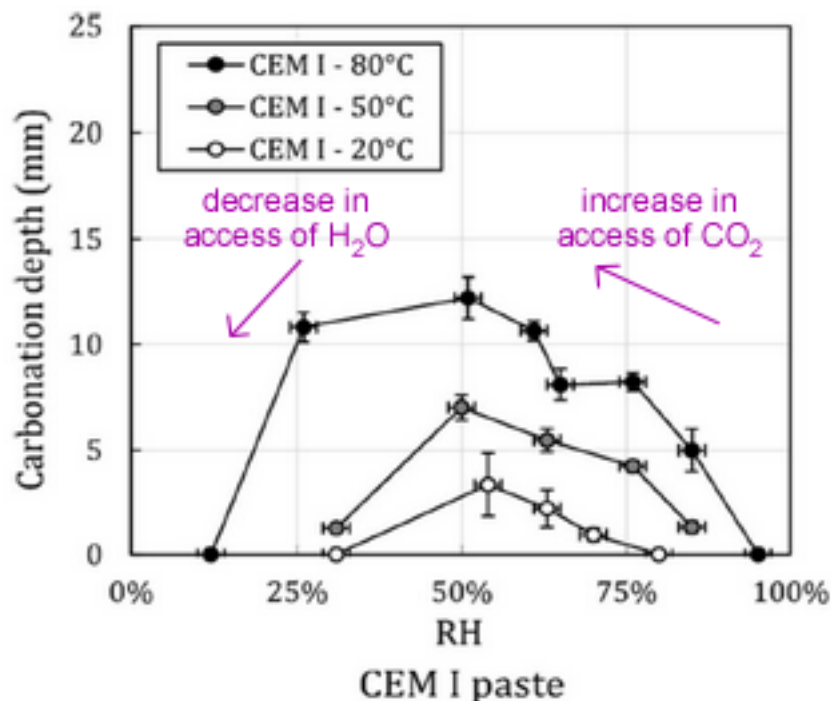


Figure 4-13: Carbonation after 7 days as a function of relative humidity from von Greve-Dierfeld, et al., (2020) when exposed to 50 vol% CO₂, paste with water / binder ratio of 0.4, additions in purple.

Anaerobic steel corrosion rates are usually determined from the hydrogen gas leaving an experimental set-up in which steel is exposed to a solution. This solution can be representative for a clay pore water, granitic pore water or cementitious pore water. The measurement of a constant hydrogen flux is representative for disposal of waste on the long-term, the so-called long-term corrosion rate. What needs to be assessed is whether there is sufficient supply of water through the concrete towards the waste. Hereto, a diffusion model for water is used in which the diffusion value for water decreases with decreasing saturation degree. Consequently, there can be different diffusion values for water inside a porous medium.

For ILW/organic: First, it needs to be assessed whether there is sufficient water available for biodegradation of organic waste. As explained in section 2.3, for most of the studies related to organic waste degradation, biodegradation is presented as a major degradation mechanism, producing significant amount of gases. These degradation processes require water as also explained in section 2.3. Most microbes require water activities higher than 0.9 (Swanson et al., 2018) i.e. a relative humidity of 90% or a maximum in suction pressure of 14 MPa. With the moisture storage function of COVRA's waste package concrete, it can be deduced that the saturation degree at 20°C is 0.8 at exposure of a relative humidity of 90%. The initial water content after fabrication is lower i.e. 0.7. The storage - usually at dry conditions - can further reduce the water content before disposal. Consequently, it would take some time during the post-closure phase to achieve the sufficiently wet conditions for biodegradation of waste, especially for indurated clay. Moreover, the organic waste is put in steel drums that are compacted. The moisture content of waste in these steel drums is limited. Waste acceptance criteria for to-be-compacted-waste require the moisture content to be less than 1% of the filled waste drum for

example at COVRA. The anaerobic corrosion of the steel drums also requires water but this corrosion process is possible at lower saturation degrees of concrete than microbial degradation of concrete. Consequently, it is therefore cautiously envisaged that first the steel drums will be anaerobically corroded before the organic waste can be biodegraded.

4.3.4.2 Mathematical model

The transport of water takes place by non-linear diffusion of water in the conceptual model. The diffusion equation for the transport of water to be solved is:

$$\frac{\partial w}{\partial t} = \nabla \cdot (D_w \nabla w) + R_w \quad (4-25)$$

where D_w is the diffusion coefficient for water as a function of the saturation degree derived from Millington and Quirk (1961) by assuming the same extrapolation with the saturation degree (S_w) as for the permeability:

$$D_i = \frac{1}{16} D_{0,w} \times \varphi^4 \times S_w^{10/3} \quad (4-26)$$

A pre-factor of $1/16$ was needed in order to have a well comparison with the measurements and predictions for concrete exposed to a relative humidity between 40% and 100% with a (capillary) porosity of 13% and 21% (see section 3.2). The value of $1/16$ can be regarded as part of the tortuosity related to the size and distribution of pores. The tortuosity for dissolved species is in the $S_w^{10/3}$ -term. $D_{0,w}$ values for diffusion of water in water are temperature dependent.

Examples of sources of CO_2 are air to which a waste package is exposed during storage and CO_2 evaporated from the clay pore solution until the pressure of water in the excavated damaged zone is equal to the formation pressure. R_w in equation 4-25 can be a source term for water when the reaction between ingress CO_2 and a cementitious mineral such as portlandite results into the production of water. R_w can also be a sink term for water when the reaction between ingress CO_2 and a cementitious mineral such as a CSH mineral low in calcium result into the consumption of water. Overall consumption of water is assumed to take place for the experimental results with the investigated waste package concrete in section 3.2.3.2. As a first approximation, no water consumption by carbonation of concrete is assumed i.e. $R_w=0$.

The concrete container with ILW steel is presented in section 2.1.2. Figure 4-14 shows the geometry in 2D used for the modelling and the boundaries used to solve equation 4-25 are highlighted. The outer boundary (Dirichlet condition) is a water concentration. The inner boundary (Neumann) is a water flux leaving the concrete simulating the consumption of water by anaerobic corrosion of ILW steel.

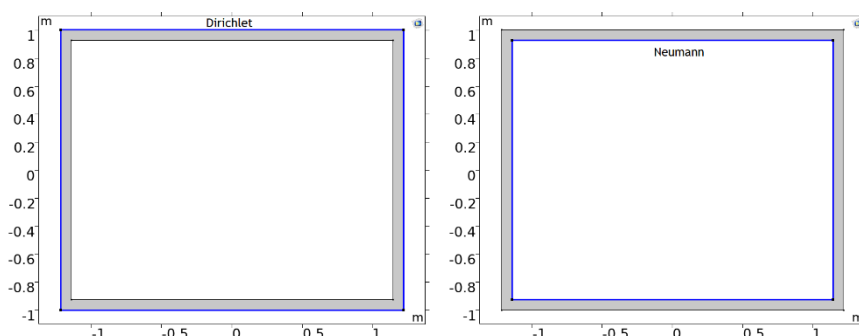


Figure 4-14: Boundaries used for the 2D modelling without indurated clay, left a water concentration, right a water flux leaving concrete.

The use of the diffusion coefficient requires the gas pressure to remain below the gas entry pressure of the porous medium. The molar hydrogen generation rate is equal to the molar water consumption rate

assuming that anaerobic corrosion leads to the formation of magnetite (see section 4.3.4.1). The flux of water leaving concrete is therefore equal to the flux of dissolved hydrogen into the concrete. Hydrogen is quite insoluble and a hydrogen gas pressure will develop.

The amount dissolved hydrogen becoming gaseous hydrogen is determined by the hypothetical gaseous pressure from the dissolved hydrogen molar concentration, $p_{H_2_from_dissolved}$ being larger than this pressure from the molar gaseous hydrogen molar concentration, $p_{H_2_from_gas}$. This pressure from the molar dissolved hydrogen concentration $[H_{2,diss}]$ is expressed by:

$$p_{H_2_from_dissolved} = [H_{2,diss}] \times K_{Henry(H_2,T)} \times \frac{1}{\varphi} \times \frac{1}{S_w} \quad (4-27)$$

where K_{Henry} is e.g. at 20°C: 1237 L atm/mol, φ is the porosity and S_w is the saturation degree. This pressure from the molar gaseous hydrogen concentration $[H_{2,gas}]$ is expressed by:

$$p_{H_2_from_gas} = [H_{2,gas}] \times R \times T \times \frac{1}{\varphi} \times \frac{1}{S_w} \quad (4-28)$$

where R is the molar gas constant 8.314 J mol⁻¹K⁻¹ assuming ideal gas and T is temperature. The reaction of dissolved hydrogen to become gaseous hydrogen is an interplay between different sizes of pores. As the smaller pores are dehydrated at smaller relative humidity than the larger pores, the smaller pores contain the dissolved hydrogen. The larger pores ensure the transport of gaseous hydrogen through concrete. Although the distribution in size of pores in waste package has been determined (Mladenovic et al., 2024), it would be a too hard exercise computationally to calculate the evaporation of dissolved hydrogen from the water with the smaller pores as a function of the saturation degree of concrete. As a first approximation, a single size in pores is assumed:

$$R_{H_2,gas} = 4\pi r_{pore} D_{H_2,diss}(S_w, T, \varphi) \quad (4-29)$$

The single radius used in the modelling is the critical radius. The number of pores (N_{pore}) is determined by the porosity as explained in section 3.2.3. The transport of gaseous hydrogen is determined by:

$$\frac{\partial [H_2(gas)]}{dt} = \nabla \left(D_{H_2,gas} \nabla H_2(gas) \right) - R_{gas,H_2} [H_2(diss)] N_{pore} \quad (4-30)$$

This transport equation is solved with no flux at the side of the waste package where dissolved hydrogen is generated and the gaseous hydrogen content similarly as described for gaseous oxygen and carbon dioxide in section 3.2 but then with a partial pressure of hydrogen in air i.e. 5.5×10⁻⁷ atmosphere.

Experimental support of a diffusion coefficient for gas was gathered for oxygen and the same description is used for hydrogen. The only difference is that the temperature dependent value for diffusion of gaseous oxygen is assumed to be 10.000 times the value for dissolved oxygen in water and the temperature dependent value for diffusion of gaseous hydrogen in air is assumed to be 10.000 times the value for dissolved hydrogen in water. This transport equation is solved with the flux of dissolved hydrogen equal to the water consumption rate and the dissolved hydrogen similarly as described for dissolved oxygen and carbon dioxide in section 3.2. The experimental support for this diffusion coefficient is the thickness and extent of reacted zones in concrete for the two different porosities (13% and 21%) and two different temperatures (5°C and 20°C) in a reaction rate that is also defined by the size of the reacted mineral and number of minerals with that size per volume.

The transport of dissolved hydrogen is determined by:

$$\frac{\partial [H_2(diss)]}{dt} = \nabla \left(D_{H_2,diss} \nabla H_2(diss) \right) + R_{gas,H_2} [H_2(diss)] N_{pore} \quad (4-31)$$

The diffusion coefficient of a dissolved gas is similar to diffusion coefficient of water except that the temperature dependent value of diffusion of dissolved gas in water is different from this temperature dependent value of water in water.

The large variety in diffusion values as a function of time and space as obtained from the diffusion coefficients makes the calculation computationally expensive. Therefore, 1D calculations have been performed. Figure 4-15 shows as a function of time: the calculated saturation degree of water, diffusion

value for gaseous hydrogen and the associated developed hydrogen pressures for a water consumption / hydrogen generation rates of $5 \times 10^{-8} \text{ mol m}^{-2} \text{ s}^{-1}$ assuming an initial water saturation of 70%.

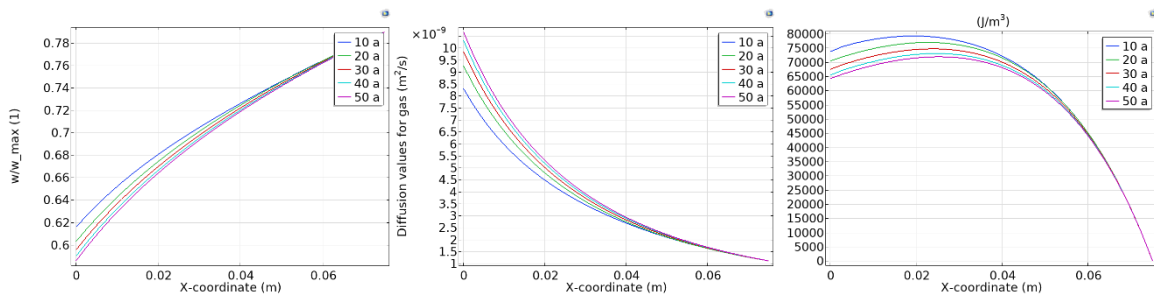


Figure 4-15: Saturation degree, diffusion values for gas and hydrogen gas pressure ($\text{J/m}^3 = \text{Pa}$) inside a wall of waste package concrete at 20°C when exposed to a relative humidity of at 75.47%. Parameters used in the simulations $r_{pore} = 3 \text{ nm}$; $N_{pore} = 1.15 \times 10^{24} \text{ m}^{-3}$. $D_{0,w}(20^\circ\text{C}) = 2.032 \times 10^{-19} \text{ m}^2 \text{ s}^{-1}$; $D_{0,H2,diss}(20^\circ\text{C}) = 4.89 \times 10^{-9} \text{ m}^2 \text{ s}^{-1}$.

The initial saturation degree is assumed to be 70% inside the waste package wall since the water content of a waste package content after fabrication has been estimated to be 70% in section 3.2.1.1. The saturation degree inside this wall is approaching a steady state after 50 years. The diffusion value for hydrogen gas as a function of time and space will increase until a steady state is formed. The hydrogen pressure inside the waste package wall will decrease as a function of time due to this increase in diffusion value for hydrogen gas as the gas transport is faster with decreasing saturation degree. Most importantly, the hydrogen gas pressure will not exceed gas entry pressure of 49 MPa (see Table 4-22) inside the waste package concrete wall. Consequently, the developed diffusion model for water may be assumed with the waste package parameters obtained from COVRA waste package concrete.

For a disposal cell with indurated clay, the water availability for the waste package concrete is competing with water for the healing of cracks in the excavated damaged zone for the first thousands of years, the influx of water from the clay into waste package concrete is smaller than exposure to a relative humidity of 75%. The healing of cracks is modelled here as re-saturation. Again, the diffusion equation to be solved is equal to equation 4-25 except that the initial and boundary conditions are different to simulate the transport of water in the concrete of the waste package within a disposal cell with indurated clay. Figure 4-16 shows the boundaries and Figure 4-17 shows the initial values.

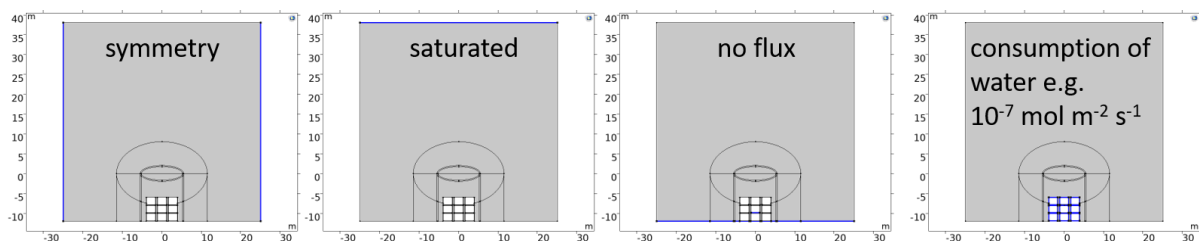


Figure 4-16: Boundaries used in the 2D modelling with indurated clay, Dirichlet (saturated), Neumann (symmetry, no flux and consumption).

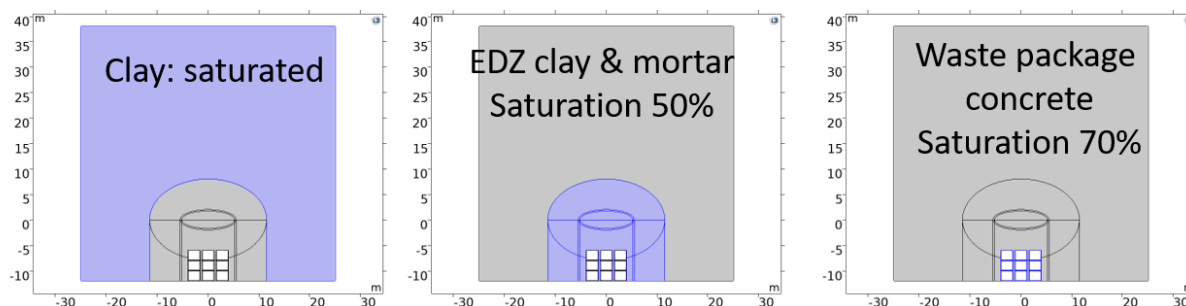


Figure 4-17: Initial saturation degrees in the 2D modelling with indurated clay.

4.3.4.3 Parameter values

Only fully saturated porous media are considered for an ILW disposal cell in clay in Task 4 (Samper et al. 2022). In representative disposal cells, cementitious materials are initially not saturated. For example concrete is initially unsaturated after hardening. But its initial saturation degree is guessed. For waste package concrete, there is sufficient evidence that initial saturation degree is 70% for fabricated waste package concrete with a porosity of 13% (see section 3.2.1). Waste packages are usually stored at dry conditions. This storage condition might cause an even lower saturation degree at start of disposal. Table 4-22 shows the parameters for the cementitious materials as input for the modelling.

Table 4-22: Input physical data from experimental results

	Genuchten					K_{sat} m ²	$D_w(S_w=1)$ m ² s ⁻¹	$D_{w,ch}$ m ² s ⁻¹
	α (20°C) × 10 ⁻⁴ m ⁻¹	1/ α MPa	n (m)	ϕ	r_c × 10 ⁻⁹ m			
waste package concrete	2.0	49	2.0 (0.50)	0.13	3.0	7.3×10 ⁻²⁰	8.3×10 ⁻¹²	3.0×10 ⁻¹³ $S_w=0.4$
cementitious backfill	8.2	12	1.7 (0.41)	0.21	20	2.2×10 ⁻¹⁸	1.6×10 ⁻¹¹	6.6×10 ⁻¹⁴ $S_w=0.2$

$D_{0,w}(20^\circ\text{C})=2.023\times 10^{-9}$ m²/s, s_{ch} is saturation degree at a relative humidity of 40% and associated diffusion value. Genuchten parameters and K_{sat} as described in Mladenovic et al. (2024). Diffusion values at 20 °C see section 3.2.1

The porosity’s for waste package concrete and backfill have been taken from COVRA’s samples as experimental support is available for the diffusion coefficients for water in the range of relative humidity between 40% and 100% ($S_w=1$). The saturation degree in equilibrium with a relative humidity of 40% is larger for a less porous medium.

The reference value for the water Callovo-Oxfordian clay is 4×10^{-21} m² (Levasseur et al., 2021). A value of 4×10^{-20} m² is proposed in Samper et al., (2022) i.e. a ten times larger value. The main characteristic of the Excavation Damaged Zone in indurated clays such as Callovo-Oxfordian is the low saturation degree of about 50%. As only fully saturated porous media are considered for an ILW disposal cell in clay in Task 4, the impact of the Excavation Damaged Zone on the availability of water for the anaerobic corrosion of steel cannot be estimated with the parameters provided in Samper et al., 2022.

The main characteristic of a disposal cell with indurated clay is that the transport properties of the engineered porous media are larger than the transport properties in the clay host rock. In order to satisfy this main characteristic, as a first approximation, in the models used by COVRA, for indurated clay such as Callovo-Oxfordian clay, a ten times smaller diffusion value at saturation was assumed than for waste package concrete but the same value for porosity as waste package concrete was used in order to get some information on the impact of the clay and EDZ on the water availability.

4.3.5 Models used by BRGM

4.3.5.1 Numerical tools

MARTHE-PHREEQC is an extension of MARTHE (<http://marthe.brgm.fr/>), which has been upgraded by coupling with the chemical module of PhreeqC (Parkhurst and Appelo, 2013). The coupling algorithm is purely sequential: at each time step, MARTHE computes the hydraulic heads and the velocities in the whole domain. It then transports energy in order to determine the temperature field, and transports all the dissolved chemical elements considered. Then, geochemistry is computed using the PhreeqC module in each cell discretized.

4.3.5.2 Simulation scenario and model parameters

A 1D radial geometry was chosen based on the intermediate-level radioactive waste (ILW) described in Huang et al. (2021). The studied geometry (Figure 4-18b) was simplified from the more complex geometry studied by the authors (Figure 4-18a). The Figure 4-18a shows that a part of polymers and their products (e.g. small acids, complexing ligands and dissolved gases) are directly in contact with cement phases. Therefore, the steel considered in the 1D radial geometry was assumed as a porous and permeable media.

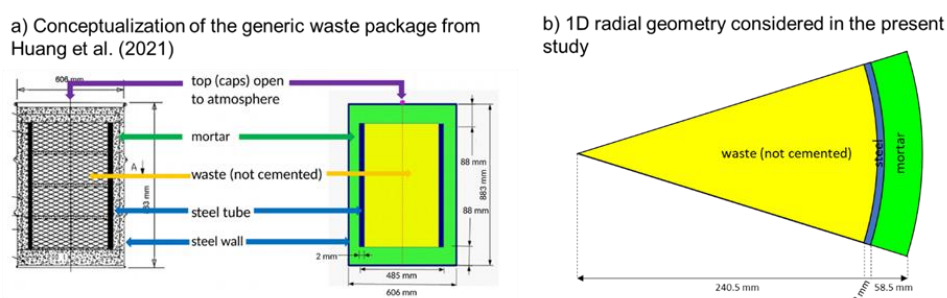


Figure 4-18: Geometries considered by (a) Huang et al. (2021) and (b) in the present study.

The currently capabilities of MARTHE-PHREEQC do not allow the multiphasic transport of gases (i.e. the formation of a bubble leading to a liquid desaturation). Nevertheless, it is possible to arbitrarily set the liquid saturation at 50%. Although such a consideration constitutes a rough simplification of expected processes (e.g., gas formation and transport), the modelling strategy allowed the identification of main alteration fronts due to the production of the gas phases: $\text{CO}_2(\text{g})$, $\text{HCl}(\text{g})$ and $\text{CH}_4(\text{g})$ by polymer radiolysis as well as $\text{H}_2(\text{g})$ from iron corrosion under anaerobic conditions. Additionally, organic molecules released in the aqueous phase (i.e. hydrolysis) interacted with cement phases. Such a process was not considered in the study of Huang et al. (2021), partially because the Swiss repository concept involves dry drums.

The physical parameters (e.g. permeability, porosity etc.) were extracted from Huang et al. (2021). Overall, considered materials were consistent with works carried out in the framework of the subtask 3.2 of ACED. Thus, a pH dependence of the corrosion rate was assumed. Moreover, a CEM I was selected rather a mortar. Regarding chemical interactions, the main differences arise from the introduction of polymer degradations, which were detailed earlier. Initial amounts of cellulose and PVC considered for the modelling application are reported in Table 4-23. The amount of PVC is calculated

considering a cellulose/PVC ratio = 4, according to Advocat et al. (2014). Following these authors, the amount of phthalates corresponds to the industrial PVC plastunion composition.

BRGM extracted degradation model for cellulose (section 3.3.3) and PVC (section 3.3.4) by hydrolysis and radiolysis from literature and experiment carried out in CORI.

Table 4-23: Amounts of initial organic polymers assuming a porosity of 0.33.

Material		mol L ⁻¹ of solution	mol L ⁻¹ of rock
Organic waste / Cellulose (C ₆ H ₁₀ O ₅)		3.331	1.10
PVC		23.027	7.60
Phthalates		4.388	1.45

4.4 Results of the modelling cases at waste package scale

The calculations at the waste package level in task 3.3 should be complementary to those in task 4, and allow conclusions for task 4. The models used in task 4 are explained in Samper et al. (2020).

The reference system is the one described in section 4.1. The parameters can be varied for the modelling of task 3.3, to focus on a specific location or process.

4.4.1 Modelling cases and results by PSI

PSI modelled both waste sorts, organic waste in 200l drums and metallic (decommissioning) waste in concrete containers with help of so-called mixing-tank models. These models allow to calculate evolution of a homogenized waste package considering time-dependent internal (or external) processes, namely the degradation of organic matter, the corrosion of steel, the dissolution of aggregates in cementitious materials and the consumption (or release) of water by reactions. The models ignore the effects of liquid saturation, transport of water in the drum, transport in aqueous and gas phase, and spatial material heterogeneities. Therefore, they will not provide a very realistic evolution in time but give information on overall mass balances and possible evolution pathways. Important information gained from such models are for example the amount of external water needed to drive internal reactions, or the possible amount of gas released for given kinetic parameterizations.

4.4.1.1 Organic waste: mixing tank calculations

Setup and initial conditions

For the simulation of an organic waste package (see Section 4.1.2), a thermodynamic system was created with help of GEM-Selektor. The system in Table 4-24 contains the waste materials (cellulose, steel/iron), the drum itself (steel/iron), and the unhydrated infill mortar (water, cement CEM 42.5, “mikropoz” micro silica, and aggregates). For the starting setup, the infill mortar materials except the aggregates are equilibrated to get the hydrated water. The resulting initial water phase composition is given in Table 4-25 and the (solid) phase composition of the waste package is given in Table 4-26.

Table 4-24: Input for waste package modelling.

Property	Name	Quantity	Units	Remarks
xa_	Aqua	56100	g	Water for hydration of infill mortar
xa_	NaCl	7.5e-05	g	Account for non-zero Cl
xa_	OPC-Norm	92250	g	A 'compos object' with composition of CEM 42.5
xa_	SiO2	187500	g	Includes “mikropoz” and reactive aggregate
xd_	cellulose	370.048	M	Organic waste
bi_	Fe	812.965	M	Represents all steel/iron in the waste package
bi_	Inrt	0	g	Only needed for inert aggregate
dll_	cellulose	370.048	M	Fixes cellulose to initial amount
dll_	Fe	812.965	M	Fixes iron to initial amount
dll_	Qtz	461.851	M	Fixes aggregate amount for kinetic control...amount is not identical to input of Qtz (as mikropoz is reacted)

The initial equilibrated system contains still some free water (14.55 kg or 14.54 l) that was not consumed during hydration. The total volume of all phases is about 192 l, which is smaller than the assumed total volume of 216 l for the “200 l drum”. This indicates that a considerable part of the ‘porosity’ in the drum is not water filled. The mixing tank calculations assume that as long as water is present in the waste package, it is homogeneously distributed and can be used for all reactions.

The composition and properties of the pore water, as well as the reacted solid (solid) phase composition is typical for such a mortar. The addition of silica fume (“mikropoz”) prevents the formation of portlandite. Still pH is high (>12.5) due to the presence of alkali ions (potassium).

Calculated conditions are reducing. Iron is exclusively bound in magnetite and ferrihydrite, because the thermodynamic setup does not contain the iron containing siliceous hydrogarnet solid solution present in CEMDATA 18. Inclusion of this phase would take up all the reactive iron (from CEM 42.5) in the initial system.

Table 4-25: Initial pore water properties of the equilibrated system.

Properties	Value	Element name	Concentration [mol/kg]
temperature [K]	298.150	Al	7.782929e-04
system volume [m ³]	0.192	C	1.068991e-04
system mass [kg]	441.250	Ca	4.285075e-04
pressure [Pa]	100000.0	Cl	8.820092e-08
porosity [-]	0.0758	Fe	1.452071e-07
pH [-]	12.670	H	1.106225e+02
pe [-]	-3.669	K	6.620882e-02
ionic strength [mol kg ⁻¹]	0.070	Mg	1.614208e-09
Eh [V]	-0.217	Na	9.428803e-04
		O	5.535910e+01
		S	3.885599e-03
		Si	3.985234e-04

Table 4-26: Initial equilibrated phase composition.

Phase	Volume [dm ³]	Mass [kg]	Mass fraction based on dry weight [-]
aq_gen	14.539	14.550	0.000000
CSHQ	52.528	123.596	0.289655
Cellulose	40.000	60.000	0.140614
Ettringite	8.319	14.768	0.034611
C2ASH8	4.409	8.535	0.020002
Calcite	1.634	4.428	0.010378
Iron	5.766	45.400	0.106398
Magnetite	0.00060	0.00313	0.000007
Ferrihydrite-mc	0.975	2.526	0.005921
OHhydrotalcite	1.764	3.551	0.008323
Inert_Quartz	1.564	4.142	0.009707
Quartz	60.322	159.750	0.374385

Time dependent evolution

The time-dependent evolution of the waste package was calculated with mixing tank models. Two model variants were calculated:

- A model with reactive quartz aggregates. The kinetic control of aggregate dissolution is described in Section 4.3.1.5.
- A model with inert (non-reactive) quartz aggregates. Technically the model parameterization for the calculation are used, only the reactive surface area was set to zero.

Figure 4-19 and Figure 4-20 shows the evolution of pH, the amounts of water, waste materials, aggregates, and amount of released gases for the variant with reactive aggregates and inert aggregates, respectively. The calculated evolution of mineral phase assembly is shown in Figure 4-21. In the organic waste package, the steel corrosion and aggregate dissolution seem fast processes which are finished

after about 300 years. Organic waste degradation is much slower and needs about 3000 years. It should be noted that steel corrosion is slow in the first 80 years. When pH drops below 12, steel corrosion is accelerated strongly. The opposite is visible for aggregate dissolution, which slows down with decreasing pH.

The pH decrease is mainly driven by organic waste degradation, which drives carbonation of cementitious infill by release of CO₂. At early times aggregate dissolution drives pozzolanic reaction, which also lower pH, but to a comparatively lower degree.

The amount of free water in the drum is increasing at early times, because carbonation of cement minerals (C-S-H) is releasing water. When pH drops below 12 and iron corrosion is strongly accelerated, the amount of water is dropping to about half of the initial value. Once all iron is corroded, water amounts are increasing again due to release by carbonation of cement minerals. Calculations for similar waste packages by e.g. Wieland et al. (2018) consume the available water quite quickly. The difference in behaviour can be tracked back to the following differences:

- The waste packages in this report contain much more fast-degrading organic waste, which increases significantly the water release due to carbonation.
- The waste packages in this report contains much less steel, which decreases the consumption of water due to iron corrosion.

The model variant with inert aggregates gives practically the same results; only a very small shift in time for pH dependent processes can be identified. This shows that carbonation caused by organic matter degradation is the dominating process for cement degradation and pH evolution in the drum.

The temporal mineralogical evolution is driven by the degradation of cellulose and the corrosion of steel. The degradation of cellulose is assumed to be pH independent with a fixed rate. The released CO₂ is immediately reacting with cement phases causing carbonation of cement. During this process, calcium is leached from cement phases to form calcium carbonate (calcite). The leaching of calcium first causes a change of Ca to Si ratio in the C-S-H phase and once the Ca/Si ratio is minimal a dissolution of C-S-H. In parallel, other cement phases (ettringite, hydrotalcite, strätlingite) are dissolved and zeolites are formed. Excess silica is precipitated as amorphous silica. The dissolution of C-S-H releases relevant amounts of water, which counterbalances the consumption of water by cellulose degradation and steel corrosion. Steel corrosion is accelerated once pH drops below pH 12 and is fastest for pH smaller 10.5 (cf. Figure 4-4 and Section 4.3.1.2). The corrosion of steel transforms Fe(0) to magnetite, which causes a strong increase in solids volume. During carbonation, high volume (low-density) cement phases are replaced by denser phases (calcite, amorphous silica). In the waste package, degradation of waste materials and waste cement interactions cause a net decrease of solid volume and increase of water, which is equivalent to an increase in porosity.

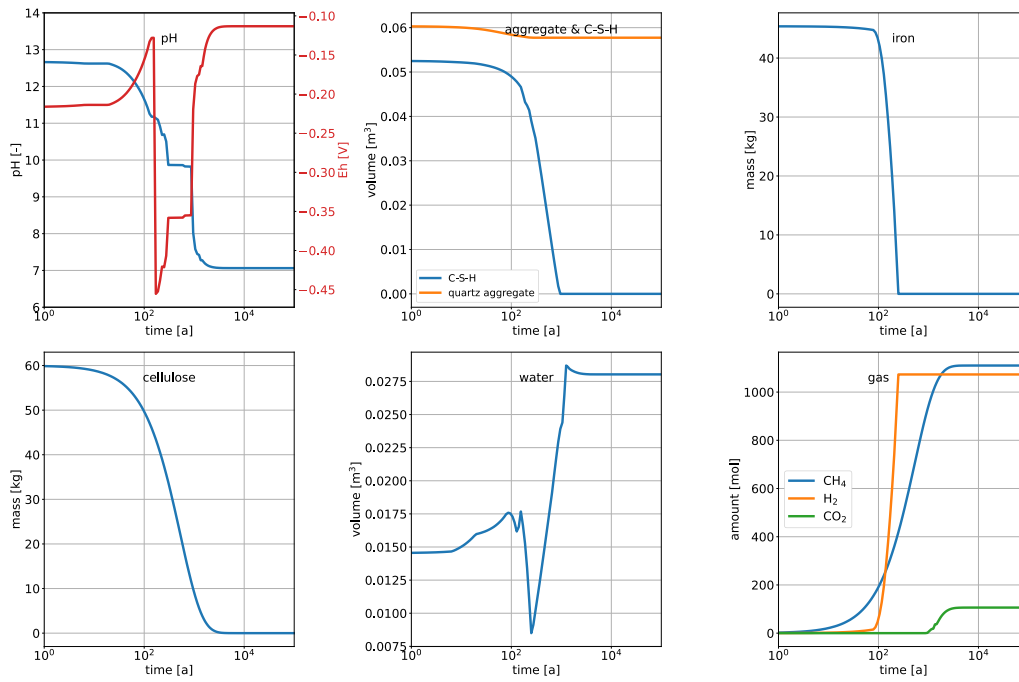


Figure 4-19: Time dependent evolution of pH (upper left), aggregate amount and C-S-H (upper right), iron (middle left), cellulose (middle right), liquid water (lower left), and gases (lower right) for the model variant with reactive aggregates.

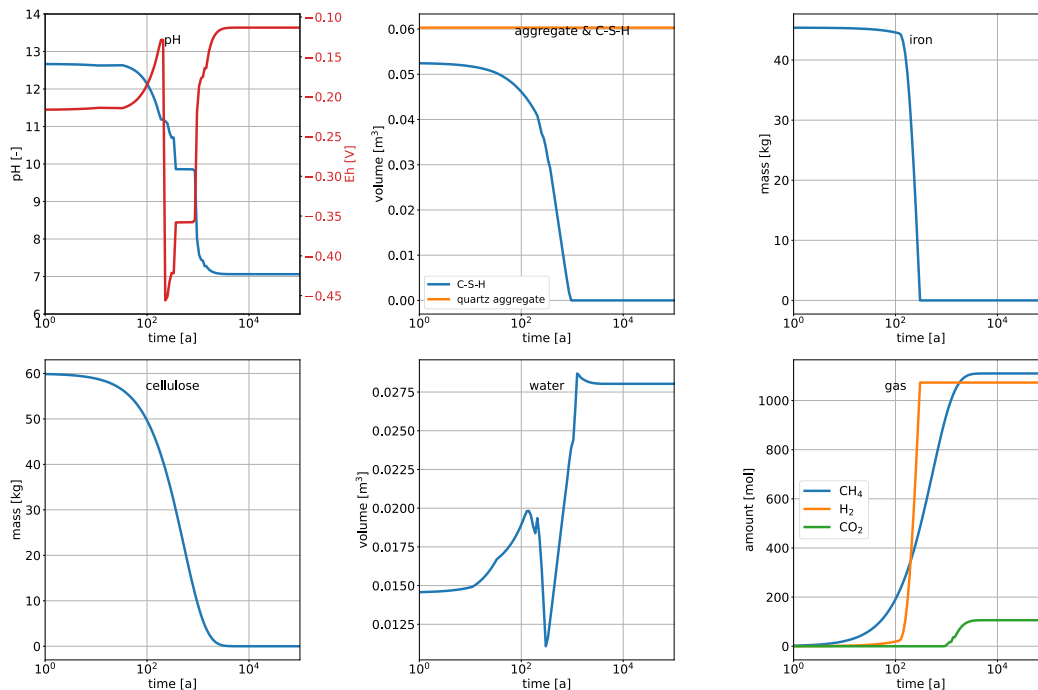


Figure 4-20: Time dependent evolution of pH (upper left), aggregate amount and C-S-H (upper right), iron (middle left), cellulose (middle right), liquid water (lower left), and gases (lower right) for the model variant with inert aggregates.

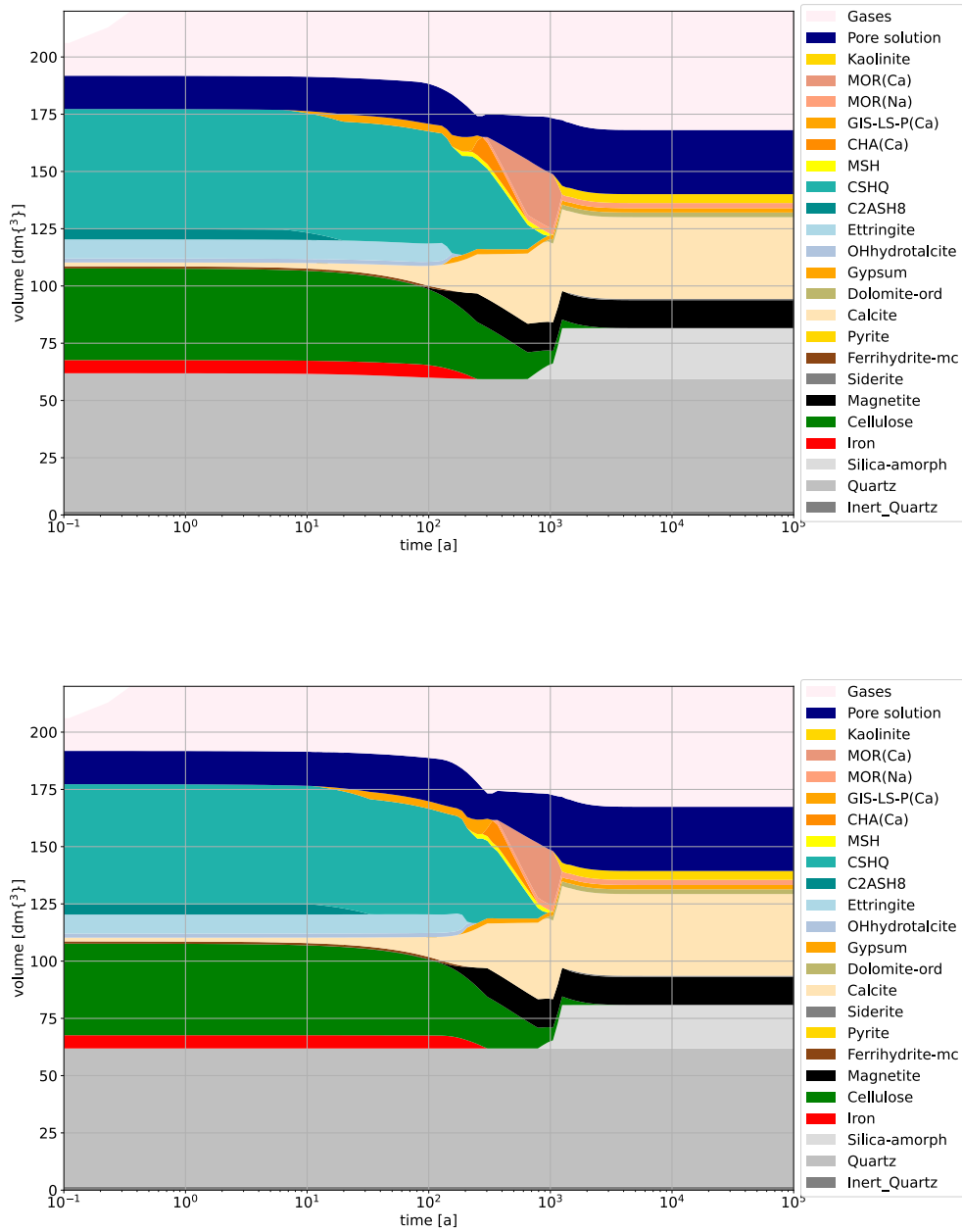


Figure 4-21: Temporal evolution of Phase volumes for reactive aggregates (top) and inert aggregates (bottom). Phase names are as in PSI/Nagra / CEMDATA/zeolite TDB. MOR: mordenite, GIS-LS-P: gismondine low-silica P zeolite, CHA: chabazite, MSH: magnesium-silicate-hydrate, CSHQ: C-S-H solid solution model following Kulik (2011), C2ASH8: strätlingite.

4.4.1.2 Metal waste mixing tank calculations

Setup and initial conditions

Like the thermodynamic setup of organic waste sort, input files for metal waste calculations were created in GEM-Selektor. The setup was then used to calculate the time-dependent evolution of the waste package with time.

First, from GEM-Selektor input for 1 l container concrete and for 1l infill mortar were imported. The bulk composition of both hydrated cementitious materials (incl. pore solution) were scaled to give the desired volumes of container wall concrete and infill mortar (see Table 4-1). Both materials were combined in one setup by summing up the corresponding bulk composition. The lower and upper constraints¹⁰ for kinetically constrained components (iron, quartz aggregate) were scaled by the same factors and summed to fix the amount of quartz aggregate to the desired initial aggregate amount. The steel waste and reinforcement steel was added as Fe(0) to the bulk composition. Upper and lower constraints for the iron phase were fixed to the initial amount of steel present in the waste package.

The resulting bulk composition was equilibrated taking into account the constraints for steel and reactive quartz aggregates. The calculated pore solution (Table 4-27) and mineral phase composition (Table 4-28) is a kind of average of container concrete and waste package infill mortar.

Table 4-27: Initial pore water properties of the equilibrated metal waste container system.

Properties	value	Element name	Concentration [mol/kg]
temperature [K]	298.15	Al	1.453339e-04
pressure [Pa]	100000.000	C	7.256766e-05
system mass [kg]	18621.594	Ca	1.045299e-03
system volume [m ³]	5.736	Cl	2.985116e-07
void space fraction [-]	0.0850	Fe	1.129918e-07
liquid volume fraction [-]	0.0485	H	1.101784e+02
ionic strength [mol kg ⁻¹]	0.157	K	1.548392e-01
pH [-]	13.067	Mg	1.475570e-09
pe [-]	3.462	Na	2.395594e-03
Eh [V]	0.204	O	5.517353e+01
		S	1.369551e-03
		Si	9.085930e-05

¹⁰ Upper and lower constraints bound the allowed mineral amount (dependent components) in the GEM formalism implemented in GEM-Selektor and xGEMS. They can be used to define out-of-equilibrium amounts of minerals, which are calculated externally with help of kinetic relations.

Table 4-28: Initial phase composition of the equilibrated metal waste container.

Phase	Volume fraction [-]	Mass [kg]	Mass fraction based on dry weight [-]
aq_gen	0.0485	290.421	---
CSHQ	0.215	2940.100	0.160388
Ettringite	0.039	411.048	0.022423
C4AcH11	0.025	322.263	0.017580
Calcite	0.033	528.055	0.028806
C3FS0.84H4.32	0.0099	180.567	0.009850
Iron (steel)	0.149	6967.000	0.380063
OHhydrotalcite	0.0082	98.730	0.005386
Inert_Quartz	0.0044	68.834	0.003755
Quartz (aggregate)	0.432	6814.574	0.371748

Time dependent evolution without considering waters influx from surrounding materials

The evolution of the metallic waste package is largely controlled by two processes, steel corrosion and aggregate-cement reactions. While steel corrosion is slowest at high porewater pH, dissolution of aggregate is fastest at high pH.

Both processes consume water to form reaction products (see mineral phase evolution in Figure 4-23) and consume the initially present 290 kg of free water in less than hundred years (cf. lower left of Figure 4-22). One should note, that the steel corrosion process has the much higher water consumption rate. In the first hundred years, the aggregate-cement reactions will not proceed far enough to lower the pH significantly (below 12 or even 11). The corrosion of several hundreds of kg steel and the dissolution of the iron bearing siliceous hydrogarnet will cause the formation of magnetite. Furthermore, hydrogen gas will be release in large quantities (Figure 4-22). Some cement phases will be dissolved, e.g monocarbonate, while straeltingite will be formed. Most importantly, the dissolution of several hundreds of kg silica aggregate will cause the transformation of C-S-H with high Ca/Si ratio into C-S-H with lower Ca/Si ratio.

After the water is consumed, all reactions in the waste package stop. One could speculate that in reality, waste packages will dry during interim storage and during the time, they are situated in ventilated emplacement caverns before repository closure. In addition, under atmospheric conditions oxic corrosion of steel will happen, which consumes the humidity in waste packages even faster (as oxic corrosion rates are much faster, see e.g. Duro et al. 2014).

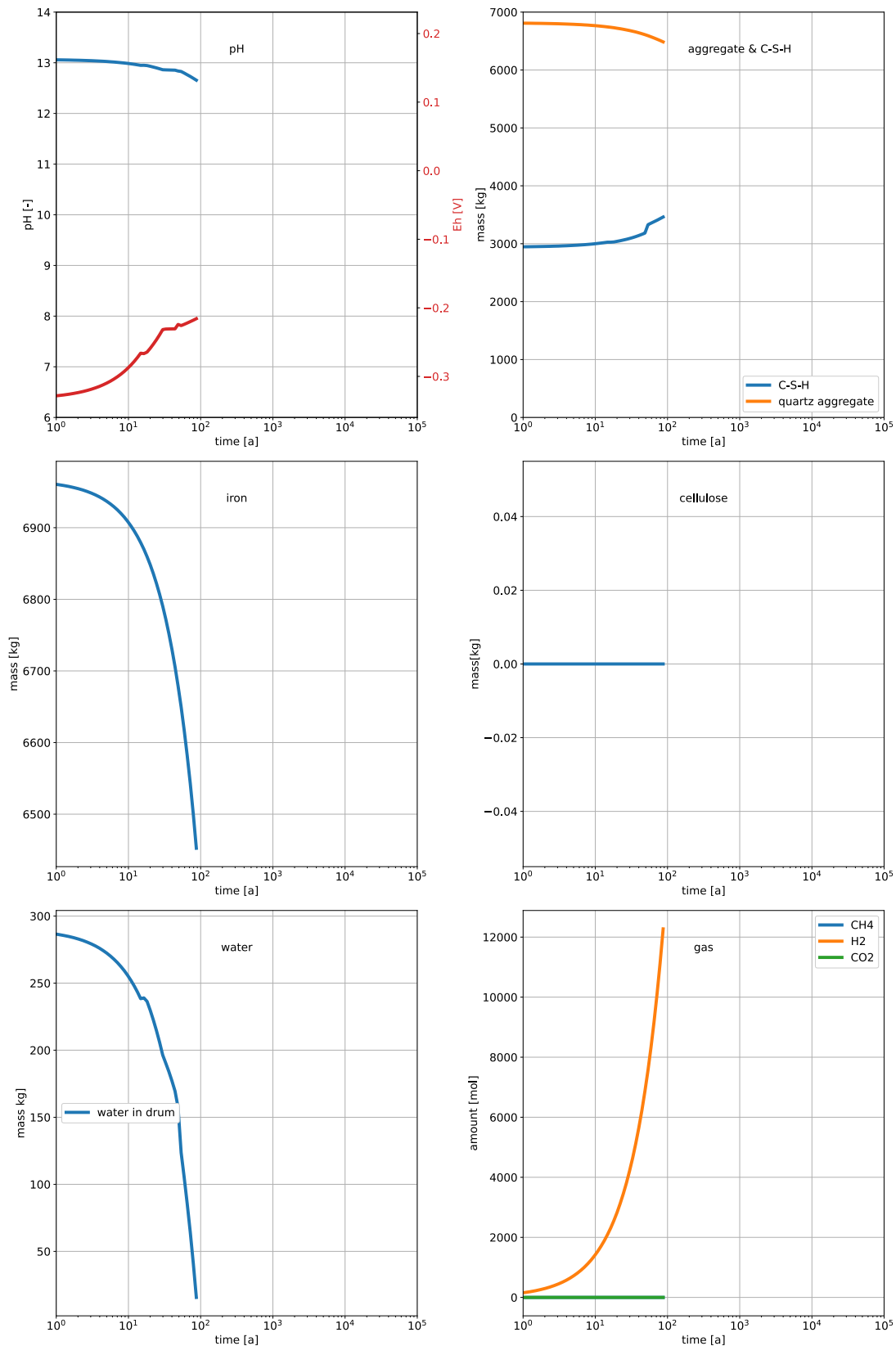


Figure 4-22: Time dependent evolution of pH (upper left), aggregate amount and C-S-H (upper right), iron (middle left), cellulose (middle right), liquid water (lower left), and gases (lower right).

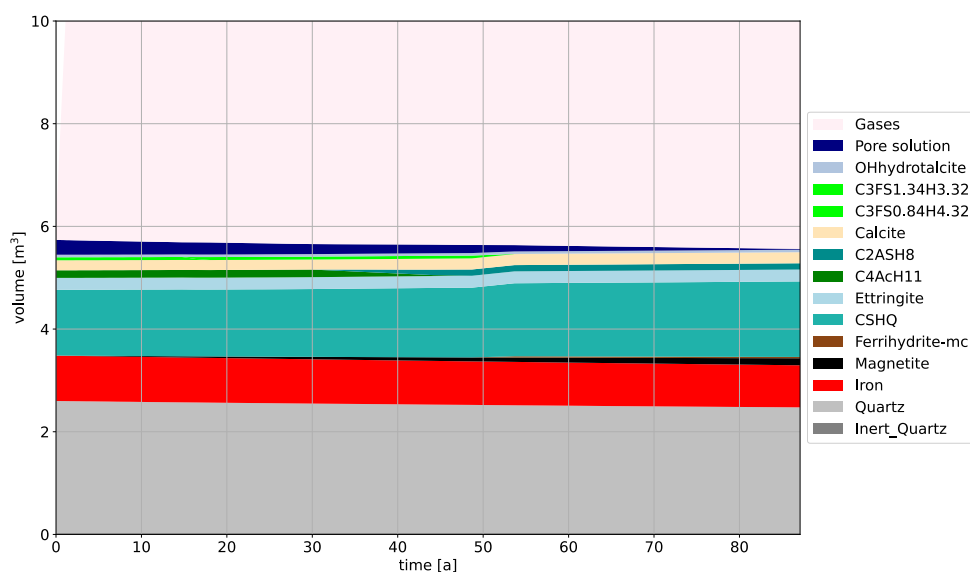


Figure 4-23: Temporal evolution of Phase volumes. Phase names are as in PSI/Nagra / CEMDATA/zeolite TDB.

Time dependent evolution with considering waters influx from surrounding materials

To evaluate the evolution of the waste sort if the waste package is placed in a water-filled environment, a second scenario was calculated in which the water present in the system is kept constant. This mimics a situation where water consumed by metal corrosion and aggregate-cement reactions is quickly replenished by influx of water into the waste package.

In total, about 3000 kg of water are needed to corrode all metal waste in the model waste form (“cumulative water added” in lower left of Figure 4-24). The small “shoulder” in the steel degradation visible in the amount of steel in Figure 4-24 is related to the implementation of two different steel surface to weight ratio for steel waste and the steel reinforcement of the container walls.

In this scenario the aggregate-cement interaction will proceed, until the solubility of the siliceous (quartz) aggregate is the same as the one of C-S-H with a low Ca/Si ratio. The cementitious material is now in a typical degradation III stage, which is characterized by the presence of C-S-H with low Ca/Si ratio (Berner, 1992; Jacques et al., 2010; Kosakowski et al., 2014). At this condition the pH is at about 10.5 (Figure 4-24) and all other cement phases are dissolved (Figure 4-25) and replaced by zeolite phases. In addition, gypsum is formed as result of ettringite dissolution.

After complete corrosion of all metals, the main corrosion product, magnetite, will occupy considerably more space than is available in the waste container (Figure 4-25). It can be assumed that in reality corrosion products will slow down or even block water transport towards metal surfaces. This process cannot be considered in the mixing tank approach.

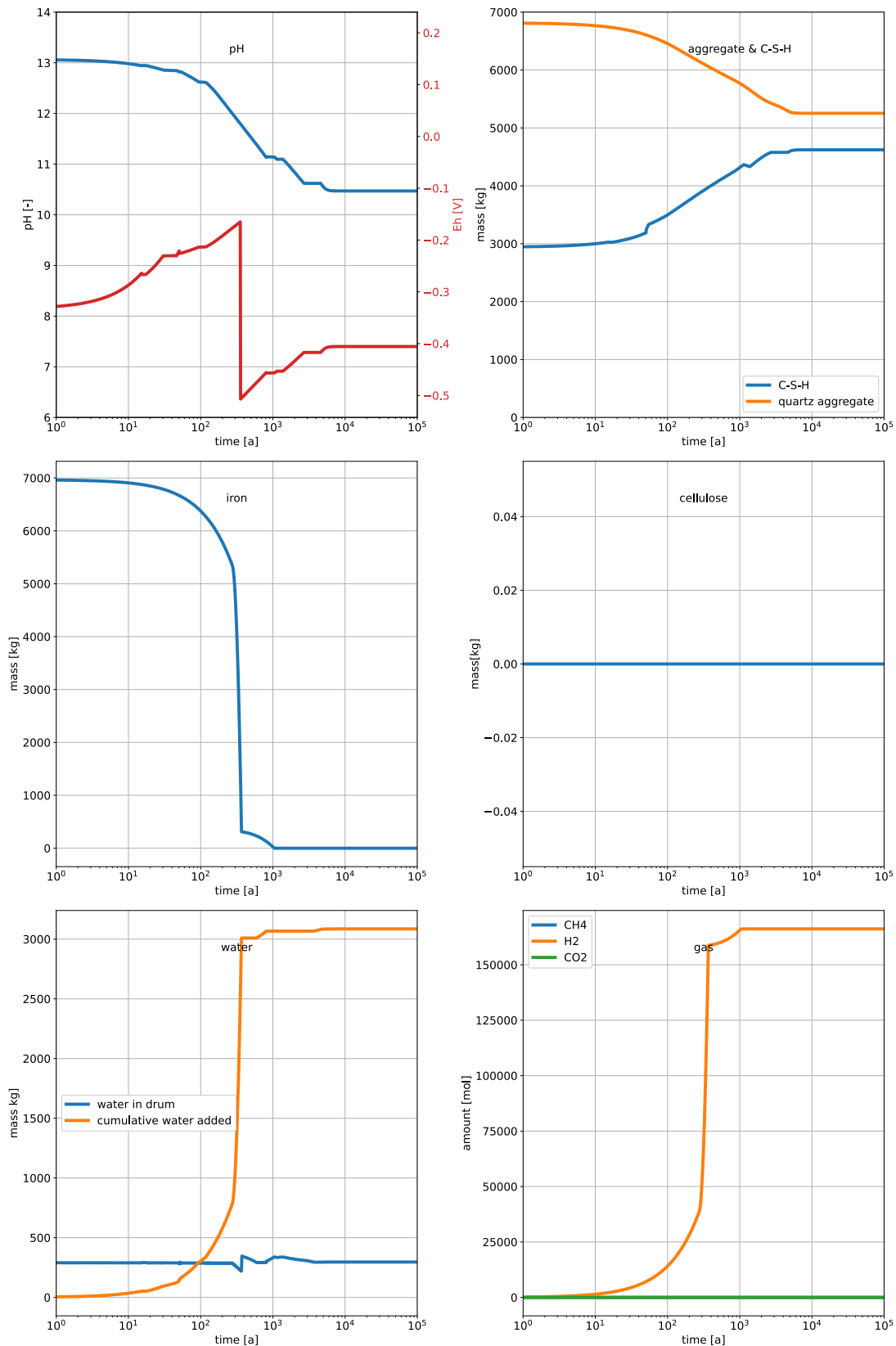


Figure 4-24: Time dependent evolution of pH (upper left), aggregate amount and C-S-H (upper right), iron (middle left), cellulose (middle right), liquid water (lower left), and gases (lower right).

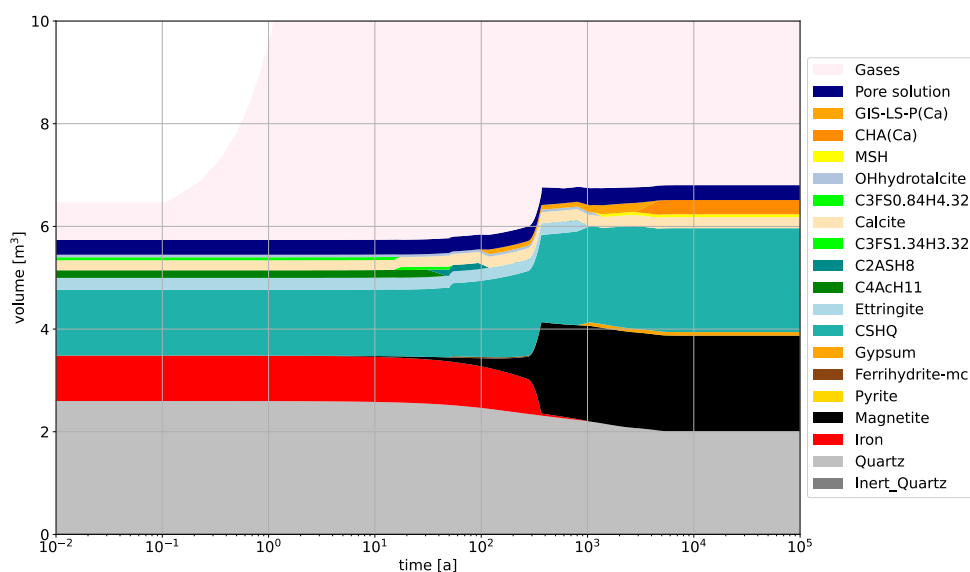


Figure 4-25: Temporal evolution of Phase volumes. Phase names are as in PSI/Nagra/CEM DATA/zeolite TDB.

Aggregate reactivity

In metal waste sort, due to the absence of large amounts of degradable organics, the pH is mainly controlled by the aggregate-cement reaction, i.e. the pozzolanic reaction in case of siliceous aggregates. The decrease of the initial high pH below a pH of 10.5 will accelerate metal corrosion by two orders of magnitude. It is therefore of special interest to compare the evolution of this waste sort for different infill materials and evaluate the influence of the pH dependence of metal corrosion rates.

For the model variant with inert aggregates, the corrosion of steel is the only chemical process considered in the model. Therefore, mineralogical changes in cement phases are negligible and only transformation of steel to magnetite is visible in Figure 4-27. Total amounts of hydrogen produced are identical and water consumed to drive the steel corrosion are only minimally smaller in Figure 4-26 as for the model variant with reactive aggregates in Figure 4-24. The small difference in water consumption can be attributed to the small formation of C-S-H in the model that consider reactive aggregates.

More significant is the slower progress of steel corrosion and hydrogen consumption because pH is constant for inert aggregates (Figure 4-26).

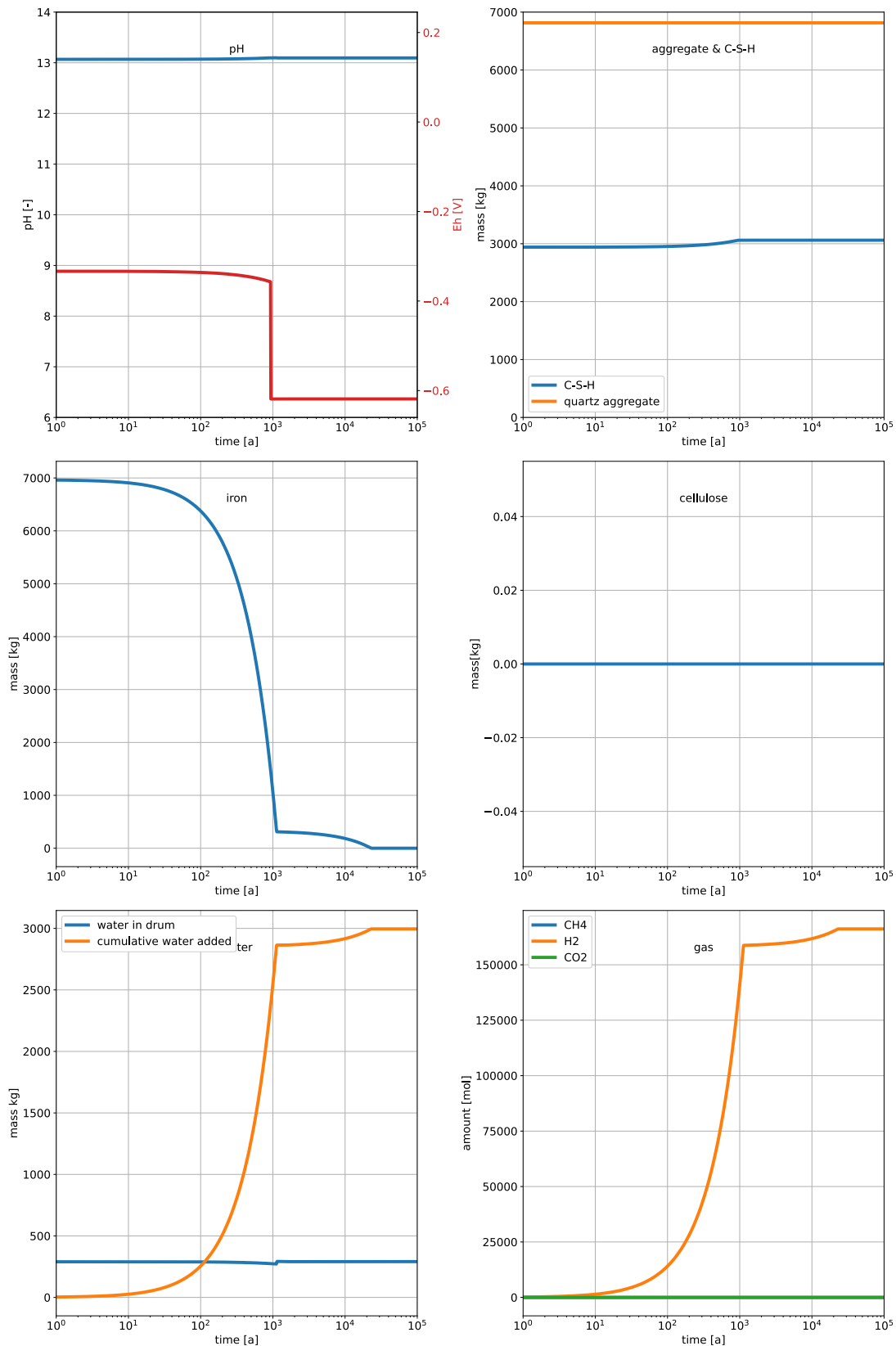


Figure 4-26: Time dependent evolution of pH (upper left), aggregate amount and C-S-H (upper right), iron (middle left), cellulose (middle right), liquid water (lower left), and gases (lower right).

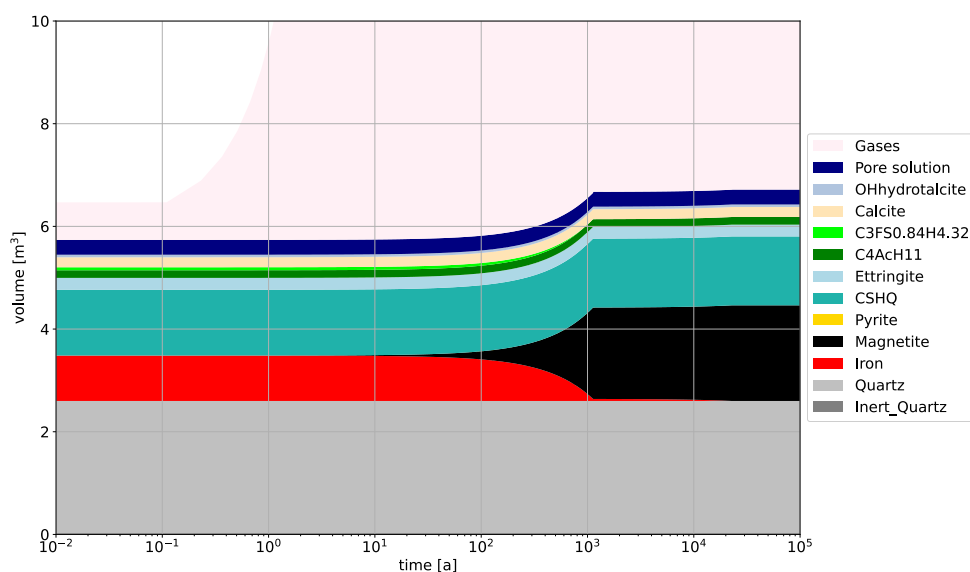


Figure 4-27::Temporal evolution of Phase volumes. Phase names are as in PSI/Nagra / CEMDATA/zeolite TDB.

Influence parametrization of steel corrosion

Figure 4-28 from Kosakowski and Wieland (2022) visualizes the link between temporal change of pH of the pore solution (left figure) and the mole amount of hydrogen gas produced by metal corrosion (right figure). The modelled waste sort is very similar, but not identical to the one modelled in this report. Major differences are related to the used container wall concrete, the recipe for infill mortar and the metal inventory, which is mostly composed of steel, and in addition small amounts of aluminium, zinc, copper, and brass. The reference model for iron corrosion is parameterised in such a way that corrosion rates above pH 10.5 are low and increase a hundredfold as soon as the pH drops below 10.5. All modelled scenarios that utilise this corrosion parameterisation therefore show the same gas release until pH drops below 10.5. Please note that for pH values between 12 and 10.5 no reliable information on degradation rates exist. Therefore, two scenarios were added with an alternative pH dependence of iron corrosion, where the corrosion rates change linearly from the low rate (above pH 12) to the high rate below pH 10.5 (cf. Chapter 4.3.1.2). As soon as hydrogen is no longer produced, all metals are corroded. The fast hydrogen production in the first three years can be attributed to corrosion of minor amounts of aluminium and zinc which are modelled with a fast constant corrosion rate following Wieland et al. (2018). The much faster onset of corrosion and gas production for the alternative iron corrosion implementation demonstrates that these small arbitrary changes might significantly influence the temporal evolution of the waste sorts.

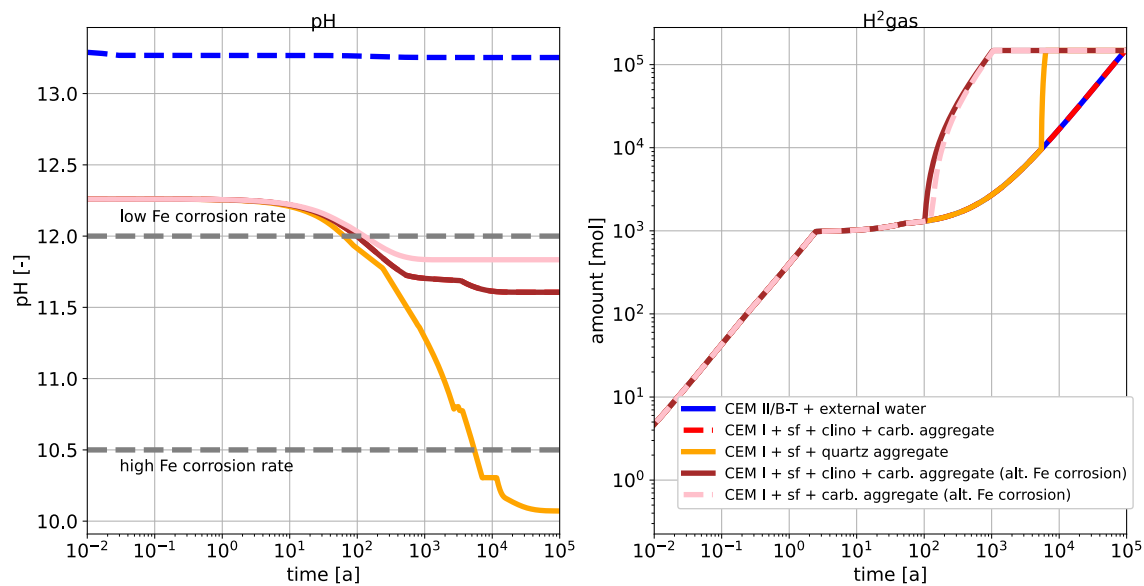


Figure 4-28: pH evolution of the pore solution with time for different modelled scenarios (left) and cumulative hydrogen gas released by metal corrosion (right). Scenarios differ in terms of cementitious infill and the rate laws used for iron corrosion. sf: silica fume, clino: clinoptinolite (from Kosakowski and Wieland, 2022).

4.4.2 Modelling cases and results by UFZ

In this section we will show the simulated evolution of the waste package, mainly reflected in the gas and capillary pressure changes and the corresponding flow regime that is controlled by the gas generation rates. In the basic reference case, the mortar permeability is set to $1\text{e-}19\text{ m}^2$ and the van Genuchten characteristic pressure is given as $1\text{e}5\text{ Pa}$, five different stages can be identified covering the 500 years of evolution in the waste package:

Stage 1 (0-50 years): In this first stage, the initial gas generation is high and it is primarily facilitated by the pore water content present within the waste matrix.

Stage 2 (50-70 years): The gas production decreases when the initial water content approaches the residual saturation threshold (set to 0.2 in the model configuration). Once the saturation drops below this level, the relative humidity also decreases and consequently leads to a lower chemical reactivity. Meanwhile, the low liquid saturation levels cause the capillary pressure to rise, resulting in more water being transported into the waste matrix from the adjacent mortar.

Stage 3 (70-120 years): The rate of gas production is constant while water supply, that sustains the chemical reactions, comes from further drying of the drum mortar and a reversal of liquid flow into the drum.

Stage 4 (120- 200 years): The gas production continues to decrease during this stage, as the drum mortar has dried out. The liquid flow into the drum is increasing due to the capillary effect.

Stage 5 (200+ years): The gas production stabilizes at a low but constant level, as a steady flow of water supply from the domain boundary, facilitated by the host rock and flow through the exterior mortar, is established.

4.4.2.1 Stage 1, 0 – 50 years: Initial pressure build up and drying of the waste

The initial pressure build-up primarily results from two key processes: the degradation of group 1 organic waste, such as cellulose, and the corrosion of metal waste. Figure 4-29a shows the total initial gas generation rate, which is nearly continuous until 45 years (see Figure 4-29b). As a result of the gas production, the gas pressure increases to a maximum of 0.3 MPa within the lower left drum after one year (Figure 4-30a). This area experiences the highest pressure because the gas must pass through the narrow drum opening and the tight spaces between the drums, leading to higher gas fluxes in these bottlenecks.

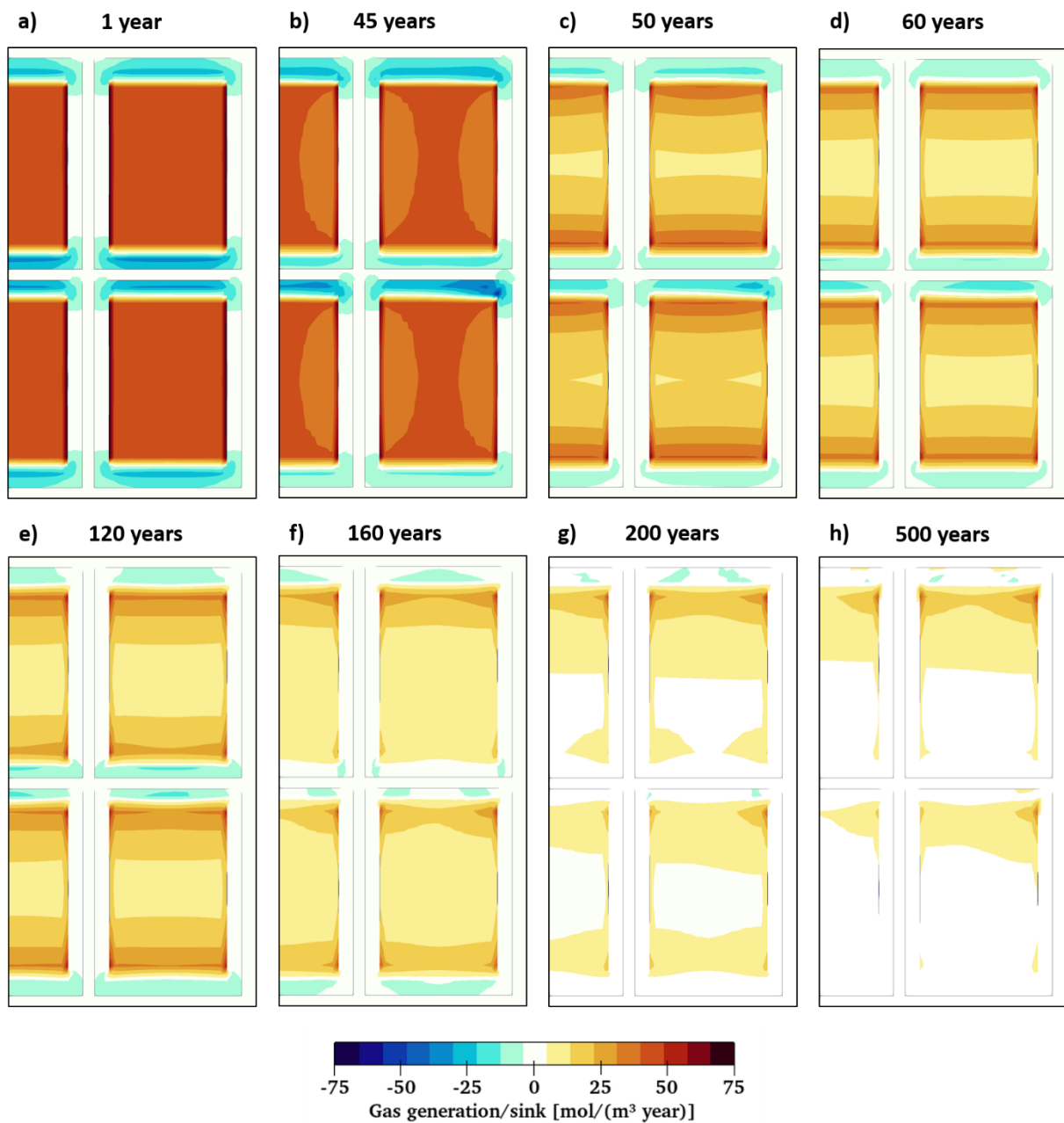


Figure 4-29. Total gas generation rate (positive values) and CO₂ sink of cement carbonation reaction (negative values) for the base case: $k = 5e-19 \text{ m}^2$, $p_d = 1e5 \text{ Pa}$

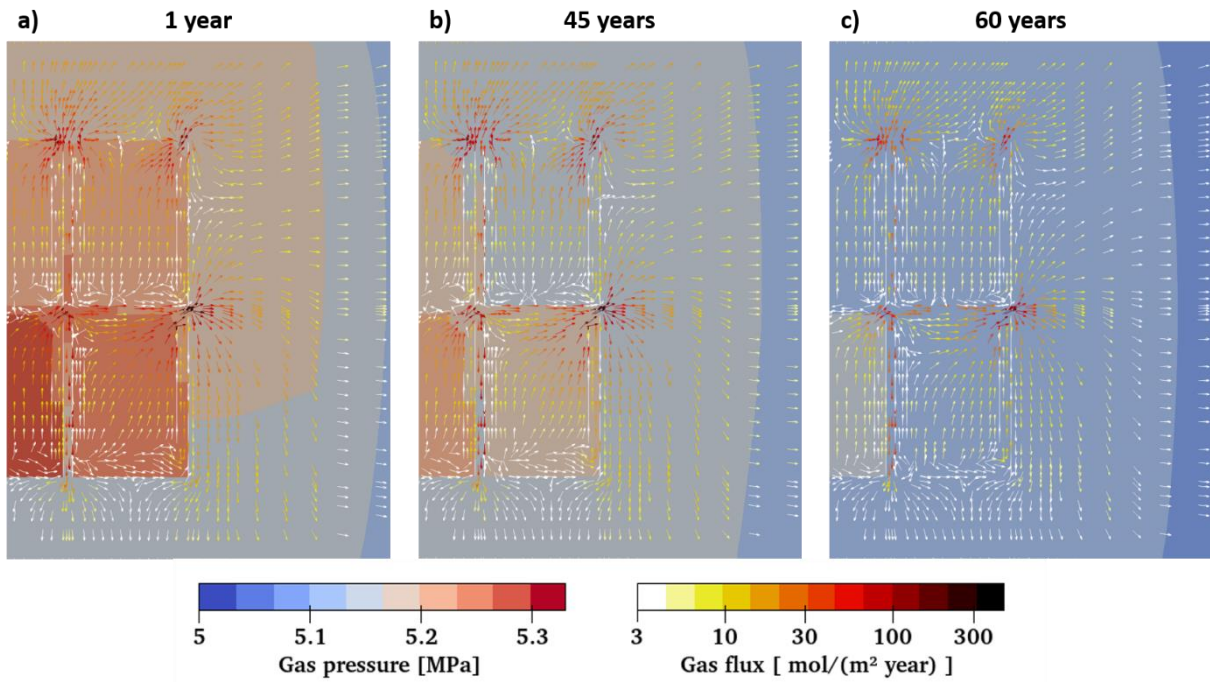


Figure 4-30: Gas pressure (face colour) and gas flux (arrows, legend in log scale) for the base case.

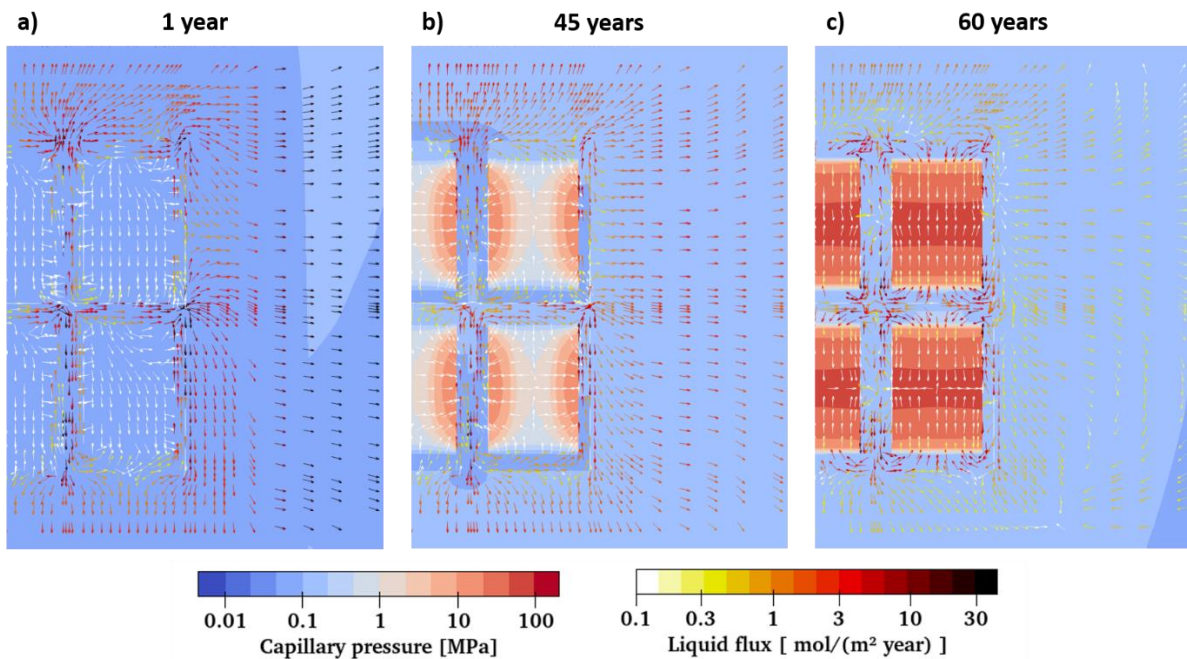


Figure 4-31: Capillary pressure (face colour) and liquid flux (arrows, legend in log scale) for the base case.

4.4.2.2 Stage 2, 50 – 70 years: Drying out of the drum mortar

After about 50 years, the gas production has significantly decreased (Figure 4-29c) because of the water sustaining the chemical reaction within the waste has been depleted. When the liquid saturation approaches the residual liquid saturation of 0.2, the capillary pressure starts to increase by two orders

of magnitude (see Figure 4-31d-f). This leads to a change in the liquid flow regime inside of the drum at around 45 years. Before that, a small amount of liquid is flowing out of the waste, largely driven by the high gas pressure. In the new flow regime, liquid originally inside the pore space of the mortar starts to be sucked back into the waste, driven by the high capillary pressure there (see Figure 4-31d,e,f). Within the waste, water vapour diffusion is the second main transport mechanism for water flow towards the centre of the waste package.

4.4.2.3 Stage 3, 70 – 120 years: Reversal of the liquid flux field at the outer mortar and host rock

Between 70 and 120 years the gas generation rate is nearly constant and comparable to stage 2 (see Figure 4-29d, e). In this stage, two sources of water are sustaining the chemical reactions. First, the mortar liquid saturation inside of the drum is further decreasing when supplying water to the waste (see Figure 4-32c and Figure 4-33d (represented by the purple and blue lines). Second, the decrease in liquid saturation leads to an increase of the capillary pressure of the mortar within the drum (see Figure 4-33c). The increase in capillary pressure results to a reversal of the liquid flow into the drum starting at around 70 years. After 70 years, the liquid flow into the drum is further increasing and after 100 years the entire liquid flow regime has reversed (see Figure 4-32c). The time lag between liquid flow reversal between at the drum opening and at the mortar host rock transition could be explained by the higher capillary of the host rock compared to the mortar.

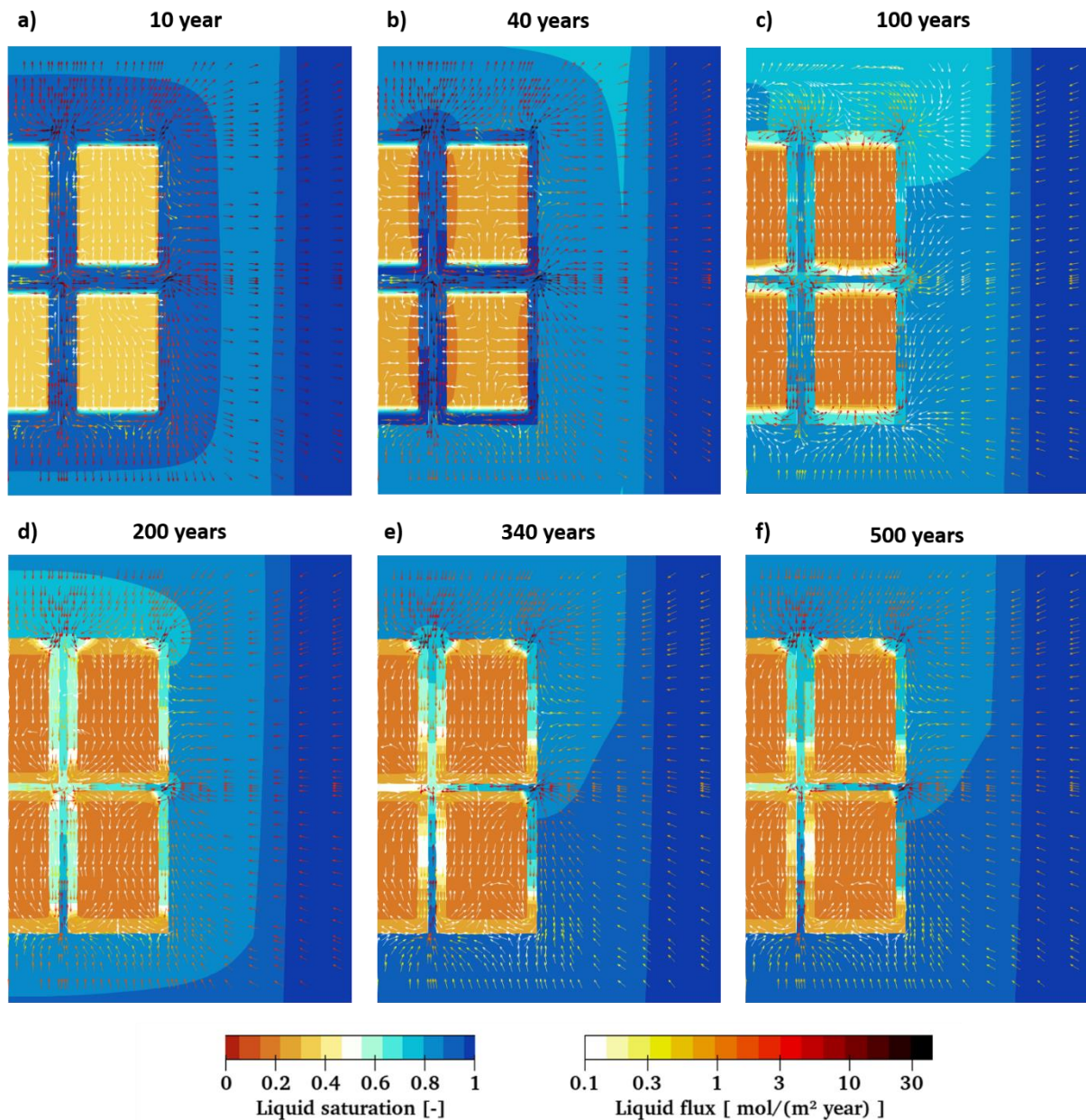


Figure 4-32: Liquid saturation (face colour) and liquid flux (arrows) for the base case after 10, 40, 100, 200, 340, 500 years.

4.4.2.4 Stage 4, 120-200 years: Second decrease of gas generation rate

In this stage, the initial water content of the mortar within the drum has so far decreased that water supply into the waste is further decreasing (see Figure 4-29e,f,g). The reversal of the liquid flow into the drum is not sustaining the gas generation rate resulting in predominantly lower rates in the lower part of the drum. In this stage the feedback system is going to reach a new equilibrium where water supply from the host rock has to match the water consumed by the chemical reactions. The capillary pressure increases inside of the drum and also close to drum opening (Figure 4-33c). Simultaneously, gas pressure is decreasing, due to decreasing gas production rates, leading to an increase in liquid flow from the host rock towards the drum (Figure 4-32d). The counter-flow of gas and liquid leads to an increase in gas saturation within the entire outer mortar area, because the higher gas entry pressure of the granitic host rock holds the gas within the mortar (Figure 4-32c). The maximum gas saturation of ca. 0.8 is reached after approximately 110 years and is shifted towards the top of the container.

4.4.2.5 Stage 5, after 200 years: Constant gas generation rate and (back) saturation of the mortar

After 160 years, gas generation rates have become nearly constant again, when water supply from the host rock matches the water consumption of the chemical reactions (Figure 4-33e). The gas generation rates are decreasing with a minimal rate, because the degradation rate drops along with less amount of degradable waste. In this stage, the liquid saturation of the outer mortar is slowly increasing (Figure 4-32d-f and Figure 4-33d). At the bottom of the container, liquid saturation is increasing faster to 0.95 after 500 years. But at the top of the container liquid saturation is still at 0.8 after 500 years.

After 500 years, around 25% percent of cellulose has been degraded. At the top corners of the waste material, where water supply is the highest, 50% percent of cellulose has been degraded locally. The cement carbonation is primarily located at a thin layer on top of the waste material with the thickness of one mesh element, where the cement is fully carbonated.

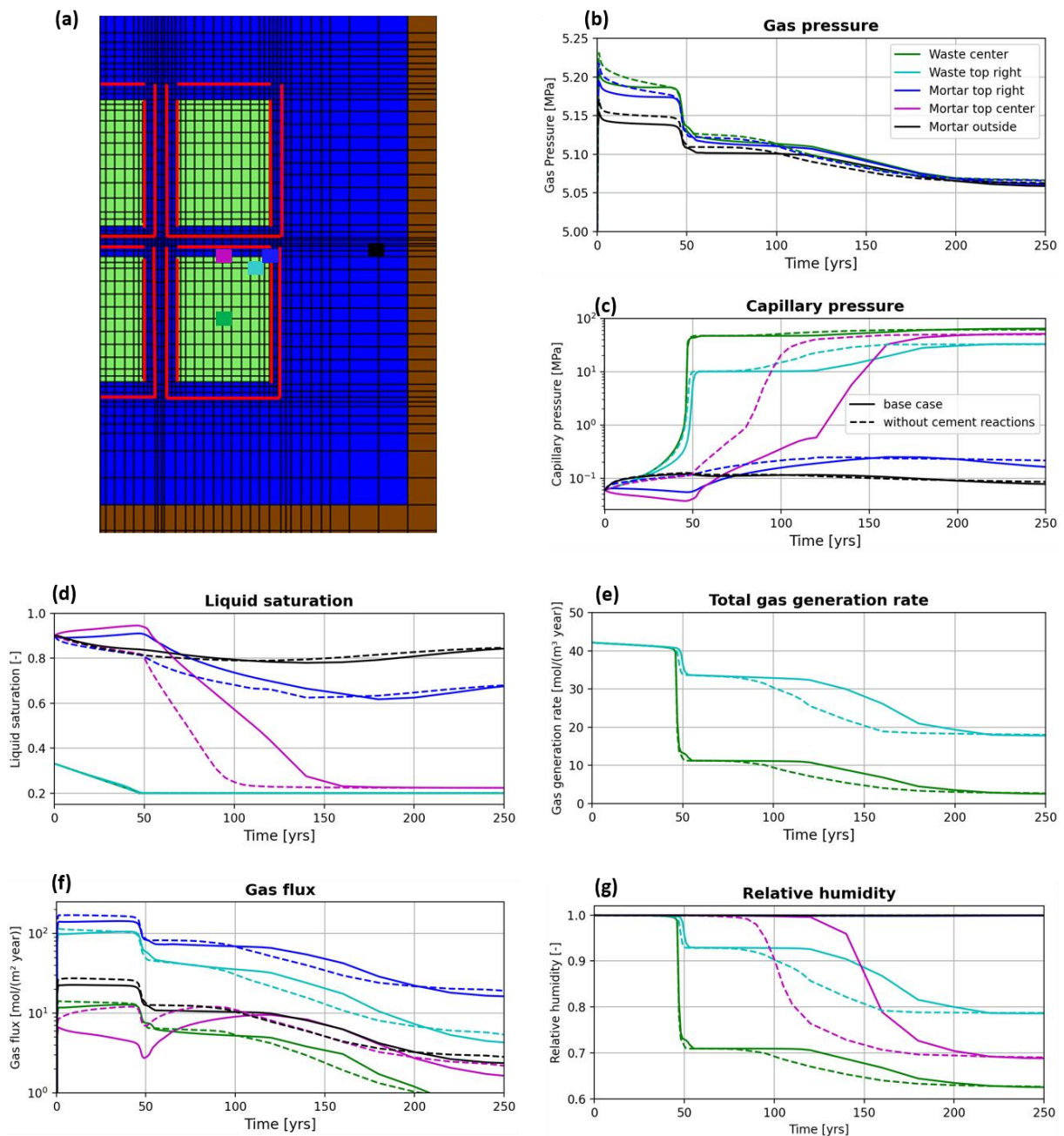


Figure 4-33: Time series plots. Continuous lines show the base case and dashed lines show the base case without cement carbonation and ASR. Panel (a) shows the location of mesh nodes corresponding

to the time plots. The other panels show gas pressure (b), capillary pressure (c) total gas generation rate (d), liquid saturation (e), chemical reactivity (f), relative humidity (g).

4.4.2.6 Sensitivity analysis

4.4.2.6.1 Impact of the cement carbonation

The concrete carbonation reaction consumes CO₂, which has been generated within the waste, and releases free water into the pore space. This CO₂ uptake reduces slightly the initial pressure build up within the drum (see Figure 4-33a). Between 100 and 200 years a time period with higher gas generation rates appears, because the water release of the carbonation reaction increases the liquid saturation of the mortar close to the waste. This leads to higher water flux into waste and to higher gas generation rates including CO₂, which is than available for the cement carbonation reaction. This time period with different gas generation ends when the carbonation reaction rate has decreased inside of the drum due to a low chemical reactivity when the liquid saturation approaches to dry conditions (S_i = 0.6).

4.4.2.6.2 Impact of the mortar permeability

In the initial time period until 50 years, during which gas production is controlled by the initial water content of the waste, the observed gas pressure is much lower for the high permeability case because a lower pressure gradient is needed to expel the gas from the drum. A varying permeability shows no difference for the mortar liquid saturation at the drum opening because the liquids, that were pushed away, are replaced by water production of the cement carbonation reaction (blue lines in Figure 4-34c). This is not the case at the top centre location (purple lines in Figure 4-34c), because the water flux is much lower here. In the high permeability case, there is no second decrease in the gas generation rate after 100 years, because after the initial water in the waste is depleted, the water supply is sustained by water transport from the host rock through the mortar. This is indicated from the high liquid saturation of the mortar both within the drum (see blue and purple dashed lines) and outside of it (black dashed line). The total gas generation rate is slowly decreasing in the high permeability case, reflecting its dependency on the decreasing amount of non-degraded waste.

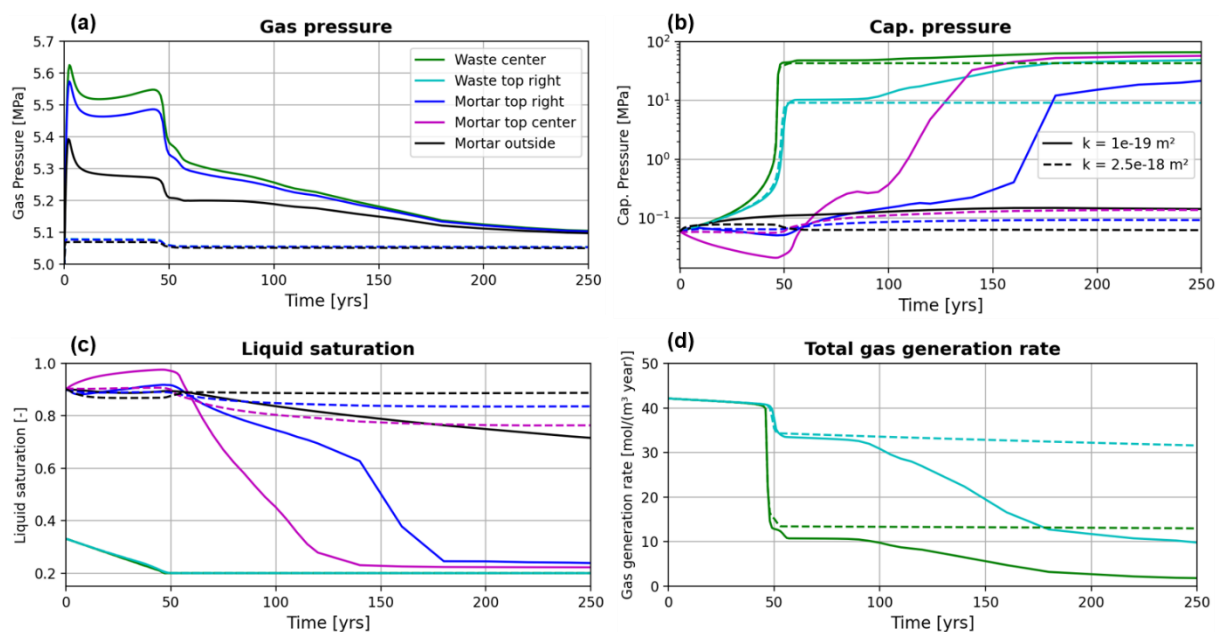


Figure 4-34: Time series plot for different mortar permeability. The van Genuchten characteristic pressure is set to $p_d = 1e5$ MPa and the mortar chemical reactions are activated. Panels show gas pressure (a), capillary pressure (b), liquid saturation (c), total gas generation rate (d). Location of nodes are shown in Figure 4-33a.

4.4.2.6.3 Impact of the mortar van Genuchten characteristic pressure p_d

The initial liquid saturation is a function of the initial capillary pressure and the chosen van Genuchten characteristic pressure for each material. A higher van Genuchten characteristic pressure increases the initial liquid saturation (see eq. 4 in section 4.3.2) and thereby decreases the relative gas permeability of the mortar. This results in a higher gas pressure (Figure 4-35a) being required to obtain the same gas flux, and also triggers pore water displacement. This pore water displacement is indicated by a small decrease in the mortar liquid saturation close to waste in the first year, despite the water production within the mortar (see blue and purple dashed lines in Figure 4-35c).

The simulation run with a higher p_d reaches a steady state much more quickly. The higher p_d leads to a higher capillary pressure and ensuring that the liquid saturation is always above 0.9. When the mortar within the drum begins to dry a bit after 50 years, a reverse liquid flux promptly initiates due to a capillary pressure difference of 0.1 MPa between inside the drum (blue line) and outside of the mortar (black line). This reversal provides a sustainable water supply to maintain a steady-state gas generation rate.

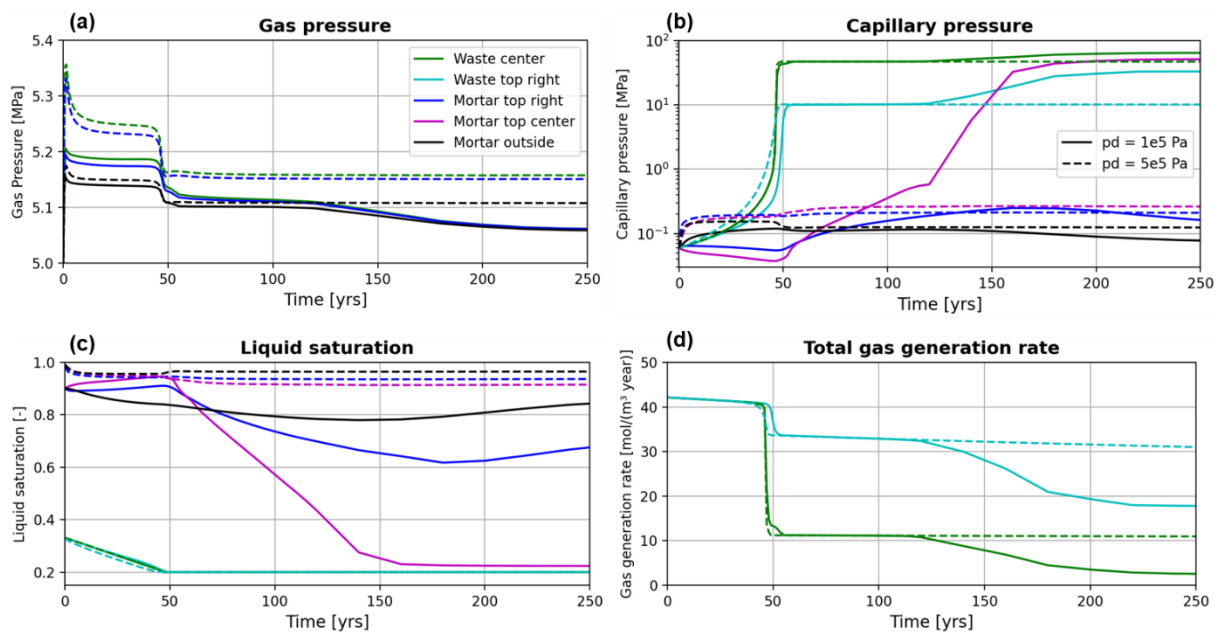


Figure 4-35: Time series plot for different van Genuchten characteristic pressure of the mortar. Mortar permeability is set to $k = 5e19$ m² and the mortar chemical reactions are activated. Panels show gas pressure (a), capillary pressure (b), liquid saturation (c), total gas generation rate (d). Location of nodes are shown in Figure 4-33a.

4.4.2.7 Discussion

The simulation results show how the water supply and gas generation feedback loop works in a waste package, in which the gas generation rates depend on the initial water availability and water transport,

which in turn depends on gas pressure and properties of the backfill material and the host rock. Through the modelling results of the model, we have identified and characterized four stages in the hydrological evolution of the multiple-drum container setup. To accurately model local drying and cement degradation within the waste container, it is crucial to employ a coupled model that considers the real material composition within the container, as well as for each waste drum. This, in turn, has a significant impact on gas production rates and the distribution of gases within the waste repository and its near field.

In a low ILW waste repository different mortar and cementitious material will be utilized. Therefore, we conducted a sensitivity analysis showing the differences in gas generation rates and gas pressure evolution based on the hydraulic properties of the mortar. In our simplified model we have focused only on the two primary hydraulic parameters: the van Genuchten characteristic pressure and the permeability, which proved highly valuable understanding in the feedback system. Additionally, parameters like porosity and initial water content depend on the mortar recipe. It is worth noting that the material properties of compressed waste inside a drum have uncertainties as well (see Huang et al. 2021). A sensitivity analysis for these parameters would also be of interest. In our model setup the main simplification is the small modelling domain. With a larger model domain including more drums and containers, the same amount of initial water in the drum and mortar may lead to higher gas pressure within the first 50 years of the repository evolution. This scenario needs to be investigated with a gallery-scale model simulation.

For the future, an interesting prospect is to expand this model spatially. Specifically, we could simulate a cross-section of a disposal gallery containing several stacked drum containers, employing various concrete and mortar materials. Such an approach would allow us to assess how container composition and waste density affect the evolution of gas production rates and the desaturated area in the near-field repository.

4.4.3 Modelling cases and results by SCK CEN

After 500 y, about 0.43 mol cellulose /dm³ has been degraded. Figure 4-36 summarizes some variables after 500 y of interaction between cement and CO₂ originating from cellulose degradation. In this time frame, limited alterations outside the waste drum are visible. Of course, the pH in the waste zone is rather low due to the production of CO₂ and no buffer reactions. A small gradient in pH and partial pressure of CO₂ (calculated from the saturation index of CO_{2(g)} – this is of course theoretical pressure as there is no gas phase) is visible inside the drum illustrating the diffusion of CO₂ from the waste package into the surrounding matrix. Of course, in contrast to the multiphase model described in section 4.4.2 (Figure 4-29), the degradation rates (and amounts) of cellulose is constant in time and space (within the waste zone) as there is no saturation-dependent limitations in this simulation.

The most striking feature is the small shell of calcite precipitation at the top and the bottom of the waste drum. In a wider region, CSH is decalcified: transformation of CSH-1.6 into CSH1.2 to CSH0.8 in a very sharp front, and a larger region CSH0.8 persists; close to the waste zone, also CSH0.8 is completely dissolved.

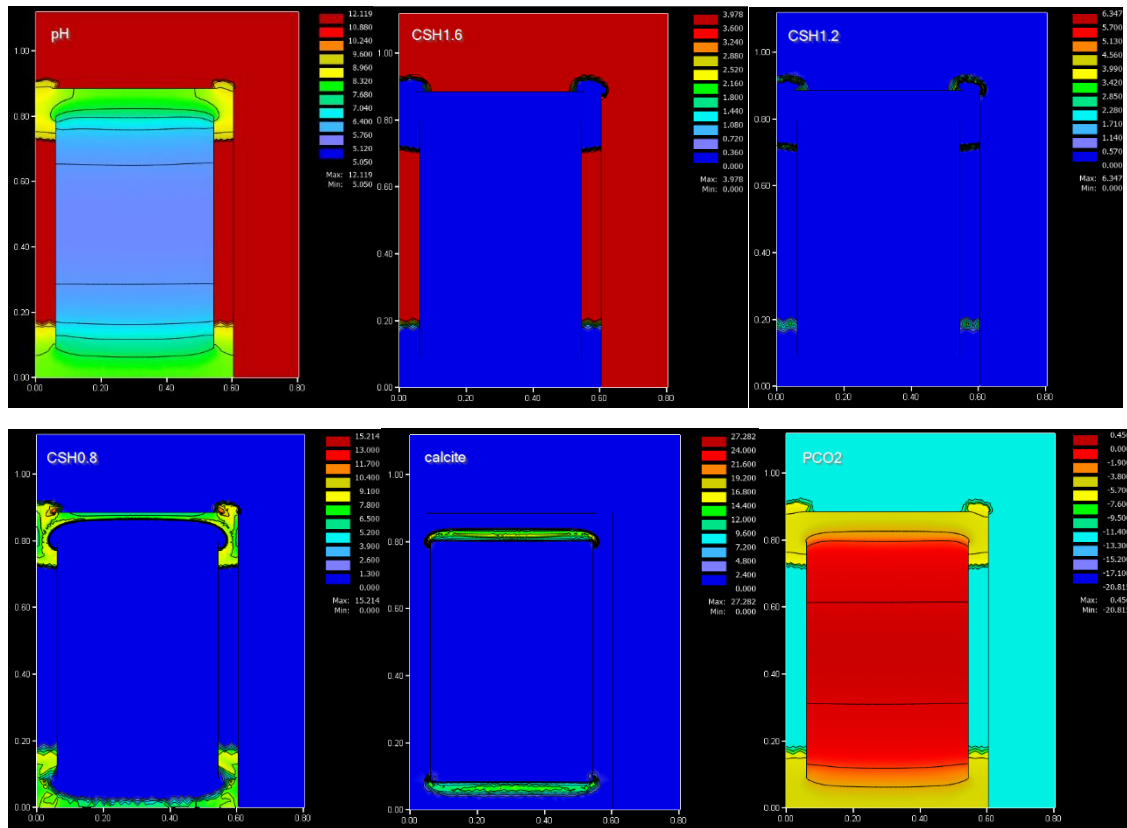
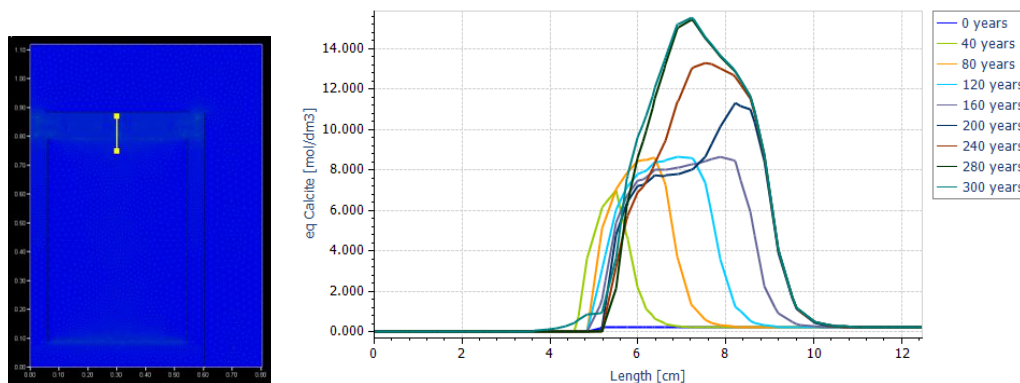


Figure 4-36: Contours of pH, CSH1.6, CSH1.2, CSH0.8, calcite and $\text{Log}_{10}(P_{\text{CO}_2})$ after 300 y in a waste drum with organic waste and container backfill. Mineral amounts are in mol/dm^3 ; distance is in meter.

Figure 4-37 shows profiles of calcite and CSH1.2 along a transect from inside to waste zone to the upper lid of the waste drum (see also in Figure 4-37). Interestingly, during the first 150-200 y, a calcite front is progressing along the transect with more or less constant amount of calcite formed indicating that it is local transformation of cement phases to calcite. This is obvious when looking to the profiles of CSH1.2 (the last cement phase) which is depleted in the zone of about 10 cm between in that period. At larger times, we see an increase in calcite precipitation in the zone between 6 and ~9 cm, which is caused by Ca diffusing into that zone from further away from the waste zone (linked to the decalcification of CSH), without a further progression of the calcite precipitation front. It seems that under diffusive saturated conditions and in the considered time frame, there is a somewhat small reactive shell where CO_2 diffusing from the waste zone and Ca diffusing from the backfill meet and precipitate as calcite.



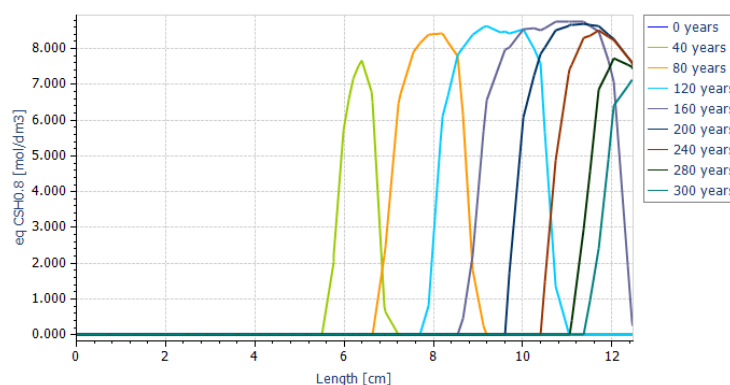


Figure 4-37: Amounts of calcite (top) and CSH1.2 (bottom) along the transect showed in the left plot (extending from the waste zone through the waste drum backfill) at selected times.

Of course, the results presented here are for fully saturated conditions where CO_2 is only transported by diffusion in the aqueous phase. Location of a calcite shell or even the presence of such a calcite shell can be different in case the system is partially saturated; CO_2 can then diffuse in a much faster way throughout the porous system in the gas phase compared to Ca in the aqueous phase. It is then possible that a shell develops further from the waste zone; or even no shell development with CO_2 diffusion always quickly to the location of “fresh” cement phases. Information of saturation states at given moments obtained with the model described in section 4.4.2 could be combined with the more detailed geochemical calculations to evaluate precipitation fronts of calcite and degradation fronts of cement phases.

4.4.4 Modelling cases and results by COVRA

4.4.4.1 ILW/steel waste package

First, only the waste package is considered, presented in section 2.1.2.

Assessing the maximum in anaerobic corrosion rate of steel at waste package scale can be done at different saturation degrees and different water consumption rates. The difference in initial water content shows the time-dependency of the consumption of water by the anaerobic corrosion of steel:

- 1) An initial water content equal to the maximum in water content i.e. porosity times the density of liquid water;
- 2) An initial water content equal to 70% of this maximum in water content since the water content of a waste package content after fabrication has been estimated to be 70% in section 3.2.1.

The outer boundary (Dirichlet) has been set equal to the equilibrium content of water when exposed to a relative humidity in order to simulate storage and the operational phase of the disposal facility. A relative humidity of 75.47% is used. The inner boundary (Neumann) is a flux of water with which water is consumed to simulate the consumption of water by anaerobic corrosion. Figure 4-38 shows the calculated saturation degree at a corner of the inside of concrete and at midst of the inside of concrete for these two cases with two different water consumption rates: $10^{-7} \text{ mol H}_2\text{O m}^{-2}\text{s}^{-1}$ and $5 \times 10^{-8} \text{ mol m}^{-2}\text{s}^{-1}$.

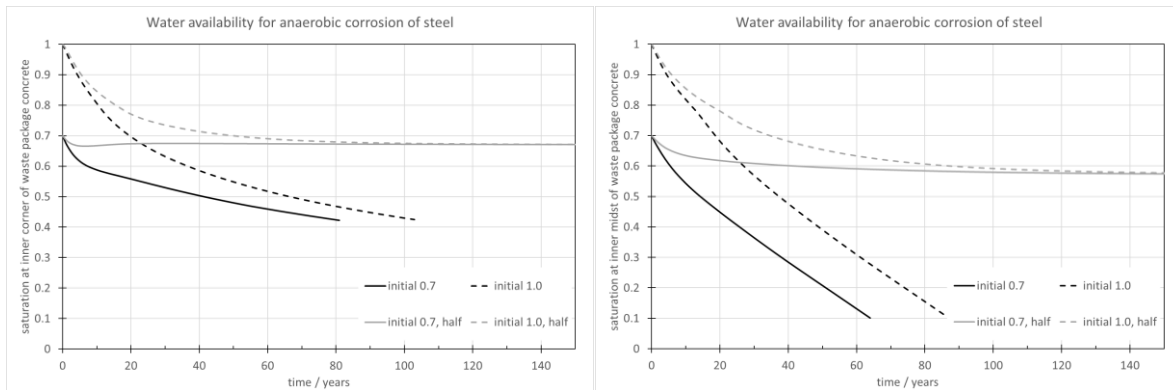
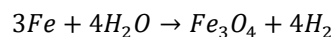


Figure 4-38: Saturation degree of concrete at two positions of the inside of concrete for a water consumption rate of 3.2 mol H₂O m⁻²year⁻¹ and 1.6 mol H₂O m⁻²year⁻¹ (half). The moisture storage function and parameters for diffusion as found for waste package concrete at 20°C in section 3.2.1 are used.

A consumption rate of water of 1.6 mol/m² per year is sufficiently low to obtain a steady state in the saturation of concrete. This steady state is achieved after about 130 years. A two times larger consumption rate of water obtains such low saturation degrees that a saturation degree is approaching 0 after 110 years with the used parameters of waste package concrete and exposure to a relative humidity of 75.47%. A constant water consumption rate as used in the modelling is not representative since a saturation degree of 0.7 decreases the corrosion rate more than two orders in magnitude and a corrosion rate cannot be measured for a cementitious material with a saturation degree below 0.2 (Stefanoni et al., 2018).

In the post-closure phase, saturation of concrete might eventually be achieved. However, a consumption rate of 3.2 mol/m² per year for a single waste package is still too high to calculate the saturation degree within concrete beyond 130 years.

The maximums in consumption rates of water also determines the maximums in anaerobic corrosion rates of steel. The container will be filled with 6640 kg of waste (carbon steel) as explained in section 2.1.2. The density of structural steel is 7850 kg m⁻³ which is about 1.41×10⁵ mol Fe m⁻³. The long term anaerobic corrosion rate of carbon steel has been deduced in the state of the art of ACED to have a value of 0.1 µm per year in case of sufficient access of water (Neeft et al., 2022). The hydrogen generation rate becomes 1.87×10⁻² mol H₂ m⁻²year⁻¹ assuming the following corrosion reaction:



The hydrogen generation rate is equal to water consumption rate. The volume of steel in this package is 0.84 m³ if the steel waste would be a steel massive block but this waste is composed of some kind of metallic tubes as shown in Figure 2-4 in section 2.1.2. The surface area exposed to a cement matrix is consequently much larger. Nevertheless, the minimum in consumption of water would be 0.1 mol H₂O per year assuming a cubical volume of 0.84 m³ of steel i.e. and edge of 0.94 m. The inner surface of the concrete waste package in Figure 2-4 in section 2.1.2 is 17.33 m². Consequently, the minimum in water consumption rate for the metallic waste would 6×10⁻³ mol H₂O m⁻² year⁻¹. This minimum is almost three orders in magnitude smaller than the maximum in possible consumption rate for waste package concrete. Consequently, the anaerobic corrosion of metallic steel may not be limited by the transport properties for water within the waste package concrete if the surface area of steel waste within the waste package is 1000 times less than used here without indurated clay.

4.4.4.2 ILW/steel disposal cell indurated clay

For a disposal cell with indurated clay, the minimums in steady state are however smaller since the water availability for the waste package concrete is competing with water for the healing of cracks in the excavated damaged zone for the first thousands of years, the influx of water from the clay into waste package concrete is smaller than exposure to a relative humidity of 75%. Again, the diffusion equation to be solved is equal to equation 3-13 in section 3.2.1 except that the initial and boundary conditions are different to simulate the transport of water in the concrete of the waste package within a disposal cell with indurated clay. Figure 4-16 and Figure 4-17 shows the boundaries and initial saturation degrees.

Figure 4-39 shows that with parameters described in section 4.3.4.3, the saturation degree becomes too small for waste package concrete just after 33 years instead of 110 years with exposure to a relative humidity of 75% with the same consumption rate. For a better readability, the saturation degree and water content only at $x=0$ (the line graphs) are shown as well. A ten times smaller consumption rate than used in Figure 4-39 results in a too low saturation degree just after 690 years. Figure 4-40 shows that a steady state is still not achieved with the earlier defined minimum in water consumption rate for the metallic waste of $6 \times 10^{-3} \text{ mol H}_2\text{O m}^{-2} \text{ year}^{-1}$.

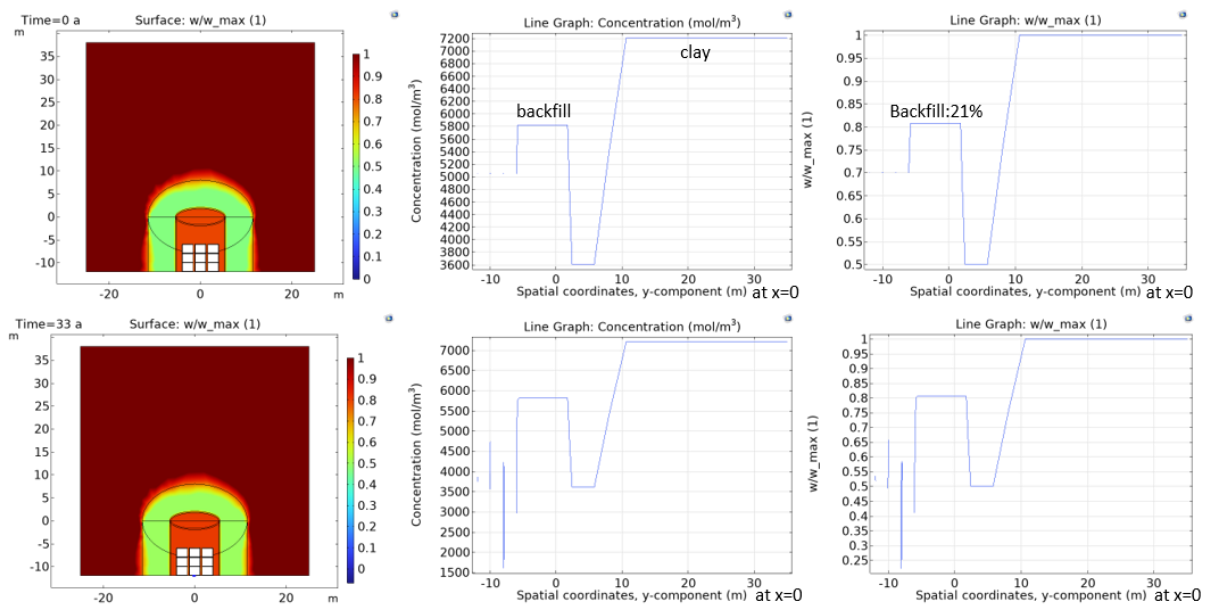


Figure 4-39: Saturation degree and water content for a water consumption rate of $3.2 \text{ mol H}_2\text{O m}^{-2} \text{ year}^{-1}$ at start (0 years; all upper figures) and after 33 years (all lower figures). The parameters for diffusion as found for waste package concrete and foamed concrete at 20°C in section 3.2.1 are used. Saturation degree for the backfill is overestimated since a porosity of 13% was used instead of 21%.

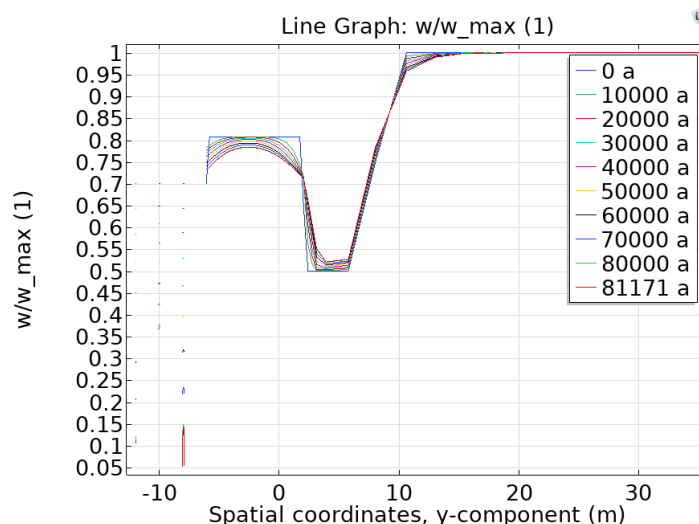


Figure 4-40: Saturation degree for a water consumption rate of $6 \times 10^{-3} \text{ mol H}_2\text{O m}^2\text{year}^{-1}$ at $x=0$ in Figure 4-39. The parameters for diffusion as found for waste package concrete and foamed concrete at 20°C in section 3.2.1 are used. Saturation degree for the backfill is overestimated since a porosity of 13% was used instead of 21%.

4.4.4.3 Concluding perspective

All reactions with which water is consumed or produced have an impact of the transport of water within the disposal cell. Such calculations require a variable value for transport of water within all porous mediums in the disposal cell. These calculations have been made. ACED looks primarily at representative disposal cells. Representative values for transport of water within waste package concrete, their initial water content after fabrication and moisture storage function are essential to determine the extent of the reactions and their associated consequences. With these representative values and transport mechanism, it can be stated that the generation of hydrogen gas by anaerobic corrosion of steel is limited by the transport of water. Biodegradation requires larger saturation degrees of concrete than anaerobic corrosion of steel. Generation of carbon dioxide by biodegradation is therefore envisaged to take place after the corrosion of the available steel within the waste package is completed.

4.4.5 Modelling cases and results by BRGM

BRGM extracted degradation model for cellulose (section 3.3.3) and PVC (section 3.3.4) from literature and experiment carried out in CORI. Kinetics were implemented in a radial geometry (Figure 4-18b). Due to a lack of experimental data, cellulose, PVC and phthalates alteration rates were not pH dependent and led to homogeneous polymer degradations (Figure 4-41). Overall, cellulose was expected to degrade faster than other polymers.

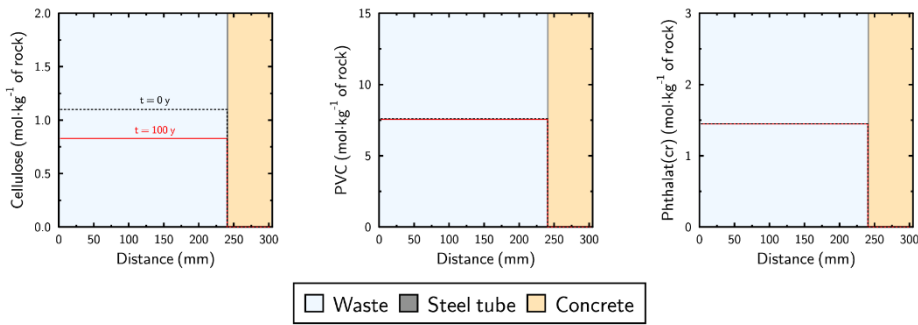


Figure 4-41: Simulated polymer profiles at 100 years.

Alteration products of polymers are reported on Figure 4-42. Acid conditions in the waste area were mainly related to the PVC degradation (HCl(g) production) while pH conditions remained basic in the steel and concrete areas. High ISA concentrations were expected due to the fast cellulose alteration.

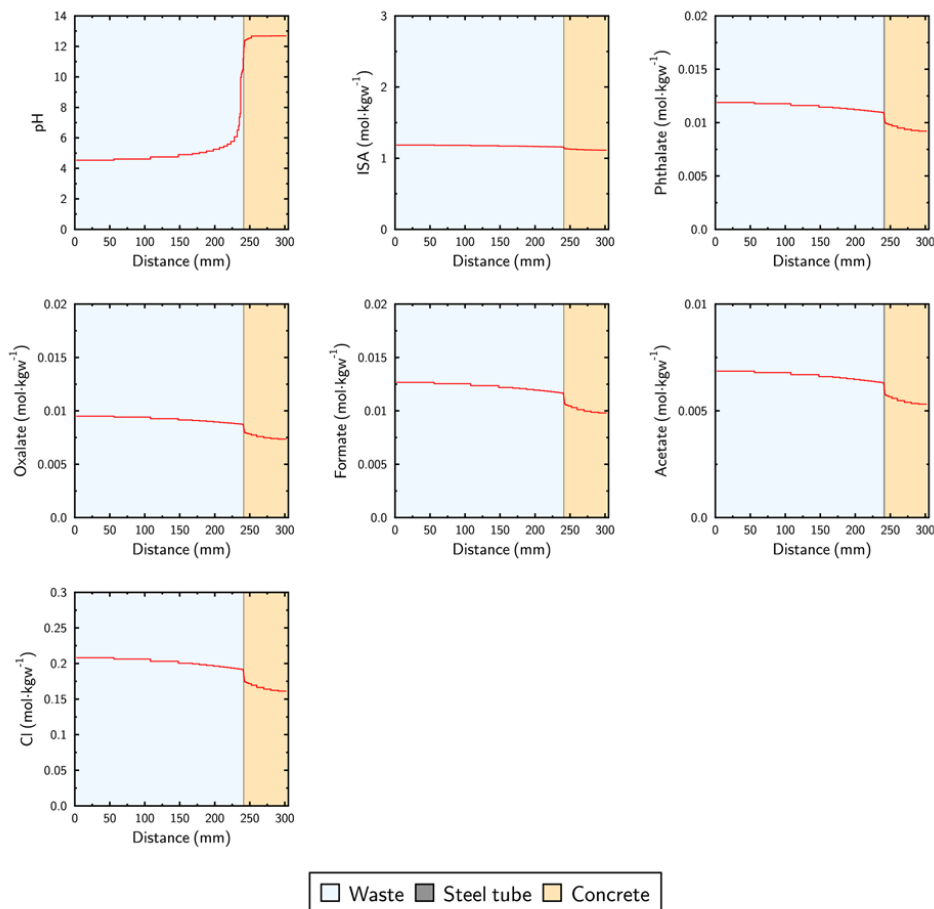


Figure 4-42: Simulated alteration products at 100 years.

Despite strong limitations of MARTHE-PHREEQC regarding the gas consideration, $\text{CO}_2(\text{g})$, $\text{CH}_4(\text{g})$, $\text{HCl}(\text{g})$ and $\text{H}_2(\text{g})$ saturation indices were calculated (Figure 4-43). Polymer degradations should lead to high $\text{CO}_2(\text{g})$ and $\text{CH}_4(\text{g})$ pressures. In contrast, low $\text{HCl}(\text{g})$ pressure can be expected due to high solubility of the gas, which has been confirmed with CORI experiments (Henry's Law constant: $2.3 \cdot 10^{-5} \text{ atm}^{-1}$). Moreover, a $\text{CH}_4(\text{g})$ production from the $\text{CO}_2(\text{g})$ and $\text{H}_2(\text{g})$ released from cellulose degradation and iron corrosion was thermodynamically predicted. Overall, the methanation (Sabatier) reaction is exothermic and leads to a decrease in the number of gaseous moles (Ducamp et al., 2018). From a thermodynamic point of view, low temperatures are necessary to obtain high CH_4 conversions, while the reaction kinetics increase with temperature according to the Arrhenius law (Ducamp et al., 2018). Thus, a rigorous calculation of the total gas pressure must consider both the ILW waste temperature and a kinetic control of the Sabatier reaction. Thus, a rigorous calculation of the total gas pressure must consider both the ILW waste temperature and a kinetic control of the Sabatier reaction.

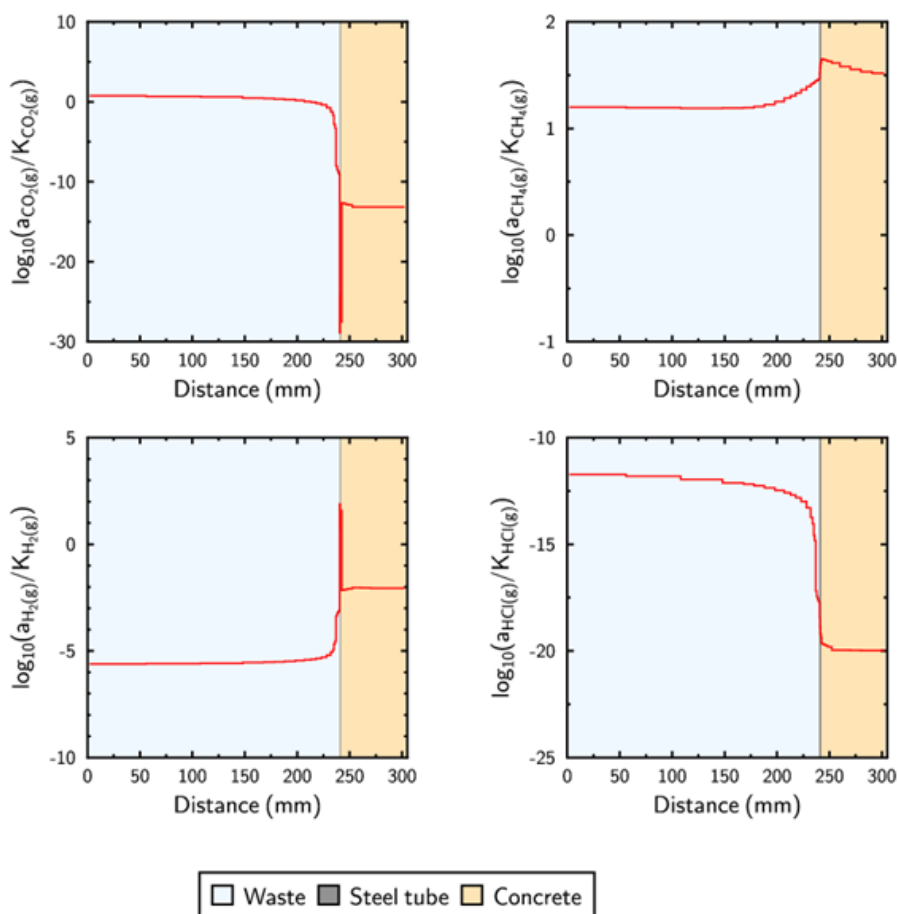


Figure 4-43: Simulated gas saturation indices at 100 years.

Acidic conditions in the waste area resulted in a high corrosion at the intrados of the steel tube (Figure 4-44). Magnetite was expected on both sides of the steel tube while siderite was expected only on its intrados.

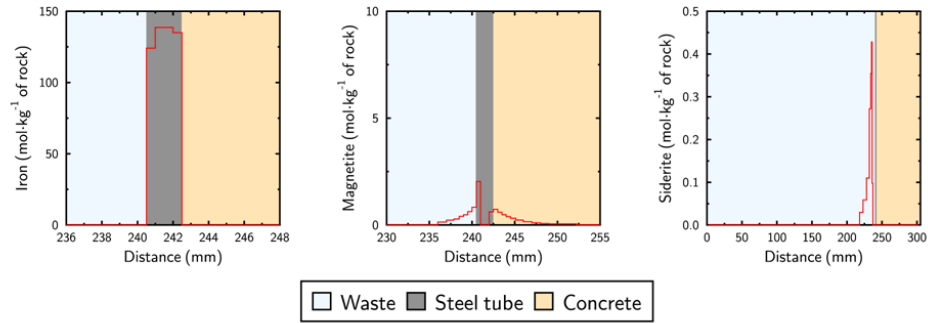


Figure 4-44: Simulated iron corrosion and corrosion products at 100 years

Simulated concrete alteration at 100 years is reported on Figure 4-45. Alteration profile was characterized by dissolution of portlandite followed by conversion of CSH1.6 to CSH1.2.

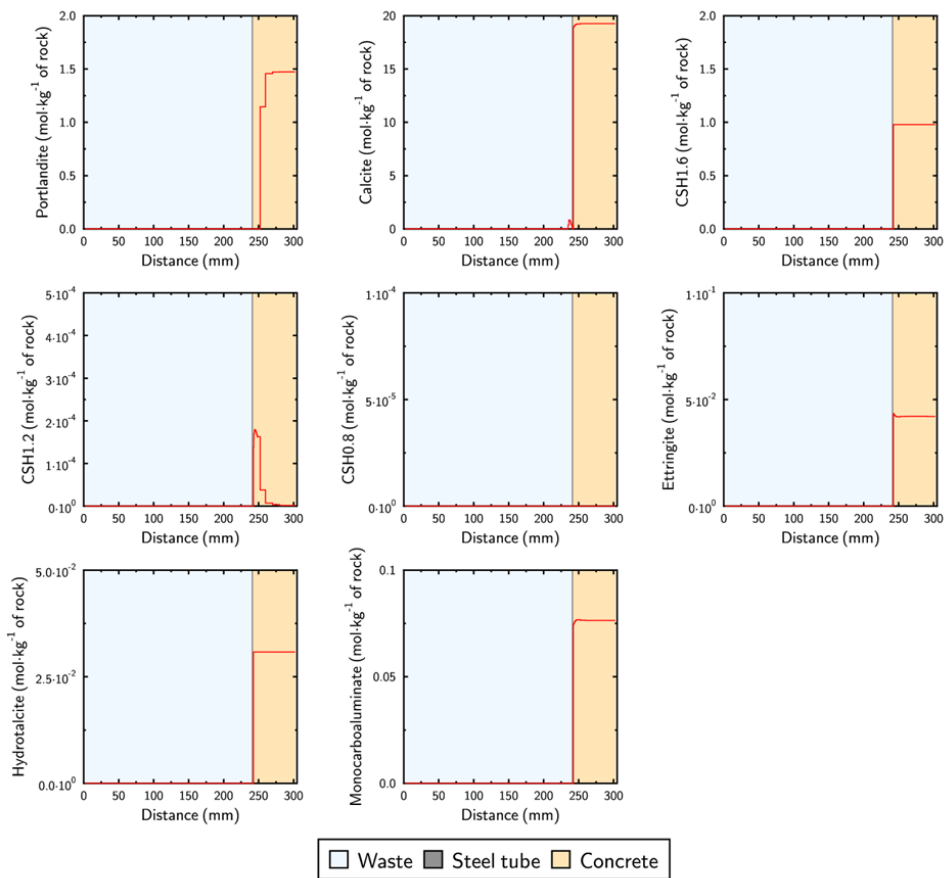


Figure 4-45: Simulated concrete alteration at 100 years.

5 Synthesis for upscaled modelling

5.1 Input from the experiments and their modelling

5.1.1 Gas generation from metal corrosion and organic matter degradation

The large-scale in situ Gas Generation Experiment established in Olkiluoto, Finland, provides the data representing coupled processes of organic waste degradation, pH buffering and microbial gas generation. Some aspects regarding gas generation, the composition of water sample, and microbial activities were monitored during a long-term period. Among them, the gas generation rates and composition are particularly important input for modelling. The gas generation rates were found increasing over time, with pH value of the tank water dropping from 11.5 to around 6.8. The composition of the generated gasses includes H₂, CH₄, CO₂, O₂ and N₂, with CH₄ as the first detected and dominant gas occupying a high-volume fraction between 50% and 90%. The volume fraction of CO₂ was measured during the first 9 years and at the later period of experiment, and it stabilised at a vol% of approximately 9.5%. The generated CO₂ is released out of the waste package, reacting with backfill cementitious material to form calcite, which deteriorates the performance of backfill material. The measured/calculated gas generation rates contribute to the modelling work, and the modelling in waste package can be upscaled to the scale of disposal cell predicting the long-term performance of cementitious backfill material, which has been planned in Task 4.2 in ACED.

BRGM extracted degradation model for cellulose (section 3.3.3) and PVC (section 3.3.4) by hydrolysis and radiolysis from literature and experiment carried out in CORI. These were used for modelling of chemical degradation of waste drum materials.

5.1.2 Water transport in concrete

COVRA extracted from their experiments data on water transport in concrete, that can be used to parameterize water transport models. Waste package concrete that is and has been manufactured for conditioning of compacted waste was investigated. Its water saturated permeability was determined by the formula in Millington and Quirk (1961) with the critical size in pores (r_c) and porosity (φ):

$$K_{sat} = \frac{1}{8} \varphi r_c^2$$

The critical size in pores (3.0 nm at 20°C) was determined from the characteristic pressure. This characteristic pressure is the reciprocal of the (temperature-dependent) α Genuchten parameter. The Genuchten parameters for this waste package concrete are presented in Mladenovic et al. (2024). These parameters have been determined in a range in relative humidity between 6% and 100%. The suction pressure for water becomes 380 MPa at a relative humidity of 6% and 20°C by which even water out of pores with a size of 0.38 nm is extracted. The samples were first exposed to tap water for 5 months in order to achieve saturation. Carbonation rims were negligible by which the change in weight of the samples could be solely attributed to the change in weight of the water content in the sample. Its porosity could therefore be gravimetrically determined and was 13%. The porosity could not gravimetrically be determined in the usual range of relative humidity from 50% till 100% since about half of the porosity volume required larger suction pressures to extract the water from this type of geological representative concrete.

For cubical concrete specimens that were initially saturated, Richards' equation was used in the prediction of the weight of water in the samples as a function of time during exposure to a relative humidity at a temperature of 5°C or 20°C. A physically unrealistic high pore compressibility needed to be used in order to have a good comparison between the measurements and modelling. The weight of water in the samples as a function of time can also be predicted with non-linear diffusion. Millington and Quirk (1961) also provided an expression for the unsaturated permeability of concrete. The same extrapolation with the saturation degree (S_w) was used for the diffusion coefficient for water and dissolved gas.

$$D_i = \frac{1}{16} D_0 \times \varphi^{\frac{4}{3}} \times S_w^{10/3}$$

A pre-factor of $1/16$ was needed in order to have a well comparison with the measurements and predictions for concrete exposed to a relative humidity between 40% and 100% with a (capillary) porosity of 13% and 21%. For gases, a Millington and Quirk a-like diffusion coefficient may be used in which the temperature dependent value for $D_{\text{gas},0}$ is 10.000 times the value of dissolved gas in water.

$$D_{\text{gas}} = \frac{1}{16} D_{\text{gas},0} \varphi^{4/3} (1 - S_w)^{10/3} \quad \text{if} \quad S_e < 1 - \left(\frac{1}{10.000}\right)^{3/10}$$

Concrete is initially unsaturated after hardening. But its initial saturation degree is usually guessed for modelling. For waste package concrete, there is sufficient evidence that initial saturation degree is 70% for fabricated waste package concrete with a porosity of 13%. This storage condition might cause a lower saturation degree at start of disposal. For a mortar (foamed concrete see section 3.2.1) with a (capillary) porosity of 21%, the initial saturation degree was even smaller i.e. 50%. That mortar, considered as a backfill to eliminate void volume of emplaced waste in a disposal tunnel, was also fabricated with a relatively low water to cement ratio of 0.36. Usually, low water to cement ratios are used to fabricate cementitious materials in order to enhance the durability.

5.2 Modelling the waste packages

5.2.1 Mixing tank models

The simple mixing tank model by PSI suggests that for completely corroding the steel inventory (~7000 kg) more than 3000 kg (~ 3 m³) of water is needed. Initially about 500 kg of water could be stored in the accessible porosity. Furthermore, after corrosion of all steel in a waste container, about 166000 mol of H₂ are released; at standard conditions, this corresponds to ~ 3720 m³.

The period for metal corrosion depends on the initial composition of the container infill mortar, and specifically on the reactivity of the aggregates. Any potential process that causes degradation of cementitious materials and lowers pore water pH will accelerate metal corrosion (cf. Figure 4-28). If aggregates are reactive and pH dependence of steel corrosion for pH 10.5 – 12 is assumed, corrosion of complete steel inventory takes about 1000 years, while for non-reactive aggregates and high pH (>12) this takes 100x longer.

The simple mixing tank model by PSI predicts that for the organic waste sort defined in the ACED project not excessive amounts of external water are needed to drive steel corrosion and cellulose degradation. If there is initially enough water present in the waste package, water consumption by before mentioned processes is balanced with water production by cement carbonation caused by CO₂ released during organic matter degradation. For a waste drum there are about 1070 mol of H₂ is released by steel corrosion, 100 mol CO₂ and 1100 CH₄.

Both waste degradation processes, steel corrosion and degradation of cellulose, happen at about the same time scale and are completed within a few thousands of years. Similarly cement degradation by aggregate-cement reaction and cement carbonation happen initially at similar time scales. In the end, carbonation will be the dominating process, because of pH decrease with cement degradation progress, dissolution of reactive aggregates will slow down, while CO₂ release by organic matter degradation will (only) slow down with decreasing organic matter inventory. One should note that the mixing tank model does not consider the influence of water saturation on chemical reactions and that therefore reaction rates are independent from saturation state of the waste package.

A comparison of the results of Section 4.4.1 with those of Wieland et al. (2018) shows, that the evolution of waste packages, the consumption of external water and the release of gases from the waste package is highly dependent on waste inventory, the amount of cement present and the assumptions on kinetics of reactions.

The above conclusion can be confirmed by comparison of the mixing tank calculations with those from the reactive transport model in section 4.4.2. A simple comparison gives apparent inconsistent results.

While the same chemical model is used, the mixing-tank model gives nearly constant water content, while the waste package in the UFZ models dries out relatively quickly. The reason for the different behaviour is, beside the absence of mass transport between waste package and its environment in the mixing tank model, that the mixing-tank calculations are based on the waste package setup given in Section 4.1, while the reactive transport model is based on the similar, but not identical, setup used also in Huang et al. (2021). On the one side, the setup from Section 4.1 contains significantly more fast degrading cellulose, which results for the assumed carbonation reactions (Section 4.3.1.4) in significantly higher release of water. On the other side, the mixing-tank model contains much less steel (waste), which drastically reduces water consumption by steel corrosion. The difference in material inventories is big enough to explain the more balanced consumption and release of water in the mixing tank model, while the reactive transport model shows a strong net consumption of water in the waste package.

5.2.2 Reactive transport in a drum

SCK CEN calculated the alterations in backfill mortar and concrete as a consequence of degradation of organic waste which produces CO₂. They explicitly considered drum geometry in their 2D coupled-reactive-diffusive transport model. They assumed fully water saturated conditions with diffusive transport of in water dissolved CO₂ only. It seems that under diffusive saturated conditions and in the considered time frame of few hundred years, there is a somewhat small reactive shell where CO₂ diffusing from the waste zone and Ca diffusing from the backfill meet and precipitate as calcite. Of course, the results presented here are for fully saturated conditions where CO₂ is only transported by diffusion in the aqueous phase. Location of a calcite shell or even the presence of such a calcite shell can be different in case the system is partially saturated; CO₂ can then diffuse in a much faster way throughout the porous system in the gas phase compared to Ca in the aqueous phase. It is then possible that a shell develops further from the waste zone; or even no shell development with CO₂ diffusion always quickly to the location of “fresh” cement phases. Information of saturation states at given moments obtained with the mixing-tank models from Section 4.4.2 or multiphase model from Section 4.4.2 could be combined with the more detailed geochemical calculations to evaluate precipitation fronts of calcite and degradation fronts of cement phases.

BRGM extracted degradation model for cellulose (section 3.3.3) and PVC (section 3.3.4) from literature and experiment carried out in CORI. Kinetics were implemented in a 1D model with radial geometry (Figure 4-18b). They found that the degradation of PVC releases HCl, which in turn would result in acidic conditions in waste compartment, where pH is not fully buffered by cement. The production of CO₂ by degradation of cellulose and PVC will contribute to acidic conditions in waste compartment and will cause carbonation of cementitious materials.

5.2.3 Water transport towards waste packages

All reactions with which water is consumed or produced have an impact of the transport of water within the disposal cell. Such calculations require a variable value for transport of water within all porous mediums in the disposal cell. Such calculations have been made by COVRA. ACED looks primarily at representative disposal cells. Representative values for transport of water within waste package concrete, their initial water content after fabrication and moisture storage function are essential to determine the extent of the reactions and their associated consequences. With these representative values and transport mechanism, it can be stated that the generation of hydrogen gas by anaerobic corrosion of steel is limited by the transport of water. Biodegradation requires larger saturation degrees of concrete than anaerobic corrosion of steel. Generation of carbon dioxide by biodegradation is therefore envisaged to take place only if water saturation in the waste material is high enough. Within the ACED project, the dependency of biodegradation of organic matter on water saturation is not considered by the PSI mixing tank model but included in the degradation rate of organic matter (see Eq. 4-19 and Table 4-20) in the UFZ two-phase multi-component model. In the UFZ model, the dependence of chemical reactions on saturation degree is included in form of a chemical reactivity factor.

Nevertheless, the relation could not be parameterized thoroughly due to lack of experimental data for specific reactions (organic matter degradation, metal corrosion).

5.2.4 Reactive multi-phase models

UFZ calculated the evolution of a waste container that contains several 200 l drums with organic waste embedded in cement backfill. They used a coupled reactive transport model simulating the component based two-phase flow process. Four gas components, including N₂, CO₂, CH₄ and H₂, are considered in the model. The gas flux is either generated by the kinetic degradation of organic matter or the corrosion of steel metal, which is pH dependent. In addition, the model also includes a look-up table for concrete degradation, which consumes some CO₂ gas and changes the pH (Huang et al.,2017; 2021).

The simulation results show how the water supply and gas generation feedback loop works in a waste package, in which the gas generation rates depend on the initial water availability and water transport, which in turn depends on gas pressure and properties of the backfill material and the host rock. Through the modelling results of the model, UFZ has identified and characterized four stages in the hydrological evolution of the multiple-drum container setup:

- Stage 1, 0 – 50 years: Initial pressure build up and dry out of the waste compartment. In this stage gas generation rates in the waste compartment are high and not reduced due to lack of water. Part of the water in the drum is expelled together with the generated gas from the drum.
- Stage 2, 50 – 70 years: Drying out of the drum infill mortar. After water in the waste compartment is consumed, gas generation rates are controlled by humidity transport from infill mortar towards the inner waste compartment.
- Stage 3, 70 – 120 years: Reversal of the liquid flux field in the backfill mortar and host rock. Most of the water in the drum is consumed and water flow transport out of the drum stops. Instead, water will enter the drum as the capillary suction inside the drums is higher than outside the drums.
- Stage 4, 120-200 years: Second decrease of gas generation rate. The system is in a transition state, where slowly an equilibrium between gas generation and a constant inflow of water from the container is approached after about 200 years.

To accurately model local drying and cement degradation within the waste container, it is crucial to employ a coupled model that considers the real material composition within the container, as well as for each waste drum. This, in turn, has a significant impact on gas production rates and the distribution of gases within the waste repository and its near field. The two-phase flow models by UFZ and the simplified diffusion model of COVRA show that for dry conditions water transport in the drum and water transport in the surrounding barriers is dominated by humidity transport in gas phase.

In a low ILW waste repository different mortar and cementitious material will be utilized. Therefore, UFZ conducted a sensitivity analysis showing the differences in gas generation rates and gas pressure evolution based on the hydraulic properties of the mortar. In the simplified model UFZ has focused only on the two primary hydraulic parameters: the van Genuchten characteristic pressure and the permeability, which proved highly valuable understanding in the feedback system. Additionally, parameters like porosity and initial water content depend on the mortar recipe. It's worth noting that the material properties of compressed waste inside a drum have uncertainties as well (see Huang et al. 2021). A sensitivity analysis for these parameters would also be of interest. In our model setup the main simplification is the small modelling domain. With a larger model domain including more drums and containers, the same amount of initial water in the drum and mortar may lead to higher gas pressure within the first 50 years of the repository evolution. This scenario needs to be investigated with a gallery-scale model simulation. For the future, an interesting prospect is to expand this model spatially. Specifically, UFZ could simulate a cross-section of a disposal gallery containing several stacked drum containers, employing various concrete and mortar materials. Such an approach would allow us to assess how container composition and waste density affect the evolution of gas production rates and the desaturated area in the near-field repository.

6 Recommendations for future experimental and numerical work

For a repository situated in a low-permeable clay host rock, release of the produced gas and inflow of water is limited. It might be possible that for such a situation, the transport of water in gas and/or liquid phase into the waste package could be a limiting process.

- This could be only investigated with help of process models on disposal cell space that couple two phase transport of gases and humidity with chemical reactions that change porosity and transport parameters.
- The modelling of the transport of water in unsaturated concrete is usually performed with transport mechanisms and parameter values that are only measured at fresh intact materials. For materials that are subject to long-term changes (e.g. cement degradation, clay-cement interaction, waste degradation, metal corrosion), material and transport parameters might drastically change. Currently, in nearly all modelling studies such changes are not considered.
- The alteration rate of waste highly depends on the availability of water and therefore more experimental data on the transport of water in geological disposal representative concrete is needed.
- The physical and/or chemical reasonability of parameter values used in models is usually not addressed in modelling but can be very important in the extent of predicted outcomes. It is therefore recommended that the experimental range from which the parameter values have been derived is indicated in any modelling.
- For example, the experimental range in relative humidity may have been too small for van Genuchten parameters obtained from a porous medium if the gravimetrically determined porosity is not provided as well.
- Upon transformation of steel into magnetite, the volume of solids will increase drastically. This would drastically increase internal stresses in the container and the surrounding.

The most influential long-term reactions were parameterized in terms of simple kinetic expressions. For many processes these expressions are conservative estimates and are not well supported by experimental data or process understanding. To reduce uncertainties and avoid overly conservative approaches that might significantly alter predicted evolution pathways for cementitious materials or the whole disposal cell further investigations are needed specifically for processes that produce gases and/or contribute to extended degradation of cementitious materials.

- In terms of model parameterization, the corrosion of steel at moderately high pH (pH 10.5 – 12) is not yet supported by experimental data. This is a sensitive pH range, as many (slightly degraded) cementitious materials have an equilibrium pH in this range.
- The long-term degradation of organic matter (abiotic and biotic) and its pH dependence specifically for slow degrading materials under repository conditions is not well understood. The gas generation rates were found significantly influenced by pH values. The rate can be increased 4 times faster with pH values dropping from 11.5 to around 6.8, which indicates the importance of placing cementitious material as a backfill material inside the waste packages.
- The expected initial saturation degrees of waste package concrete and backfill are significantly lower than often assumed in performance assessment studies. Waste package concrete is often initially unsaturated after manufacturing and storage under dry conditions. Low initial saturation degree is expected to slow down many chemical reactions, will hinder the microbial alteration of e.g. organic waste. This is important for disposal of especially radioactive waste since its hazard potential decays with time.
- It is generally accepted that a low water saturation of porous media will slow down various chemical processes. What is largely missing is an experimentally derived quantification of the slow down for the various processes (corrosion, degradation of organic matter, cement-aggregate reactions...) in relevant materials (cement-based materials, wastes...). Specifically for corrosion of steel (or metals in general) it was found that high amounts of water are needed to drive the reactions.

7 References

- Abadie, P.-M., 2018. National Inventory of Radioactive Materials and Waste 2019: the essentials, Catalogue of families, 2018 synthesis report, geographical inventory.
- Abrahamsen, L., Arnold, T., Brinkmann, H., Leys, N., Merroun, M., Mijndonckx, K., Moll, H., Polvika, P., Ševců, A., Small, J., Vikman, M., Wouters, K., 2015. A Review of Anthropogenic Organic Wastes and Their Degradation Behaviour, MIND D1.1, p. 97. Grant agreement no: 661880
- Advocat, T., Esnouf, S., Dauvois, V., Ferry, M., Caron, N., Ngono-Ravache, Y., Cochin, F., 2014. Quantification de la radiolyse des matériaux polymères contenus dans les colis de déchets MAVL, Sciences du démantèlement des installations nucléaires, Paris, Académie des Sciences, p. 25.
- Ahlström, J., 2015. Corrosion of steel in concrete at various moisture and chloride levels (Report 2015:133). Energiforsk.
- ACI, 2000. 116R-90: Cement and Concrete Terminology (Report ACI 116R-00). Farzam, H. (ACI C. 116 chairman), American Concrete Institute.
- Altmaier, M., Blin, V., García, D., Henocq, P., Missana, T., Ricard, D., 2021. State-of-the-art report on cement-organic-radionuclide interactions, CORI Technical Report. EURAD-Cori EJP, p. 97.
- Andra 2016a. Safety Options Report - Operating Part (DoS-Exp).
- Andra 2016b. Safety Options Report - Operating Part (DoS-AF).
- Atkinson, A., Goult, D.J., Hearne, J.A., 1985. An assessment of the long-term durability of concrete in radioactive waste repositories, Mat. Res. Soc. Symp. Proc. Materials Research Society, v. 50, p. 239-246. <https://doi.org/10.1557/PROC-50-239>
- Bažant, Z., Najjar, L., 1972. Nonlinear water diffusion in nonsaturated concrete. Mater. Constr. 5, 3–20. <https://doi.org/10.1007/BF02479073>
- Beckingham, L.E., Steefel, C.I., Swift, A.M., Voltolini, M., Yang, L., Anovitz, L.M., Sheets, J.M., Cole, D.R., Kneafsey, T.J., Mitnick, E.H., Zhang, S., Landrot, G., Ajo-Franklin, J.B., DePaolo, D.J., Mito, S., Xue, Z., 2017. Evaluation of accessible mineral surface areas for improved prediction of mineral reaction rates in porous media. Geochim. Cosmochim. Acta 205, 31–49. <https://doi.org/10.1016/j.gca.2017.02.006>
- Ben Zeineb, H., Le Milbeau, C., blanc, p., Ollivier, P., André, L., Boussafir, M., 2021a. Chemical degradation of polymers and additives in alkaline solution: influence of temperature, Goldschmidt 2021, Lyon, France.
- Ben Zeineb, H., Le Milbeau, C., blanc, p., Ollivier, P., André, L., Boussafir, M., 2021b. Fate of Plastics and Their Additives in Alkaline Solution at Different Temperatures, 30th International Meeting on Organic Geochemistry (IMOG 2021). European Association of Geoscientists & Engineers, Online, France, pp. 1-2.
- Berner, U.R., 1992. Evolution of pore water chemistry during degradation of cement in a radioactive waste repository environment. Waste Manag. 12, 201–219. [https://doi.org/10.1016/0956-053X\(92\)90049-O](https://doi.org/10.1016/0956-053X(92)90049-O)
- BNFL. 2002. "Drigg Post-Closure Safety Case: Near-Field Biogeochemistry." BNFL Report.
- Brantley, S.L., 2008. Kinetics of Mineral Dissolution, in: Kinetics of Water-Rock Interaction. Springer New York, New York, NY, pp. 151–210. https://doi.org/10.1007/978-0-387-73563-4_5
- Brown, A., Small, J., Pimblott, M., Goodacre, R., Lloyd, J.R., 2014. The impact of ionizing radiation on microbial cells pertinent to the storage, disposal and remediation of radioactive waste. The University of Manchester (United Kingdom), p. 43.

Cohen, S., 2006. Preliminary Review of the Degradation of Cellulosic, Plastic and Rubber Materials in the Waste Isolation Pilot Plant, Possible Effects on Magnesium Oxide Safety Factor Calculations. US EPA Document EP-D-05-002S. Prepared by Cohen and Associates, Vienna, Virginia, USA.

Colombani, J., 2006. Etude de la radiolyse gamma du poly(chlorure de vinyle) : application à l'étude de la dégradation par irradiation et par lixiviation du PVC industriel, p. 1 vol. (190 p.).

COMSOL, 2021. Subsurface Flow Module User's Guide <https://doc.comsol.com/6.0/doc/com.comsol.help.ssf/SubsurfaceFlowModuleUsersGuide>.

Dauzères A., Helson O., Churakov S., Montoya V., Zghondi J., Neeft E., Shao J., Cherkouk A., Mijndonckx K., Sellier A., Deissmann G., Arnold T., Lacarrière L., Griffa M., VIDAL T., Neji M., Bourbon X., Ibrahim L., Seigneur N., Poyet S., Bary B., Linard Y., Le Duc T., Hlavackova V., Pasteau A., Jantschik K., Middelhoff M., Perko J., Tri Phung Q., Seetharam S., Shan W., Singh A., Lloyd J., Vilarrasa V. (2022): Initial State of the Art on the chemo-mechanical evolution of cementitious materials in disposal conditions. Final version as of 09/11/2022 of deliverable D16.1 of the HORIZON 2020 project EURAD. EC Grant agreement no: 847593.

Deissmann, G., Ait Mouheb, N., Martin, C., Turrero, M.J., Torres, E., Kursten, B., Weetjens, E., Jacques, D., Cuevas, J., Samper, J., Montenegro, L., Leivo, M., Somervuori, M., Carpen, L., 2021. Experiments and numerical model studies on interfaces (Deliverable D2.5 of the HORIZON 2020 project EURAD. EC Grant agreement no: 847593). European Joint Programme on Radioactive Waste Management (EURAD).

Dienes, G.J., Vineyard, G.H., 1957. Radiation effects in solids, Interscience Publishers, Monographs in physics and astronomy.

Diomidis, N., 2014. Scientific basis for the production of gas due to corrosion in a deep geological repository (Nagra Arbeitsbericht NAB 14-21). Nagra, Wettingen, Switzerland.

Diomidis, N., Cloet, V., Leupin, O.X., Marschall, P., Poller, A., Stein, M., 2016. Production, consumption and transport of gases in deep geological repositories according to the Swiss disposal concept (Nagra Technical Report 16-03). Nagra, Wettingen, Switzerland.

Donohoe, C.J., 2010. The effect of ionizing radiation on the corrosion resistance of ILW containers, p. 25.

Ducamp, J., Bengaouer, A., Baurens, P., Fehete, I., Turek, P., Garin, F., 2018. Statu quo sur la méthanation du dioxyde de carbone : une revue de la littérature. Comptes Rendus Chimie 21, 427-469. <https://doi.org/10.1016/j.crci.2017.07.005>

Duro, L., Domènech, C., Grivé, M., Roman-Ross, G., Bruno, J., Källström, K., 2014. Assessment of the evolution of the redox conditions in a low and intermediate level nuclear waste repository (SFR1, Sweden). Appl. Geochemistry 49, 192–205. <https://doi.org/10.1016/j.apgeochem.2014.04.015>

Evans, R., Marconi, U.M.B., Tarazona, P., 1986. Fluids in narrow pores: Adsorption, capillary condensation, and critical points. J. Chem. Phys. 84, 2376–2399. <https://doi.org/10.1063/1.450352>

Lindgård, J., Andiç-Çakır, Ö., Fernandes, I., Rønning, T.F., Thomas, M.D. a., 2012. Alkali–silica reactions (ASR): Literature review on parameters influencing laboratory performance testing. Cem. Concr. Res. 42, 223–243. <https://doi.org/10.1016/j.cemconres.2011.10.004>

Fenchel, T., Blackburn, H., King, G. M., Blackburn, T. H. 2012. Bacterial biogeochemistry: the ecophysiology of mineral cycling. Academic press. <https://doi.org/10.1016/C2010-0-67238-5>

Fischer, C., Kurganskaya, I., Schäfer, T., Lüttge, A., 2014. Variability of crystal surface reactivity: What do we know? Appl. Geochemistry. <https://doi.org/10.1016/j.apgeochem.2014.02.002>

Furcas, F.E., Lothenbach, B., Isgor, O.B., Mundra, S., Zhang, Z., Angst, U.M., 2022. Solubility and speciation of iron in cementitious systems. Cement and Concrete Research 151, 106620. <https://doi.org/10.1016/j.cemconres.2021.106620>

Giffaut, E., Grivé, M., Blanc, P., Vieillard, P., Colàs, E., Gailhanou, H., Gaboreau, S., Marty, N., Madé, B., Duro, L., 2014. Andra thermodynamic database for performance assessment: ThermoChimie. *Applied Geochemistry* 49, 225-236. <https://doi.org/10.1016/j.apgeochem.2014.05.007>

Gin, S., Delanoe, A., Tocino, F., Ferrand, K., Goethals, J., Sterpenich, J., Fabian, M. 2023. High level radioactive waste package – Characterization of glass/steel/buffer interaction experiments. Final version as of 04.05.2023 of deliverable D2.12 of the HORIZON 2020 project EURAD. EC Grant agreement no: 847593.

Glaus, M.A., Van Loon, L.R., 2008. Degradation of Cellulose under Alkaline Conditions: New Insights from a 12 Years Degradation Study. *Environmental Science & Technology* 42, 2906-2911. <https://doi.org/10.1021/es7025517>

Glaus, M.A., Van Loon, L.R., 2009. Chemical reactivity of isosaccharinic acid in heterogeneous alkaline systems. Paul Scherrer Institute, p. 85.

Graham, J., R., Plant, Small J., D. Smalley. 2003. "Program User's Guide for the Code GRM, Version 4.1, BNFL Report 00/EN00127/7/1." Drigg Post-Closure Safety Case Report DTP/150.

Govaerts, J., Jacques, D., Samper, J., Neeft, E., Montoya, V., 2022. Model abstraction methods for upscaling and integration of process knowledge in reactive transport models for geological disposal of radioactive waste. Final version as of 10.01.2022 of deliverable D2.18 of the HORIZON 2020 project EURAD. EC Grant agreement no: 847593. <http://www.ejp-eurad.eu/>.

Grattan-Bellew, P.E., Katayama, T., 2019. So-Called Alkali-Carbonate Reaction (ACR), in: Sims, I., Poole, A. (Eds.), *Alkali-Aggregate Reaction in Concrete: A World Review*. CRC Press. <https://doi.org/10.1201/9781315708959-3>

Hewlett, P.C., 1998. *Lea's Chemistry of Cement and Concrete*, Lea's Chemistry of Cement and Concrete. Elsevier Ltd. <https://doi.org/10.1016/B978-0-7506-6256-7.X5007-3>

Höglund, L.O., 2014. The impact of concrete degradation on the BMA barrier functions, SKB report, R-13-40, p. 485.

Holz, M., Heila, S.R., Saccob, A., 2000. Temperature-dependent self-diffusion coefficients of water and six selected molecular liquids for calibration in accurate ¹H NMR PFG measurements, *Physical Chemistry Chemical Physics*, v. 2, p. 4740-4742. <https://doi.org/10.1039/B005319H>

Huang, Y., Nagel, T. & Shao, H. 2017. Comparing global and local implementations of nonlinear complementary problems for the modelling of multi-component two-phase flow with phase change phenomena. *Environ. Earth Sci.* 76, 643. <https://doi.org/10.1007/s12665-017-6970-5>

Huang, Y., Shao, H., Wieland, E., Kolditz, O., Kosakowski, G., 2018. A new approach to coupled two-phase reactive transport simulation for long-term degradation of concrete. *Construction and Building Materials* 190, 805–829. <https://doi.org/10.1016/j.conbuildmat.2018.09.114>

Huang, Y., Shao, H., Wieland, E., Kolditz, O., Kosakowski, G., 2021. Two-phase transport in a cemented waste package considering spatio-temporal evolution of chemical conditions. *npj Materials Degradation* 5, 4. <https://doi.org/10.1038/s41529-021-00150-z>

Holmén J G, Stigsson M, 2001. Modelling of future hydrogeological conditions at SFR. SKB R-01-02, Svensk Kärnbränslehantering AB.

IAEA, 2009. Classification of Radioactive waste (General Safety Guide No. GSG-1). Vienna, Austria. Retrieved from https://www-pub.iaea.org/MTCD/Publications/PDF/Pub1419_web.pdf

Idiart, A., Laviña, M., 2019. Modelling of concrete degradation in a one-million-year perspective – Hydro-chemical processes (SKB Report R-19-13). SKB, Solna, Sweden.

Jackson, M.D., Mulcahy, S.R., Chen, H., Li, Y., Li, Q., Cappelletti, P., Wenk, H.-R., 2017. Philipsite and Al-tobermite mineral cements produced through low-temperature water-rock reactions in Roman marine concrete. *American Mineralogist*, v. 102, no. 7, p. 1435-1450. <http://dx.doi.org/10.2138/am-2017-5993CCBY>

Jacques, D., Šimůnek, J., Mallants, D., van Genuchten, M.T. 2006. Operator-splitting errors in coupled reactive transport codes for transient variably saturated flow and contaminant transport in layered soil profiles. *Journal of Contaminant Hydrology* 88, 197-218. <https://doi.org/10.1016/j.jconhyd.2006.06.008>

Jacques, D., Simunek, J., Mallants, D. van Genuchten, M.T. 2018. The HPx software for multicomponent reactive transport during variably-saturated flow: Recent developments and applications. *Journal of Hydrology and Hydromechanics* 66(2), 211-226. <https://doi.org/10.1515/johh-2017-0049>

Jacques, D., Wang, L., Martens, E., Mallants, D., 2010. Modelling chemical degradation of concrete during leaching with rain and soil water types. *Cem. Concr. Res.* 40, 1306–1313. <https://doi.org/10.1016/j.cemconres.2010.02.008>

Jenni, A., Wersin, P., Thoenen, T., Baeyens, B., Ferrari, A., Gimmi, T., Mäder, U.K., Marschall, P., Hummel, W., Leupin, O.X., 2019. Bentonite backfill performance in a high-level waste repository: a geochemical perspective (Nagra Technical Report NTB 19-03). Wettingen, Switzerland.

Johnson, L., Marschall, P., Zuidema, P., Gribi, P., 2004. Effects of post-disposal gas generation in a repository for spent fuel, high-level waste and long-lived intermediate level waste sited in opalinus clay, Switzerland, p. 184.

Lamouroux, C., Cochin, F., 2012. Study of Long Term Behavior of Intermediate Level Long Lived Waste Packages: An Overview of the R&D Approach and Results. *Procedia Chemistry* 7, 559–566. <https://doi.org/10.1016/j.proche.2012.10.085>

Lasaga, A.C., 1981a. Transition state theory, in: Lasaga, Anthonio C., Kirkpatrick, J. (Eds.), *Kinetics of Geochemical Processes*. De Gruyter, Berlin, Boston, pp. 135–170. <https://doi.org/10.1515/9781501508233-008>

Lasaga, A.C., 1981b. Kinetics of geochemical processes, *Kinetics of Geochemical Processes, Reviews in Mineralogy Vol. 8*. De Gruyter, Berlin, Boston. <https://doi.org/10.1515/9781501508233>

Levasseur, S., Collin, F., Daniels, K., Dymitrowska, M., Harrington, J., Jacobs, E., Kolditz, O., Marschall, P., Norris, S., Sillen, Z., Talandier, J., Truche, L., Wedling, J., 2021 Initial State of the art on gas transport in clayey materials. Deliverable 6.1 of the HORIZON 2020 project EURAD, Work Package Gas. EC Grant agreement no: 847593

Knight, L., 2003. Scwat Hill, [http://www.natural-analogues.com/nawg-library/na-overviews/analogue review](http://www.natural-analogues.com/nawg-library/na-overviews/analogue-review).

Kolditz, O., Görke, U.-J., Shao, H., Wang, W. & Bauer, S. 2016. Thermo-Hydro-Mechanical-Chemical Processes in Fractured Porous Media: Modelling and Benchmarking. *Terrestrial Environmental Sciences*, Springer. <https://doi.org/10.1007/978-3-319-29224-3>

Kónya, J., Nagy, N.M., 2018. Nuclear and radiochemistry. Elsevier. <https://doi.org/10.1016/C2011-0-06943-0>

Koch, A.L. 1998. The Monod Model and Its Alternatives. In: Koch, A.L., Robinson, J.A., Milliken, G.A. (eds) *Mathematical Modeling in Microbial Ecology*. Chapman & Hall Microbiology Series. Springer, Boston, MA. https://doi.org/10.1007/978-1-4615-4078-6_4

Kosakowski, G., Berner, U., 2013. The evolution of clay rock/cement interfaces in a cementitious repository for low- and intermediate level radioactive waste. *Physics and Chemistry of the Earth, Parts A/B/C* 64, 65–86. <https://doi.org/10.1016/j.pce.2013.01.003>

Kosakowski, G., Berner, U., Wieland, E., Glaus, M.A., Degueldre, C., 2014. Geochemical evolution of the L/ILW near-field (Nagra Technical Report NTB 14-11). Nagra, Wettingen, Switzerland, Switzerland.

Kosakowski, G., Huang, Y., Wieland, E., 2020. Influence of material heterogeneities, process couplings and aggregate reactivity on the geochemical evolution of the L/ILW repository (Nagra Arbeitsberichte NAB 20-11). Wettingen, Switzerland.

Kosakowski, G., Wieland, E., 2022. Assessing the impact of chemical processes on the long-term evolution of waste packages by geochemical modelling, in: NUWCEM 2022 - International Symposium on Cement-Based Materials for Nuclear Wastes May 4-6 2022, Avignon, France. CEA.

Kosakowski, G., Churakov, S. V., Glaus, M.A., Typhaine, G., Hummel, W., Kulik, D.A., Ma, B., Martin, L., Miron, G.D., Prasianakis, N.I., 2023. Geochemical Evolution of the L/ILW - Near Field (Nagra Technical Report NTB 23-03). Nagra, Wettingen, Switzerland.

Kulik, D. A., 2011. Improving the structural consistency of C-S-H solid solution thermodynamic models. *Cem. Concr. Res.* 41, 477–495. <https://doi.org/10.1016/j.cemconres.2011.01.012>

Kurganskaya, I., Rohlfs, R.D., 2020. Atomistic to meso-scale modelling of mineral dissolution: Methods, challenges and prospects. *Am. J. Sci.* 320, 1–26. <https://doi.org/10.2475/01.2020.02>

Kursten, B., Druyts, F., Macdonald, D.D., Smart, N.R., Gens, R., Wang, L., Weetjens, E., Govaerts, J., 2011. Review of corrosion studies of metallic barrier in geological disposal conditions with respect to Belgian Supercontainer concept. *Corros. Eng. Sci. Technol.* 46, 91–97. <https://doi.org/10.1179/1743278210Y.0000000022>

Le Caër, S., 2011. Water Radiolysis: Influence of Oxide Surfaces on H₂ Production under Ionizing Radiation. *Water* 3, 235–253. <https://doi.org/10.3390/w3010235>

La Plante, E.C., Oey, T., Hsiao, Y.H., Perry, L., Bullard, J.W., Sant, G., 2019. Enhancing Silicate Dissolution Kinetics in Hyperalkaline Environments. *Journal of Physical Chemistry C* 123, 3687–3695. <https://doi.org/10.1021/acs.jpcc.8b12076>

Leemann, A., Katayama, T., Fernandes, I., Broekmans, M.A.T.M., 2016. Types of alkali–aggregate reactions and the products formed. *Proc. Inst. Civ. Eng. - Constr. Mater.* 169, 128–135. <https://doi.org/10.1680/jcoma.15.00059>

Leupin, O.X., Smith, P., Marschall, P., Johnson, L., Savage, D., Cloet, V., Schneider, J., Senger, R., 2016. Low- and intermediate-level waste repository-induced effects (Nagra Technical Report NTB 14-14). Nagra, Wettingen, Switzerland.

Levasseur, S., Collin, F., Daniels, K., Dymitrowska, M., Harrington, J., Jacops, E., Kolditz, O., Marschall, P., Norris, S., Sillen, X., Talandier, J., Truche, L., Wendling, J., 2021. Initial State of the Art on Gas Transport in Clayey Materials. Deliverable D6.1 of the HORIZON 2020 project EURAD, Work Package Gas. EC Grant agreement no: 847593., www.ejp-eurad.eu.

Lindgård, J., Andiç-Çakır, Ö., Fernandes, I., Rønning, T.F., Thomas, M.D. a., 2012. Alkali–silica reactions (ASR): Literature review on parameters influencing laboratory performance testing. *Cem. Concr. Res.* 42, 223–243. <https://doi.org/10.1016/j.cemconres.2011.10.004>

Liu, S., Jacques, D., Govaerts, J., Wang, L., 2014. Conceptual model analysis of interaction at a concrete–Boom Clay interface. *Phys. Chem. Earth, Parts A/B/C* 70–71, 150–159. <https://doi.org/10.1016/j.pce.2013.11.009>

Lothenbach, B., Wieland, E., 2006. A thermodynamic approach to the hydration of sulphate-resisting Portland cement. *Waste Manag.* 26, 706–19. <https://doi.org/10.1016/j.wasman.2006.01.023>

Lothenbach, B., Matschei, T., Möschner, G., Glasser, F.P., 2008. Thermodynamic modelling of the effect of temperature on the hydration and porosity of Portland cement. *Cem. Concr. Res.* 38, 1–18. <https://doi.org/10.1016/j.cemconres.2007.08.017>

Lothenbach, B., Kulik, D.A., Matschei, T., Balonis, M., Baquerizo, L., Dilnesa, B., Miron, G.D., Myers, R.J., 2019. Cemdata18: A chemical thermodynamic database for hydrated Portland cements and alkali-activated materials. *Cem. Concr. Res.* 115, 472–506. <https://doi.org/10.1016/j.cemconres.2018.04.018>

Lüttge, A., Arvidson, R.S., Fischer, C., 2013. A Stochastic Treatment of Crystal Dissolution Kinetics. *Elements* 9, 183–188. <https://doi.org/10.2113/gselements.9.3.183>

- Marty, N.C.M., Tournassat, C., Burnol, A., Giffaut, E., Gaucher, E.C., 2009. Influence of reaction kinetics and mesh refinement on the numerical modelling of concrete/clay interactions. *J. Hydrol.* 364, 58–72. <https://doi.org/10.1016/j.jhydrol.2008.10.013>
- Masateru, N., Masahiro, K., Takao, T., Kenji, N., Yoshitaka, I., 2007. Pozzolanic reactions between natural and artificial aggregate and the concrete matrix, in: 2007 World of Coal Ash (WOCA). p. 14.
- Massazza, F., 1998. Pozzolana and Pozzolanic Cements, in: *Lea's Chemistry of Cement and Concrete*. Elsevier, pp. 471–635. <https://doi.org/10.1016/B978-075066256-7/50022-9>
- Matschei, T., Lothenbach, B., Glasser, F.P., 2007. The role of calcium carbonate in cement hydration. *Cem. Concr. Res.* 37, 551–558. <https://doi.org/10.1016/J.CEMCONRES.2006.10.013>
- Marty, N.C.M., Claret, F., Lassin, A., Tremosa, J., Blanc, P., Madé, B., Giffaut, E., Cochapin, B., Tournassat, C., 2015. A database of dissolution and precipitation rates for clay-rocks minerals. *Appl. Geochemistry* 55, 108–118. <https://doi.org/10.1016/j.apgeochem.2014.10.012>
- Meeussen, J.C.L. 2003. ORCHESTRA: An object-oriented framework for implementing chemical equilibrium models. *Environmental Science & Technology* 37(6), 1175-1182. <https://doi.org/10.1021/es025597s>
- Millington, R.J., Quirk, J.P., 1961. Permeability of porous solids, *Transactions of the Faraday society*, v. 57, p. 1200-1207. <https://doi.org/10.1039/TF9615701200>
- Mladenovic, A., Neeft, E., Deissmann, G., Dähn, R., Geng, G., Koskowski, G., Markku, L., 2019. ILW: Report describing the selected experiments and the existing/expected experimental results. Final version as of 24.12.2019 of deliverable D2.11 of the HORIZON 2020 project EURAD. EC Grant agreement no: 847593., ejp-eurad.eu, p. 51.
- Mladenovic, A., E. Neeft, R. Dähn, Y. Gu, and L. Markku (2024): Intermediate level radioactive waste packages – Characterization of waste and backfill degradation experiments. Final version as of 18.01.2024 of deliverable D2.13 of the HORIZON 2020 project EURAD. EC Grant agreement No.: 847593.
- Moreno, L., Skagius, K., Södergren, S., Wiborgh, M., 2001. Gas related processes in SFR (SKB Rapport R-01-11). Swedish Nuclear Fuel and Waste Management Co, Stockholm, Sweden.
- Moropoulou, A., Bakolas, A., Aggelakopoulou, E., 2004. Evaluation of pozzolanic activity of natural and artificial pozzolans by thermal analysis. *Thermochim. Acta* 420, 135–140. <https://doi.org/10.1016/j.tca.2003.11.059>
- Nagra, 2008a. Modellhaftes Inventar für radioaktive Materialien MIRAM 08 (Nagra Technical Report NTB 08-06). Nagra, Wetingen, Switzerland.
- Nagra. 2008b: Effects of Post-disposal Gas Generation in a Repository for Low- and Intermediate-level Waste Sited in the Opalinus Clay of Northern Switzerland. (Nagra Technical Report NTB 08-07). Nagra, Wetingen, Switzerland.
- Nagra, 2014. Modellhaftes Inventar für radioaktive Materialien MIRAM 14 (Nagra Technical Report NTB 14-04). Nagra, Wetingen, Switzerland.
- Neeft, E., Jacques, D., Deissmann, G., 2022. Initial State of the Art on the assessment of the chemical evolution of ILW and HLW disposal cells. D 2.1 of the HORIZON 2020 project EURAD. EC Grant agreement no: 847593., <http://www.ejp-eurad.eu/>.
- Neeft, E., Weetjens E., Vokal A., Leivo M., Cochapin B., Martin C., Munier I., Deissmann G., Montoya V., Poskas P., Grigaliuniene D., Narkuniene A., García E., Samper J., Montenegro L., Mon A. 2019. Treatment of chemical evolution in National Programmes, D 2.4 of the HORIZON 2020 project EURAD. EC Grant agreement no: 847593.
- Neeft, E.A.C., 2004. Mechanical behaviour and diffusion of gas during neutron irradiation of actinides in ceramic inert matrices [Doctoral PhD]: Delft University of Technology.

- Noiriel, C., Daval, D., 2017. Pore-Scale Geochemical Reactivity Associated with CO₂ Storage: New Frontiers at the Fluid-Solid Interface. *Acc. Chem. Res.* 50, 759–768. <https://doi.org/10.1021/acs.accounts.7b00019>
- Papadakis, V.G., Vayenas, C.G., Fardis, M.N., 1991. Fundamental modelling and experimental investigation of concrete carbonation, *ACI Materials Journal* v. 88, no. 4, p. 363-373. <https://doi.org/10.14359/1863>
- Palandri, J.L., Kharaka, Y.K., 2004. A compilation of rate parameters of water-mineral interaction kinetics for application to geochemical modelling (Open File Report 2004-1068). U.S. Geological Survey, Menlo Park, California.
- Pabalan, R.T., Yang, L., Chiang, K. –T., 2013. Boric Acid Corrosion of Concrete Rebar. *EPJ Web Conf.* 56, 06005. <https://doi.org/10.1051/epjconf/20135606005>
- Parkhurst, David L., C. A. J. Appelo. 2013. "Description of input and examples for PHREEQC version 3—a computer program for speciation, batch-reaction, one-dimensional transport, and inverse geochemical calculations." *US geological survey techniques and methods* 6 (A43): 497.
- Poller, A., Mayer, G., Darcis, M., Smith, P., 2016. Modelling of Gas Generation in Deep Geological Repositories after Closure (Nagra Technical Report 16-04). Nagra, Wettingen, Switzerland.
- Poller, A., Smith, P., Mayer, G., Hayek, M. 2014. Modelling of radionuclide transport along the underground access structures of deep geological repositories (No. NTB--14-10). National Cooperative for the Disposal of Radioactive Waste (NAGRA).
- Poonosamy, J., Klinkenberg, M., Deissmann, G., Brandt, F., Bosbach, D., Mäder, U., Kosakowski, G., 2020. Effects of solution supersaturation on barite precipitation in porous media and consequences on permeability: Experiments and modelling. *Geochim. Cosmochim. Acta* 270, 43–60. <https://doi.org/10.1016/j.gca.2019.11.018>
- Prasianakis, N.I., Curti, E., Kosakowski, G., Poonosamy, J., Churakov, S. V., 2017. Deciphering pore-level precipitation mechanisms. *Sci. Rep.* 7, 13765. <https://doi.org/10.1038/s41598-017-14142-0>
- Roberge, P.R., 2019. Handbook of Corrosion Engineering, Third Edition, 3rd editio. ed. McGraw-Hill Education, New York.
- Román-Ross, G., Idiart, A., Grandia, F., Silva, O., Duro, L., 2015. Evaluation of a gas experiment Phase I, Final Report – Literature review and scoping calculations. ENSI, Brugg, Switzerland, p. 84.
- Russell, D., Basheer, P.A.M., Rankin, G.I.B., Long, A.E., 2001. Effect of relative humidity and air permeability on prediction of the rate of carbonation of concrete. *Proc. Inst. Civ. Eng. - Struct. Build.* 146, 319–326. <https://doi.org/10.1680/stbu.2001.146.3.319>
- Samper, J, Lu, C., Montenegro, L., 2008. Coupled hydrogeochemical calculations of the interactions of corrosion products and bentonite, *Physics and Chemistry of the Earth* 33 306–316. URL: <https://doi:10.1016/j.pce.2008.10.009>.
- Samper J., Montenegro L., De Windt L., Montoya V., Garibay-Rodríguez J., Grigaliuniene D., Narkuniene A., Poskas P., Cochapin, B., 2022: Conceptual model formulation for a mechanistic based model implementing the initial SOTA knowledge (models and parameters) in existing numerical tools. Final version as of 15.07.2022 of deliverable D2.16 of the HORIZON 2020 project EURAD. EC Grant agreement no: 847593.
- Samson, E., Marchand, J., 2007. Modelling the transport of ions in unsaturated cement-based materials, *Computers and Structures*, v. 85, p. 1740-1756. <https://doi.org/10.1016/j.compstruc.2007.04.008>
- Šavija, B., Luković, M., 2016. Carbonation of cement paste: Understanding, challenges, and opportunities. *Constr. Build. Mater.* 117, 285–301. <https://doi.org/10.1016/j.conbuildmat.2016.04.138>

- Shah, V., Bishnoi, S., 2021. Understanding the process of carbonation in concrete using numerical modelling, *Journal of advanced concrete technology*, v. 19, p. 1148-1161. <https://doi.org/10.3151/jact.19.1148>
- Shi, C., Day, R.L., 2001. Comparison of different methods for enhancing reactivity of pozzolans. *Cem. Concr. Res.* 31, 813–818. [https://doi.org/10.1016/S0008-8846\(01\)00481-1](https://doi.org/10.1016/S0008-8846(01)00481-1)
- Shi, C., Wu, Y., Riefler, C., Wang, H., 2005. Characteristics and pozzolanic reactivity of glass powders. *Cem. Concr. Res.* 35, 987–993. <https://doi.org/10.1016/j.cemconres.2004.05.015>
- Silva, O., Coene, E., Molinero, J., Lavina, M., Idiart, A.E., 2019. Gas release from the BHK vault – Multiphase flow modelling of the near-field (SKB Report R-19-06). SKB, Solna, Sweden.
- Simunek, J., Brunetti, G., Jacques, D., van Genuchten, M.T., Sejna, M. 2024. Developments and Applications of the HYDRUS Computer Software Packages since 2016. *Vadose Zone Journal*, e20310. <https://doi.org/10.1002/vzj2.20310>
- Simunek, J., Sejna, M., Brunetti, G. and van Genuchten, M.T., 2022a. The HYDRUS Software Package for Simulating One-, Two-, and Three-Dimensional Movement of Water, Heat, and Multiple Solutes in Variably-Saturated Porous Media, Technical Manual I, Hydrus 1D, Version 5.x. p. 334, PC Progress, Prague, Czech Republic.
- Simunek, J., van Genuchten, M.T. and Sejna, M., 2022b. The HYDRUS Software Package for Simulating One-, Two-, and Three-Dimensional Movement of Water, Heat, and Multiple Solutes in Variably-Saturated Porous Media, Technical Manual II, Hydrus 2D/3D, Version 5.x. p. 283, PC Progress, Prague, Czech Republic.
- Sims, I., Brown, B., 1998. Concrete Aggregates, in: *Lea's Chemistry of Cement and Concrete*. Elsevier, pp. 907–1015. <https://doi.org/10.1016/B978-075066256-7/50028-X>
- Small, J., S., Nykyri, M., Vikman, M., Itävaara, M., Heikinheimo, L., 2017. "The biogeochemistry of gas generation from low-level nuclear waste: Modelling after 18 years study under in situ conditions." *Applied Geochemistry* 84: 360-372. <https://doi.org/10.1016/j.apgeochem.2017.07.012>
- Small, J., Nykyri, M., Helin, M., Hovi, U., Sarlin, T., Itävaara, M., 2008. "Experimental and modelling investigations of the biogeochemistry of gas production from low and intermediate level radioactive waste." *Applied Geochemistry* 23 (6): 1383-1418. <https://doi.org/10.1016/j.apgeochem.2007.11.020>
- Smart, N.R., Blackwood, D.J., Marsh, G.P., Naish, C.C., O'Brien, T.M., Rance, A.P., Thomas, M.I., 2004. The anaerobic corrosion of carbon and stainless steel in simulated cementitious repository environments: A summary review of Nirex Research (Report AEAT/ERRA-0313). AEA Technology, Harwell, UK.
- Stankovskiy, A., 2011. Calculation of decay power release, activity and absorbed dose in Eurobitum intermediate level waste. SCK-CEN, Mol, Belgium.
- Stefanoni, M., Angst, U.M., Elsener, B., 2018. Electrochemistry and capillary condensation theory reveal the mechanism of corrosion in dense porous media, *Nature Scientific Reports*, v. 8, no. 7407, p. 1-10. <https://doi.org/10.1038/s41598-018-25794-x>
- Stein, M., 2014. Erläuterungen zur Verpackung radioaktiver Abfälle im Endlagerbehälter (Arbeitsbericht NAB 14-104). Nagra, Wettingen, Switzerland.
- Steiner, S., Lothenbach, B., Proske, T., Borgschulte, A., Winnefeld, F., 2020. Effect of relative humidity on the carbonation rate of portlandite, calcium silicate hydrates and ettringite. *Cem. Concr. Res.* 135, 106116. <https://doi.org/10.1016/j.cemconres.2020.106116>
- Suckling, P., Avis, J., Humphreys, P., King, F., 2011. T2GGM Version 2: Gas Generation and Transport Code (Report NWMO DGR-TR-2011-33). Nuclear Waste Management Organization (Canada), Toronto, Canada.

Swanson, J.S., Cherkouk, A., Arnold, T., Meleshyn, A., Reed, D.T., 2018. Microbial Influence on the Performance of Subsurface, Salt-Based Radioactive Waste Repositories. An Evaluation Based on Microbial Ecology, Bioenergetics and Projected Repository Conditions., NEA No. 7387.

Swenson, E.G., Gillott, J.E., 1964. Alkali-carbonate rock reaction. *Highw. Res. Rec.* 45, 21–40.

Tecon, R., Or, D., 2017. Biophysical processes supporting the diversity of microbial life in soil. *FEMS Microbiology Reviews* 41, 599–623. <https://doi.org/10.1093/FEMSRE/FUX039>

Thoenen, T., Hummel, W., Berner, U., Curti, E., 2014. The PSI/Nagra chemical thermodynamic database 12/07 (PSI Bericht Nr. 14-04). Paul Scherrer Institut, Villigen, Switzerland.

Thomas, M.D.A., Fournier, B., Folliard, K.J., 2013. Alkali-Aggregate Reactivity (AAR) Facts Book (Report FHWA-HIF-13-019), Book. U.S. Department of Transportation, Federal Highway Administration.

Thouvenot, P., Bildstein, O., Munier, I., Cochevin, B., Poyet, S., Bourbon, X., Treille, E., 2013. Modelling of concrete carbonation in deep geological disposal of intermediate level waste. *EPJ Web Conf.* 56, 05004. <https://doi.org/10.1051/epjconf/20135605004>

Tofts, P.S., Lloyd, D., Clark, C.A., Barker, G.J., Parker, G.J.M., McConville, P., Baldock, C., Pope, J.M., 2000. Test Liquids for Quantitative MRI Measurements of Self-Diffusion Coefficient In Vivo, *Magnetic Resonance in Medicine*, v. 43, p. 368-374. [https://doi.org/10.1002/\(SICI\)1522-2594\(200003\)43:3<368::AID-MRM8>3.0.CO;2-B](https://doi.org/10.1002/(SICI)1522-2594(200003)43:3<368::AID-MRM8>3.0.CO;2-B)

Trotignon, L., Thouvenot, P., Munier, I., Cochevin, B., Piault, E., Treille, E., Bourbon, X., Mimid, S., 2011. Numerical Simulation of Atmospheric Carbonation of Concrete Components in a Deep Geological Radwaste Disposal Site During Operating Period. *Nucl. Technol.* 174, 424–437. <https://doi.org/10.13182/NT11-A11750>

Uras, S., Zovini, C., Paratore, A., Tits, J., Pflingsten, W., Dahn, R., Meeussen, H., Seetharam, S.C., 2021. State of the art in packaging, storage, and monitoring of cemented wastes (Deliverable 7.1 of the Predis project), EC Grant Agreement No. No 945098.

van Eijk, R.J., Brouwers, H.J.H., 2000. Prediction of hydroxyl concentrations in cement pore water using a numerical cement hydration model, *Cement and Concrete Research*, v. 30, no. 11, p. 1801-1806. [https://doi.org/10.1016/S0008-8846\(00\)00413-0](https://doi.org/10.1016/S0008-8846(00)00413-0)

van Genuchten, M.T., 1980. A closed form equation for predicting the hydraulic conductivity of unsaturated soils, *Soil. Sci. Soc. Am. J.*, v. 44, p. 892-989. <https://doi.org/10.2136/sssaj1980.03615995004400050002x>

van Loon, L., Glaus, M., 1997. Review of the kinetics of alkaline degradation of cellulose in view of its relevance for safety assessment of radioactive waste repositories. *Journal of Polymers and the Environment* 5, 97-109. <https://doi.org/10.1007/BF02763593>

Vehmas, T., Itälä, A., 2019. Compositional parameters for solid solution C-S-H and the applicability to thermodynamic modelling, KIT Scientific reports 7752: Proceedings of the Second Workshop of the Horizon 2020 Cebama project, p. 293-300.

Vehmas, T., Leivo, M., Holt, E., Alonso, M.C., García, J.L., Fernández, A., Isaacs, M., Rastrick, E., Read, D., Vašíček, R., Hloušek, J., Hausmannová, L., Večerník, P., Červinka, R., Havlová, V., Lange, S., Klinkenberg, M., Bosbach, D., Deissmann, G., Montoya, V., Mouheb, N.A., Adam, C., Schild, D., Schäfer, T., (2017). Published, Cebama reference mix design for low-pH concrete and paste, preliminary characterisation, in Proceedings 2nd Annual Workshop of the Collaborative Project CEBAMA, Espoo (Finland), Place, Published, KIT Scientific Reports 7752, p. 149-160.

Venhuis, M.A., Reardon, E.J., 2001. Vacuum Method for Carbonation of Cementitious Wasteforms. *Environ. Sci. Technol.* 35, 4120–4125. <https://doi.org/10.1021/es0105156>

Velbel, M.A., 1990. Influence of Temperature and Mineral Surface Characteristics on Feldspar Weathering Rates in Natural and Artificial Systems: A First Approximation. *Water Resour. Res.* 26, 3049–3053. <https://doi.org/10.1029/WR026i012p03049>

Vernaz, E., Bonin, B., 2008. Conditionnement des déchets nucléaires. CEA Saclay; Groupe Moniteur.

Vikman, M., Sohlberg, E., 2022, The influence of chemical conditions on gas generation in the disposal of low level maintenance waste (KaMu), VTT Technical Research Centre of Finland. 23 p. VTT Research Report; No. VTT-R-00151-22

von Greve-Dierfeld, S., Lothenbach, B., Vollpracht, A., Wu, B., Huet, B., Andrade, C., Medina, C., Thiel, C., Gruyaert, E., Vanoutrive, H., Saéz del Bosque, F., Ignjatovic, I., Elsen, J., Provis, J.L., Scrivener, K., Thienel, K.-C., Sideris, K., Zajac, M., Alderete, N., Cizer, O., Van den Heede, P., Hooton, D.H., Kamali-Bernard, S., Bernal, S.A., Zhao, Z., Shi, Z., De Belie, N., 2020. Understanding the carbonation of concrete with supplementary cementitious materials: a critical review by RILEM TC 281-CCC, *Materials and Structures*, v. 53, no. 136, p. 34. <https://doi.org/10.1617/s11527-020-01558-w>

von Greve-Dierfeld, S.M., 2015. Bemessungsregeln zur Sicherstellung der Dauerhaftigkeit XC-exponierter Stahlbetonbauteile: Technische Universität München.

Wagner, T., Kulik, D.A., Hingerl, F.F., Dmytrieva, S. V., 2012. GEM-SELEKTOR geochemical modelling package: TSolMod library and data interface for multicomponent phase models. *Can. Mineral.* 50, 1173–1195. <https://doi.org/10.3749/canmin.50.5.1173>

Warthmann, R., Mosberger, L., Baier, U., 2013. Langzeit-Degradation von organischen Polymeren unter SMA-Tiefenlagerbedingungen (Nagra Technical Report NTB 13-04). Nagra, Wettingen, Switzerland.

Watkinson, D., Lewis, M., 2004. ss Great Britain iron hull: modelling corrosion to define storage relative humidity, in: *Metal 2004*. pp. 88–102.

White, A.F., Brantley, S.L., 2003. The effect of time on the weathering of silicate minerals: why do weathering rates differ in the laboratory and field? *Chem. Geol.* 202, 479–506. <https://doi.org/10.1016/j.chemgeo.2003.03.001>

Wieland, E., Kosakowski, G., Lothenbach, B., Kulik, D.A., Cloet, V., 2018. Preliminary assessment of the temporal evolution of waste packages in the near field of the L/ILW repository (Nagra Arbeitsbericht NAB 18-05). Nagra, Wettingen, Switzerland.

Wieland E, Kosakowski G, Lothenbach B, Kulik DA, 2020. Geochemical modelling of the effect of waste degradation processes on the long-term performance of waste forms. *Appl Geochemistry* 115:104539. <https://doi.org/10.1016/j.apgeochem.2020.104539>

Pozzolanic activity - Wikipedia [WWW Document], n.d. URL https://en.wikipedia.org/wiki/Pozzolanic_activity#Reaction (accessed 9.25.20).

De Windt, L., Miron, G.D., Fabian, M., Goethals, J., Wittebroodt, C., 2020. First results on the thermodynamic databases and reactive transport models for steel-cement interfaces at high temperature (Final version as of 18.02.2021 of deliverable D2.8 of the HORIZON 2020 project EURAD. EC Grant agreement no: 847593).

Winter, N.B., 2009. Understanding Cement: An introduction to cement production, cement hydration and deleterious processes in concrete. WHD Microanalysis Consultants, Woodbridge, UK.

Xu, T., Senger, R., Finsterle, S., 2008. Corrosion-induced gas generation in a nuclear waste repository: Reactive geochemistry and multiphase flow effects. *Appl. Geochemistry* 23, 3423–3433. <https://doi.org/10.1016/j.apgeochem.2008.07.012>

Zhu, C., 2005. In situ feldspar dissolution rates in an aquifer. *Geochim. Cosmochim. Acta* 69, 1435–1453. <https://doi.org/10.1016/j.gca.2004.09.005>